DENSITY DRIVEN VORTEX MOTION IN NARROW CHANNEL SUPERCONDUCTORS

by

JONATHAN STEWART WATKINS

A thesis submitted to
The University of Birmingham
for the degree of
DOCTOR OF PHILOSOPHY

School of Physics and Astronomy
The University of Birmingham

September 24th, 2015

Abstract

We present simulations and continuum calculations of the rheology and structure of vortex matter confined to flow in narrow channels.

First, through the use of Langevin dynamics we perform two-dimensional Couette flow simulations of the vortex liquid in a homogeneous magnetic field. In this sheared geometry we report wall slip at the channel boundary for high shear rates. A result that contrasts with the Newtonian constitutive relation suggested by Marchetti and Nelson(Marchetti, M. C. & Nelson, D. R. *Phys. Rev. B* **42** , 9938 (1990)). We also find structural ordering near the solid channel boundaries above the bulk melting temperature, T_m^{bulk}.

We also present simulations and analysis of a novel field gradient applied to a narrow channel superconductor. Here the "solid" vortex lattice flows plastically by enlisting two distinct populations of dislocations. One that relaxes density along the channel and the other that relaxes shear stresses at the boundary. In spite of the lack of a commensurate field over the majority of the channel, the vortex glass remains commensurate with the width of the channel along its entire length by stretching parallel to the flow direction. This non-equilibrium system reaches a steady-state marked by a stable density profile and localised repeatable non-linear dislocation motion. We are further able to show the source of this non-linearity is due to image forces in the channel edges.

For wider channels we discuss and implement a novel vortex reservoir geometry designed to generate a continuous source of circular grain boundary scars - *bubbles*. The presence of the bubbles in the channel does not alter the density of the channel but does disturb the steady-state structure and motion of the other populations of dislocations.

Finally we discuss the details of a new versatile simulation software that was created for this research, VLSim. This software utilises object-orientation techniques to allow fast future prototyping of varied geometry and magnetic fields.

To my family

Acknowledgements

I must first thank my wife, Jen. Without you this would never have been possible. Your support with the children and positive attitude have kept me going for the past four years. To my children, Oliver, Molly, Esme and Bodhi, thank you for your patience through the last few months. Hopefully, from now onwards, we can read bedtime stories in person instead of over FaceTime. You are a wonderful family and I feel so lucky to have the support and love of you all.

To my parents, who have helped in more ways than I can list. It seems surreal that we are here and I have you to thank for unwavering support, love and kindness.

Very special thanks must be extended to my supervisor, Dr. Nicola Wilkin. Despite being the busiest person I have ever met, your tireless support over the past four years is the primary reason that I have been able to complete this thesis. You have supported me, not only with the PhD, but in all aspects of my work and home life. It has been very trying at times and I am eternally grateful to you.

I also wish to thank Professor Mike Gunn for his enlightening conversations and silent support. You too have helped me in immeasurable ways that I can probably never repay, but for which I am very grateful.

To all my friends in the theory group, past and present. You have all kept me sane through the years with conversations about anything but physics. I have loved coming to work for the past four years because of you all.

Contents

List of Figures

Chapter 1

MOTIVATION

The results presented in this thesis focus on the structure and rheology of vortex matter in narrow channel superconductors. Vortex matter in its ground state forms a triangular lattice at low temperatures. Due to thermal fluctuations, inhomogeneous magnetic fields, stress fields or geometric constraints, this structure can contain defects called dislocations, marking local regions where the 6-fold symmetry of a pair of neighbouring vortices has been replaced by a pair of vortices, that are 5 and 7 fold coordinated respectively. Dislocations will prove central to the research described; a simple picture of a dislocations in both a square and triangular geometry is shown in Fig. 1.1.

Dislocations are ubiquitous in the physical sciences. They are topological objects that emerge out of the underlying structure of a system. Intensively studied, many aspects of dislocations are well understood, for instance how they interact with stresses in the system and with each other. However, properties such as their maximum speeds still have no complete description. A microscopic description of plasticity requires the presence of dislocations. Dislocations provide a mechanism by which planes of material are able to shear against each other. Due to their ubiquitous nature, exploration of dislocations in one system can shed light on aspects of dislocations in physically unrelated systems.

To demonstrate the range of physical systems which dislocations are relevant, we highlight here a few diverse examples. Here we will present a small selection from different fields of the physical sciences. Imaging dislocations in different systems is reliant on

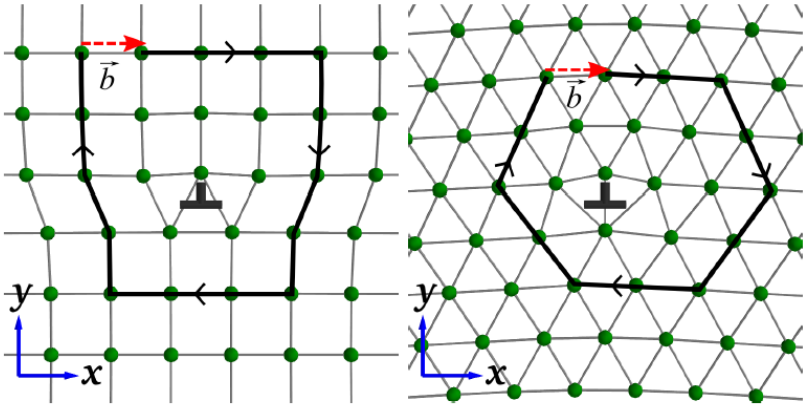

Figure 1.1: **a** Dislocation in a square lattice. **b** Dislocation in a triangular lattice. The 'T' shape marks the centre of the dislocation, and points towards an extra row of additional material that creates the dislocation. Figure from Ref[1].

the ability to image the underlying material structure. This often requires advanced techniques. For example using electron tomography and 3D Fourier filtering Chen *et al.*[2] were able to produce images of the core structure of 3D dislocations at atomic resolution, Fig. 1.2.

Other systems are easier to image. A popular system is that of bubble rafts, Fig. 1.3. These rafts of bubbles floated on the surface of water provide a two-dimensional system to explore dislocations on the macroscale.

Dislocations are also relevant in microscopic biological systems. Recent work by Amir *et al.*[1], explored the growth, by elongation, of E-coli bacteria. They showed that dislocations were a plausible mechanism by which new structural material is added to the walls of these bacteria. The hexagonal structure in Fig. 1.4 shows the dislocation mechanism they suggested. The presence of dislocations can be inferred by tracking fluorescently labeled proteins, such as MreB, whose position strongly correlates with the sites where material is added to the structure.

A branch of materials science that has proved to be very fertile ground for the study of dislocations is colloids. These two-phase systems have highly tuneable complicated structures. Fig. 1.6 shows a confocal microscope image of rod shaped silica arrange in rows. The dislocations in this structure are easily seen in the images, marked by a

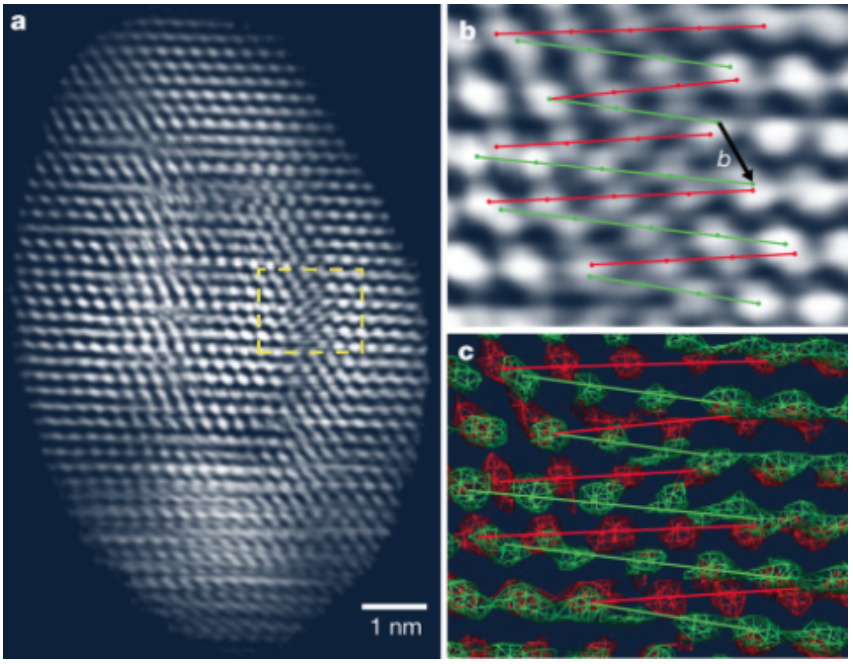

Figure 1.2: Three-dimensional imaging of dislocations in a nanoparticle at atomic resolution. Figure from Ref[2].

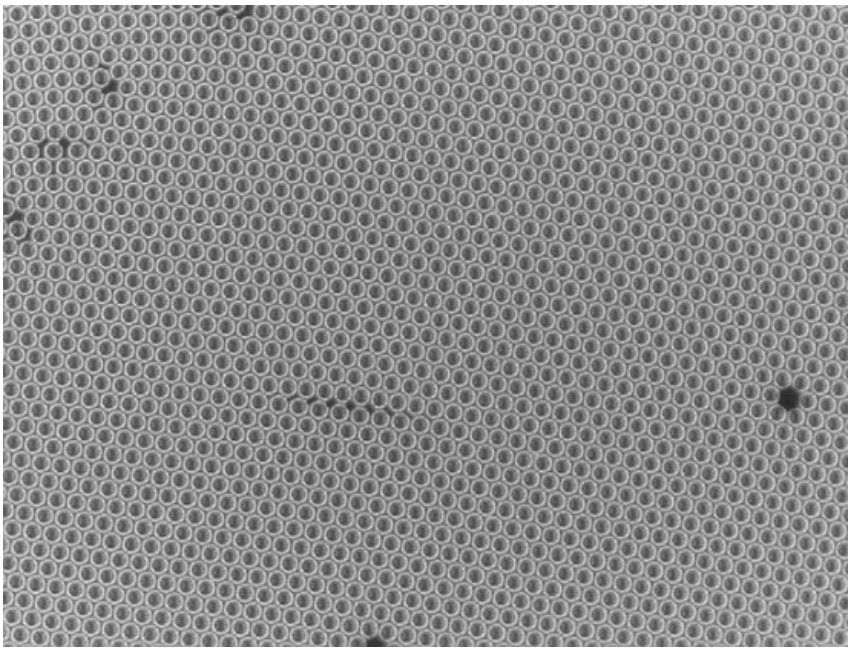

Figure 1.3: Bubble rafts showing dislocations, vacancies and grain boundaries. Figure from Ref[3].

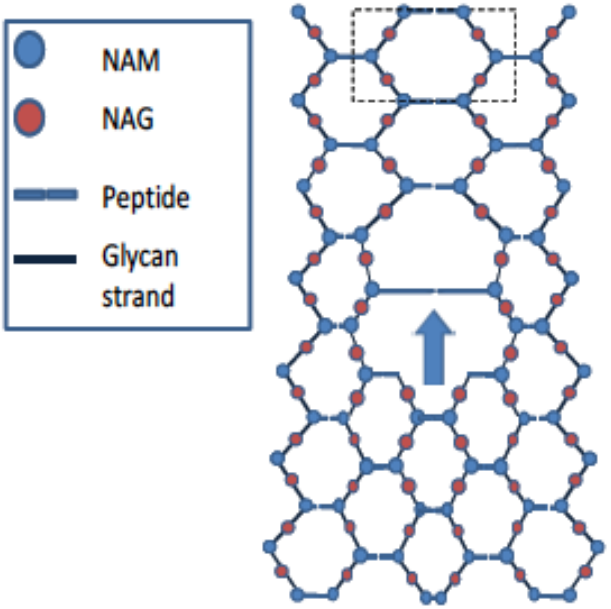

Figure 1.4: Glycan strands added into the peptidoglycan mesh at the site of an edge dislocation in the Bacteria cell wall. Figure from Ref[1].

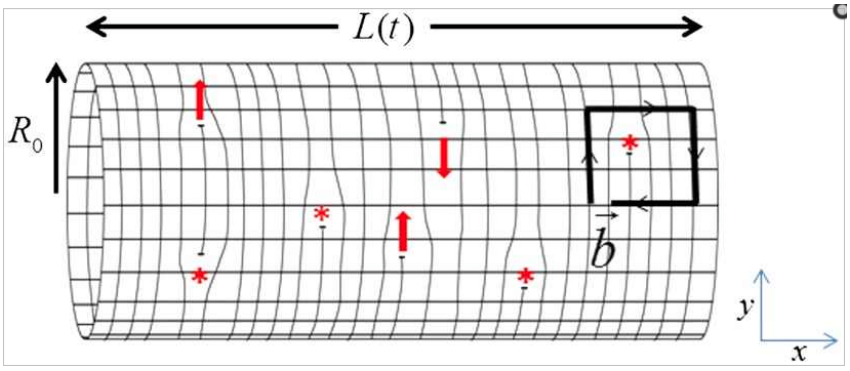

Figure 1.5: Dislocation-mediated growth of bacterial cell walls. Schematic illustration of active (arrows) and inactive (asterisk) dislocations in an otherwise ordered peptidoglycan mesh. The dislocations with arrows attached are activated by the enzymatic machinery and move with velocity v. Those with asterisks are inactive. Figure from Ref[1].

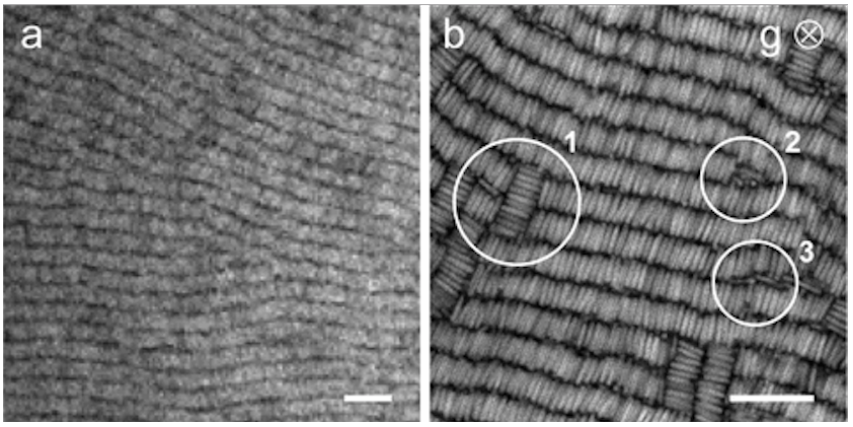

Figure 1.6: Confocal microscopy images of colloidal silica rods showing several types of defects including edge dislocations. Figure from Ref[4].

transition from 2 to 1 rows of rods.

Finally, dislocations have been imaged by a range of methods in superconducting vortex matter. Fig. 1.7 shows a dislocations in Nb, imaged using a Lorentz force microscope[5].

For this thesis we choose to examine the properties of vortex matter in thin channel geometries. Much like colloidal systems these systems are highly tuneable. Interaction strengths of the vortex material, sizes of elastic moduli and density of the system are all easily altered, often by orders of magnitudes.

1.1 Thin Channel Low Dimensional Superconductors

Thin channel superconductors are formed by etching a channel of width w and length L out of a double layer of superconducting material. A popular[26] choice is aNb_3Ge/NbN. The thin top layer is made of NbN and is $\sim$ 50nm thick. The bottom layer is made from a layer of aNb_3Ge often around 500nm thick. The etch is to reveal a channel of aNb_3Ge between walls of NbN. The geometry of this system can be seen in Fig. 1.8. When this channel is placed in a magnetic field at very low temperature, vortices form that thread the channel perpendicular to the surface. The vortices in the channel edges become pinned to material defects in NbN but are essentially free to move in the weak pinning environment of the aNb_3Ge channel. Each vortex carries a quantum of magnetic

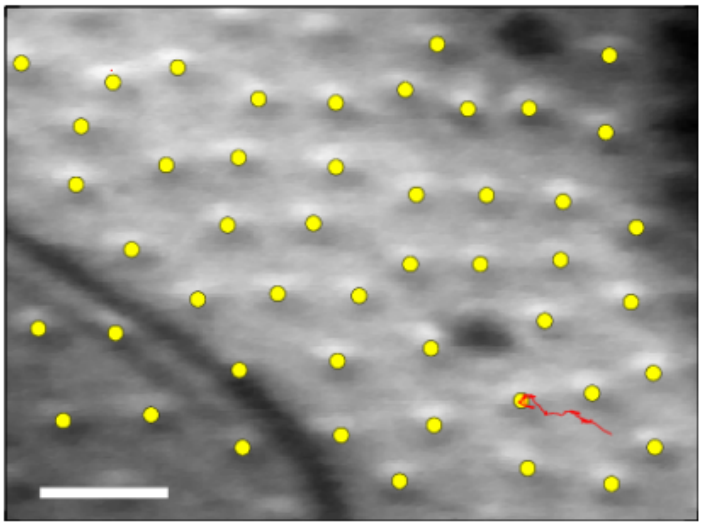

Figure 1.7: Lorentz Force measurements of a Nb narrow channel shows defects in the triangular lattice. Figure from Ref[5].

flux so the number of vortices for a given field can be calculated.

From Fig. 1.8 we see the vortices line up such that rows emerge that are parallel to the channel edges.

The motivation of this thesis comes from the many groups[27, 28, 29, 30, 31, 25, 32, 33, 19] who have conducted research into various aspects of vortex matter in these narrow channels systems. In the majority of cases three key parameters are varied. The channel widths, the applied magnetic field and the applied current. For this thesis the most critical parameters from these previous experiments are the channel width and magnetic field.

For a given field the spacing between rows of vortices can be calculated. When a channel width is an integer multiple of this row spacing the system is known as *commensurate* and in a weakly pinned channel a perfect lattice can form free of defects at equilibrium. If this is not the case and the width is a non-integer multiple of the row spacing this will lead to an *incommensurate* lattice that contains a population of dispersed dislocations.

Many authors[34, 35, 6, 22, 28] have studied the commensurability effects of vortex matter driven by a Lorentz force(coherent driving force). For channel widths that are

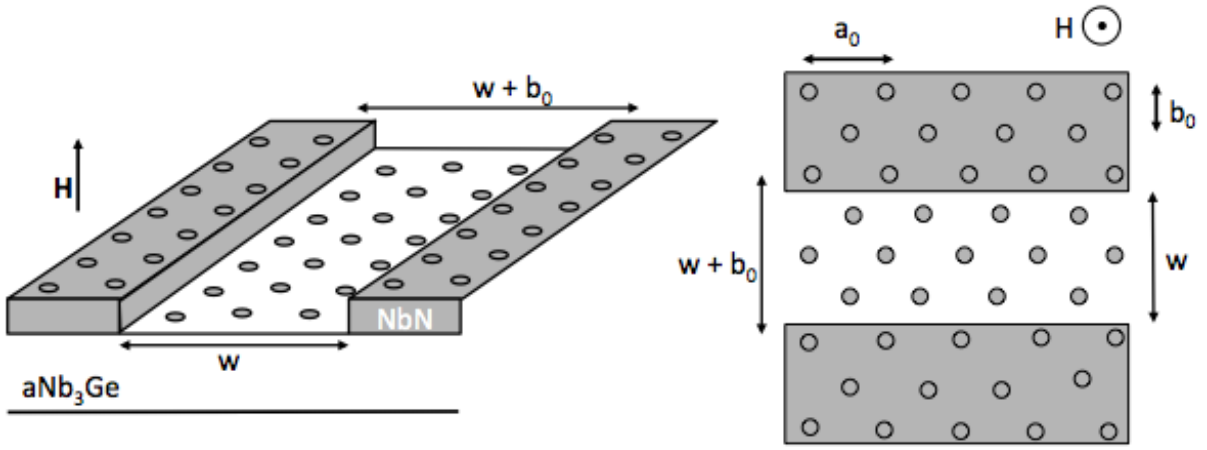

Figure 1.8: Schematic of a narrow channel superconductor. The bilayer is constructed by etching out a channel through the top layer of strongly pinned NbN to expose the weakly pinned channel of aNb_3Ge.

incommensurate with the applied field, dislocations form in the vortex matter that mediate plastic flow, Fig. 1.9. Other measures of the bulk properties such as current and voltage, show features such as Shapiro-like steps in $I - V$ curves, Fig. 1.10. This type of feature allows the inference of dislocations in the incommensurate regime where the critical current raises and dislocations are employed to enable the vortex matter to flow plastically.

For this thesis we explore aspects of the structure of the vortex liquid in stationary channels and sheared geometry. We propose and explore simulations of a novel channel set up that allows a commensurate vortex structure for a large range of B-fields and channel width, thereby minimising the population of required dislocations. Finally we present a channel geometry ideally suited to the exploration of circular grain boundaries, their collapse mechanism and their response to a static stress field.

1.2 Overview of Thesis Chapters

This thesis begins with an exploration into the **Phenomenology of the Flux Line Lattice**, Chapter 2. Here we present the fundamental physics and describe the limits

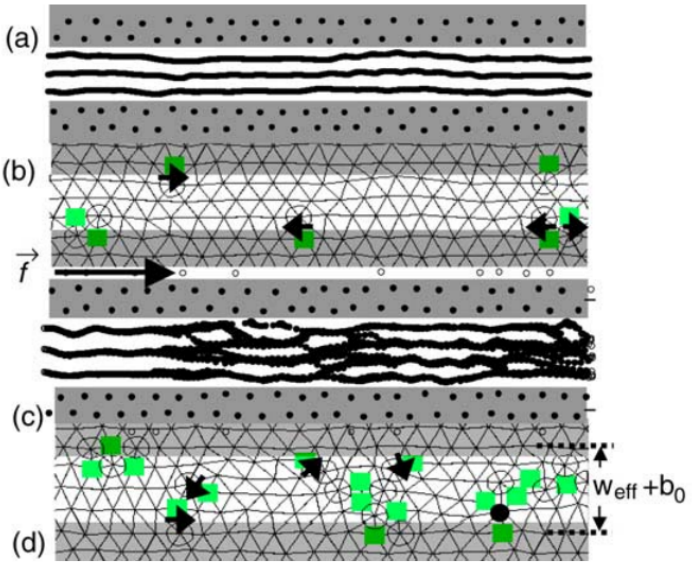

Figure 1.9: **a**, **b** Show the commensurate lattice. **c**, **d** show dislocations in an incommensurate lattice. Figure from Ref[6].

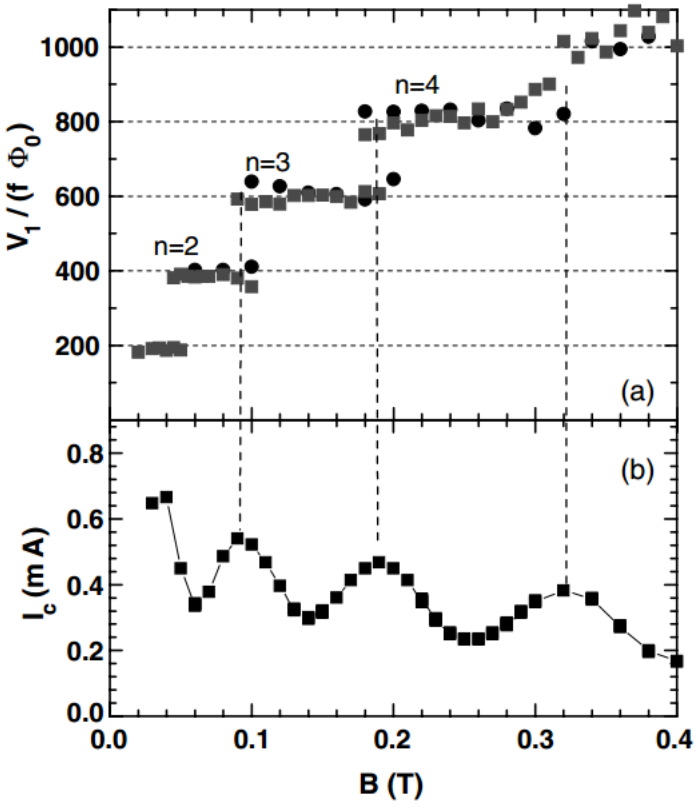

Figure 1.10: Shapiro-like steps in IV curves at T=1.94 K. Figure from Ref[6].

that allow us to explore the vortex state in the regime chosen for this thesis. Then follows **Crystal Defects in Two Dimensions**, Chapter 3. This chapter discusses defects in general with particular focus on edge dislocations in two dimensions. We quantify the dislocations with the aid of the Burgers vector and Burger circuit and discuss the stress fields around dislocations and forces between them. We then move on to talk about **Non-Newtonian Fluids**, Chapter 4. This chapters presents the background physics for liquids, describing constitutive equations that may be present in the vortex liquid.

After the extensive physical background, Chapter 5 **Simulating the Vortex Lattice**, details the overdamped Langevin dynamics required to simulate the vortex lattice. Here we discuss the simulation software that has been created to achieve this, enabling exploration of the wide array of system setups we will discuss in the results.

The final three chapters detail the results of this thesis. The first of these **Shear Flow in the Vortex Liquid**, Chapter 6, presents the results of two-dimensional Couette Flow simulations and calculations that investigate the rheology of the vortex liquid. Chapter 7, **Density Driven Vortex Lattice** begins with a reformatted version of our paper "Extrusion of a Vortex Lattice: Two Reaction Populations of Dislocations". This chapter details the novel simulation setup of a field gradient applied along the length of a narrow channel superconductor and an analysis of the plastic flow seen in this system. Finally, Chapter 8, **Circular Grain Boundaries in the Vortex Lattice** explores a proposed vortex reservoir that creates a steady supply of circular grain boundaries. We discuss the physical realisation of this reservoir and present preliminary investigations into this system.

Chapter 2

PHENOMENOLOGY OF THE FLUX LINE LATTICE

This chapter introduces the fundamental physics of the superconducting state, concentrating on phenomena relevant to this thesis. Particular focus will be given to the interaction of vortices arranged in a regular array of straight parallel lines called the *flux line lattice*(FFL). Following a brief history of superconductors we give an overview of the three key theories describing the superconducting state[7]. We will explore the breakthrough of Abrikosov in discovering the vortex state and discuss the cross over point in behaviour from type I to type II superconductivity. Having described where the vortex state comes from, we will discuss interactions in the flux line lattice that give rise to many of the phenomena throughout this thesis. We will then move on to the results of elastic theory calculations that enable us to understand how the FLL responds to deformations. Finally, we will explore aspects of the melting transition from vortex solid to vortex liquid.

2.1 History

Superconductivity was first discovered by H. Kamerlingh Onnes[36] in 1911 from his measurements of supercooled mercury, tin and lead. Using his newly developed refrigeration technique of liquid helium he was able to cool these elemental metals down to a few Kelvin above absolute zero. For each material, below a critical transition temperature

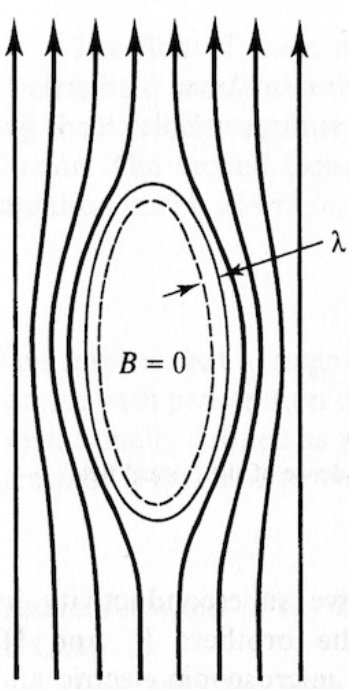

Figure 2.1: Flux explusion from a type I supercondcutor. Figure from Ref[7].

T_c, he found they possessed no measurable electrical resistance. He called this phenomena *perfect superconductivity* and it is known as the first hallmark of superconductivity. In 1933, work by Meissner and Ochsenfeld[37] lead to the second hallmark of superconductivity, *perfect diamagnetism*. This effect describes the complete flux expulsion of magnetic field from a sample of superconducting material as it is cooled below T_c, Fig. 2.1. The mechanism for this can be attributed to the formation of persistent currents on the material surface in response to an incident magnetic field. These supercurrents lead to an induced magnetisation of the material. In pure metal superconductors(except V and Nb), below a critical field value, H_c, the induced magnetic field perfectly cancels the applied field, leaving no flux penetrating the material, except for within a small distance from the surface of the material, Fig. 2.2. Above H_c the flux again begins to penetrate the material and the superconducting state is lost. The localised field penetrating the material $\mathbf{B} = \mu_0\mathbf{H} + \mathbf{M}$ where $\mathbf{H}$ is the external field and $\mathbf{M}$ is the magnetisation caused by the supercurrents on the surface. The magnetisation curve is shown in Fig. 2.3a. In the superconducting phase of a conventional superconductor $\mu_0\mathbf{H} = -\mathbf{M}$. The form of $H_c(T)$ was found empirically[7] to be given by Eq. (2.1) and is shown in Fig. 2.3b[7].

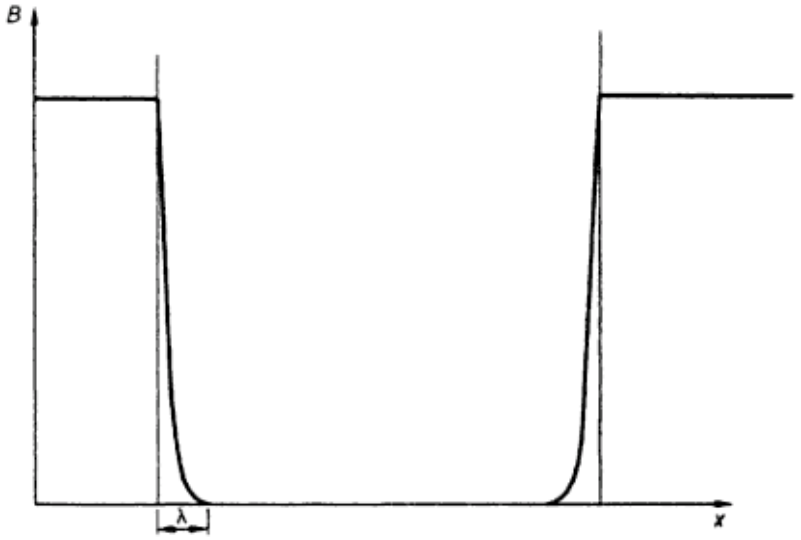

Figure 2.2: Flux penetrating over a length λ at the edge of a type I superconductor. Figure from Ref[8].

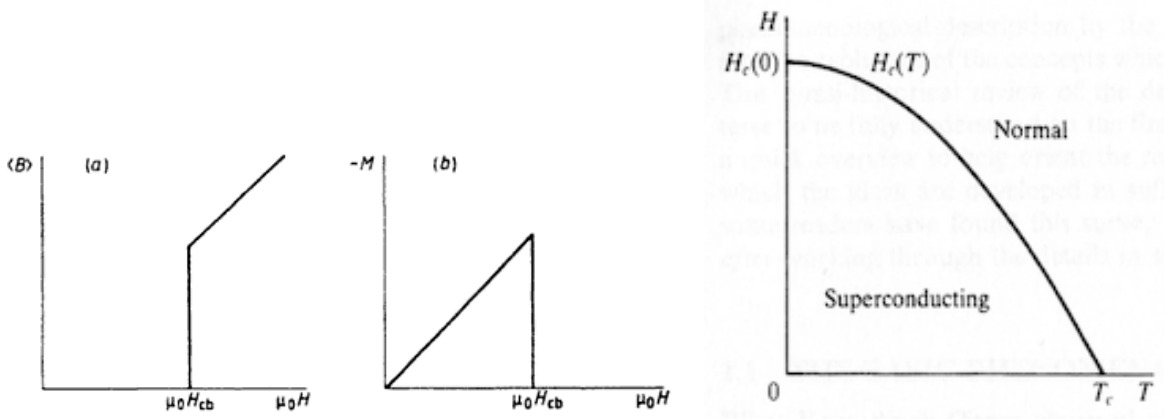

(a) Magnetisation curve for a type I superconductor. Figure from Ref[8].

(b) Temperature dependence of critical field. Figure from Ref[7].

Figure 2.3: Type I Superconductor

$$H_c(T) \approx H_c(0)[1 - (T/T_c)^2] \tag{2.1}$$

In conventional superconductors the abrupt change of state at $H_c(T)$ from normal to superconducting gives a first order transition at finite temperatures[7].

The transition temperatures of the early superconductors were only a few degrees above absolute zero. In the subsequent years materials that are able to remain in the superconducting state up to much higher temperatures have been found. The highest transition temperature of any elemental superconductor was found in Nb to be $9.2K$ and in amorphous alloys, such as aNb_3Ge, transition temperatures have been found up to $23K$. Then in 1986 Bednorz and Müller discovered high-T_c superconductors (HTSCs)[38]. These layered materials exhibited significantly higher transition temperatures of $T_c \approx 92.5K$ ($YBa_2Cu_3O_7$) and $T_c \approx 120K$ ($Bi_2Sr_2Cu_3O_{10}$). Transition temperatures as high as $T_c \approx 164K$ have been found in pressurised H_g compounds[39, 40].

The discovery of flux expulsion led to the early pioneering work of the London brothers[41]. In 1935 they wrote down a set of equations relating the electric current to the magnetic field in a superconductor. Starting from perfect conductivity and Maxwell's equations they found a relationship between the change in superconducting current $\dot{\mathbf{J}}_s$ and the change in magnetic field $\dot{\mathbf{B}}$, with respect to time. Their first attempt started from

$$\dot{\mathbf{J}}_s = \frac{n_s e^{*2}}{m^*}\mathbf{E} \tag{2.2}$$

$$\nabla \times \dot{\mathbf{J}}_s = -\frac{n_s e^{*2}}{m^*}\dot{\mathbf{B}} \tag{2.3}$$

$$\nabla \times \mathbf{B} = \mu_0 \mathbf{J}_s \tag{2.4}$$

where n_s is the density of superconducting charge carriers, e^* is their charge and m^* the mass. Using these equations they showed

$$\nabla^2 \dot{\mathbf{B}} = \frac{1}{\lambda^2}\dot{\mathbf{B}} \tag{2.5}$$

which can be interpreted as a field penetrating a superconducting material in the normal state that is locked in upon cooling the material below the superconducting transition temperature. However, this effect was not seen experimentally[37] and prompted them to reformulate their ideas. Their breakthrourgh was to remove the time dependence from Eq. (2.3) yielding the London Equations

$$\dot{\mathbf{J}}_s = \frac{n_s e^{*2}}{m^*}\mathbf{E} \qquad (2.6)$$

$$\nabla \times \mathbf{J}_s = -\frac{n_s e^{*2}}{m^*}\mathbf{B} \quad (2.7) \qquad \nabla \times \mathbf{B} = \mu_0 \mathbf{J}_s \qquad (2.8)$$

With these equations they found

$$\nabla^2 \mathbf{B} = \frac{1}{\lambda^2}\mathbf{B} \qquad (2.9)$$

The London equations[1] were the first consistent description of the phenomenology of the superconducting state. Through their formulation they introduced two key parameters, the density of superconducting electrons n_s (they only gave an upper limit for n_s as the density of normal electrons) and the magnetic penetration depth λ. The penetration depth is empirically described as $\lambda(T) \approx \lambda(0)[1-(T/T_c)^4]^{-1/2}$ which diverges near T_c as $(T_c - T)^{-1/2}$. The Londons' theory, motivated by the discovery of the Meissner effect, described the phenomenology of superconductors in terms of the electric and magnetic fields. A new theory would ultimately give the first concrete description of the mircoscopic behaviour of the superconducting state. The existence of an energy gap had been postulated by Daunt and Mendelsson[42] in 1946 and later proof of its existence could also be inferred from work by Corak *et al.*[43] in 1954 and Glover and Tinkham[44, 45] in 1957. Then in 1957 Bardeen, Cooper and Schrieffer (BCS) showed the existence of weak coupling between electrons of opposite charge and spin caused by electron-phonon interactions. These coupled electrons are known as Cooper pairs and are the quasi-particles responsible for superconductivity. The BCS theory predicted that the minimum energy

[1] See Appendix B for full derivation of the London equations.

required to break this Cooper pair was $E_g = 2\Delta_g(T)$. Where Δ_g is the energy gap between ground state electrons and quasi-particle excitations. BCS were able to show that E_g was zero at T_c and raised to a limiting value of $E_g = 2\Delta_g(0) = 3.528KT_c$ as the system was cooled below the transition temperature

The final description of the superconducting state to be discussed was put forward by Ginzburg and Landau[46] in 1950. Their theory describes superconductivity by introducing a pseudo-wavefunction for the superconducting electrons. This wave function ψ is then the order parameter within Landau's theory of phase transitions. The number of superconducting electrons is related to ψ as

$$n_s = |\psi(x)|^2 \tag{2.10}$$

This measure gives $\psi = 0$ in the normal state and $\psi \neq 0$ in the superconducting state. GL theory also introduced a length scale $\xi(T)$ called the coherence length, the length over which the magnetics field varies. Together with the London penetration depth λ they define the GL parameter $\kappa = \lambda/\xi$. In conventional superconductors, seen by Meissner *et al.* and Onnes, the parameter $\kappa \ll 1$ and the theory state this corresponds to a positive domain wall cost between coexisting normal and superconducting domains. In 1959, two years after the release of BCS theory, Gor'kov demonstrated that GL is a limit of the BCS theory that was *especially* useful for describing spatial variation in magnetic fields[47].

Following on from GL theory the next significant advance was made by (one of Landau's students) Abrikosov[48]. In 1957 Abrikosov investigated what would happen if $\kappa \gg 1$. He showed that the surface energy cost would be negative leading to the formation of multiple domain walls, thereby maximising the surface area - the effect only limited[49] by ξ. He named this state type II superconductivity. He demonstrated that the transition between type I and type II occurred at $\kappa = 1/\sqrt{2}$. In his work Abrikosov stated that we would see a continuous transition from normal to fully superconducting state due to the presence of vortices containing normal cores of magnetic flux. He said surrounding these vortices would be supercurrents that screen the superconducting do-

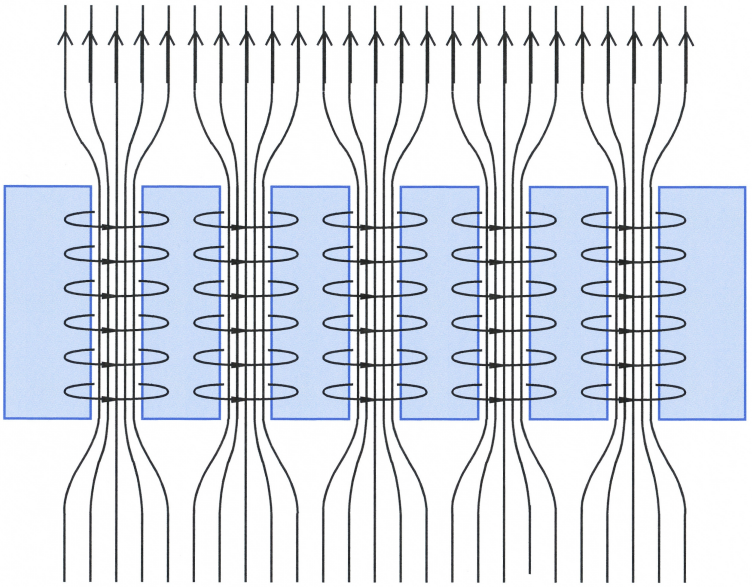

Figure 2.4: Flux tubes threading a type II superconductor. Figure from Ref[9].

mains from the penetrating magnetics fields[7]. Fig. 2.4 shows a schematic of these flux lines penetarting through a piece of superconductor. The second order nature is seen in the magnetisation curves for type II superconductors shown in Fig. 2.5 where it can be seen that flux penetration begins at H_{c_2} and goes fully superconducting at H_{c_1}. In type II materials $H_{c_1} < H_c < H_{c_2}$ and $H_{c2} = \sqrt{2\kappa}H_c$ [7].

Abrikosov[49] also calculated the form of the stable regular arrangement of these flux lines. At the time he calculated this to be a square lattice but it was later shown to be triangular, due to a simple numerical error. The triangular lattice in superconductors is known as - the *Abrikosov lattice*.

It took seven years for the first experimental evidence of the vortex lattice to be produced. In 1964 weak Bragg peaks were seen in small angle neutron scattering measurements[50] of Nb allowing the inference of the lattice structure. In 1967 the FFL was imaged by Essman and Träuble [51] with a magnetic decoration technique using ferromagnetic microcrystals that could be seen through an electron microscope, Fig. 2.6. Since these first images many other techniques have been used to probe the vortex lattice. Spatial resolution of the density of states of the quasi particles was measured using scanning

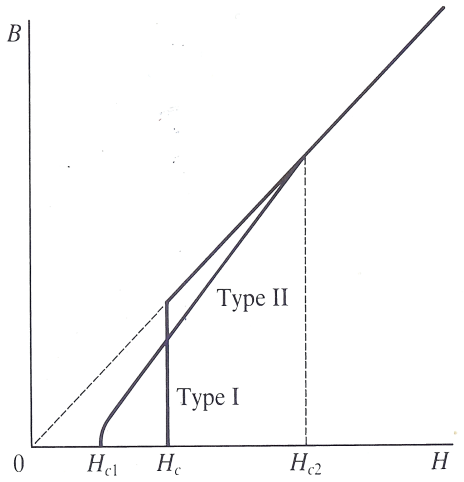

Figure 2.5: Magnetisation curves for Type I and II superconductors. H is the applied field and B is the resultant field in the superconductor. H_{c_1} and H_{c_2} are the lower and upper critical fields for a type II superconductor. H_c is the critical field for a type I. Figure from Ref[8].

tunnelling microscopes by Hess *et al.*[52, 53] in 1990. Single fluxon resolution has since been achieved by Bending *et al.*[54] in 1990 and by Stoddart *et al.*[55] in 1993 using a microscopic Hall probe. Of particular relevance to this thesis is the work of Schuster *et al.*[56] in 1993 who used magneto optics to visualise *motion* of the flux lines in YBCO and the work of Brüll *et al.*[57] in 1991, Brawner and Ong[58] in 1993, Brawner *et al.*[59] in 1993 and Xing *et al.*[60] in 1994 who used scanning Hall probes and Tamegai *et al.*[61] in 1992, and Zeldov *et al.*[62] in 1994, amongst others who used Hall-sensor arrays to gain more quantitative measurements of the vortex lattice whilst still retaining some spatial resolution of the vortex lattice. The FFL was imaged using magnetic decorationin the new HTSC[63]. These materials have layers containing pancake vortices that repel each other in the same layer and attract in different layers leading to flux lines threading through the material[10].

Important to understanding of the vortex lattice is the quantisation of magnetic flux. In a type II superconductor each vortex carries a quantum of magnetic flux,[2] Φ_0. From the quantisation condition and the triangular arrangement of the vortex lattice the number density of the vortices and the associated lattice parameters can be calculated. The

[2]See Appendix C for a the proof of flux quantisation

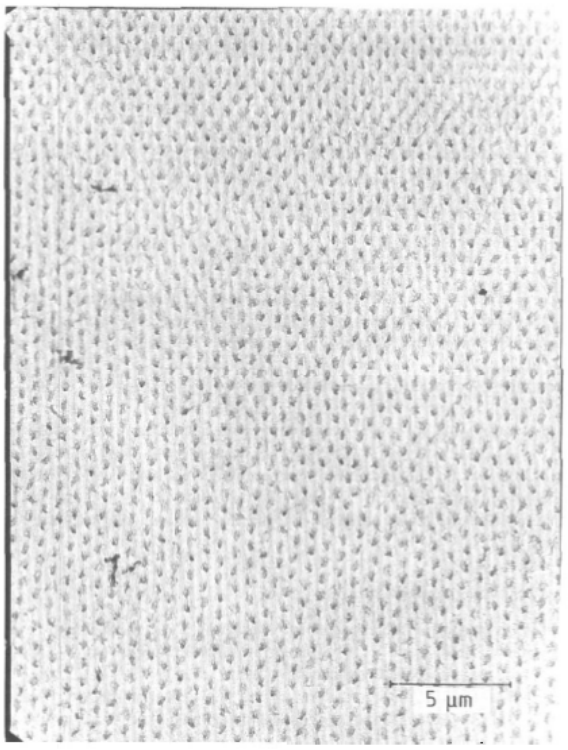

Figure 4. The flux-line lattice observed at the surface of type-II superconductors in an electron microscope after decoration with Fe microcrystallites. (*a*) PbIn alloy ($T_c = 7.5$ K, $\kappa = 2$) at $T = 1.2$ K in a remanent magnetic field of 70 G, yielding a flux-line spacing $a = 0.6\,\mu$m.

Figure 2.6: Image seen through an electron microscope of a decorated vortex lattice. Figure from Ref[10].

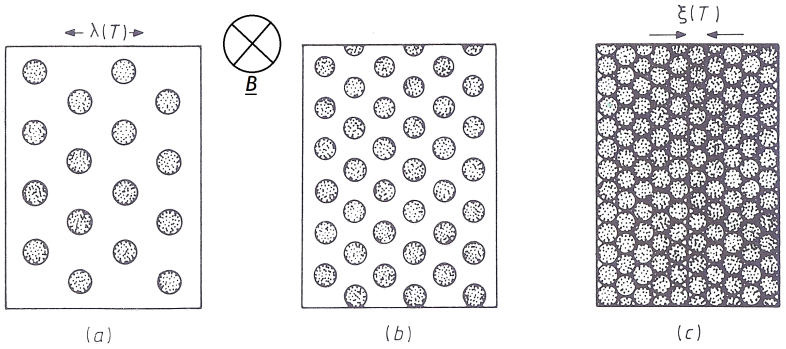

Figure 2.7: At low fields vortices are separated $\mathcal{O}(\lambda)$. Upper limit of vortex density is reached when vortices are spaced $\mathcal{O}(\xi)$. Figure from Ref[8].

number of vortices per unit area is given in terms of the local magnetisation field B and the flux quantum Φ_0 as

$$n_v = \frac{B}{\Phi_0} \tag{2.11}$$

For a section of material, ignoring boundary effects, the vortices would be arranged as shown in Fig. 2.7. The series of images show the effect of increasing the applied field and therefore the density of the vortices. It is clear from these images that there is an upper limit for density (or applied field). In the upper limit the cores, which are of size ξ and separation λ, overlap and the superconducting phase is destroyed; there is full flux penetration and the superconducting phase disappears. This corresponds to $\kappa \sim 1$.

The separation is governed by the strength of the local B-field and resulting density of vortices. From Eq. (2.11) we can calculate the lattice parameters of the vortex lattice for a given B as

$$a_0^2 = \frac{2\Phi_0}{\sqrt{3}B} = \frac{2}{\sqrt{3}n_v} \tag{2.12}$$

This corresponds to the vortex spacing and determines the strength of repulsion between the vortices. For the triangular lattice vortices align in rows and we can calculate the separation of these rows as

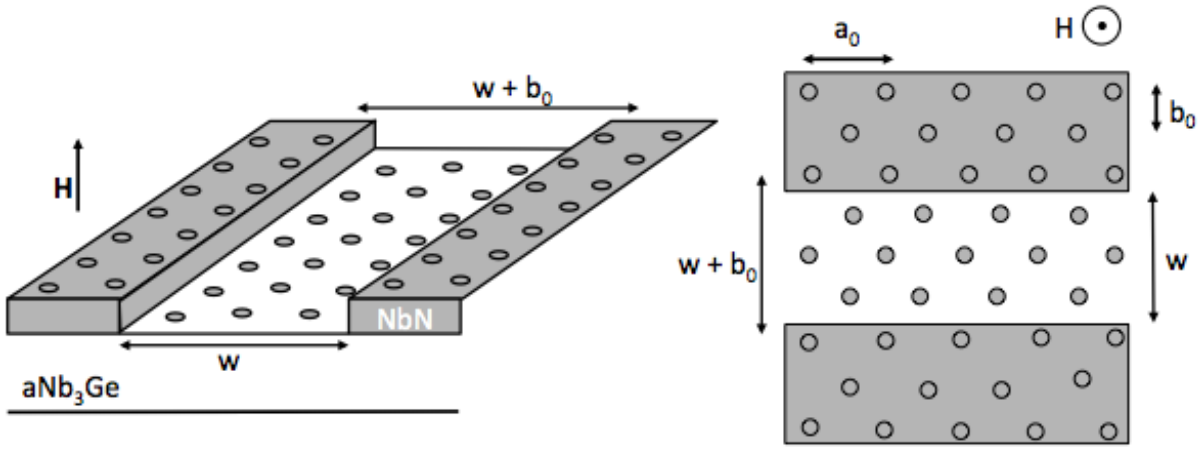

Figure 2.8: aNb_3Ge/NbN layered system

$$b_0 = \frac{\sqrt{3}a_0}{2} \tag{2.13}$$

.

These *lattice parameters* are shown in Fig. 2.8 for the aNb_3Ge/NbN superconducting layered system.

2.2 Interactions in the Flux Line Lattice

In the following section we will discuss four types of interaction felt by the flux lines.

- The mutually repulsive force felt by flux lines that is responsible for the arrangement of the vortex lattice.
- A Magnus force generated by the presence of an applied electric current that creates motion of the FLL.
- A viscous drag due to the scattering of the quasiparticle from the vortex cores.
- A pinning force due to the interaction of the vortex lattice with the material defects of size $\sim \lambda$

2.2.1 Force Between Straight Parallel Flux Lines

A simple approach for deriving the force between flux lines is the London equations. This approach is possible for materials where $\kappa \gg 1$ and scenarios with small magnetic fields $\tilde{b} \ll B/B_{c2}$ (the London limit). This is the case for materials such as aNb_3Ge which we will be investigating in this thesis (Experimental results by Kes *et al.*[64] show $\kappa \sim 60$ for prepared $a Nb_3Ge$ samples. At this κ with fields of $B \sim 0.25T$, lattice spacing is around $100nm$ with the vortex cores size of $\sim a_0/100$). In this setting the magnetic fields of the vortex lattice can be written down as the linear superposition of the single flux line expression from the London equations. This result is applicable for straight parallel flux lines in materials where the thickness $d \gg \lambda$, such as the experimental samples generated by many experimental groups[35, 22, 6]. It is also applicable to layered HTSCs where superconducting layers (interleaved with planes of CuO_2) are separated by $s \ll \lambda$. From the London equations[3] the field at a distance r from the vortex core is given by

$$B(r) = \frac{\Phi_0}{2\pi\lambda^2} \int_0^\infty \exp\left(-\frac{r}{\lambda}\cosh t\right) dt = \frac{\Phi_0}{2\pi\lambda^2} K_0\left(\frac{r}{\lambda}\right) \tag{2.14}$$

The Bessel function, $K_0(x)$ has limits

$$K_0(x) = \begin{cases} -\ln(x) & x \to 0 \\ \sqrt{\frac{\pi}{2x}}\mathrm{e}^{-x} & x \to \infty \end{cases} \tag{2.15}$$

The current associated with this field is also radially symmetric and defined as

$$J(r) = \frac{|B'(r)|}{\mu_0} = \frac{\Phi_0}{2\pi\mu_0\lambda^3} K_1\left(\frac{r}{\lambda}\right) \tag{2.16}$$

where we have used the relationship $K_0'(r/\lambda) = -K_1(r/\lambda)/\lambda$.

Throughout this thesis we work in the $\kappa \gg 1$ limit and $\lambda > a_0$. In this regime the magnetic fields of vortices are long ranged and overlap with many vortices whereas the

[3] See Appendix D for a full derivation

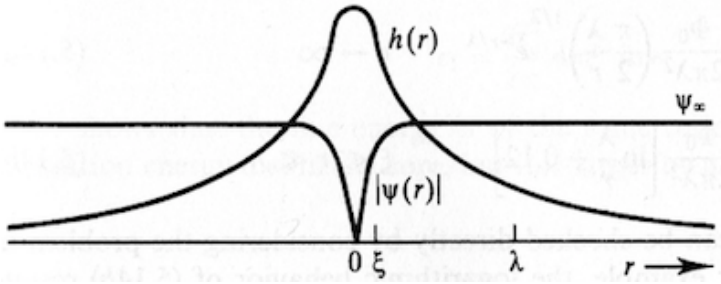

Figure 2.9: In the high κ limit the core vortex is small and isolated with the magnetic fields from the vortices are long range and overlap neighbouring vortices. Figure from Ref[7].

vortex cores (of size ξ) remain small and isolated, Fig. 2.9.

From the linear superposition of fields from two neighbouring vortices[7] the interaction energy is found to be

$$U(r) = \frac{\Phi_0^2}{2\pi\mu_0\lambda^2} K_0\left(\frac{r}{\lambda}\right). \tag{2.17}$$

To calculate the force between two vortices we can calculate $\mathbf{f}_2(\mathbf{r}_2) = \mathbf{J}_1(\mathbf{r}_2) \times \Phi_0\hat{\mathbf{B}}$ where $\mathbf{J}_1(\mathbf{r}_2)$ is the current induced by a vortex at the origin at the position of a second vortex at $\mathbf{r}_2$. Alternatively, we can differentiate the interaction energy with respect to position ($f(r) = -\mathrm{d}U(r)/\mathrm{d}r$). Both yield the same result of

$$f(r) = \frac{\Phi_0^2}{2\pi\mu_0\lambda^3} K_1\left(\frac{r}{\lambda}\right) \tag{2.18}$$

The values of the constants are

$$\Phi_0 = \frac{h}{2e} = 2.067 \times 10^{-15}\ \mathrm{Wb} \tag{2.19}$$

$$\mu_0 = 4\pi \times 10^{-7} \frac{\mathrm{Vs}}{\mathrm{Am}} \tag{2.20}$$

This potential has been used by many authors in vortex lattice simulations[65, 34, 28, 66, 32]. A modification to this potential for $\kappa \sim 1$ is used by Brass and Jensen[27, 67].

They performed simulations of the vortex lattice using a potential proposed by Brandt [68, 69]

$$U(r) = \frac{\Phi_0^2}{2\pi\mu_0\lambda^2}\sum_i\sum_{i>j}\left(K_0(\frac{r_i - r_j}{\lambda'}) - K_0(\frac{r_i - r_j}{\xi'})\right) \tag{2.21}$$

where $\lambda' \approx \lambda/(1-\tilde{b})^{1/2}$, $\xi' = \xi/[2(1-\tilde{b})]^{1/2}$ and $\tilde{b} = B/B_{c2}$ and it is written as the sum over all vortices. This reduces to the London potential, Eq. (2.17) in the London limit of large κ ($\lambda \gg \xi$). This potential describes magnetic repulsion and an attractive condensation energy. For the simulations in this thesis we will be using the potential of Eq. (2.17).

2.2.2 Motion of Flux Lines

As already discussed in §2.1 experimental imaging of vortex motion has been seen in the FLL. The most common vortex motion is the result of an applied current perpendicular to the flux line. The magnitude and direction of this Magus force (or Lorentz force) felt by the vortices is given by $\mathbf{F}_L = \mathbf{j} \times \Phi_0\hat{\mathbf{B}}$ resulting in a coherent driving force[7]. Bardeen and Stephenson showed[70] in an ideal material (free from defects), vortex motion is only resisted by drag due to the interaction of the quasi-normal cores with the superconducting material[12]. They found the viscous drag constant of proportionality to be given by

$$\gamma \approx \frac{\Phi_0 H_{c2}}{\rho_n c^2} \tag{2.22}$$

where ρ_n is the resistivity of the material in the normal state. The key feature is that γ is independent of B and only depends on the upper critical field. This *flux flow* of vortices induces a resistive voltage in the sample. The resistance of this was proved to be $\sim B\rho_n/H_c$. This induced voltage would make the superconductor useless for zero resistivity applications. However, in materials where defects[7] in the material structure are of order λ, these defects cause the vortices to experience a pinning force that

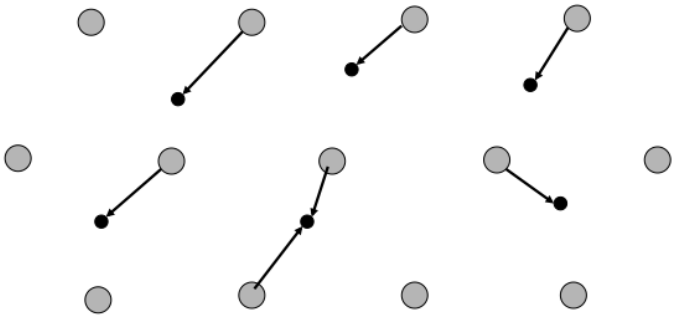

Figure 2.10: Random distribution of pinning sites interact with the vortex lattice. Grey circles represent vortices. Black circles represent the random distribution of pinning cites. Figure reproduced from Ref[8].

can halt the vortex motion and enable the superconductor to retain its zero resistivity hallmark, Fig. 2.10. The energy barrier created by these pinning sites can be overcome for sufficiently large applied currents or thermal activation allowing the flux lines to jump between pinning sites. Some of the key work in recent years has been to find materials where strong pinning enables large currents to be applied that do not overcome this energy barrier. The use of superconductors in superconducting magnets depends on finding materials with this property. Thermal activation at sufficiently high temperatures allows bundles of flux lines to move cooperatively between pinning sites. The cooperative nature is due to the long interaction range of vortices for $\lambda \gg a_0$. This phenomena is described by the Anderson-Kim Flux-Creep[71, 72, 8] theory where the jump rate is given by $R = \omega_0 e^{-F_0/k_B T}$, where w_0 is the attempt frequency or characteristic vibration frequency of the flux bundle. $F_0 = U - BJlSa$ is the average barrier energy of a bundle of area S and length l interacting with a well of depth U and width a.

Three important regimes emerge. At finite, but low temperature $T < T_m$, in the absence of an applied current we would observe a potential energy landscape as seen in Fig. 2.11a. Here flux bundles are confined to local potential wells created by the random pinning sites. For a current where $0 < j < j_c$ (j_c is a critical current), flux bundles will cooperatively jump between pinning sites at a slow rate given by R, this is the *flux creep* scenario, Fig. 2.11b. At $j > j_c$ there is no longer an energy barrier, resulting in

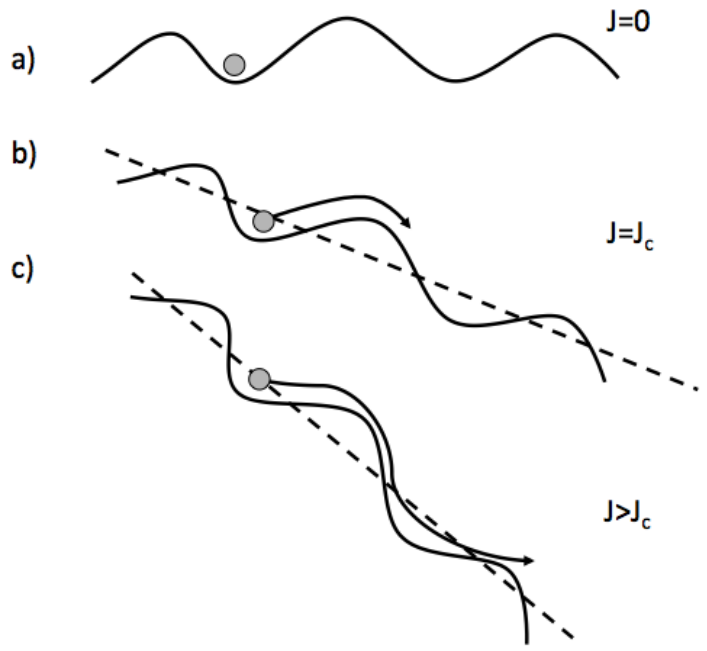

Figure 2.11: A flux gradient allows vortex bundles to overcome the potential energy barrier. Figure reproduced from Ref[8].

flux flow, Fig. 2.11c. It has also been shown[11, 73] analytically and from simulations that dynamical ordering of the FLL is present above a crystallisation current j_t (where $j_t > j_c$). The phase diagram, Fig. 2.12, shows that flux flow exhibits plastic behaviour for low j and T changing to a moving crystal (Even weak disorder will break long range order, so technically this is a glass.) phase above $j_t(T)$

Since the focus of this thesis is on weakly pinned material we choose to simulate a pin-free channel work with no applied Lorentz force. For our simulations flux flow and creep phenomena by the discussed mechanisms should not occur. Vortex motion in this thesis is generated by other mechanisms that will be discussed in Chapters 5, 6 and 7.

2.3 Elastic Properties of the Flux Line Lattice

The literature on linear elasticity of the FLL is extensive[10]. We summarise here the key results that will enable us to understand how the FLL responds to deformations, in particular related to the melting transition that is discussed in the next section. In

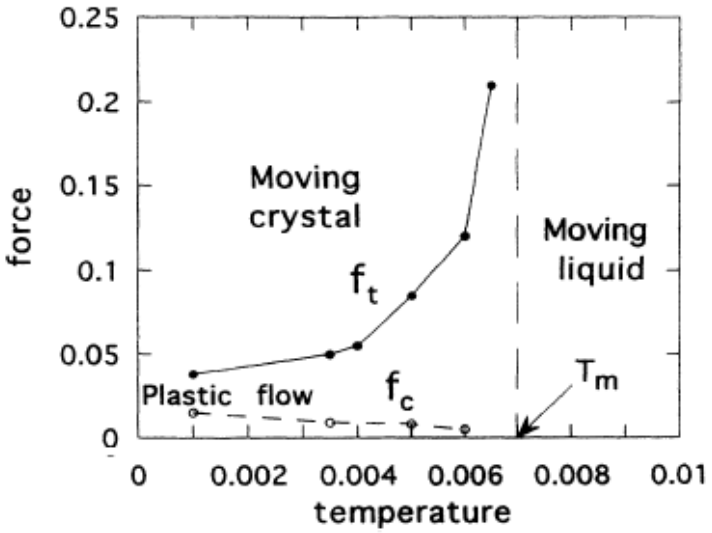

Figure 2.12: Phase diagram of the moving vortex lattice. $f_t(T)$ marks the transition from plastic flow to a moving crystal. $f_c(T)$ corresponds to the cross over between flux creep and flux flow. Figure from Ref[11].

discussing the elastic properties our focus will be on the k and λ dependence of the elastic moduli. The three elastic moduli that are discussed are for compression or bulk (c_{11}), tilt (c_{44}) and shear (c_{66}). The derived[74, 75] expressions for the elastic moduli are

$$c_{11} \approx c_{44} \approx \frac{B^2}{\mu_0}(1 + k^2\lambda^2)^{-1} \tag{2.23}$$

$$c_{66} = \left(\frac{B\Phi_0}{16\pi\lambda^2\mu_0}\right)\left(1 - \frac{1}{2\kappa^2}\right)\left(1 - \tilde{b}\right)^2\left(1 - 0.58\tilde{b} + 0.29\tilde{b}^2\right) \tag{2.24}$$

where $\tilde{b} = B/B_c2$. We will be interested in the $\tilde{b} \ll 1$ and $\kappa \gg 1$ regime which simplifies c_{66} to

$$c_{66} = \left(\frac{B\Phi_0}{16\pi\lambda^2\mu_0}\right) \tag{2.25}$$

The interpretation of these expressions is that the FLL is soft for short wavelength perturbations, i.e. when $2\pi/k < 2\pi\lambda$, k is large (short wavelength) so c_{11} and c_{44} are small. This gives a *soft* lattice. For long wavelength perturbations, small k, c_{11} and c_{44}

are large, i.e. the FLL is resistant to large scale (uniform) compression. Hence the FLL is long range incompressible, but short range compressible. To quote Brandt[10] who was the pioneer in this field, "This exact result might appear counter-intuitive since large λ means a long-range interaction between the flux lines, which sometimes is erroneously believed to lead to a stiff FLL.".

These expressions also allows us to make a more quantitative argument about the straight line nature of the FLL. Straight parallel flux lines are expected in $a\mathrm{Nb_3Ge}$ since there is weak pinning and a large tilt modulus. This results in the coherence length[64] along $\hat{\mathbf{z}}$ (parallel to $\mathbf{B}$) to be $L_c \gg d$.

2.4 Melting of the Flux Line Lattice

Thermal fluctuations cause distortions in the FLL. For large enough fluctuations the stable Abrikosov lattice can melt into a vortex liquid phase above which there is a loss of long range translational and rotational order. Here we will discuss a simple approach, developed for conventional crystals, that finds a good approximation for the size of vibrations that make the FLL unstable. Combining fluctuation dissipation theory and the elastic moduli of §2.3 we are able to estimate the melting temperature, T_m. Via a simple argument we then present a second estimate of the dislocation[4] mediated 2D Kosterless-Thouless transtion temperature, T_m^{2D}.

The requirement for 2D melting is that the longitudinal correlation length $L_c > d/2$[76] (where $L_c = (c_{44}/c_{66})^{1/2} R_c$[77], with R_c is defined as the transverse correlation length over which there is short range order). This is experimentally verified for films of $a\mathrm{Nb_3Ge}$ by Berghuis *et al.*[78] ($d > 2\mu m$), Kes *et al.*[64] ($d > 1\mu m$) and Wördenweber *et al.*[76] ($d > 5\mu m$). For $L_c < d/2$ fluctuations appear in all directions leading to 3D melting of the FLL, whereas for $L_c > d/2$ the flux lines are considered straight and parallel and the system is considered 2D.

[4]Dislocations are a defect is the lattice structure that will be discussed at length in Chapter 3.

The Lindemann melting criteria is based on determining the fluctuations in the distances between nearest neighbours of the FLL. The criteria[79] states that a crystalline lattice is unstable to fluctuations on the order of $c_L a_0$ ($c_L \sim 0.1 - 0.2$ depending on the material). The Lindemann criteria is then formally stated as

$$< u^2(T_m) >_{th} \approx c_L^2 a_0^2. \tag{2.26}$$

Using fluctuation dissipation theory[5] leads to an estimate of the melting temperature of a finite system of size L

$$T_m^{\mathrm{FDT}} \approx \frac{c_{66}\pi(c_L a_0)^2}{k_B \ln(L/a_0)}. \tag{2.27}$$

T_m can also be estimated by assuming that nucleation of dislocations is responsible for the onset of melting in 2D crystalline systems[10, 80, 7]. An excellent argument by Huberman and Doniach[81] in 1979 and Fisher[82] in 1980 considers a circular disk of material of radius R. The cost of nucleation of a single dislocation of core size a is $U = (a^2 d c_{66}/4\pi)\ln(R/a)$ with each dislocation adding an entropy of $S = k_B \ln(R/a)$ (where R^2/a^2 comes from counting the possible positions of the dislocation core). This leads to a free energy of $F = (a^2 d c_{66}/4\pi)\ln(R/a) - T k_B \ln(R/a)$. Setting $F = 0$ and rearranging finds a transition from positive to negative free energy at $T_m^{\mathrm{2D}} = a^2 d c_{66}/4\pi k_B$ (This is lower[10] that the T_{BKT} phase transition predicted by Berezinskii[83], Kosterlitz and Thouless[84].). At $T < T_m^{2D}$ nucleation of a dislocation increases free energy, whilst at $T > T_m^{2D}$ nucleation decreases free energy.

While the two expressions differ, both are proportional to c_{66}. At melting there is also a vanishing shear modulus[85, 86].

Evidence of dislocation mediated melting has been seen experimentally by Berghuis *et al.* in films of aNb_3Ge, from resistivity measurements of Schmidt *et al.*[87] and from experiments of Theunissen *et al.*[88] who show a good agreement with dislocation mediated

[5] See Appendix H for the derivation.

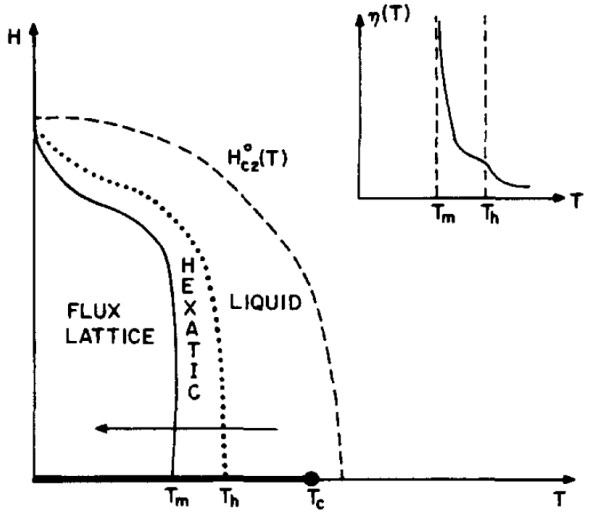

Figure 2.13: Phase diagram for a thin-film. Figure from Ref[12].

melting above $T = 0.2T_c$.

The highly cited work by Nelson[80] postulates the two stage melting through and the existence of an hexatic phase, defined by the loss of long range order, without the continuous symmetry of the liquid state.

For thin-films a possible phase diagram is shown in Fig. 2.13. The lower critical field H_{c1} drops to zero preventing the formation of a Meissner phase[12] and for a 3D superconductor a possible phase diagram of a pure material, Fig. 2.14, shows a transition from flux lattice to isotropic liquid through the intermediate hexatic phase. Here we see the presence of the Meissner region below which we see perfect diamagnetism.

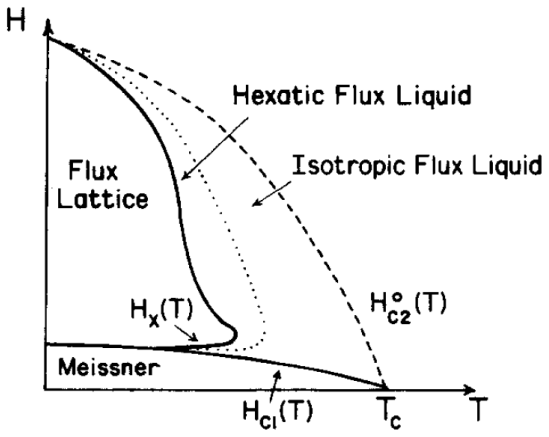

Figure 2.14: 3D phase diagram of the FLL. Figure from Ref[12].

Chapter 3

CRYSTAL DEFECTS IN TWO DIMENSIONS

The field of crystal defects is large - as their properties underpin the understanding of most physical materials, hence this chapter will concentrate on aspects of crystalline defects relevant to this thesis. We will start with an overview of crystalline defects, focussing on defects that are seen in 2D systems. We then focus further on *dislocations*, as they will be key to the physical system we will explore. To do this we need to discuss the Burgers vector, a key parameter in identifying and classifying dislocations. We show how to calculate it in theory and in practice from simulation data.

We next explore a selection of systems in which dislocations occur, making it a ubiquitous phenomena throughout the physical sciences. We will show that dislocations have associated stress fields that can interact with other stresses in the material (including those generated by other dislocations) leading to forces on the dislocations themselves.

We then consider linear arrangements of dislocations, known as grain boundaries. The phenomena of grain boundaries will be split into two key types of low and high angle tilt boundaries between grains of differing crystallographic orientation. Finally, we highlight two central analysis methods; Delaunay Triangulation, a technique that allows us to quickly find the coordination number of atoms and hence the dislocations, and measurements of effective *order parameters* that allow us to categorise the degree of translational and rotational order in our system. Throughout this discussion (unless otherwise stated) we will refer to lattice points as atoms or particles, although this is not

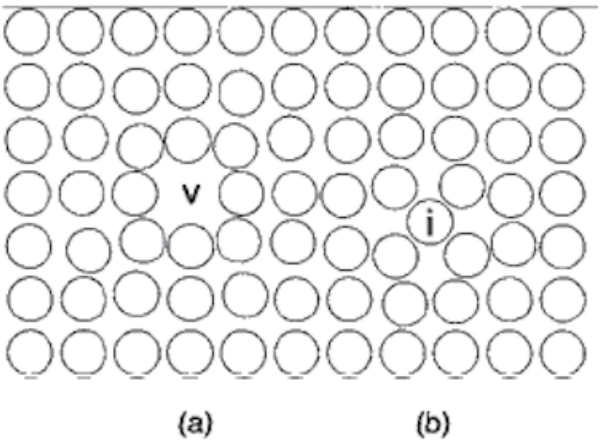

Figure 3.1: **a** Vacancy **b** Interstitial. Figure from Ref[13].

necessary in general. Instead, they may be populated by other objects such as vortices, colloidal particles or soap bubbles.

3.1 Introduction to Crystalline Defects

Defects mark places where there is a deviation from the perfect lattice structure. For the triangular lattice this corresponds to places that have a coordination number (number of nearest neighbour points) other than 6. In 3D, there are many defect types. They can be point defects (interstitials or vacancies), line defects (edge or screw dislocations), planes (grain boundaries) or volume (bubbles or voids) defects. In 2D geometries relevant to thesis only point defects, edge dislocations and grain boundaries are possible.

3.2 Point Defects

In the following section we give a description of point defects, these are rarely seen in the systems we simulate and so will not be covered in detail. Point defects arise when a single particle from an otherwise perfect system is added or removed. Fig. 3.1 shows an *interstitial* where a particle has been added and a *vacancy* where a particle has been removed. These defects cause local changes in the lattice structure, particles around the

point defects are displaced from their original positions. Displacements in the surrounding material are common to all defects and one of the sources of stress and strain in the lattice. Point defects have a defined equilibrium concentration at finite temperatures. At equilibrium[89] the number of point defects n_p, is given by

$$\frac{n_p}{N - n_p} = \exp\left(\frac{-E_f}{k_B T}\right) \tag{3.1}$$

where, E_f is the formation energy and N is the number of atoms in the crystal. From experimental data[13], the formation energy for one of these point defect is $E_f = 8k_B T_m$ where T_m is the melting temperature. This calculation estimates approximately 10^{-5} defects per atom at the onset of melting[13].

3.3 Dislocations

Dislocations are the focus of the remainder of this chapter. The discovery of dislocations begins with the first estimates of shear stresses calculated in 1926 by Frenkel[90]. He was attempting to calculate the applied shear stress needed to glide one plane of atoms over another, Fig. 3.2. This type of deformation, where atoms take up new positions when stresses are removed is called *plastic deformation*. Frenkel started by assuming that the atoms are formed into periodic lattice with row spacing b and atomic separation a. Then he assumed that shearing a plane of atoms required the simultaneous movement of the entire plane of atoms through a distance a. He estimated the energy of the lattice to be a periodic sine function. The shear stress is defined as proportional to the spatial derivative of the measured work which led to an estimate of shear stress of

$$\tau = \frac{c_{66} a}{2\pi b} \sin \frac{2\pi x}{a} \tag{3.2}$$

where c_{66} is the shear modulus from elastic theory. The maximum value of the shear stress occurs when $x = a/4$, leading to a maximum value of

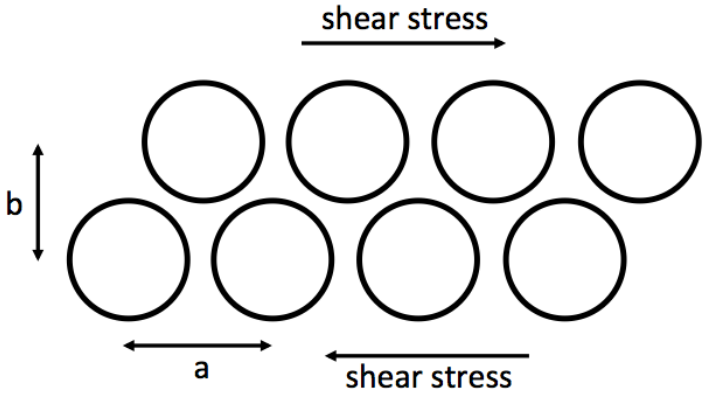

Figure 3.2: Frenkel's model of shear in plastic deformation. Lattice layers move cooperatively in response to shear stress. Figure reproduced from Ref[13].

$$\tau_{\text{fkl}} = \frac{c_{66}a}{2\pi b} \tag{3.3}$$

This result led to the first estimate of the maximum shear stress required for plastic deformation, $\tau_{\text{fkl}} \approx c_{66}/5$. The estimate was later revised by Mackenzie to $\tau_{\text{mac}} \approx c_{66}/30$ using a more accurate potential. At the time of Mackenzie the best experimental measurements of the shear stress in bulk materials were $\tau \approx c_{66}10^{-9}$, orders of magnitude lower than the theoretical values. However one measurement that did better agree with Mackenzie's estimate was the measurement of shear stresses required to deform whiskers of various metals[91]. These whiskers have at least one reduced spatial dimension[16]. In these materials $\tau \approx c_{66}/15$. The discrepancy between the values of shear stress in bulk material led many authors to postulate that defects were the cause of plastic flow, however these authors all tried defect arrangements of defects types that were already discovered at the time. None of these were able to solve the problem. A number of years after Frenkel's work, in 1934 Orowan[92], Polyanyi[93] and Taylor[94] all predicted the existence of the dislocation, a new type of defect and a mechanism by which plastic flow can occur at much lower stress levels in bulk materials. The dislocation mechanism meant movement of one plane against another did not have to happen cooperatively. Fig. 3.3 shows how the lattice planes rearrange themselves as the dislocation passes. With the dislocation mechanism only a small local change is required to effect a large change in

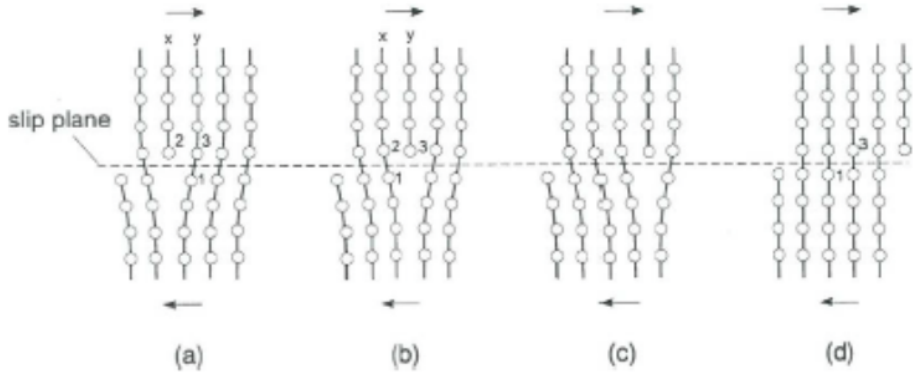

Figure 3.3: A small change in the position of (1) causes a large change in the connections across the plane. Figure from Ref[13].

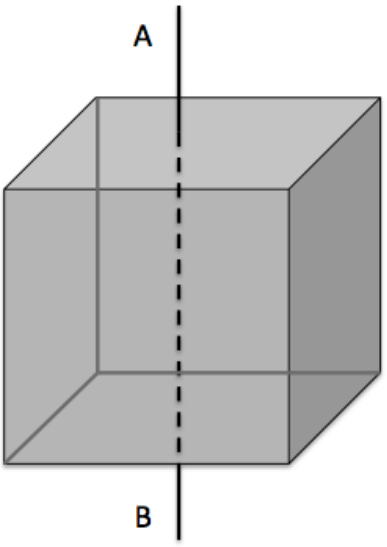

Figure 3.4: AB line through the continuum.

the lattice structure.

Later work by Peierls[95] and Nabarro[96] was able to calculate the stress more accurately by taking into account the local periodicity of the lattice along with the elasticity of the surrounding material. It also demonstrated that in the absence of dislocations the theoretical value of Mackenzie was closer to the actual value required to shear the system[1].

[1]See §2.4

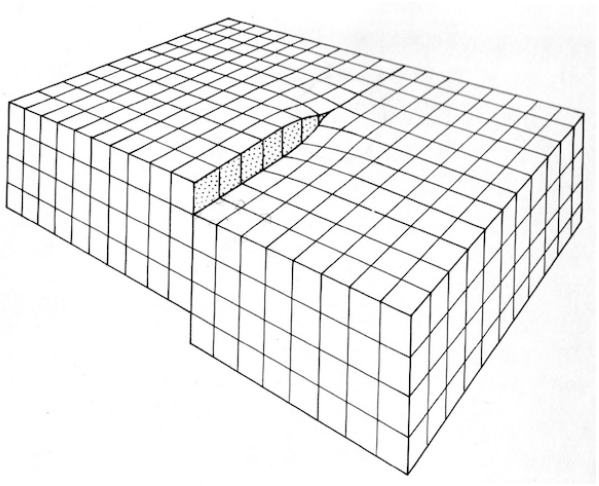

Figure 3.5: Screw dislocation. Figure from Ref[14].

3.3.1 Burgers Vector

Dislocations are line defects that can be categorised into three types, *edge*, *screw* and *mixed* (mixed dislocations are deformations made up of edge and screw dislocations, which are not relevant to this thesis). Edge and screw dislocations are best illustrated with an example. To create a screw dislocation the perfect lattice in Fig. 3.4 is cut along the line AB. The material on one side of the cut is then shifted parallel to the line AB. This creates a deformation as illustrated in Fig. 3.5. In this case the line AB marks a screw dislocation. To create an edge dislocation, a cut is also made along the line AB, but this time we displace the material perpendicular to the line AB. This creates the edge deformation seen in Fig. 3.6. In 2D geometries the normal to the plane is parallel to the dislocation line AB. It is quite clear from this construction that only edge dislocations are possible in flat geometry.

To quantitatively describe these deformations we now introduce the *Burgers vector*, $\mathbf{b}$, first described by Burgers[97] in 1939. The Burgers vector quantifies the degree of mismatch in a section of crystalline material. It is defined as the contour integral circling the dislocation line as

$$\mathbf{b} = \oint \frac{\partial \mathbf{u}}{\partial l} \mathrm{d}l \tag{3.4}$$

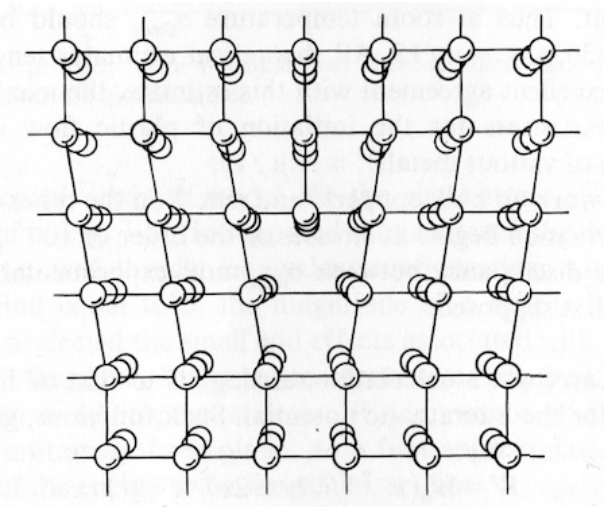

Figure 3.6: Edge dislocation. Figure from Ref[14].

In practice, calculation of this quantity follows a method introduced by Frank[98] in 1951. This method is commonly know as the *Burgers Circuit*. A complication is that there are two different Burgers vectors, the *true* and the *local* Burgers vectors. For the true Burgers vector, the value of **b** is always integer multiples of the lattice vectors of the perfect lattice. For the local Burgers vector, strain fields and thermal fluctuations around the dislocation cause the value to slightly deviate from the perfect lattice vectors. We will discuss both, however throughout the rest of this thesis we will implement the *local* Burgers vector, that, for sufficiently large Burgers circuits (away from the strain fields of the dislocations), tends to the true value. We will perform this procedure on a single dislocation, however it is just as applicable for calculating the Burgers vector of a group of dislocations.

To construct the true Burgers vector we draw a circuit in the deformed crystal around the line of a dislocation, in a plane with normal parallel to the dislocation line. The example in Fig. 3.7a, shows the circuit around an edge dislocation. In this example we can see that to complete the clockwise circuit we must go *4 up, 4 right, 4 down, 3 left*. The broken symmetry is due to the plane of atoms removed or added when creating the edge dislocation. We then take this circuit and draw it again in an undeformed perfect lattice. This circuit, shown in the lower image of Fig. 3.7a, does not return to the starting point. The true Burgers vector is defined as the right hand (clockwise) circuit with the

Burgers vector joining the **S**tart and **F**inish points(RHSF).

To construct the local Burgers vector a similar procedure applies, Fig. 3.7b. This time a circuit is drawn in the perfect lattice first, e.g. *4 up, 4 right, 4 down, 4 left.* The circuit is then drawn around the dislocation line in the deformed lattice. The local Burgers vector is defined as RHFS. With this circuit, the expansion of material below the dislocation line would make the local Burgers vector larger than the true Burgers vector. If the start of this circuit had been draw above the dislocation line the opposite would have been true.

In practice the local method is easier to calculate and since the true Burgers vector must be a multiple of lattice vectors, for simple cases the correct lattice vector is easy to identify. For the edge dislocation the Burgers vector is always perpendicular to the dislocation line. The analysis for a screw dislocation is similar but the resulting Burgers vector is parallel to the dislocation line. Calculation of the local Burgers vector can be easily implemented as a computational procedure[2].

There is a lot on confusion in the literature as to the sense of Burgers circuit. To calculate the local Burgers vector we use the same convection as Nelson[1], the clockwise circuit, with $\mathbf{b}$ defined as the vector between the finish and start points, RHFS.

With this definition of $\mathbf{b}$ we are able to easily identify the glide or slip plane along which a dislocation line will move. The glide plane is defined by the normal $\mathbf{b} \times \hat{\boldsymbol{\xi}}$ where $\hat{\boldsymbol{\xi}}$ is the direction of the dislocation line. For an edge dislocation this is well defined but for the screw dislocation $\mathbf{b} \times \hat{\boldsymbol{\xi}} = 0$ since $\mathbf{b}$ is parallel to $\hat{\boldsymbol{\xi}}$. This make the definition of a glide plane inappropriate for a screw dislocations[14].

Finally, from this definition we see that Burgers vector is conserved. If we draw a circuit around a pair of dislocations $\mathbf{b}_1$ and $\mathbf{b}_2$, this would be equivalent to a single dislocation with Burgers vector $\mathbf{b}_3$, where the sum of the Burgers vectors is $\mathbf{b}_1 + \mathbf{b}_2 = \mathbf{b}_3$. This conservation of Burgers vector is a very important property and is illustrated in Fig. 3.8.

[2]See Appendix J

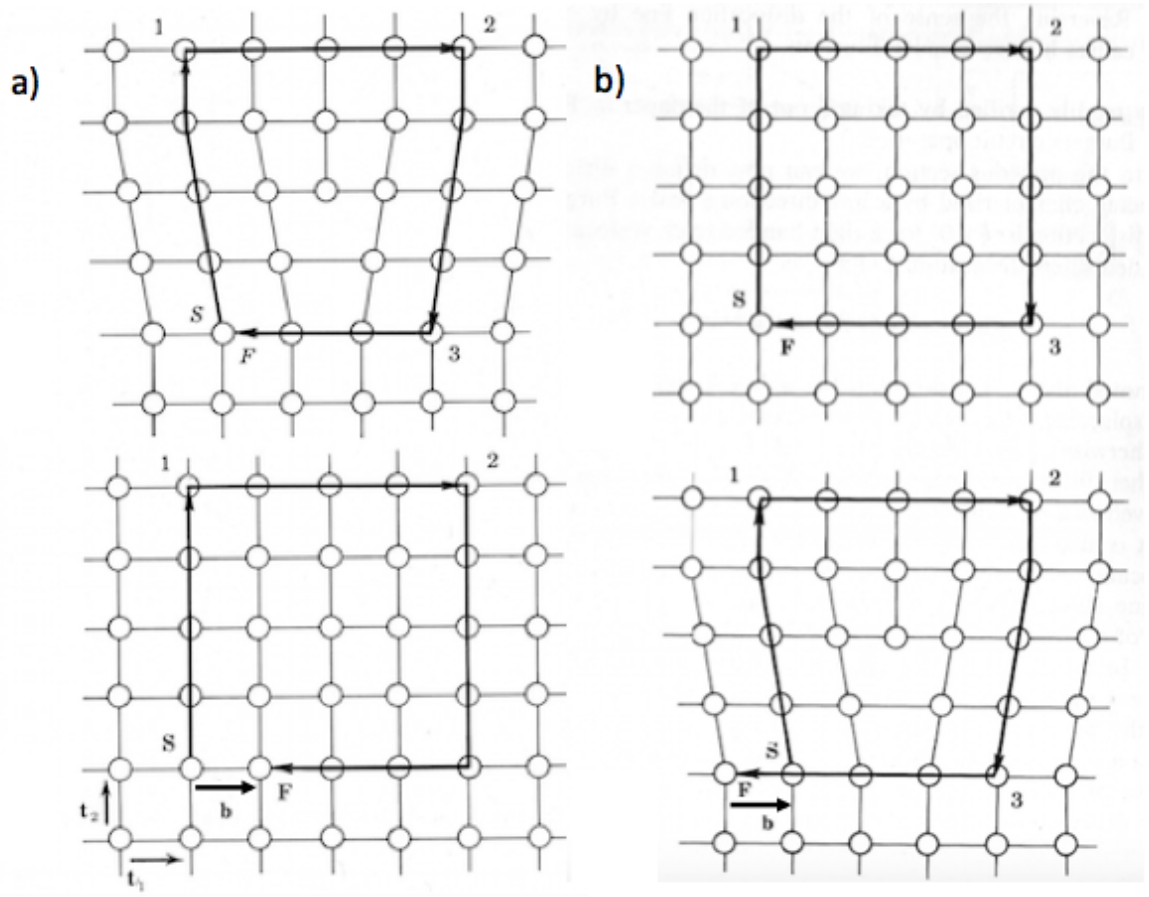

Figure 3.7: **a** Burgers circuit to find the true Burgers vector. **b** Burgers circuit to find the local Burgers vector. Figure modified from Ref[14].

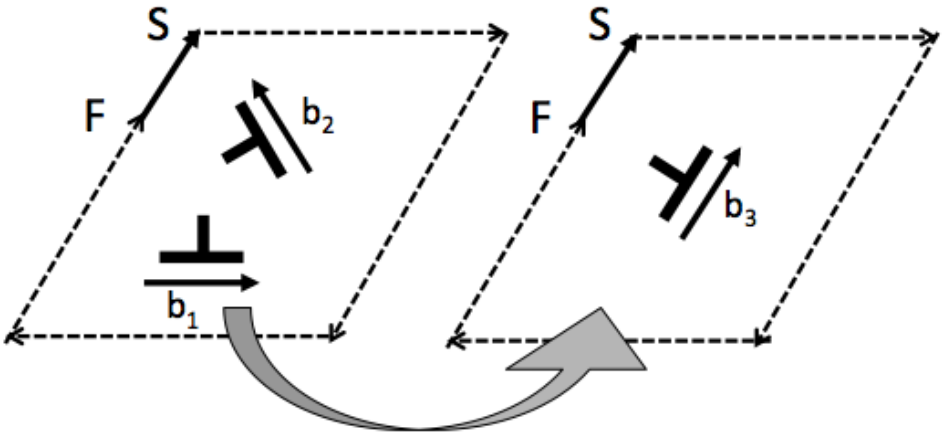

Figure 3.8: Burgers vector is conserved after a dislocation reaction. $\mathbf{b}_1 + \mathbf{b}_2 = \mathbf{b}_3$.

3.3.2 Elastic Theory of Dislocations

Even though the lattice has discrete character, much can be learnt about the behaviour of dislocations by modelling the system as a continuum. This approach is very successful at reproducing the displacements of the particles in the presence of the dislocation, everywhere except close to the dislocation line. In a radius of $a/2$[14] around the dislocation line, continuum theory fails to accurately predict the properties of the lattice. This is due to the lattice character becoming relevant at these small length scales. Here we will present highlights from the linear elastic theory calculations of Kosevich[99]. The methods and results are generally well known and derived by a number of other authors[16, 14].The starting point for the derivation is the equilibrium equation

$$\frac{\partial \sigma_{ij}}{\partial x_j} + f_i^{(s)} = 0 \tag{3.5}$$

where σ_{ij} is the stress tensor and $f_i^{(s)}$ is the force density at the surface. From this it is possible to obtain the general formula for the displacement field around a dislocation

$$u_i(\mathbf{r}) = -c_{jklm} b_m \int_{\Sigma_s} n_l \frac{\partial}{\partial x_l} \mathcal{G}_{ij}\left(\mathbf{r} - \mathbf{r}'\right) \mathrm{d}\Sigma' \tag{3.6}$$

Where c_{jklm} is the elastic modulus tensor (defined using the elastic constants λ and μ as $c_{jklm} = \lambda\delta_{ik}\delta_{lm} + \mu\delta_{im}\delta_{kl}$), b_m is the Burgers vector, $\mathcal{G}_{ij}$ is the Green's tensor, λ is the Lamé constant and μ is the shear modulus. In practice, this is often difficult to solve. However, for simple dislocations, such as an edge dislocation, we instead solve the equilibrium equation, Eq. (3.5). The derivation of the displacement fields along with the stress and strain tensors can be found by following Weertman and Weertman[16]. The displacement fields are not radially symmetric, there is tension created where material is removed above the dislocation and compression below.

The following fields are for a Burgers vector at the origin $\mathbf{b} = (b, 0)$ we label each component with the superscript b. In the flat geometry relevant to this thesis the stress fields are

$$\sigma^b_{xx} = -\frac{\mu b}{2\pi(1-\nu)}\frac{y(3x^2+y^2)}{(x^2+y^2)^2} = -\frac{\mu b}{2\pi(1-\nu)}\frac{y(3x^2+y^2)}{r^4} \tag{3.7}$$

$$\sigma^b_{yy} = \frac{\mu b}{2\pi(1-\nu)}\frac{y(x^2-y^2)}{(x^2+y^2)^2} = \frac{\mu b}{2\pi(1-\nu)}\frac{y(x^2-y^2)}{r^4} \tag{3.8}$$

$$\sigma^b_{xy} = \frac{\mu b}{2\pi(1-\nu)}\frac{x(x^2-y^2)}{(x^2+y^2)^2} \tag{3.9}$$

where $\nu = \lambda/(2\lambda+\mu)$ is the Poisson ratio. For normal materials ν is not usually greater that 1/2[16].

To find the fields for $\bar{\mathbf{b}} = (-b, 0)$ simply set b to $-b$ in the above equations (or equivalently $x \to -x$ and $y \to -y$).

3.3.3 Forces Between Dislocations - Peach-Koehler

As seen in §3.3.2, dislocations have associated stress fields, which are long range[99] and interact with the stress fields created by externally applied stresses or those of other dislocations. The stress field created by one dislocation causes a force on a neighbouring dislocation. This force is a function of the Burgers vector of the neighbour and the stress field created by the first dislocation. The force relationship was first derived by Peach and Koehler[100] in 1950.

For an edge dislocation on a 2D surface in the presence of a stress field σ the components of force on the dislocation are

$$F_x = \sigma_{yk} b_k \tag{3.10}$$

$$F_y = -\sigma_{xk} b_k \tag{3.11}$$

where b_k denotes the kth component of the Burgers vector. From these two relationships the forces between Burgers vectors at any orientation can be calculated. We will consider here some basic examples as an illustration.

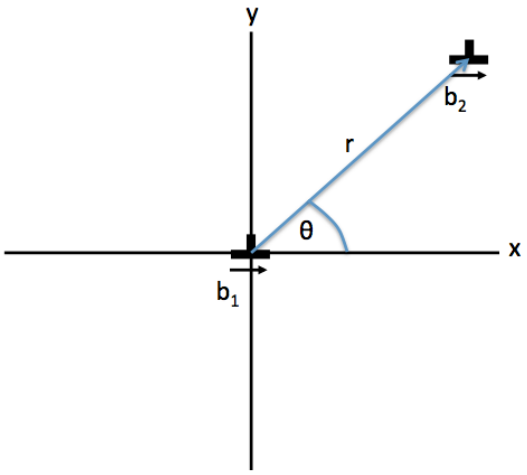

Figure 3.9: Two parallel edge dislocations with parallel Burgers vector.

Consider first, a dislocation at the origin with a Burgers vector $\mathbf{b_1} = (b, 0)$. We then place a second dislocation with a Burgers vector $\mathbf{b_2} = (b, 0)$ in the stress field at a position (x, y). Fig. 3.9 illustrates the setup. First we need the stress field induced by the dislocation at the origin. For this system it is straight forward since we can use the stress results stated above. We will only need the σ^b_{xy} and σ^b_{xx} results. The forces on $\mathbf{b}_2$ then become

$$F_x = \frac{\mu b^2}{2\pi(1-\nu)} \frac{x(x^2-y^2)}{(x^2+y^2)^2} \tag{3.12}$$

$$F_y = \frac{\mu b^2}{2\pi(1-\nu)} \frac{y(3x^2+y^2)}{(x^2+y^2)^2} \tag{3.13}$$

The direction of each of these component forces is given in Fig. 3.10. We can see from the directions of forces that dislocations with the same Burgers vector would repel each other if they lie with an angle of $< \pi/4$ between them. Dislocations with the same Burgers vector that lie with a angle $> \pi/4$ will line up along the y-axis. This is the mechanism by which grain boundaries are formed, see §3.4. If the Burgers vector of one of the dislocations was reversed, the directions of all forces would be reversed. This would lead to neighbouring dislocations lying along $y = 0$ but separated in x attracting each other.

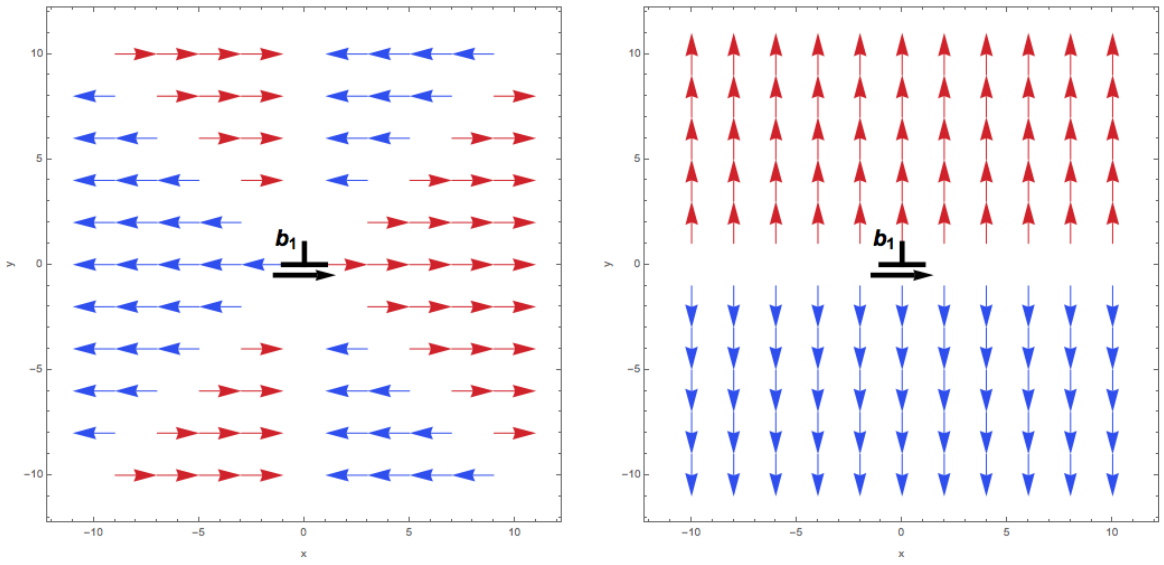

Figure 3.10: Direction of forces between dislocations with parallel Burgers vector.

From the conservation of Burgers vector, §3.3.1, we can see that this attraction of Burgers vectors of opposite sign would lead to an annihilation event, i.e. $(b, 0) + (-b, 0) = (0, 0)$.

3.3.4 Peierls-Nabarro Stress

So far the lattice has been treated everywhere as an elastic medium. This has yielded expressions for stress and strain fields that beyond the core radius produce a good agreement with experimental data[14]. Near the core, the continuum approximation fails to predict the atomic displacements and thus fails to predict the correct value of the core energy. To correctly calculate the core energy the discrete lattice structure has to be added into the calculations. This was the breakthrough of Peierls[95] in 1940 and Nabarro[96] in 1947. They postulated adding a sinusoidal force that represented the local lattice structure. This dislocation is then embedded in a periodic potential so that its energy varies as a function of position. We summarise their calculation and some of the quantities required to calculate it.

We start by considering the mis-registry across the slip boundary of a dislocation. Above the slip boundary we label the elastic medium A, below we label the elastic medium

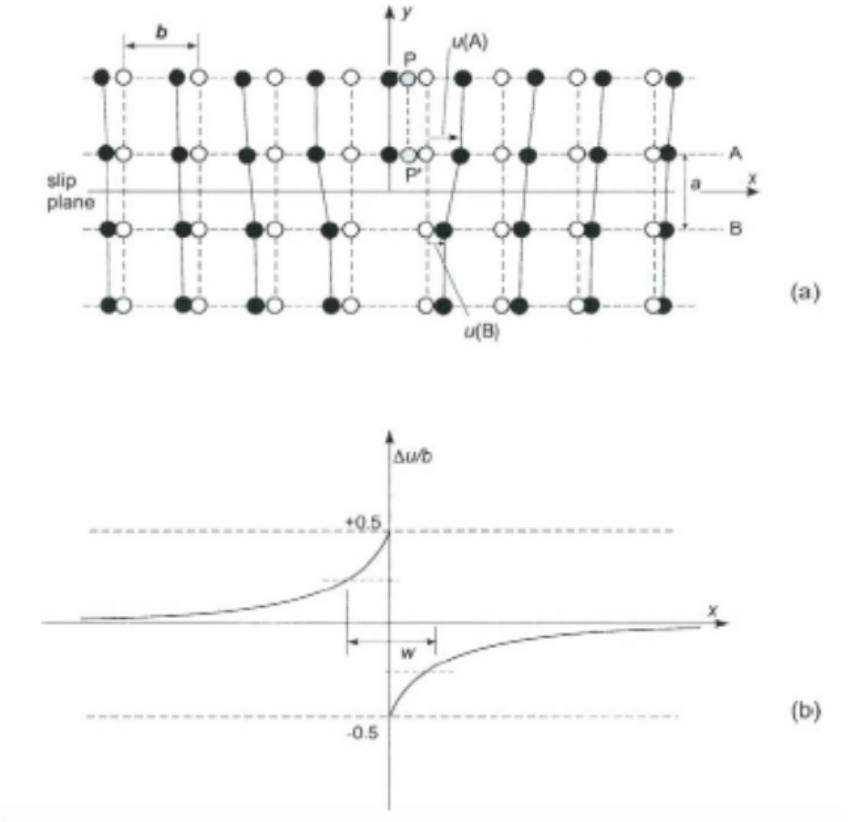

Figure 3.11: **a** Displacement of atoms around an edge dislocation. **b** Shows the misregistry across the slip plane Δu. Figure from Ref[13].

B, Fig. 3.11a. To quantify this mis-registry we introduce the *displacement difference* $\Delta u = u(B) - u(A)$. This is negative on the right of the dislocation and positive on the left, Fig. 3.11b. The width of the dislocation core is defined as half the maximum displacement, $-b/4 \leq \Delta u \leq b/4$, where b is the magnitude of the Burgers vector. The calculation of Δu now allows us to find the *Burgers vector distribution*(BVD) $f(x) = \mathrm{d}/\mathrm{d}x(\Delta u)$. This quantifies the width of the mis-registry across the boundary. Fig. 3.12 shows the BVD for various of edge dislocations. Using these two quantities Peierls and Nabarro calculated the dislocation core energy/unit length as a function of position. They included in the calculation the mis-registry Δu, a sinusoidal potential, approximating the lattice, and the elastic energy stored in the planes above and below the dislocation. Their calculations led to the result for the energy of an edge dislocation of

$$E_{\mathrm{pn}} = \frac{c_{66}b^2}{\pi(1-\nu)} \exp\left(\frac{2\pi w}{b}\right) \tag{3.14}$$

where the width $w = a/(1-\nu)$ and a is the interplane spacing and b is the magnitude of the burgers vector as defined in Fig. 3.11. Differentiating the energy and seeking the maximum value for the gradient gives the maximum force required to move the dislocation. This gives a maximum shear stress of

$$\tau_{\mathrm{pn}} = \frac{2\pi}{b^2} E_p = \frac{2c_{66}}{1-\nu} \exp\left(-\frac{2\pi w}{b}\right). \tag{3.15}$$

The final result is a core energy that causes a resistance to movement due to its interaction with the sinusoidal lattice potential.

The new value calculated by Peierls and Nabarro is much smaller than that of Frenkel and Mackenzie, $\tau_{\mathrm{pn}} \ll \tau_{\mathrm{mac}} \ll \tau_{\mathrm{fkl}}$. In fact the Peierls-Nabarro result is much closer to the experimental values of shear stress, demonstrating the importance of dislocations and the discrete structure of the lattice. However, on a plane away from the dislocation slip plane the calculations of Frenkel and Mackenzie are in much better agreement with the experimental values of stress measured in a region free from dislocations. This emphasises the

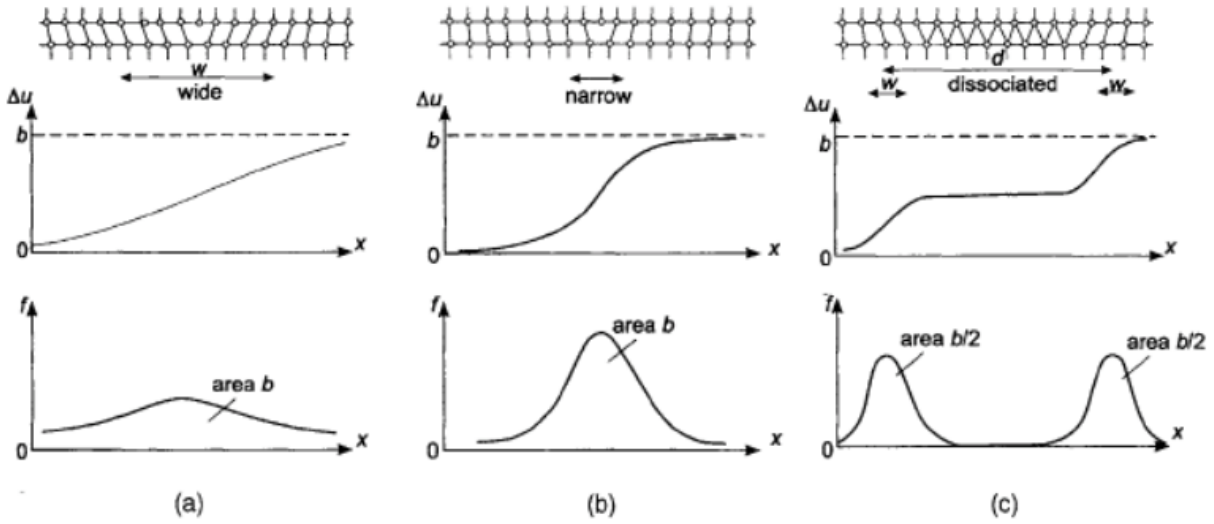

Figure 3.12: Shows the mis-registry across the slip plane and Burgers vector distribution for three different edge dislocations. Figure from Ref[13].

importance of dislocations in the softening of materials undergoing plastic deformation.

In the years since Peierls and Nabarro, computer simulations have improved the accuracy of calculation of the dislocation core energy[13].

3.3.5 Dislocation Motion

Dislocations move in response to stress fields. Motion can also be created by thermal fluctuations, enabling dislocations to overcome the local Peierls-Nabarro stress and find lower energy states.

So far we have used analogy with crystals to understand the stress fields around dislocations in the static system. Various arguments[14] have been made for crystals that describe how the stress fields vary for a moving dislocation and a possible upper limit to their movement speed. We are hesitant to continue with the analogy to crystals since arguments rely on the radiation of elastic waves and in our system most of the energy is lost due to the viscous drag. Arguments such as the Peierls-Nabarro stress still hold due to the static considerations.

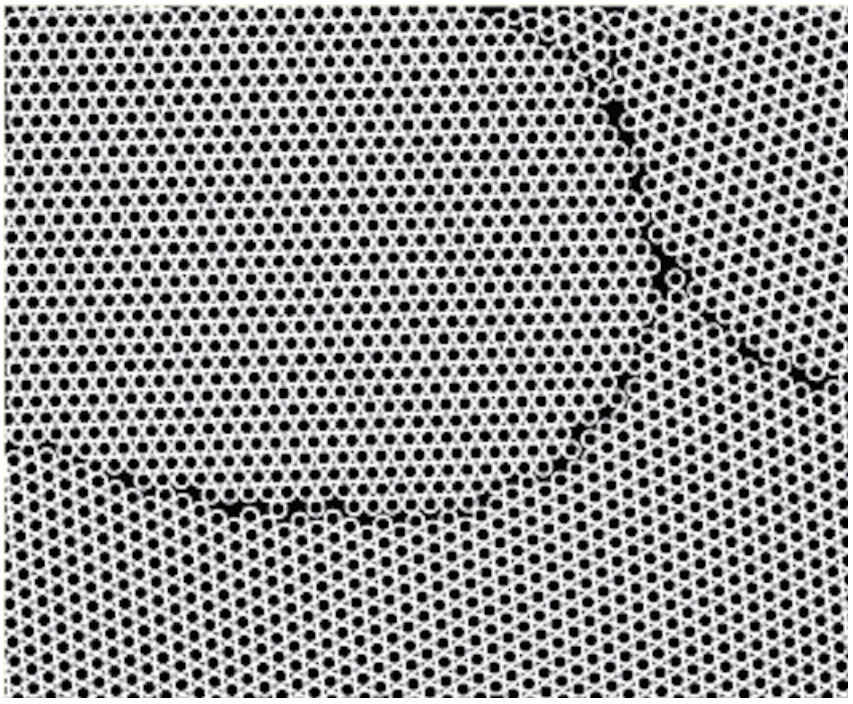

Figure 3.13: A grain boundary in a bubble raft. Figure from Ref[15].

3.4 Grain Boundaries

During the normal process of crystal formation, crystalline materials form not as a perfect single crystal, but as a composite crystal made up of smaller grains. Each of these grains is formed of material that has the same local lattice vector orientations. These grains are separated by grain boundaries, typically a few atoms thick and made up of defects. This phenomena is easily seen in bubble rafts, Fig. 3.13. The presence of these grain boundaries allow the material to remain continuous across the boundary and the individual grains to remain essentially stress free. The types of boundaries that exist between grains are often very complicated but under certain conditions they can be described as a line of separate edge dislocations.

As we saw in §3.3.3, dislocations of the same orientation will line up along an axis perpendicular to $\mathbf{b}\times\hat{\boldsymbol{\xi}}$. This is the low energy state for an array of dislocations on different slip planes. A similar situation exists along the grain boundary separating two grains of different lattice vectors. Grain boundaries can be categorised in a number of ways. We will only discuss categories of GB that exist in 2D. The first grouping of GBs is as either

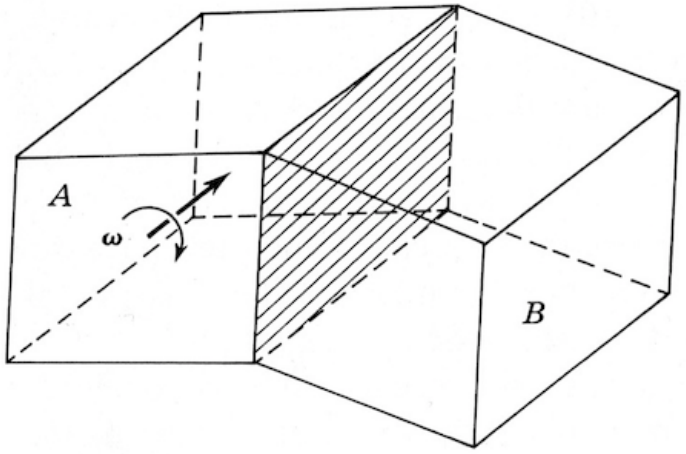

Figure 3.14: A tilt grain boundary. Rotation vector ω is parallel to the boundary. Figure from Ref[14].

tilt, *twist* or *mixed*. Fig. 3.14 and Fig. 3.15 show tilt and twist GBs respectively. For the case of tilt, all the mis-orientation is contained in the boundary, this is defined by a rotation vector ω that lies parallel to the boundary. For the twist the mis-orientation is contained in the rotation of the crystals with ω perpendicular to the boundary. A mixed dislocation occurs when ω is a sum of both types of rotation and as such ω will lie pointing neither parallel or perpendicular to the boundary. From this description, it is clear that only tilt boundaries are possible in 2D, so we will restrict ourselves to a discussion about this type of boundary.

In general, tilt grain boundaries can be curved, however since boundary tension behaves similar to surface tension, straight lines are preferred in equilibrium. Additionally, grain boundaries must either end at surfaces, join to other boundaries or close on themselves. Closed isolated boundaries, are not stable configurations and will collapse on themselves due to thermal fluctuations[24, 101]. At the junctions of grain boundaries all tensions must vanish[14].

The degree of mis-orientation across the boundary is an important parameter. For small tilts $\lesssim 20°$ the boundary structure can be described be a set of separate dislocations. This is known as a *low angle* tilt boundary and can be dealt with fairly effectively as we

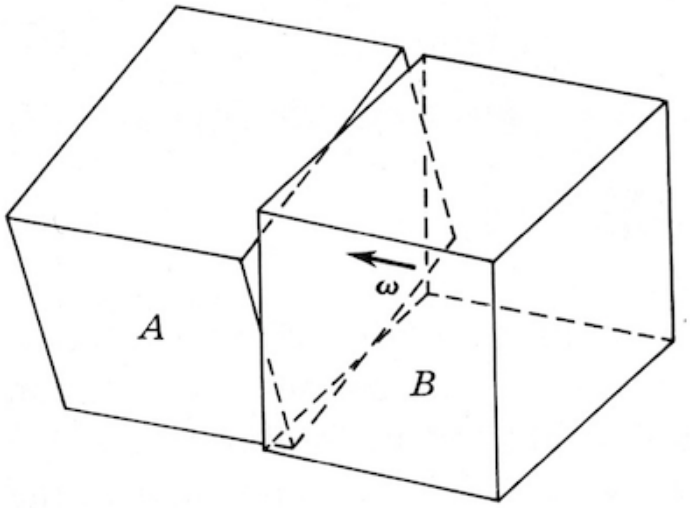

Figure 3.15: A twist grain boundary. Rotation vector ω is normal to the boundary. Figure from Ref[14].

shall see in §3.4.1. Increasing the mis-orientation increases the density of dislocations in the boundary. Above $20 - 25°$ the dislocations are overlapping to the extent that they can no longer be considered separate entities. This is a *high angle* tilt boundary. The dislocation structure of low angle grain boundaries was conclusively validated by experiments[102, 103] and agrees with the theoretical description presented in §3.4.1.

3.4.1 Low Angle Tilt Boundaries

Tilt boundaries can be further categorised by the orientation of the crystal either side of the GB. If the angle between the GB and the lattice vector on each side of the GB is equal, this is a *symmetric* tilt, Fig. 3.16 and otherwise an *asymmetric* tilt, Fig. 3.17. We will start with the symmetric tilt case and calculate the density of dislocations and orientation of the dislocations in the boundary.

Consider the arrangement of planes in Fig. 3.18. This is a symmetric boundary, at the end of each of the free planes is a dislocation with a Burgers vector perpendicular to the grain boundary. Clearly the dislocation density must be related to the number of free planes. The configuration is unstable since dislocations of the same $\mathbf{b}$ are sitting on top

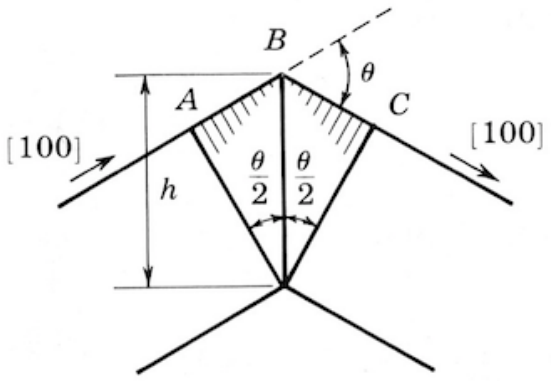

Figure 3.16: Symmetric tilt boundary. Figure from Ref[14].

of each other. The low energy configuration, seen in Fig. 3.19, displaces the ends of the planes so the dislocations are able to form in stress free locations along $x = 0$.

The number of planes ending in dislocations is simply given by

$$n_p = \frac{2h}{b} \sin \frac{\theta}{2} \tag{3.16}$$

where h is the thickness of the boundary and b is the magnitude of Burgers vector. The spacing between Burgers vectors is then simply calculated as

$$D_s = \frac{h}{n_p} = \frac{b}{2\sin(\theta/2)} \tag{3.17}$$

From this relationship we can see that when $\theta \sim 0.5$ radians the dislocations with core radius of $\sim b/2$ begin to overlap.

For an asymmetric boundary if we lined up dislocations along a boundary as we did for the symmetric case their energy from the stress fields would not be zero along the boundary, Fig. 3.20. Instead we find that a superposition of two populations of dislocations with Burgers vectors $\mathbf{b}_1 = (b, 0)$ and $\mathbf{b}_2 = (0, b)$ can be used to resolve the stresses at the end of the lattice planes, Fig. 3.21a. The average of these dislocations is

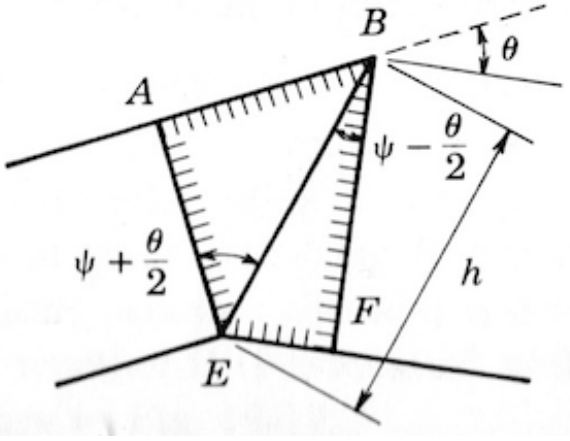

Figure 3.17: Asymmetric tilt boundary. Figure from Ref[14].

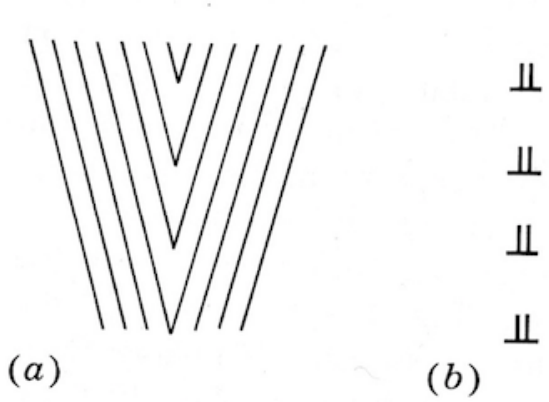

Figure 3.18: Undeformed end of planes give an unstable configuration of dislocations. Figure from Ref[14].

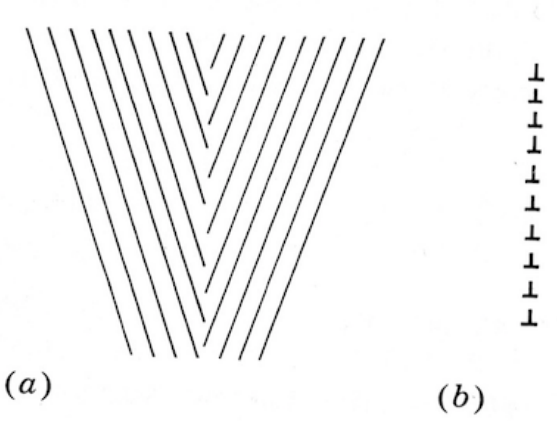

Figure 3.19: Ends of plane shift to give a dislocation at the end of each line. Figure from Ref[14].

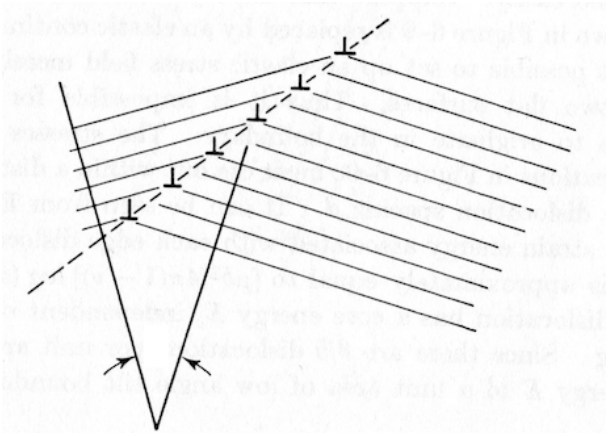

Figure 3.20: Unstable configuration of dislocations in an asymmetric grain boundary.Figure from Ref[16].

$$\mathbf{b}_3 = \frac{n_1\mathbf{b}_1 + n_2\mathbf{n_2}}{n_1 + n_2} \tag{3.18}$$

The spacing between each set of dislocations can be calculated from the angle between the boundary and planes, Fig. 3.16 as

$$D_1 = \frac{b}{\theta \cos\psi} \tag{3.19}$$

and

$$D_2 = \frac{b}{\theta \sin\psi} \tag{3.20}$$

The configuration in Fig. 3.21b eliminates long range stresses.

3.4.2 Observations of Grain Boundary Structure

Grain boundary structure was inferred from experiments[102] as early as 1953, Fig. 3.22. The presence of dislocations was seen in these experiments using regularly spaced etch pits. Other experiments by Hirsch[103] in 1956 using electron microscopy and Hedges[104] in 1953 using decorated dislocations, directly showing grain boundary structure. Recently,

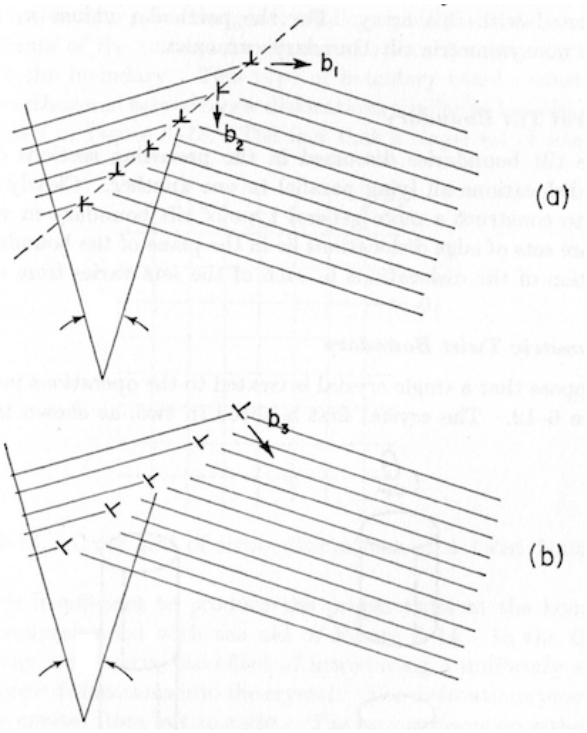

Figure 3.21: **a** Two populations of dislocations with perpendicular Burgers vector form a stable configuration in an asymmetric grain boundary. **b** The effective dislocation, $\mathbf{b}_3$, as a superposition of the dislocations in **a**. Figure from Ref[16].

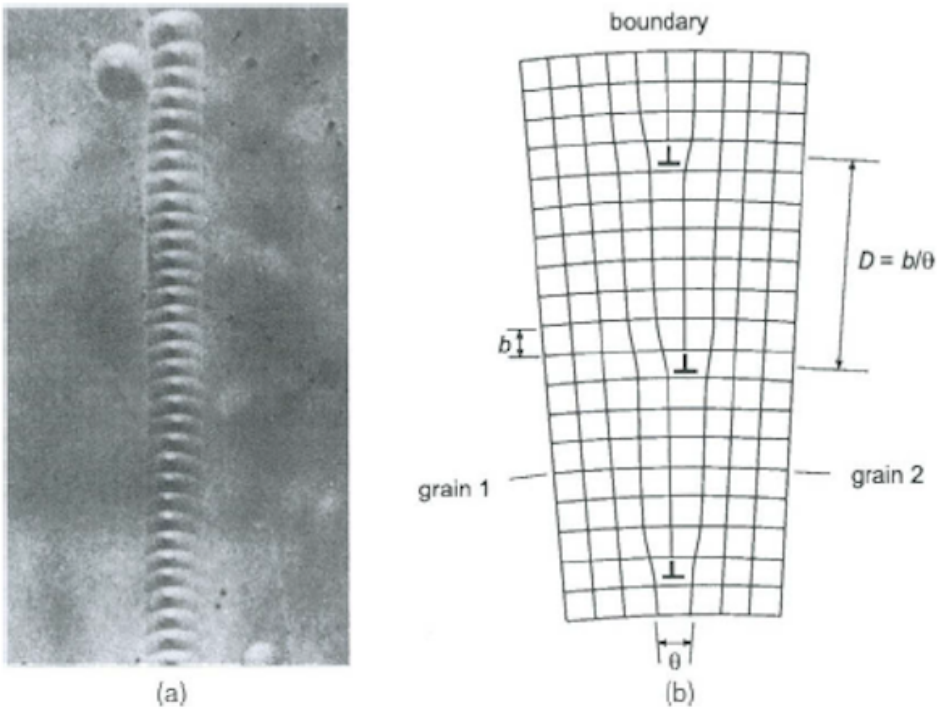

Figure 3.22: The arrangement of dislocations (right) revealed by etch pits (left) between grains of germanium crystals. Figure from Ref[14].

grain boundaries in grown crystals of graphene show the dislocation network in a high angle tilt boundary at an angle of 28°, Fig. 3.23.

Grain boundaries can also occur due to the curvature of the surface in which they are embedded. Irvine[18] demonstrates the existence of grain boundaries on domed surfaces, Fig. 3.24.

3.5 Lattice Structure in Real Space: Delaunay Triangulation

We end this chapter with a few analysis methods, necessary for dislocation physics. Delaunay triangulation[105] maximises the minimum angle between lines drawn between neighbouring particles. The result of the triangulation is a list of particles with their corresponding nearest-neighbour. A straight forward example is seen in the series of im-

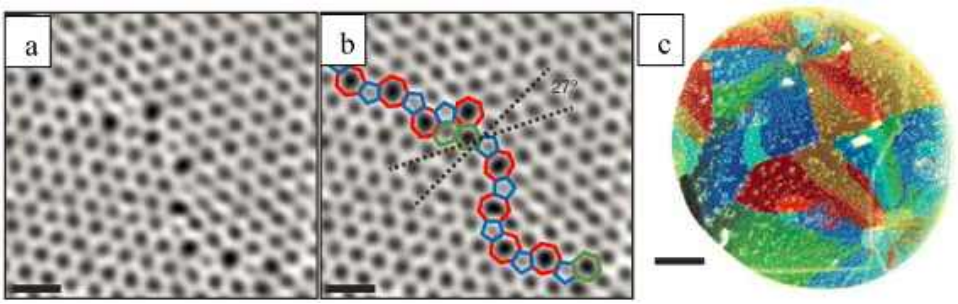

Figure 3.23: Grain boundaries in graphene grown by chemical vapour deposition **a** Two grains (bottom left, top right) in CVD graphene intersect with a 27^{deg}relative rotation. An aperiodic line of defects stitches the two grains together. **b** The image from **a** with the pentagons (blue), heptagons (red) and distorted hexagons (green) of the grain boundary outlined. Figure from Ref[17].

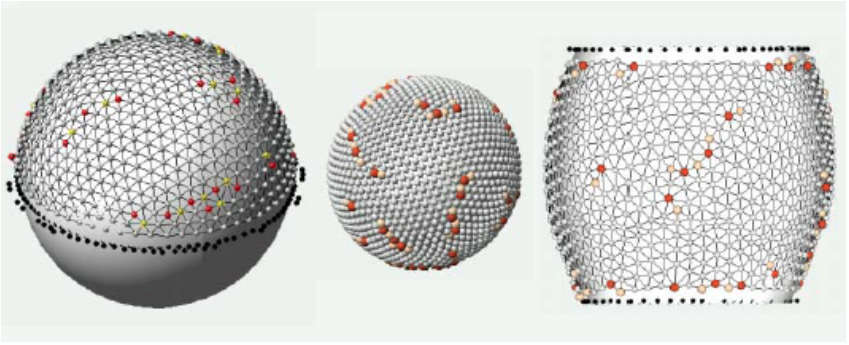

Figure 3.24: Dislocations arranged into grain boundaries are required to relax the stresses on the curved surface of a dome, a sphere and a barrel. Figure from Ref[18].

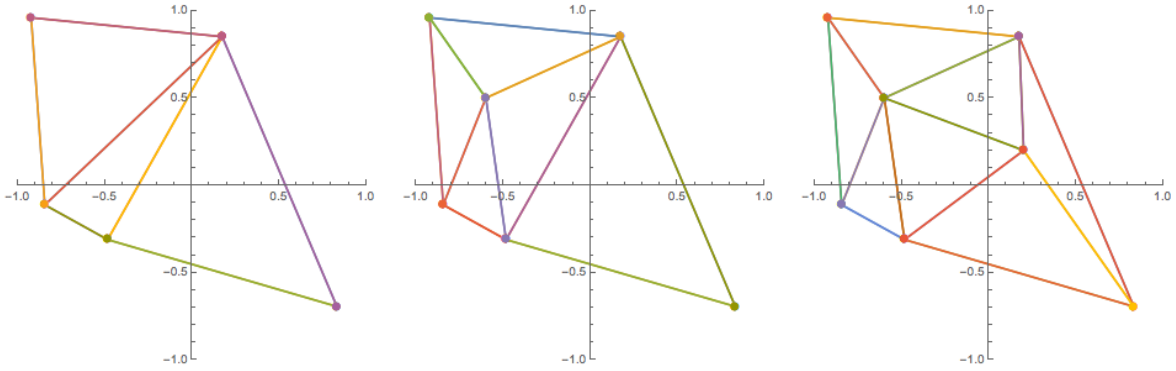

Figure 3.25: The series of images shows particles being added to a system. The Delaunay triangulation maximises the minimum angle.

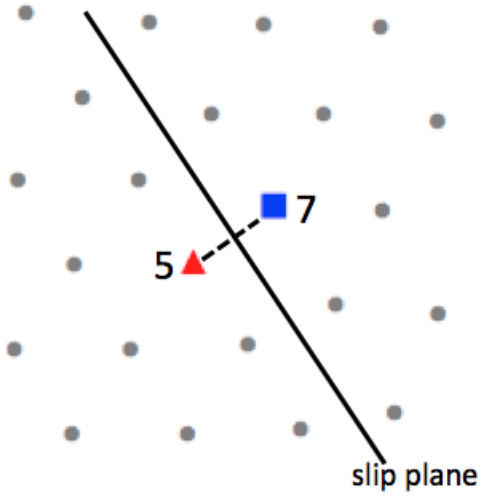

Figure 3.26: Shows a dislocation in a triangular lattice. The dislocation is marked by a pair of particles with 5 and 7 nearest neighbours.

ages in Fig. 3.25. These show the triangulations generated as new particles are added to system. The triangulation is a slow process, and is often optimised using a divide and conquer algorithm. The implementation used to analyse our simulations is based on functions available in Mathematica 10.0. From the Delaunay triangulation we are able to calculate coordination number as the length of the nearest-neighbour lists for each particle. An edge dislocation is marked by a pair of neighbouring particles having 5 and 7 nearest neighbours respectively. The vector joining this 5-7 pair is approximately perpendicular to the dislocation glide plane, Fig. 3.26.

3.6 Structure Factors and Order Parameters

The melting transition from solid to liquid in soft matter material is marked by a sharp increase in dislocation density and a loss of translational and rotational order. We have also discussed the possible existence of a hexatic phase between the solid and liquid phases characterised by a loss of translational order only. To characterise the order of the system we introduce the standard definitions of the translational and rotational (6-fold for the triangular lattice) order parameters[3].

Translational Order Parameter,

$$\Psi_T = \left| \left\langle \frac{1}{N_v} \sum_{j=1}^{N_v} \mathrm{e}^{i\mathbf{G}\cdot\mathbf{r}_j} \right\rangle \right|. \tag{3.21}$$

where $\mathbf{G}$ is the lattice vectors of the perfect lattice and N_v is the number of vortices.

Hexatic Order Parameter,

$$\Psi_H = \left| \left\langle \frac{1}{N_v} \sum_{j=1}^{N_v} \frac{1}{z_j} \sum_{k=1}^{z_j} \mathrm{e}^{i6\theta_{jk}} \right\rangle \right|^2. \tag{3.22}$$

where z_j is the number of neighbours of particle j and θ_{jk} is the angle between particle j and its kth neighbour.

From Delaunay Triangulation the density of defects (particles that are not 6-fold coordinated),

$$N_d = \frac{N_{\mathrm{mis}}}{N_v}. \tag{3.23}$$

where N_{mis} is the number of particles without 6 nearest neighbours and N_v is the number of particles (or in our case vortices). Empirically, relaxation times near melting are very long. Fig. 3.27 shows the relaxation time of the translational order parameter for various

[3]Mathematica code that calculates the order parameters are listed in Appendix E.

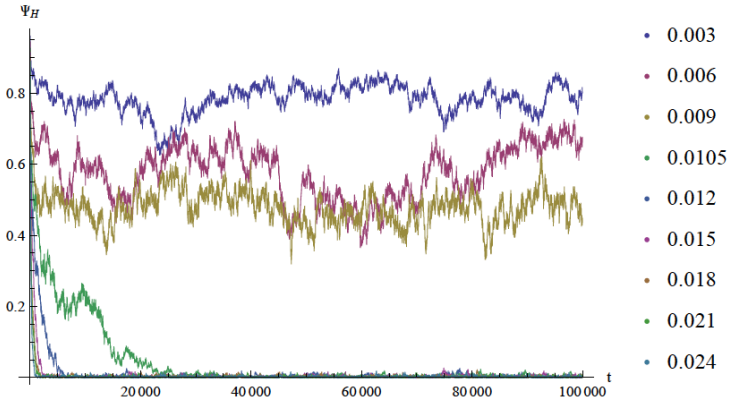

Figure 3.27: Transient behaviour of $\Psi_{\mathrm{T}}(t)$ for various temperatures. For this system $T_m = 0.133$.

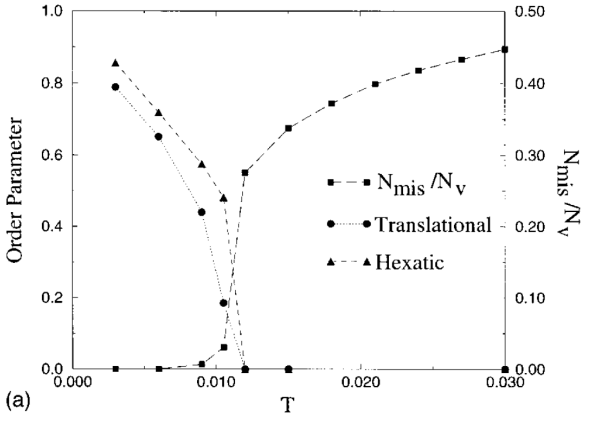

Figure 3.28: Order parameters and density of defects for 2D periodic system containing 1020 vortices. Onset of melting is seen in the dramatic changes in all three parameters around melting. For this system $T_m = 0.133$. Figure from Ref[19].

temperatures above and below the melting temperature, T_m. It is of key importance to understand how the order parameters at a particular temperature are evolving with time to ensure we produce the correct equilibrium value.

Chapter 4

NON-NEWTONIAN FLUIDS

This chapter introduces key fluid concepts necessary for discussing the rheology of the FLL in the liquid state. We will start by discussing two idealised states of matter, the *Hookean elastic solid* and the *Newtonian viscous liquid*. These two model setups will form the basis for our understanding of more exotic fluid behaviours. We will cover aspects of non-Newtonian fluids where the constitutive equations, relating stresses to strains, in the material take on a non-linear form. We will finish with a discussion on viscoelastic liquids in particular how these materials behave as either elastic solid or viscous liquid depending on the measurement timescales.

4.1 Overview

We begin by introducing the constitutive equations. We use these equations to understand viscoelasticity in the linear regime. Modifications to these equations then allow us to explore models of non-Newtonian fluids that we will discuss further in §4.2.

4.1.1 The Hookean Elastic Solid

The Hookean solid has the constitutive equation, relating stress σ to strain γ is given by

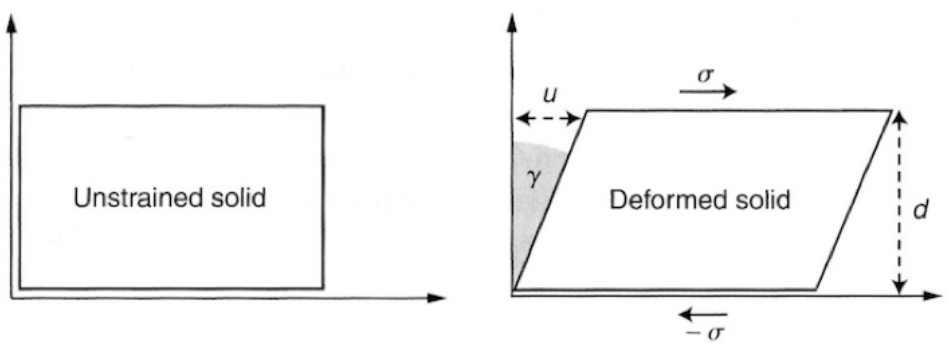

Figure 4.1: Strain induced in a sheared elastic solid by an applied stress. Figure from Ref[20].

$$\sigma = G\gamma \tag{4.1}$$

(as per Hooke's Law) where G is either the shear modulus, c_{66}, or the bulk modulus c_{11}. Fig. 4.1 illustrates stress and strain for a sheared block. Shear stress is a force per unit area $\sigma = F/A$ applied tangentially to the surface of a block of elastic solid. The strain is the resulting deformation in the material in response to this shear stress. For this case strain is defined as U/d where U is the displacement parallel to the applied shear stress and d is the thickness of the material.

These ideas work in complete analogy for a compressed elastic rod. It is important to note the absence of time dependence in the definitions of an elastic solid. In this model for an elastic solid, the elastic deformation is reversible, such that any deformation vanishes after the stress is removed, see Fig. 4.2.

4.1.2 Viscous Newtonian Liquid

Starting from the constitutive equations, we will consider the component relating shear stress to shear strain. As we saw from §2.4 the shear modulus vanished in the liquid state for the vortex lattice. This is also true of the viscous Newtonian liquid, by definition liquids are not able to support strains (i.e. static displacements from their original positions). For a Newtonian fluid the constitutive equation therefore relates the applied

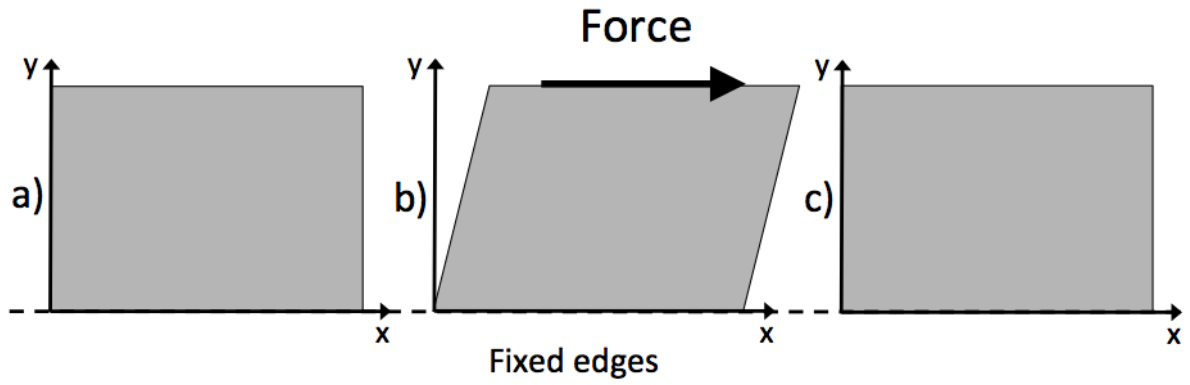

Figure 4.2: **a** Elastic solid block at reset with with no applied force. **b** Under the action of an applied shear stress, the block deforms linearly. **c** The block returns to its original shape when the shear stress is removed.

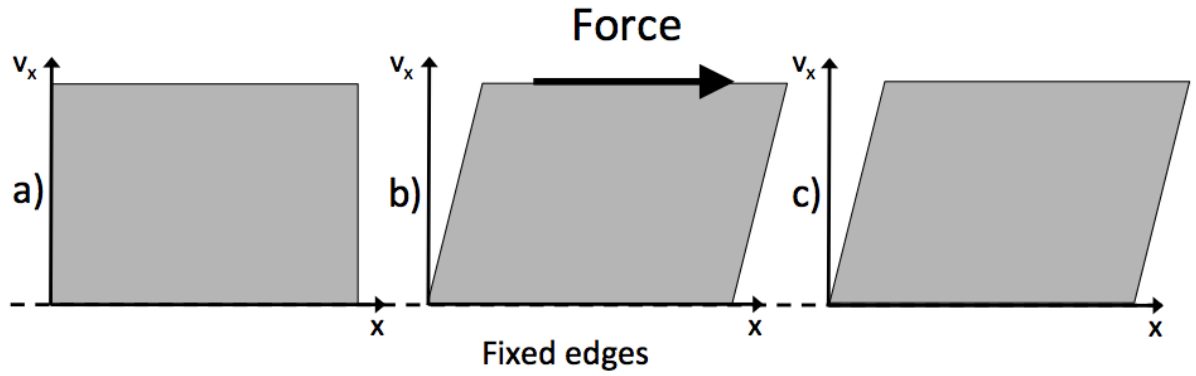

Figure 4.3: **a** A Newtonian fluid at rest. **b** An applied shear stress at the upper boundary of a fluid creates a linear velocity profile in the Newtonian viscous liquid. **c** After the shear stress is removed from the upper boundary the velocity profile persists in the fluid until is eventually slows.

shear stress to the velocity gradient, or shear rate $\dot{\gamma}$, in the moving fluid

$$\sigma = \eta\dot{\gamma} \tag{4.2}$$

Here the constant of proportionality is called the *dynamic viscosity*, or simply the viscosity. For a Newtonian fluid η is a constant, so it does not change over time or due to shear rate. To clearly distinguish this from the elastic solid, we notice that if the shear stress is removed, the flow continues, Fig. 4.3.

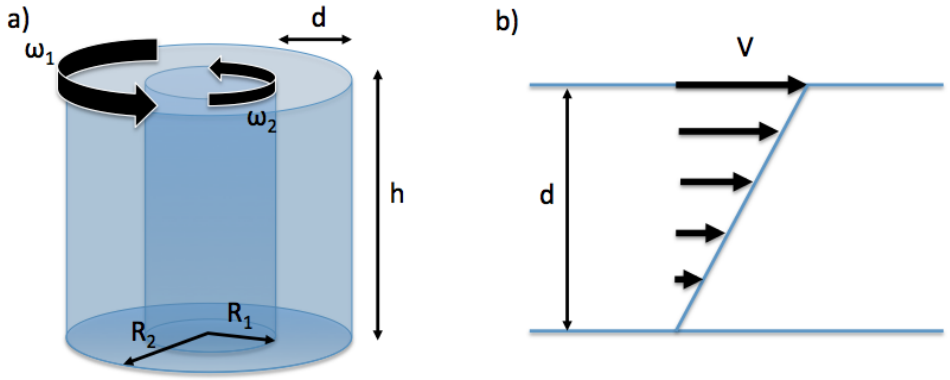

Figure 4.4: Couette flow. **a** Two co-axial cylinders rotating at different speeds. **b** 2D Couette flow, the limit cylinder radius $R_1 \to \infty$.

To ascertain the flow profile we introduce the equation of motion for a fluid, in terms of the stress tensor, since this form give us the best access to an understanding of the constitutive equations. The equation of motion is defined as

$$\rho \frac{\partial v_i}{\partial t} + \rho v_j \frac{\partial v_i}{\partial x_j} = \rho F_i + \frac{\partial \sigma_{ij}}{\partial x_j} \tag{4.3}$$

where, v_i labels the ith component of velocity, F_i the body force and ρ the density. Two common flows that are easily derived[106] are for Poiseulle flow and Couette flow. We will not cover the standard derivations of the velocity fields in terms of the Navier-Stokes equations, but will find a solution from Eq. (4.3) and Eq. (4.2).

4.1.3 Couette Flow

Couette flow describes shear flow between two walls, using the geometry in Fig. 4.4. 2D Couette flow is the limit where the cylinder radius $R_1 \to \infty$. For this system a 2D fluid, of thickness d, confined between two infinite parallel walls. The top wall in this geometry is sheared against the top surface of the fluid at a velocity V and the bottom wall is stationary. We *assume* the fluid does not slip against the walls. This is the *no-slip* boundary condition (This condition does not always hold and will be discuss later in this section.). Rearranging Eq. (4.2) gives

$$\sigma = \eta\dot{\gamma} = \eta\frac{\mathrm{d}}{\mathrm{d}y}\dot{v} \tag{4.4}$$

Clearly the shear rate is the velocity gradient across the system $\dot{\gamma} = d\dot{v}/dy$ and Eq. (4.3) reduces to

$$0 = \frac{\mathrm{d}\sigma_{xy}}{\mathrm{d}y} \tag{4.5}$$

Furthermore $v_x(y) = Vy/d$ satisfies this equation and the boundary conditions.

4.1.4 Poiseulle Flow

Consider the 2D case of flow between infinite parallel walls driven by a constant pressure gradient $F = \mathrm{d}p/\mathrm{d}x = P$. We again assume the no-slip condition at the walls such that $v(0) = 0$ and $v(d) = V$. The equations of motion reduce to

$$\frac{\mathrm{d}p}{\mathrm{d}x} = \eta\frac{\mathrm{d}\sigma_{xy}}{\mathrm{d}y} \tag{4.6}$$

$$P = \eta\frac{\mathrm{d}^2 v_x(y)}{\mathrm{d}y^2} \tag{4.7}$$

This has the parabolic solution $v_x(y) = \frac{P}{2\eta}y(y-d)$.

In the next section we will go on to look at cases where the viscosity varies as a function of shear rate.

4.2 Power Law Viscosity

Many 'everyday' liquids are not well described as a viscous Newtonian liquid[20], they frequently display shear thinning. The viscosity of these fluid is reduced as shear rates

increase. Viscosity can seen from the gradient of a stress vs shear rate graph. Fig. 4.5 shows three different types of liquid. The linear Newtonian liquid, and two non-Newtonian liquids. The lower line describes shear thinning. Simple fluids do not display shear thinning, however many polymer fluids and suspensions do. These fluids can support much higher shear rates, typically at the boundary, since the viscosity in these regions is lower in response to the high shear rates. These non-Newtonian fluids no longer have a viscosity independent of shear rate. One model for non-Newtonian fluids was put forward by Ostwald-de Waehle,

$$\eta = K\dot{\gamma}^{n-1} \tag{4.8}$$

.

Here, with $n > 1$ we have shear thickening and $n < 1$, shear thinning and $n = 1$ returns constant viscosity, consistent of Newtonian liquid. This model fails to capture the details of shear thinning or thickening fluids and more fuller descriptions are provided by Cross[107]. Real liquids can transition through a shear thinning regime to a shear thickening and then back to shear thinning[20]. This exotic behaviour is not described by either the Cross or Ostwald-deWaehle models. Fig. 4.5 and Fig. 4.6 show the stress-shear rate and viscosity-shear rate graphs for various types of material. Here we introduce the viscoplastic solid. This material behaves as an elastic solid below a critical yield stress, σ_c, and for a general viscoplastic, the material flows like a non-Newtonian liquid above σ_c. Above the yield stress the material undergoes shear thinning until viscosity plateaus at a constant value.

4.2.1 Stability of Non-Newtonian Flow

It is useful to examine the stability of non-Newtonian solutions to simple flow models. Here we will consider a pertubation to the Couette flow solution considered in §4.1.3 when the viscosity is dependent on shear rate, $\eta(\dot{\gamma})$. Following the arguments of Oswald[20] we subsitute this visocity into Eq. (4.1.3),

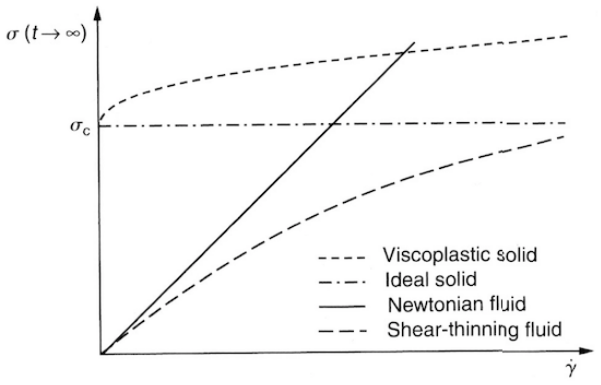

Figure 4.5: Stress in the long time limit. Figure from Ref[20].

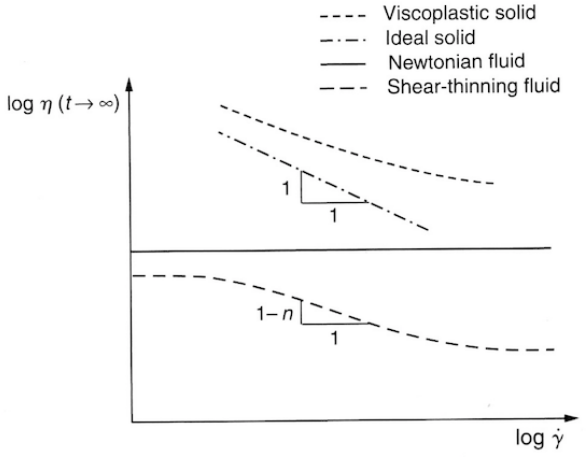

Figure 4.6: Viscosity in the long time limit. Figure from Ref[20].

$$\frac{\partial \sigma_{xy}}{\partial y} = \frac{\partial \eta(\dot{\gamma})\dot{\gamma}}{\partial y} = 0. \tag{4.9}$$

Expanding this to first order in $\dot{\gamma}$

$$\left(\eta + \dot{\gamma}\frac{\partial \eta}{\partial \dot{\gamma}}\right)\frac{\partial \dot{\gamma}}{\partial y} = 0 \tag{4.10}$$

With the boundary conditions in $v(0) = 0$ and $v(d) = V$ this has the same solution as the standard Couette flow for a Newtonian liquid,

$$v_x(y) = V\frac{y}{d} \tag{4.11}$$

We now examine the stability of the flow to a time dependent perturbation

$$v_x(y,t) = \dot{\gamma}y + c(y,t) \tag{4.12}$$

Taking the derivatives of this quantity gives the local shear rate

$$\frac{\partial v_x(y,t)}{\partial y} = \frac{\partial(\dot{\gamma}y)}{\partial y} + \frac{\partial c(y,t)}{\partial y} \tag{4.13}$$

$$\dot{\gamma} = \dot{\gamma}_0 + \frac{\partial c}{\partial y} \tag{4.14}$$

The equation of motion, Eq. (4.10), must be modified to include the time dependence since to velocity profile perturbation is time dependent. This results in

$$\rho\frac{\partial c}{\partial t} = \left(\eta + \dot{\gamma}\frac{\partial \eta}{\partial \dot{\gamma}}\right)\frac{\partial \dot{\gamma}}{\partial y}. \tag{4.15}$$

To examine the stability of the flow we can expand this to first order in $\dot{\gamma}_0$

$$\rho\frac{\partial c}{\partial t} = \left(\eta(\dot{\gamma}_0) + \dot{\gamma}_0\left(\frac{\partial \eta}{\partial \dot{\gamma}}\right)_{\dot{\gamma}_0}\right)\frac{\partial^2 c}{\partial t^2} \tag{4.16}$$

Now we let the flow perturbation have the form $c(y,t) = c_0\exp(\omega t + iky)$, this give a value for ω of

$$\omega = -\frac{k^2}{\rho}\left(\eta(\dot{\gamma}_0) + \dot{\gamma}_0\left(\frac{\partial \eta}{\partial \dot{\gamma}}\right)_{\dot{\gamma}_0}\right) \tag{4.17}$$

For $\omega > 0$ the flow is unstable so we find

$$\dot{\gamma}\frac{\partial \ln(\eta)}{\partial \dot{\gamma}} > -1. \tag{4.18}$$

If we assume a power law for viscosity, Eq. (4.8), the flow is unstable for $n < 0$. This is the case for a shear thinning fluid. In this case the shear rates can vary quickly without the viscous cost. The result is profiles that remain flat across the bulk of the channel since the shear rate is concentrated in the boundary.

4.3 Viscoelasticity

All materials can behave viscoelasticaly. For liquid this means at short timescales they behave like elastic solids while at long time scales the behave as viscous liquids (This is reversed for viscoelastic solids, such as rubber, that behave like liquids at short timescales and solid at long timescales.). In the case of water this timescale is very short, such that all familiar behaviour of water is viscous. However, at very short timescales water will behave elastically. Very viscous liquids, such as silly putty, have longer *viscoelastic relaxation times*, enabling their elastic behaviour to be easily seen.

To understand the cross over regime between elastic and viscous behaviour in liquids we turn to the Maxwell model for a viscoelastic fluid. This model consists of a spring that deforms elastically and a dashpot (a device that produces damping by viscous fric-

tion), the provides viscous damping, Fig. 4.7. This model gives a single characteristic time for viscoelastic relaxation. A more realistic description of viscoelasticity is found by chaining together combinations of springs and dashpots. These models such as the Jeffery's Model[20] are able to give multiple characteristic relaxation times. The strain for the Maxwell model system is defined as

$$\dot{\gamma} = \dot{\gamma}_E + \dot{\gamma}_v. \tag{4.19}$$

The constitutive equations for each of these parts are the elastic solid Eq. (4.1) and ideal viscous fluid Eq. (4.2). Substitution into eq.. gives Maxwells equation

$$\dot{\gamma} = \frac{\dot{\sigma}}{G} + \frac{\sigma}{\eta} \tag{4.20}$$

multiplying by η gives

$$\sigma + \tau\dot{\sigma} = \eta\dot{\gamma} \tag{4.21}$$

Here $\tau = \eta/G$ is the Maxwell relaxation time and has the solution

$$\sigma(t) = \eta\dot{\gamma}\left(1 - \exp(-\frac{t}{\tau})\right) \tag{4.22}$$

The behaviour of this equation gives

$$\sigma(t) = \begin{cases} G\dot{\gamma}t \approx G\gamma & t < \tau \\ \eta\dot{\gamma} & t > \tau \end{cases} \tag{4.23}$$

At short times the material responds elastically and at long times as a viscous liquid, Fig. 4.8. This approximation holds for a liquid in the linear regime. The linear regime is defined by two conditions that must be met. First, shear rates must be low so that objects

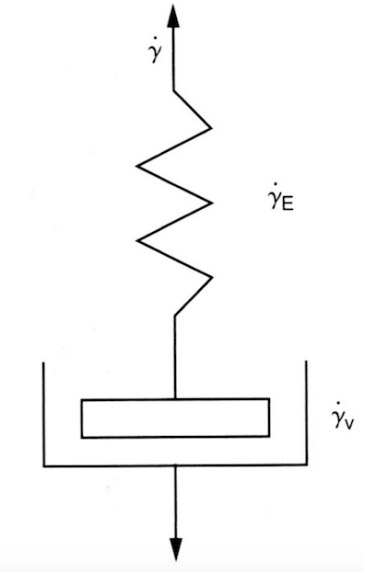

Figure 4.7: Maxwell model of a viscoelastic liquid with a single relaxation time. The model consists of a spring and dashpot. Figure from Ref[20].

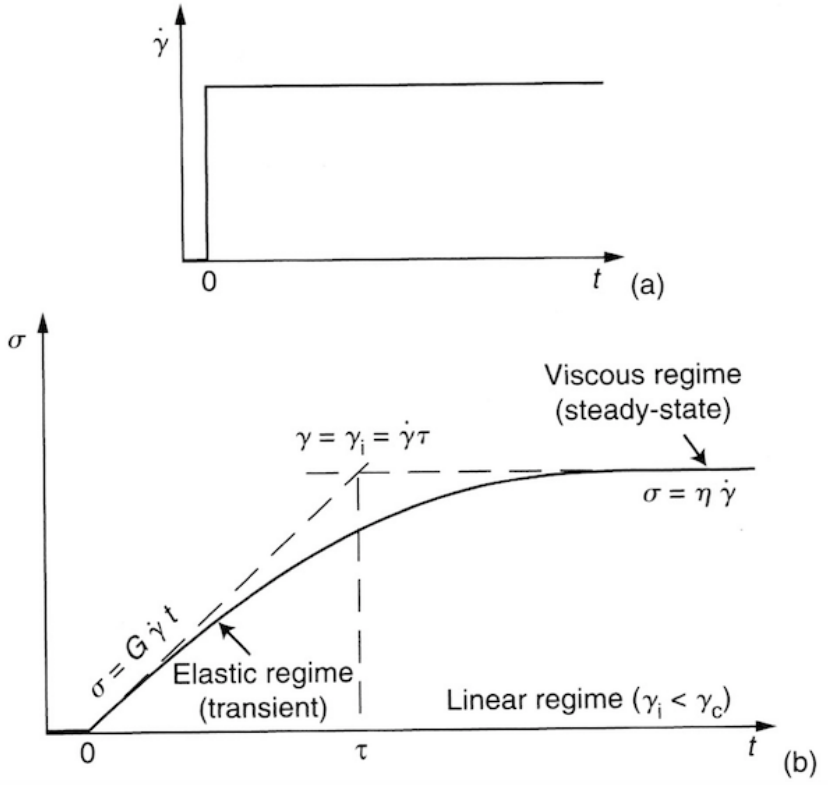

Figure 4.8: Below $\tau = \eta/G$ a viscoelastic fluid responds elastically. Above it flows like a viscous liquid. Figure from Ref[20].

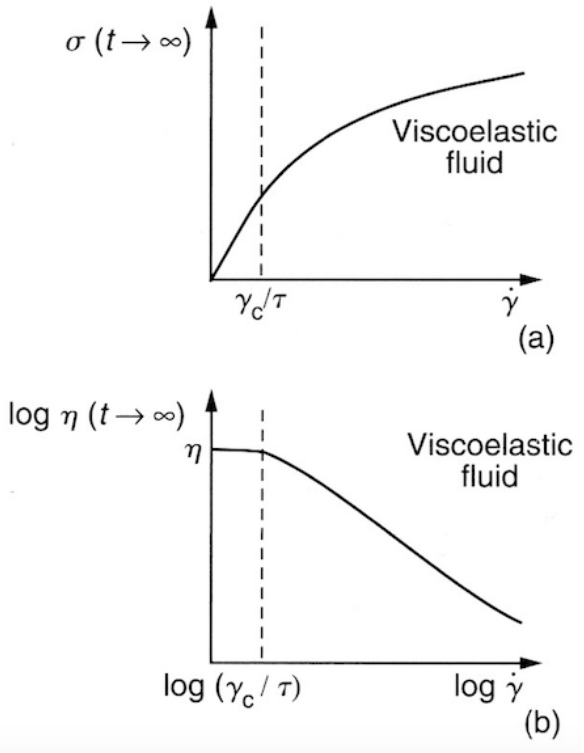

Figure 4.9: As $t \to \infty$ an viscoelastic fluid will flow as a Newtonian liquid for small shear rates. For large shear rates the fluid becomes non-linear and we see non-Newtonian behaviour. Figure from Ref[20].

of the fluid (such as colloidal particles) only deform elastically. This gives a constant shear rate, G. Also the structure of the fluid should not be altered by the shearing. This gives a constant viscosity in the viscous flow regime. In general this is not the case for most fluids and the characteristic time is written as a function of shear rate, $\tau = \eta(\dot{\gamma})/G(\dot{\gamma})$. For these systems we see a linear regime below a critical shear rate $\dot{\gamma}_c$ and a shear thinning non-linear regime above, see Fig. 4.9. Since most fluids show shear thinning behaviour, high shear rates reduce the characteristic time and elastic behaviour becomes harder to see. One regime that these conditions usually hold in is small amplitude oscillatory flow. This type of flow in the FLL is explored in Chapter 6.

Chapter 5

SIMULATING THE VORTEX LATTICE

5.1 Vortex Lattice Dynamics

To access the dynamical behaviour of the vortex lattice we employ the technique of molecular dynamics (MD). Specifically a branch of MD called Langevin dynamics (LD) that was first introduced[108, 109] as a description of Brownian motion[110]. Brownian motion is the result of a large number of collisions with the small atoms of the fluid, resulting in the apparently random motion of a large suspended particle. LD models this system by separating the effects of the fluid suspension into an average deterministic effect(viscous drag) and a random effect(thermal noise). These modifications to the equations of motion model the complicated interactions of the particle with the solvent.

To understand why we can apply LD to simulate the dynamics of the vortex lattice we must first look at a simplified model of vortex motion. A model by Bardeen and Stephenson[70] shows that in the flux flow regime[1], vortices experience a viscous drag term due to the interaction of the quasi-normal cores with the superconducting material[12]. The form of this drag term is given in Eq. (2.22). This viscous drag acts as an implicit solvent that can be suitably modelled by the drag term in the Langevin equation.

In the previous chapter we discussed melting of the vortex lattice and thermally activated flux creep. These phenomena showed how thermal fluctuations of the flux lines

[1] see §2.2.2 for a longer discussion about the flux flow regime.

cause changes of behaviour in the vortex dynamics. Thermal fluctuations acting upon the flux lines can be modelled by a coupling of the vortices to a heat bath at temperature, T. The thermal noise created by the heat bath coupling is described by the stochastic term in the Langevin equation.

To continue we start with the usual form of the Langevin equation for N particles,

$$m\mathbf{a} = -\gamma\mathbf{v} + \chi(t) \tag{5.1}$$

and build in the modifications needed to capture all the relevant features of vortex dynamics where $\mathbf{a}$ and $\mathbf{v}$ are the $3N$ components of acceleration and velocity and $\chi(t)$ is the stochastic noise term. As discussed in Chapter 2, vortices in thin superconductors interact by a 2D potential, and in the regime where $H_{c1} < B \ll H_{c2}$ the force between vortices is dependent only on the separation of the vortex centres. We also choose their motion to be confined to a 2D plane. To describe this phenomenology, vortices in the following simulations should be considered to be point particles that reside in a 2D plane. This reduces the number of components of the Langevin equation to $2N$. For the vortex lattice it is known that viscous drag is far greater than inertia[10], this is equivalent to setting $m = 0$ so that we only see terminal velocities of the vortices and no acceleration. This is often known as *overdamped Langevin dynamics*. Previously we described the vortices interacting by a repulsive Bessel function force Eq. (2.18) so an additional deterministic force term needs to be added to Eq. (5.1) to describe this. We also add additional terms to model a Lorentz force[2] $\mathbf{F}_L$ and a random site pinning force $\mathbf{F}_p$. This random pinning term is often modelled by a Gaussian force and will be discussed briefly in §5.3. These modifications the dynamics of the vortex lattice can then be described by the $2N$ equations

$$\gamma\mathbf{v} = \mathbf{F}_{vv} + \mathbf{F}_L + \mathbf{F}_p + \chi(t) \tag{5.2}$$

[2]see Chapter 2.

where $\mathbf{F}^{vv}$ is the vortex-vortex interaction.

5.2 Andersen Thermostat

The stochastic thermostat we are going to use was first described by Andersen[111] in 1980. The thermostat is designed to produce the expected energy fluctuations of the constant temperature canonical ensemble (NVT). To produce these energy fluctuations Andersen proposed the addition of a stochastic term to standard molecular dynamics that allows for the exploration of energy-momentum phase space. The addition of the stochastic term creates a Markov chain[111] where the current state is uncorrelated with any of the previous ones. The major premise of this thermostat is that *if* the Markov chains generated are *irreducible* (meaning they explore all of phase space in finite or simulation time) the time average of any quantity along a trajectory is equal to the canonical ensemble average for that same quantity. The biggest problem that occurs with this is due to the presence of local minima in phase space which causes the system to be unable to explore certain energy-momentum manifolds in finite time. This situation invalidates the premise of this thermostat.

The Andersen thermostat is constructed as a Poisson process that delivers thermal kicks to a given particle at intervals that are exponentially distributed as $p(t) = \nu e^{-\nu t}$ where ν is the average rate of kicks. The exponential distribution of events is equivalent to a particle receiving a kick in a time interval of Δ with a probability of $p = \nu\Delta = \Delta/\tau$ where τ is the average time between kicks. To create a Poisson process we require the stochastic term to have the following properties[3].

[3]The derivation of this is covered in detail in Appendix G.

Stochastic Noise Term

- Thermal kicks must be uncorrelated in time and between particles.
- The time average of the thermal kicks must be zero.
- At equilibrium the term must produce a Boltzmann distribution of the particle energies.

Mathematically this is defined as

$$\langle \chi_i(t) \rangle = 0 \tag{5.3}$$

$$\langle \chi_i(t)\chi_j(t') \rangle = 2k_B T\gamma\delta(t-t')\delta_{ij} \tag{5.4}$$

It follows from this, that the stochastic term in the Langevin equation for the ith vortex has the form

$$\chi_i(t) = (2\Delta k_B T/\gamma p)^{1/2}\mathcal{N}\Theta(p-q_j) \tag{5.5}$$

where $\mathcal{N}$ is a random number chosen from a Gaussian distribution $\mathcal{N}(0,1)$. The theta (or Heaviside) function has the usual meaning and q_j is a uniformly distributed random variate $q_j \sim \mathcal{U}(0,1)$. This description of the thermostat describes a Markov chain where collisions with the heat bath are instantaneous, moving the particle to another energy-moment manifold, with between-collision trajectories evolving deterministically according to Eq. (5.2).

To ensure we are describing a physically correct coupling with the heat bath the value of ν must be judiciously chosen. There is extensive literature on this, however, two primary methods exist that allow us to achieve this. The first is described by Andersen[111]. By construction the irreducibility condition is not dependent on the value of however Andersen states it is "*It is reasonable to choose ν so that the time for the decay of energy fluctuations along the trajectory will be the same as the time for decay of energy fluctua-*

tions of a small volume of real liquid surrounded by a much larger volume.". To do this we consider a small sample of fluid that is a a temperature ΔT higher than its surroundings. We then equate the rate of energy gain in the sample, due to stochastic collisions, with the rate of energy loss, through thermal conductivity. Andersen found the collision rate $\nu \sim \mathcal{O}(N^{-2/3})$. For the systems we will investigate $N \sim 1000$ so $\nu \approx 0.01$. The second method comes from Jensen and Brass[67, 27] who describe the requirement that thermal fluctuations must not be so frequent as to overwhelm the deterministic portions of the trajectories. They impose the requirement

$$\Delta \ll 2k_B T\gamma/\langle F\rangle^2 \ll \tau \tag{5.6}$$

where $< F >$ is the average of the deterministic forces on a given particle.

Jensen and Brass suggest a computational technique to ensure the correct distribution is being sampled. They propose that calculation of the moments of the Langevin equation can be used to check the energies in the simulation are correctly distributed. The time average over all particles can be taken for the quantities $\langle\delta\mathbf{x}\rangle$ and $\langle\delta\mathbf{x}^2\rangle$ (where $\mathbf{x}$ is the positions of the particles) and compared to the expected moments of the Fokker-Planck equation [4].

$$M_1 = \frac{1}{\Delta}\langle\delta\mathbf{x}\rangle = \frac{\langle F\rangle}{\gamma} \quad M_2 = \frac{1}{\Delta}\langle\delta\mathbf{x}^2\rangle = \frac{2k_B T}{\gamma} \tag{5.7}$$

This is a useful tool, but alone this cannot be used to ensure that the trajectories are not dominated by the stochastic terms. For this we must ensure that we are also satisfying Eq. (5.6).

[4] see Appendix G.

5.3 Integrating the Langevin Equation

The aim here is to generate an integration procedure, suitable for use in a computer. Physical constants should be set to appropriate values so as to avoid the tracking of small numbers and to simplify analysis. To do this a suitable length scale is chosen as well as a rescaling of constants.

Many integration schemes exist for standard MD. For the Langevin equation this set is much smaller since the trajectories now contain discrete jumps that preclude the calculation of, for example, the corrector step in Predictor-corrector method. For non-zero temperatures the presence of the stochastic term forces us to use the Euler method[67, 32] for integration. With a suitably small step size this method accurately generates the trajectories of the canonical ensemble[111]. The explicit integration of the Euler scheme results in the following discretised equation of motion

$$\mathbf{x}_i^{n+1} = \mathbf{x}_i^n + \left[(\mathbf{F}_{vv} + \mathbf{F}_p + \mathbf{F}_L)/\gamma\right]\Delta + (2\Delta k_B T/\gamma p)^{1/2}\mathcal{N}\Theta(p - q_j) \tag{5.8}$$

where $\mathbf{x}_i$ is the 2D position of the ith vortex, $\mathbf{F}_{vv}$ is the vortex-vortex interaction, $\mathbf{F}_p$ is the pinning force due to M randomly placed defects and $\mathbf{F}_L$ is the constant driving or Lorentz force.

The full forms for the force terms are

$$\mathbf{F}_{vv} = \sum_{j\neq i} -\frac{\phi_0^2}{2\pi\mu_0\lambda^3} K_1\left(\frac{|\mathbf{r}_{ij}|}{\lambda}\right)\hat{\mathbf{r}}_{ij} \tag{5.9}$$

$$\mathbf{F}_p = \sum_m \frac{2A_p}{{R_p}^2}|\mathbf{r}_{im}| \exp\left[\frac{-|\mathbf{r}_{im}|}{{R_p}^2}\right]\hat{\mathbf{r}}_{im} \tag{5.10}$$

$$\mathbf{F}_L = \mathbf{j} \times \Phi_0\hat{\mathbf{B}} \tag{5.11}$$

For this thesis we choose to simulate a pin-free system with no Lorentz force. We will omit the $\mathbf{F}_p$ and $\mathbf{F}_L$ terms and proceed to insert the full form for the vortex-vortex force $\mathbf{F}_{vv}$ into Eq. (5.2),

$$\begin{aligned}\mathbf{x}_i^{n+1} = \mathbf{x}_i^n & \\ &+ \sum_{j\neq i} -\frac{\phi_0^2\Delta}{2\pi\mu_0\gamma\lambda^3} K_1\left(\frac{|\mathbf{r}_{ij}|}{\lambda}\right)\hat{\mathbf{r}}_{ij} \\ &+ (2\Delta k_B T/\gamma p)^{1/2}\mathcal{N}\Theta(p-q_j). \end{aligned} \tag{5.12}$$

To rescale these equations we let

$$\frac{x}{a_0}\to x, \quad \frac{\lambda}{a_0}\to\lambda, \quad \frac{T}{a_0^2}\to T, \quad \Phi_0 a_0^2\to\Phi_0, \tag{5.13}$$

where we have used the same symbols for the rescaled terms to avoid additional notation. The power in the third term of Eq. (5.12) leads to the natural rescaling of temperature by a_0^2.

For simulation purposes we enforce a force cut-off range[34] $r_{\text{cut}} = 6\lambda$ where λ, was chosen to be $1.11a_0$ in line with the work of Besseling's group[28]. This allows us to create a soft lattice where $\lambda > a_0$ but ensures the forces are not too long range. As a measure we can consider the relative size of forces at λ and 6λ finding $K_1(6)/K_1(1) \sim 0.0022$. We let $k_B = \gamma = f_0 = 1$. (This choice of units gives a fundamental mass of $M = \gamma a_0/f_0 = 1$ and time $T = \gamma^2 a_0/f_0 = 1$.)

It was found empirically[5] that $\Delta = 0.01$ and $\tau = 1$ satisfy the Andersen and Jensen and Brass conditions. This step size satisfies Eq. (5.6) and generates the correct moments of Eq. (5.7). This step size also ensures that under normal operation there is a low probability ($P < 1\%$) that a vortex will be displaced $> a_0/50$ in a single time step[28].

[5]See app for discussion of these values.

5.4 Optimisations

The large phase space that the code will need to run over requires that it be efficient. These optimisations are selected such that they retain the accuracy of the simulation but improve the speed of summations and force calculations.

5.4.1 Force Calculations

The force between vortices is a modified Bessel function of the second kind $K_1(r)$. This function is relatively slow to calculate. The fastest versions that exist are in the Boost C++ library, an extension to C++ 03 (Most of Boost including the Bessel functions are integrated into the C++11/C++14 standards). An implementation is given in the following code block.

```
1 #include <boost/math/special_functions/bessel.hpp>
2
3 int main()
4 {
5   double r = 1.0; // distance of 1 unit
6   double f = boost::math::cyl_bessel_k(1,  r);  // K_1(r)
7 }
```

In integrating the Langevin equation the majority of the time is spent calculating the vortex-vortex interaction terms. Without optimisation there are N^2 force calculations between vortices. Clearly the call to the Bessel function routine will be preformed N^2 times so optimising the speed of the Bessel function will be beneficial. There are two standard approaches to slow force calculations. One is to find an approximation to the original function that is computational quicker whist retaining the form of the original. For the vortex-vortex interaction this is implemented by Koshelev[11], where he uses a log form of the potential which results is a simple polynomial expression for the force $f(r) = (1/r)(1 - r^2/r_{cut}^2)^2$ (For this force expression $r_{cut} = 3.33$). This is > 200 times faster than, and retains most of the features of, the Bessel function potential, Fig. 5.2. This polynomial force overestimates the Bessel function near $r = a_0$ and underestimates

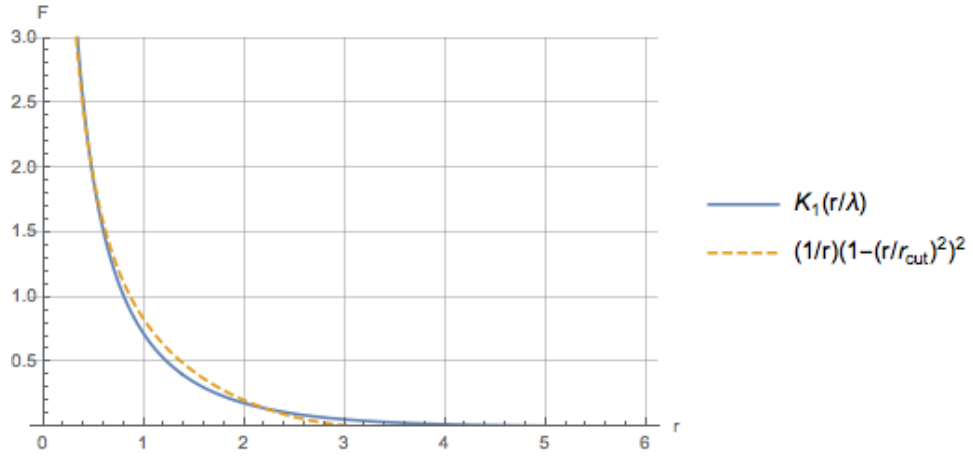

Figure 5.1: Comparison of force forms used in simulations of the vortex lattice. The polynomial force slightly overestimates the Bessel function force at $r \sim a_0$ and underestimates at $r \gtrsim 2a_0$.

for $r \gtrsim 2a_0$. The force is plotted against the Bessel function force in Fig. 5.1. The second approach, which is usually employed for complicated or non-standard potentials, is the tabulation method. This involves tabulating the potential on a discrete grid in r. The strength of the force at an arbitrary r is then calculated using the known points and an interpolation routine. For quickly varying potentials, higher order interpolation is required but for the vortex-vortex potential very accurate and fast results can be achieved with a linear interpolation. Comparison on timings are given in Fig. 5.2. For our simulations we will be using the tabulated force method since this method is > 100 times faster than the Boost function and more accurate than the polynomial force. To use this method, the forces $f(r_i)$ at M points on a uniform grid are precomputed at the start of the simulation using the numerically exact form of the potential. Here we use the C++ library function `boost::math::cyl_bessel_k(1, r)`. The result of this precomputing stage is a set of forces $f(r_i)$. To find the force at an arbitrary point $r' \notin r_1, r_2, ..., r_M$ we first find the two values of force either side of r', we label these as $f(r_-)$ and $f(r_+)$. The gradient at r_- is then $f'(r_-) = (f(r_+) - f(r_-))/h$. where h is the step size in the grid of r_i. We can calculate the interpolated value of $f(r')$ as

r	Boost Bessel	Tabulated	Polynomial
0.0312311	35.4826	35.4826	32.0137
0.0624622	17.6724	17.6724	15.9984
0.0936934	11.7167	11.7167	10.6562
0.124924	8.72747	8.72747	7.98232
0.156156	6.92643	6.92643	6.37574
0.187387	5.72048	5.72048	5.30281
0.218618	4.85526	4.85526	4.53485
0.249849	4.20349	4.20349	3.95748
0.28108	3.69438	3.69438	3.50719
0.312311	3.28542	3.28542	3.14585
timings	0.0133312	9.72E-05	6.36E-05
rel. timing	1	0.00729	0.00477
Each point calculated 10000 times			

Figure 5.2: Timings for force forms used in simulations of the vortex lattice. The fastest is the polynomial force but is less accurate than either the tabulated or Bessel function forms. The tabulated potential is significantly faster than the Boost function. Each $f(r)$ was run 10 000 times. The tabulated potential uses a linear interpolation with a step size $h = 0.0001$.

$$f(r') = \begin{cases} f(h) & r' < h \\ f(r_-) + (f(r_+) - f(r_-)) \dfrac{(r' - r_-)}{h} & h < r' \leq r_{\text{cut}} \\ 0 & r' > r_{\text{cut}} \end{cases} \tag{5.14}$$

The force is set to zero above r_{cut} and to $f(h)$ below h. This latter step avoids infinities in the calculations.

The step size of the grid is chosen as $h = 0.0001$. This leads to accurate values for the force, even close to $r = 0$ whilst still providing the required speed-up. The implementation is given in the code block below.

```
1 #include <boost/math/special_functions/bessel.hpp>
2 #include <vector>
3
4 // prototypes
5 double ftab(double r);
6 double LinearInterp(double a, double b, double f);
7
```

```
8  // initialise force
9
10 std::vector<double> pot_table;
11
12 double step = 0.0001;
13 double ostep = 1.0/step;
14 double olambda = 1 0/ 1.11;
15 double rcut = 6.66;
16 double fmax = 0;
17
18 for (long i = 1; i <= static_cast<int>(rcut / step) + 1; ++i)
19 {
20   double r = step * i;
21   double f = boost::math::cyl_bessel_k(1,  r * olambda);
22   pot_table.push_back(f);
23 }
24
25 // calculates force at r
26 // using a linear interpolation of
27 // a the tabulated potential
28 double ftab(double r)
29 {
30   double f = 0.0;
31   if (r < step) f = pot_table[0];  // special case if r < h
32   else if (r > rcut) f = fmax;  // special case if r > rcut
33   else
34   {
35     int pot_lindex = static_cast<int>(floor(r/step))-1;
36     f = LinearInterp(pot_table[pot_lindex],
37           pot_table[pot_lindex + 1],
38           r*ostep - (pot_lindex + 1));
39
40   }
41   return f;
42
43 }
44
45 // performs linear interpolation
46
47 double LinearInterp(double flow, double fhigh, double d)
48 {
49     return flow + d * (fhigh - flow);
50 }
51
52
53 int main
54 {
55   double r = 1.0; // distance of 1 unit
56   double f = ftab(r);  // tabulated K_1(r)
57 }
```

5.4.2 Cell-Linked Lists and Parallelisation

Further optimisation can be made by reducing the number of vortex-vortex interactions that we need to consider at each time step. To date we have employed a force cut-off, beyond which the force is zero. This still requires an *if-statement* for each of the N^2 interactions to decide if the vortices are beyond r_{cut}. We would prefer to have a reduced set of vortices in the summation that is made up of only vortices near to the current particle being integrated. To produce this reduced list and lower the order of the problem from N^2 we can employ the technique of *cell-linked lists*.

Computationally this is a very well understood technique and is always employed by molecular dynamics simulations where a large number of computational objects - such as particles - are being updated every iteration. The idea is built on the *list* data structure which is of vital importance to the quick storage and recovery of this type of data. The linked-list data structure allows for quick access to a sequential list of items - where random access is not required - and is particularly useful for removing items from the middle of a list very quickly. The method requires a force that falls off quickly with distance, such that it can be approximated to zero outside a chosen range. In these simulations the cut off distance is known as r_{cut} and the force follows the form of Eq. (5.14).

To implement this method, each time step, the 2D system is divided up into a regular grid of P squares with edge length r_{cut}, Fig. 5.3. Then a list is constructed of all the vortices in each of the P cells. Each cell is then iterated over with the integration for each particle being performed. Only particles in the current cell or the neighbouring cells are calculated in the force term, since these necessarily contain the subset of all possible vortices within r_{cut} of the particles in P.

For N atoms this technique allows an increase in calculation time from $O(N^2)$ to $O(N)$. A significant increase in calculation time for a large N system. The additional cost of calculating the linked-lists is an $\mathcal{O}(N)$ operation and can performed every time step without a large increase in the calculation time of the simulation.

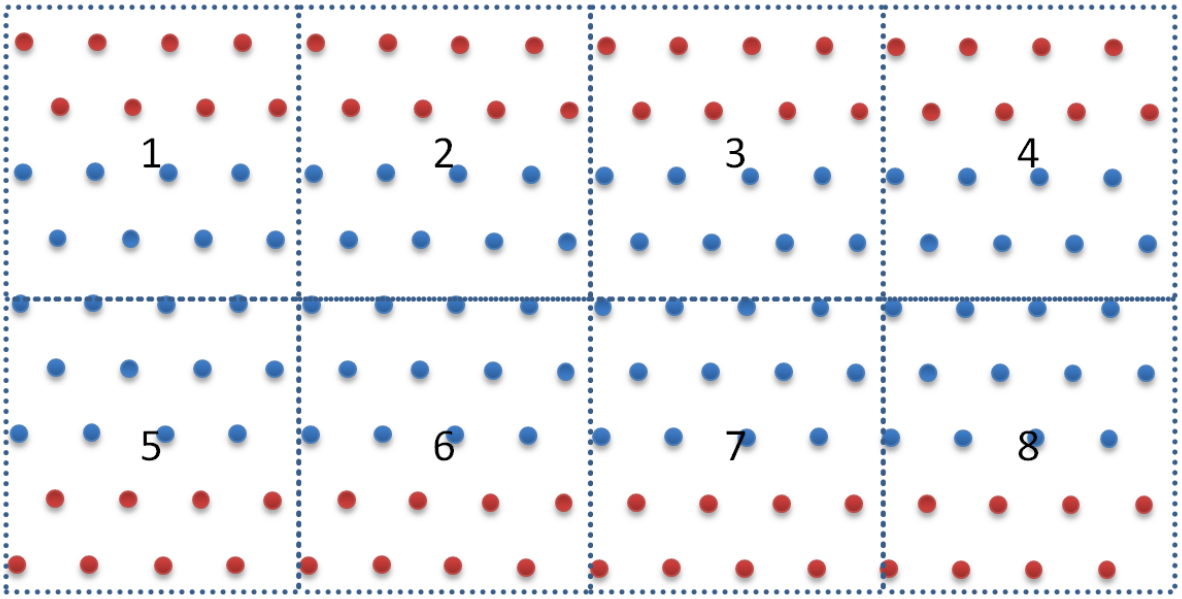

Figure 5.3: Cell Division for Cell Linked List Technique

A further advantage of using cell-linked lists is easy parallelisation on a multi-core computer. Since each time step the new positions of the vortices are calculated from the last time step. Each cell can be calculated separately on a separate core, making this kind of multi-threading very popular in MD simulations.

5.5 Vortex Lattice Simulation Software

There are many examples of good MD packages already in use throughout the MD community. One question is to explore whether any of these packages is able to simulate the vortex lattice with the range of geometries and parameters that are required for this research. The two obvious choices here are LAMMPS[112] and HOOMD-blue[113]. Both of these packages have a large user base and detailed documentation. Both are capable of dealing with custom interaction potentials but neither of these are able to be easily manipulated to simulate the overdamped Langevin dynamics or allowed fine control over the local density of vortices after the initial conditions of the simulations. Due to these obvious problems we will create a custom piece of software that allows access to the de-

tails of the simulations that are relevant to this present work. Listed below are some of the features of the Vortex Lattice Simulation (VLSim) software

- Overdamped Langevin dynamics
- Built in geometries, Channel, Tube, ShearedWall, OscWall, Custom
- Custom periodicity XY, X, Y, none
- Easy to create new geometries
- Per step analysis
- Per step physics update
- Outputs to Mathematica formated data files
- Custom input scripts
- Cross-platform compatible Windows/Linux/Mac
- Built with cmake
- Implements parallelised cell-linked lists

The remainder of this chapter discusses the code design and the feature implementations. Particular focus will be placed of the concept of *geometries* as it relates to this software.

5.5.1 Code Design

The obvious language of choice for this simulation is C++. C++03 could also be used, with the addition of libraries such as Boost. C++ is a one of the fastest languages available today and has advanced support for object orientation and well supported containers such as vectors and lists. The code will use the Pseudo factory design pattern. This pattern allows us to generate generalised code that we can add to when we require new features. The creation of an engine in this style requires good decisions about the high

level structure of the code, making sure each component and their interactions are well understood.

5.5.2 Top-Level Code Structure for the Vortex Lattice Simulation Software

The main run procedure of the program details the top-level of organisation of this code. In all the code blocks that follow, only key lines of code have been listed for brevity.

```
1
2  void CSimulation::Run()
3  {
4    std::cout << "Initialising simulation ..." << std::endl;
5
6    ReadVariablesFromBatchFile();
7    geom = CreateGeometry();
8    geom->Initialise();
9    integrator = CreateIntegrator();
10   integrator->Initialise();
11
12   std::cout << "Simulation running ..." << std::endl;
13
14   for (t=1; t<=simulation_time; ++t)
15   {
16     geom->PerStepUpdates();
17     integrator->Integrate();
18     geom->PerStepAnalysis();
19
20   }
21
22   std::cout << "Simulation finished." << std::endl << std::endl;
23
24   geom->EndofSimAnalysis();
25   OutputSimulationTimes();
26
27 }
```

Note, there are two objects that do the bulk of the work for this simulation, `integrator` and `geom`. The integrator object has no knowledge of the geometry of the system. It only takes two lists of vortices (pointers to these lists are set in the `geom->Initialise()` routine.). The first list contains the *Langevin vortices*, these are vortices that need to be integrated using Langevin dynamics and new positions and velocities found. The second

list is a superset of the first, it contains the vortices that provide the field felt by the Langevin vortices of the first list. This list contains the all vortices in the system including any vortices defining the walls of the system (or channel edge (CE)). The vortices in the second list are not integrated, their values of position and velocity do not get update by the `integrator` object. In both lists each vortex has properties x and y and vx and vy for positions and velocities.

The contents of each of these lists are generated by the `geom` object. The geometry object is responsible for populating the two lists. It understands the CE and periodicity of the system. This flexibility makes the addition of new exotic geometries easy to implement. The type of geometry is specified by a parameter in the the batch file that is read in by the `ReadVariablesFromBatchFile()` function. Here either *channel*, *tube*, *shearedwall*, *oscwall*, *wedge* or *custom* is chosen. Each of these corresponds to a different geometry object, all of which are based on the a `GeometryBase` base class. The base class is an abstract base class implementing the Interface design pattern and has the structure listed in the code block below.

```
1
2  class GeometryBase
3  {
4    public:
5    virtual ~GeometryBase(){}
6
7    virtual void InitialiseGeometry() = 0;
8    virtual void PerStepAnalysis() = 0;
9    virtual void PerStepUpdates() = 0;
10   virtual void EndofSimAnalysis() = 0;
11
12   // returns particles to be integrated
13   virtual std::list<CParticle> * GetIParticles() = 0;
14
15   // returns particles seen by integrated particles
16   virtual void GetJParticles
17           (std::list<CParticle>& vorticesList_) = 0;
18
19   // Needed by the integrator to construct cell-linked list
20   virtual double GetXLo() const = 0;
21   virtual double GetXHi() const = 0;
22   virtual double GetYLo() const = 0;
23   virtual double GetYHi() const = 0;
24   virtual double Geta0() const = 0;
25
```

```
26 };
```

Any geometries that are constructed in this simulation must inherit this base class and implement these methods. The two functions `GetIPartices()` and `GetJParticles()` return the lists we discussed in the previous paragraph. The last set of getters are used by the integrator to determine the bounds of the simulation. The integrator gets its knowledge about the system size and other parameters from the geometry class. The top four pure virtual functions are all called by the main run function to do jobs specific to each geometry. We will discuss these in later chapters. For now it is clear by the names of these functions what they do.

5.5.3 Input and Output for Vortex Lattice Simulation Software

To avoid hardcoding of parameters that would require a recompile each run, job parameters can be specified by using a parameter file. Each geometry requires slightly different parameters but there are many common elements. A listing of a sample job file is shown below. Parameters describing the geometry are listed under the `[Geometry]` tree node.

```
[Header]
outputType=1
geometry=0
simulationTime=10000
temp=0.0001
lorentzForce=0.0

[Geometry]
sourceBfield=0.25
sinkBfield=0.14
bathLength=10
bathWidth=8
channelLength=60
channelWidth=8
periodicity=

[InputData]
altPosFile=false
altPosFileName=posdata.txt
altPinsFile=false
altPinsFileName=pinsdata.txt
```

```
[GeneralParameters]
a0 = 1
binSize = 5
cellSize=6.66
pi = 3.14159265358979
forceRange=6.66
eta=1.0
kB=1.0
Ap=1
dt=0.01
tau=1
triangulationInterval=5
framedataInterval=100
drawCoordinateGrid=false
showParticleTracker=false
thermostat=Anderson
disorderDensity=0
disorderStrength=1e-11
disorderRange=0.2e-7

[BathParameters]
applyBathVelocities=false
applyStiffBath=false

[Interactions]
vvForce=1
Phi=0.2067
lambda=1.11

[Job]
jobtag=job1
```

To specific a job file the program is run using the syntax `VLSim <jobfile name>`.

The type of output generated by the program is specified by the geometry. When the geometry is initialised it registers the filestreams that is requires and then passes output to the files during the `PerStepAnalysis()` or `EndofSimAnalysis()` functions. Each geometry has a choice of which files to create. Listed below are the three common output files and a sample from each.

`posfile.txt`

```
# Output at the end of a simulation
# type x y
A 46.6158 2.52544
A 47.7663 6.23157
A 44.4337 6.25711
A 46.0577 1.59619
```

```
A 49.4663 3.46011
A 47.1861 1.60263
W 80 0.433013
W 80.5 1.29904
W 81 0.433013
W 81.5 1.29904
W 82 0.433013
```

guidata.dat

```
# This file contains frame data
# It is formatted as a Mathematica list
# Each line is a frame containing a list of particles
 # { t, numofparticles, {id1,type1,ghost1,x1,y1,velx1,vely1
    ,coordnum1},...,{idN, typoN, ghostN, xN,yN,velxN,velyN,
     coordnumN}}
{100, 518, {-1272774779, A, 0, 22.5816, 2.3013, 0.0355829,
     -0.000225265, 0}, {698648221, A, 0, 24.4601, 6.44107,
     0.0380501, -0.00110409, 0}, ... }
{200, 518, {-1272774779, A, 0, 22.6171, 2.30104, 0.0352775,
     -0.000514583, 0}, {698648221, A, 0, 24.4976, 6.43991,
     0.0369383, -0.00119137, 0}, ... }
```

framevel.txt

```
# Output each time step
# Contains the space average of the sum of the vortex
      velocities in a frame SAvx, SAvy,
# Contains the space and time average of the sum of the
      vortex velocities STAvx, STAvy
# timestep SAvx SAvy STAvx STAvy
1 0.0454276 9.60129e-05 0.0454276 9.60129e-05
2 0.0454331 9.68888e-05 0.0454303 9.64509e-05
3 0.0454308 9.76812e-05 0.0454305 9.6861e-05
4 0.0454333 0.000106322 0.0454312 9.92262e-05
5 0.0454336 0.00011608 0.0454317 0.000102597
6 0.0454323 0.0001199 0.0454318 0.000105481
```

5.5.4 Results Processing - Mathematica/Bash

VLSim is designed to be a simulation engine and has only basic analysis built in. Most of the in-simulatation analysis is to format or collate data to be output to one of the filestreams generated by the program. The analysis of the physics is done by Mathematica notebooks, additional C++ programs or bash scripts. We will discuss these when they

are used in the later chapters.

5.5.5 Job Submission to High Performance Computing Cluster

Many different properties of the dynamics of the vortex lattice can be analysed with this simulation. Generating statistically accurate sequences of data points for graphs often requires the simulation to be run many times with the same or different parameters. This type of data collection is only feasible with a supercomputer. At the University of Birmingham we have access to BlueBEAR. A high performance computing cluster designed for this type of research. Jobs are routinely submitted to BlueBEAR using MOAB job script. A sample script for the VLSim program with a basic job file (myjob.bat) is listed below.

```
#!/bin/bash
#MOAB -l nodes=1:ppn=16,walltime=1:0:0
#MOAB -j oe
#MOAB -N Simple_job

cd "$PBS_O_WORKDIR"
module load apps/intel
module load apps/boost
../../VLSim myjob.bat
```

To run multiple jobs with different parameters, we can use bash scripts to manipulate job files and perform the submission. This process requires a template job file that is modified by the `batch.sh` script. The following script runs 9 jobs with a different value for the parameter `V` and different initial positions for the vortices specified again by the `V` parameter.

`batch.sh`

```
#!/bin/bash
id=1;
walltime="10:0:0";
for i in $(ls posdata*.txt)
do
    for V in 0.0010 0.0020 0.0025 0.0040 0.0060
        0.0100 0.0200 0.0400 0.1000
    do
```

```
        printf "%s\n" "${i}";
            comment="wallvel_${V}";
            comment=$(echo $comment | sed -e "s/\./p/g");
            comment="ShearedWall-${comment}";
      printf "%s\n" "${comment}";
      jobfile="job_${comment}-${Time:(-4)}${RANDOM}.bat";
      sed  -e "s/NEWPOSDATA/${i}/g" -e "s/NEWVEL/${V}/g" -e
             "s/COMMENT/${comment}/g" shearedwall.template > "$
             {jobfile}";
      sed -e "s/WALLTIME/${walltime}/g"
           -e "s/COMMENT/${comment}/g"
       -e "s/JOBFILE/${jobfile}/g"
            bbjob.template > bbjob.run;
      msub bbjob.run;
           id=`expr $id + 1`;
    done
done
```

bbjob.template

```
#!/bin/bash
#MOAB -l nodes=1:ppn=16,walltime=WALLTIME
#MOAB -j oe
#MOAB -N COMMENT

cd "$PBS_O_WORKDIR"
module load apps/intel
module load apps/boost
VLSim JOBFILE
```

The values `WALLTIME`, `COMMENT` and `JOBFILE` are all dummy strings that are replaced for each run of the job. We can also use bash scripts to collate data from the output files generated by this set of simulations. Below is a sample bash script that collates the results from this set of runs.

```
for i in $(ls -d job*/); do
  field=$(echo ${i:26:15});
  field=$(echo $field | sed 's/\///g');
  echo $field;
  cp ${i}Vxofyprofile.txt results/$field;
  cp ${i}jobheader.ini results/jobheader_${field}.ini;
done
```

These types of scripts are useful tools for interacting with BlueBEAR (or any super-computing cluster) and become valuable time savers when analysing large sets of data or runs.

5.6 Simulation Geometries Discussion

In the following research the results will explore a number of different vortex lattice simulations(*geometries* in the simulation software). The simulations we create are all 2D or 2D wrapped on a 3D surface. The systems are formed by clean (unpinned) regions often between walls provided by two (usually) pinned regions of vortex lattice. Altering the external magnetic field alters the density of vortices within the channel, while the pinned regions are unaltered for moderate changes of field.

In the first geometry (`GeometryShearedWall`) we will explore shearing effects by moving a single wall with the other stationary whist measuring the velocities of the free vortices in the channel, Chapter 6. These simulations will be performed with periodic boundary conditions in the x-direction in an homogeneous field. A second set of related simulations(`GeometryShearedWall`), Chapter 6, will explore the effects of a single oscillating walls. The final set of simulations(`GeomteryChannel`, `GeometryTube`,`GeometryWedge`), Chapter 7 and Chapter 8, will be exploring the novel system of a channel or cylinder (the former has pinned CEs) that bridges between a source and sink vortex reservoir such that particles will flow along the channel. This system will have no periodicity and will have an implicit field gradient in x applied.

Chapter 6

SHEAR FLOW IN THE VORTEX LIQUID

Continuum calculations of the rheology of the vortex liquid were presented by Marchetti and Nelson[21]. They calculated the velocity profiles, Fig. 6.1, for a 2D pressure driven vortex liquid with the addition of a drag term in the continuum equations of motion. From this model they found an exponential velocity profile with a characteristic length of $\delta = \sqrt{\eta/\gamma}$, where η is the viscosity and γ the viscous drag, that is independent of shear rate, indicating a Newtonian viscosity.

Here we present the results of Couette flow simulations of the vortex liquid that show a boundary layer that heavily depends on wall velocity, in direct contrast to the work of Marchetti and Nelson.

We first consider the continuum solution for Couette flow in the 2D channel, where the equations of motion, Eq. (4.5), must be modified to include the viscous drag on the vortices. We then examine if the melting temperature is modified by the channel geometry and from these results we set $T > T_m^{\rm bulk}$ as our temperature for the liquid simulations. By varying wall velocity, channel width and B-field we explore the boundary layer thickness using Couette flow simulations of the vortex liquid. In the final liquid section we examine a non-Newtonian constitutive relation by probing the vortex liquid in an oscillating shear simulation.

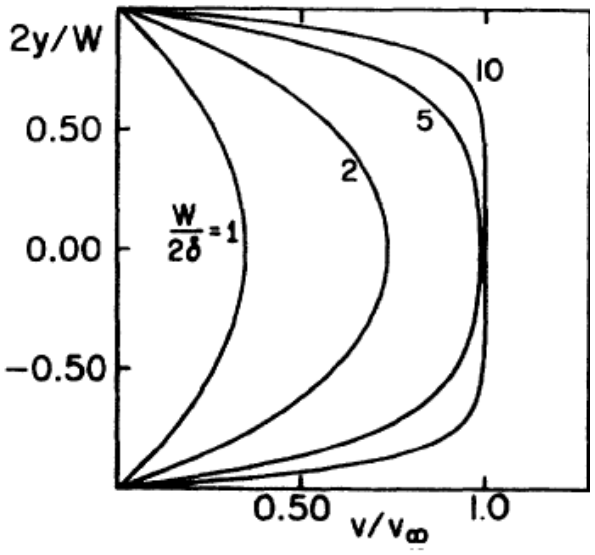

Figure 6.1: Marchetti and Nelson velocity profiles for channel flow in a channel of width W. Large boundaries layers dramatically slow the flow. Figure from Ref[21].

6.1 Continuum Solution to Couette Flow of the Vortex Liquid

For channel widths $w \gg a_0$, it is a reasonable assumption to model the vortex liquid as a continuum and calculate the expected velocity profile for Couette flow in the 2D channel. We start from the standard equations of motion for a Newtonian fluid and assume a Newtonian viscosity. We must modify the equation of motion to include a contribution due to the viscous drag. Similar calculations were performed by Marchetti and Nelson for the case of pressure driven flow in 2D[21]. We assume the velocity profile is not time dependent and so we seek a steady-state solution. The geometry of the system can be seen in Fig. 6.2. The set of equations we need to solve are

$$v = v_x(y) \qquad (6.1) \qquad\qquad \eta \frac{d^2 v_x}{dy^2} = \gamma u \qquad (6.2)$$

with the associated boundary conditions

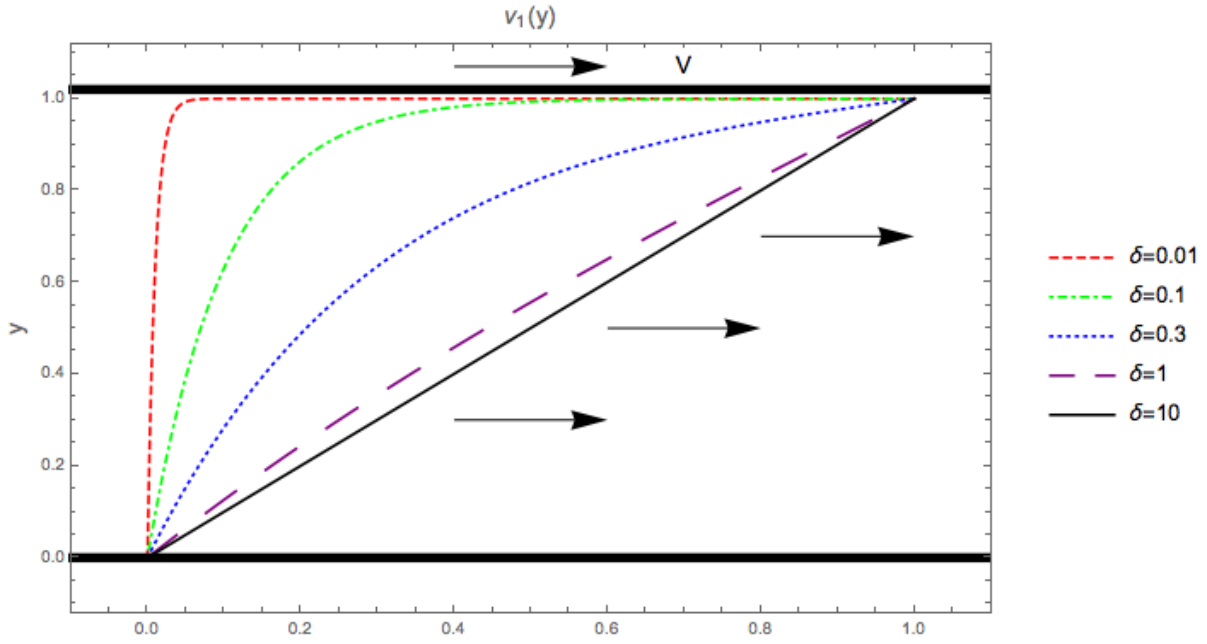

Figure 6.2: Couette flow of the vortex lattice. The upper wall is sheared with velocity V while the lower wall is left stationary. The no-slip condition is assumed. The competition between viscosity and drag forces result in a boundary layer $\delta = \sqrt{\frac{\eta}{\gamma}}$. The deviation from the Newtonian flow can be seen for $\eta/\gamma \ll 1$.

$$v_x(y=0) = 0 \qquad (6.3) \qquad\qquad v_x(y=W) = V \qquad (6.4)$$

Here the top wall of the system will be given a velocity V and the bottom wall will remain stationary. We also assume the no-slip boundary condition at the walls.

This set of equations has a straight forward general solution

$$v_x(y) = \alpha \mathrm{e}^{\sqrt{\frac{\gamma}{\eta}}y} + \beta \mathrm{e}^{-\sqrt{\frac{\gamma}{\eta}}y} \qquad (6.5)$$

with a length scale that can be identified as $\delta = \sqrt{\frac{\eta}{\gamma}}$. This length scale describes a boundary layer due to the competition between the viscosity and drag forces.

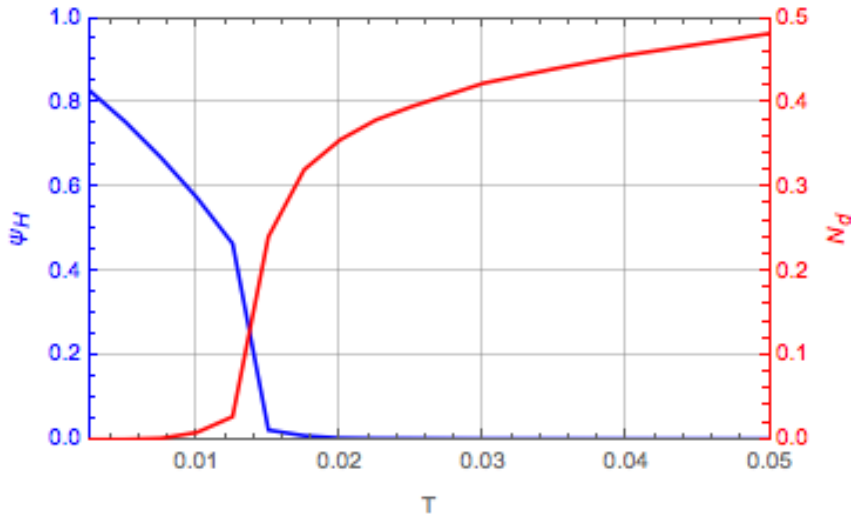

Figure 6.3: Melting transition in a periodic 30x30 system. $T_m = 0.014$

The particular solution for our boundary conditions is

$$v_x(y) = V \frac{\sinh y/\delta}{\sinh W/\delta} \tag{6.6}$$

This equation shows, as expected, that the drag forces act to slow the velocity of the whole system. The profiles for this equation are in Fig. 6.2, where we show a range of δ to illustrate the effect of the viscosity-drag interaction.

6.2 Melting Transitions in the Vortex Liquid

We first calculate the melting transition for a periodic system of size 30 x 30 at a field of B_0. In this and subsequent simulations we consider the order parameters from §3.6 to be our *effective* order parameters. In our system we have no long range order by construction. From these order parameter measures this leads to an estimate of the bulk melting temperature, $T_m^{bulk} = 0.014$, Fig. 6.3.

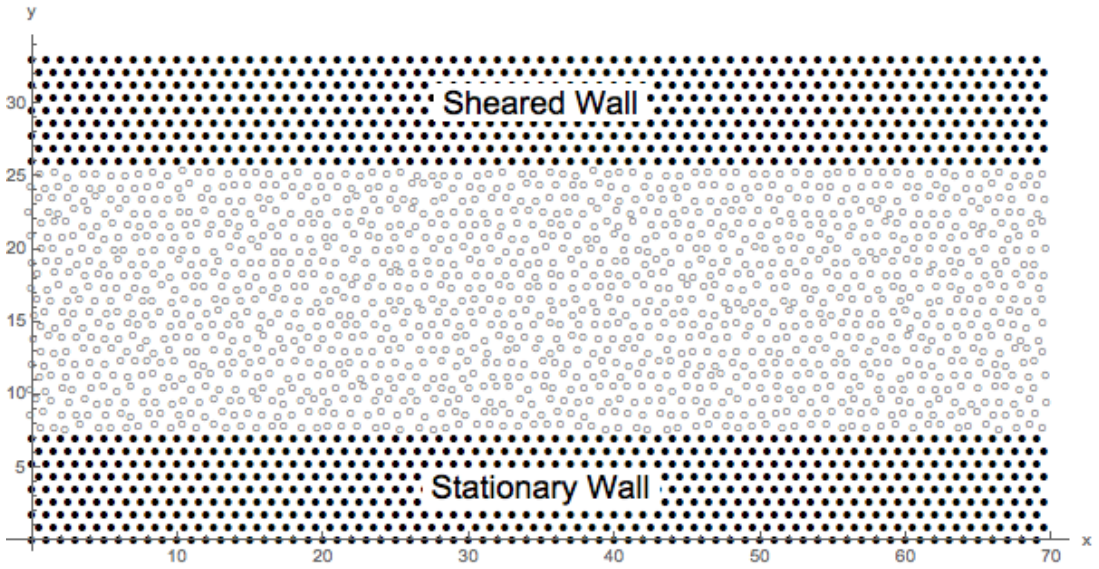

Figure 6.4: Sheared wall simulation.

6.3 Simulations of Couette Flow of the Vortex Liquid

Calculation of the continuum solution neglected effects due to the microscopic structure of the vortex matter and assumes a no-slip condition at the walls. We may expect that the structure of the liquid and its interaction with the CE might play a key role in understanding the rheology of the vortex liquid. Here we examine via simulations the microscopics of the system with the aim of establishing any additional factors controlling the flow, beyond the description of the continuum model.

In the following section we will be simulating Couette flow in the 2D vortex liquid. Unless otherwise stated simulations are performed at $T = 0.02$. We construct a channel of width w and length L, wrapped periodically in x. The channel edges are defined by an array of vortices, locally fixed as a triangular lattice with field $B_0 = 0.25T$. For all simulations the vortices in the lower CE are fixed whereas the vortices in the upper CE are usually sheared at a velocity $V\hat{\mathbf{x}}$. The geometry is illustrated as a schematic in Fig. 6.4.

6.4 No-Slip Boundary Condition

One of the major assumptions of this continuum model is the no-slip condition. This approximation enables easier analytic access to flow fields of the liquid state but microscopically the no-slip condition is not well understood[114]. Particle models of no-slip do exist, such as the bounce-back conditions[114], but these are required to be explicitly added to the simulation. An alternative to the bounce-back conditions are rough channel edges. Here hard walls are replaced by rough boundaries such that particles near the boundaries are slowed (or trapped) by their interaction with the walls. This has been shown to produce an approximation to the no-slip condition[114]. We will not add bounce back conditions, relying instead on the standard vortex-vortex interactions to provide the confining potential for the mobile vortices and any shear interaction at the channel edge. However, there may be an effect due to the 'roughness' of the CE. The arrangement of CE vortices creates a washboard potential that penetrates into the channel, imparting a shear on the vortices in the boundary layer of the channel.

6.4.1 Key Liquid Coding Algorithms

To perform the simulations we employ the basic Langevin dynamics engine described in Chapter 5. For these simulations we create a new `GeometryBase` object called `GeometryShearedWall`. Each time step we perform analysis and physical update to particle positions and momentums that are unique to this geometry. The per time step updates and analysis functions for this geometry are listed in the code block below.

```
1  // class GeometryShearedWall implementations
2
3  void GeometryShearedWall::PerStepUpdates()
4  {
5    // Add functions here to be run every timestep
6    MoveTopCE();
7  }
8
9   void GeometryShearedWall::PerStepAnalysis()
10 {
11   OutputParticlePositions();
```

```
12    CalculateVxofyProfile();
13    OutputVxofyEvolveProfile();
14  }
15
16  void GeometryShearedWall::EndofSimAnalysis()
17  {
18    OutputFinalParticlePositions();
19    OutputAverages();
20    OutputVxofyProfile();
21
22  }
```

Each time step the top CE particles (marked as type 'S' in the simulation input files) are moved at a velocity of `topwallvel`. This value is specified in the input script for the job. This update is performed by the `MoveTopCE()` function, listed below

```
1   void GeometryShearedWall::MoveTopCE()
2     {
3       double dt = sim->get_dt();
4       for (std::list<CParticle>::iterator p =
5         OtherParticlesList->begin();
6         p!=OtherParticlesList->end(); ++p)
7       {
8         if (p->get_type() =="S")  // this indicates a sheared
9                   wall particle
10        {
11          p->set_vel(topwallvel, p->get_vely());
12          p->set_x(p->get_x()+p->get_velx()*dt);
13        }
14      }
15
16     }
```

For analysis we output two velocity profiles. $< v_x(y) >$ (where vortex velocities are average is over x, bins in y of size y_{bin} and over all time steps t_{sim}) gives the average velocity profile across the channel. The results of this profile are output at the end of the simulation by the `OutputVxofyProfile()` function. We also calculate $< v(y, t_i) >$ (where spatial average is the same as the previous average but time average is up to the current time step, t_i.) is output during the simulation every 1000 time steps. Monitoring this profile enables us to ensure we are in a steady state. This analysis is contained in the `OutputVxofyEvolveProfile()` function.

The starting positions for the channel particles are labelled with i and j indices and

defined as $a_{ij} = \mathbf{e}_0 i + \mathbf{e}_1 j + (\mathcal{U}(-0.2, 0.2), \mathcal{U}(-0.2, 0.2))$. This ensures a uniform density and a randomised starting position away from the solid state.

6.5 Melting Transitions in Channel Geometry for the Vortex Liquid

We continue by repeating this procedure for the channel geometry. Due to the presence of the pinned channel edges we anticipate a cool boundary layer effect and possible ordering effects as seen in molecular dynamics simulations of Leonard-Jones fluids[115]. It is expected that the structure of the channel edges will stabilise the vortices such that order will be retained in the boundary layers up to higher temperature than in the centre of the channel. To confirm this we calculate the order parameters for melting in three sections across the channel of width $d/3$. Fig. 6.5 shows the results of these calculations where we see the enhanced melting temperature in the sections next to the CE. The melting temperature for the central region of the channel remains the same as the bulk, T_m^{bulk} (the same as the xy periodic system.). An estimate for the edge regions is more difficult as the transition regions for these sections is dramatically spread out. The system loses residual rotational order at around $T_m^{\text{channel}} = 0.03$.

To further confirm the structural differences in these regions we can examine trajectories of the vortices. At $T = 0.015 > T_m^{\text{bulk}}$ the trajectories in the edge regions remain localised and we see thermal oscillations around the triangular ground states positions, Fig. 6.6. In the central regions the trajectories are not localised and appear as fully random walks.

Next we will probe the melting temperature and trajectories of the vortices in the sheared flow. We perform simulations of the sheared vortex liquid at increasing temperatures through the melting transition for the bulk T_m^{bulk}.

The initial simulations are run for a channel width $21b_0$ and at a low wall velocity of $V \in (0.001, 0.01, 0.1)$. The order parameters for $V = 0.01$ are given in Fig. 6.7.

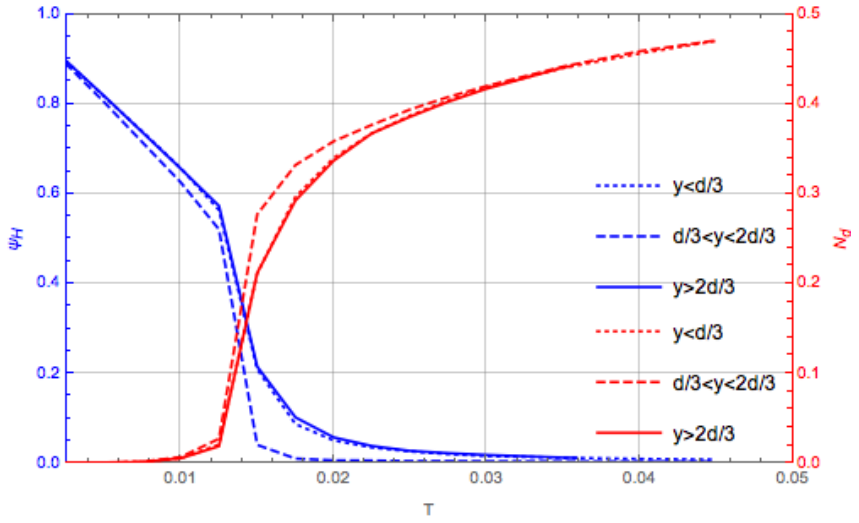

Figure 6.5: Melting transition in a channel of width $21b_0$. Order parameters are calculated in sections of width $d/3$. $V = 0.0$.

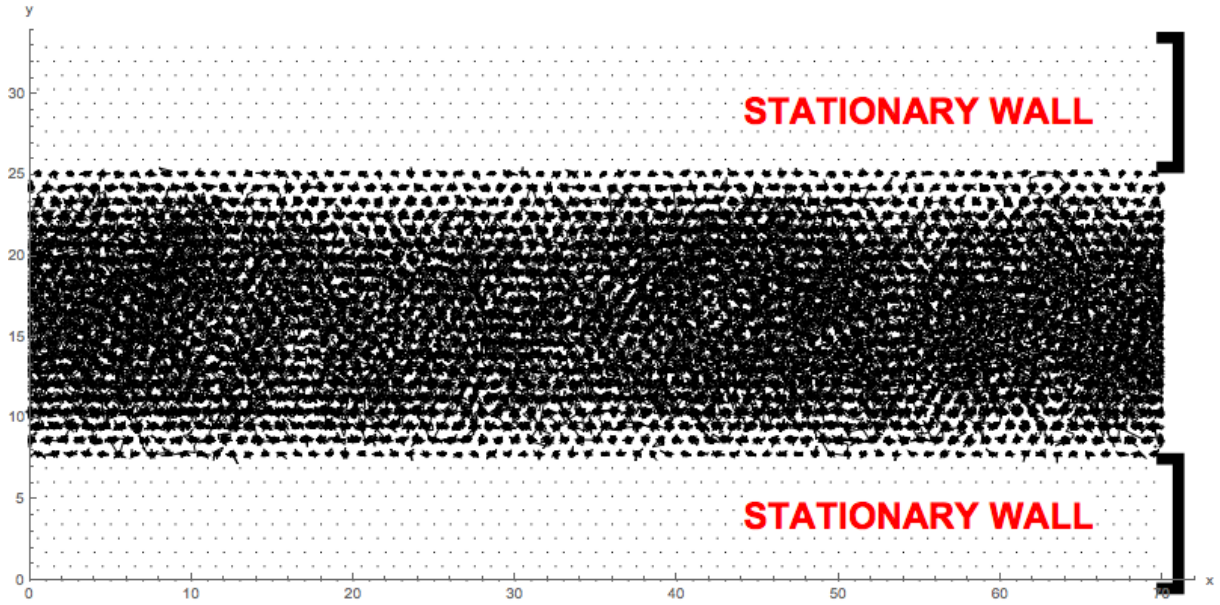

Figure 6.6: Trajectories in a channel of width $w = 21b_0$, $T = 0.015$, ordering near the channel edges is apparent from this image.

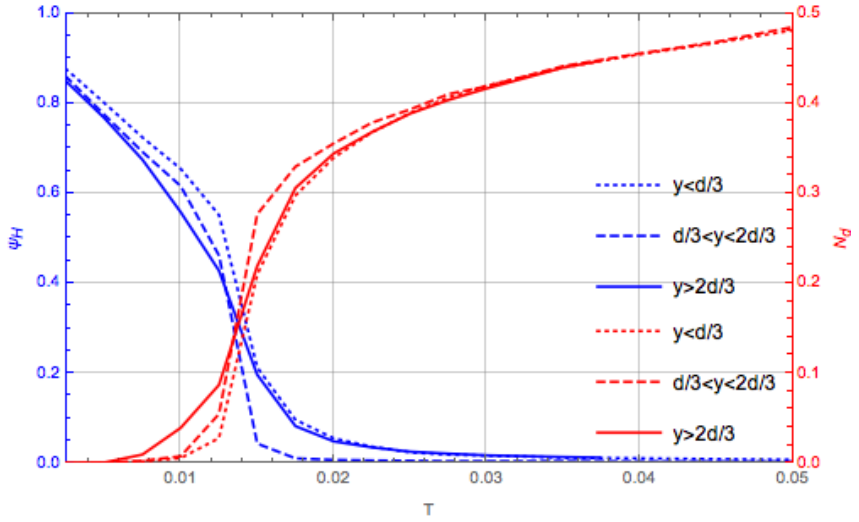

Figure 6.7: Order parameters for sections of a sheared channel of width $d/3$. The central bin melts at $T = 0.014$, whereas the sections adjacent to the walls do not fully converge to until $T \gtrsim 0.03$. $V = 0.01$.

The results indicate the same spatial differences in order parameters as in the channel simulations in the absence of shear.

6.5.1 Wall Velocity Dependence on Boundary Layer Thickness

The shear rate can potentially modify the velocity profile. We fix channel width at $w = 21b_0$ and $T = 0.02$. The sheared wall velocity $V \in (0.001, 0.002, 0.0025, 0.004, 0.006, 0.01, 0.02, 0.04, 0.1)$.

Figs. 6.8 and 6.9 show the velocity profiles for the different wall velocities. Plotted with the data points are the fits to Eq. (6.6), where the drag, $\gamma = 1$ leaving only the viscosity as a fitting parameter. We can clearly see the wall velocity effects the boundary layer thickness, Fig. 6.10. At a wall velocity $V > 0.01$ the boundary is confined to a length less than a single bin width of $2b_0$. At most this corresponds to 2 *layers* of vortices. Each velocity profile is fitted with a constant η. Normally a constant viscosity would indicate a Newtonian behaviour, however, we see that increasing wall velocity reduces the effective viscosity between simulations Fig. 6.10b.

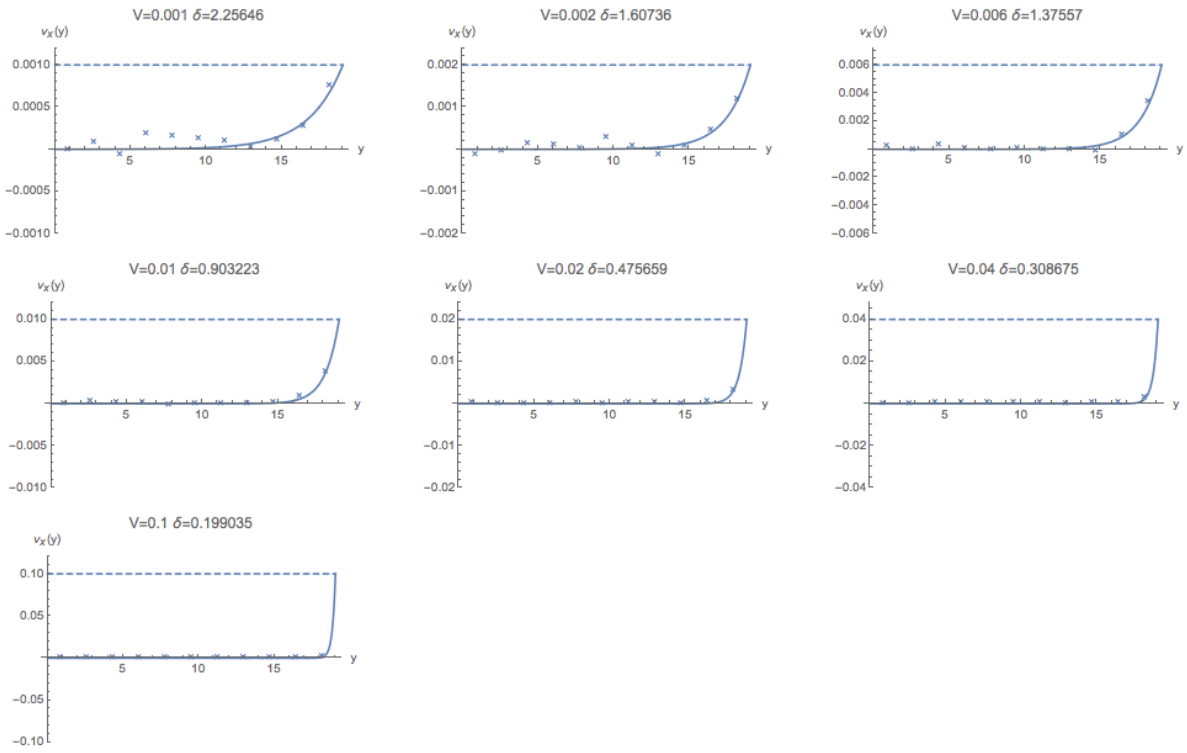

Figure 6.8: Velocity profiles for sheared wall velocities $V \in (0.001, 0.002, 0.0025, 0.004, 0.006, 0.01, 0.02, 0.04, 0.1)$. Fitted line from continuum solution, Eq. (6.6).

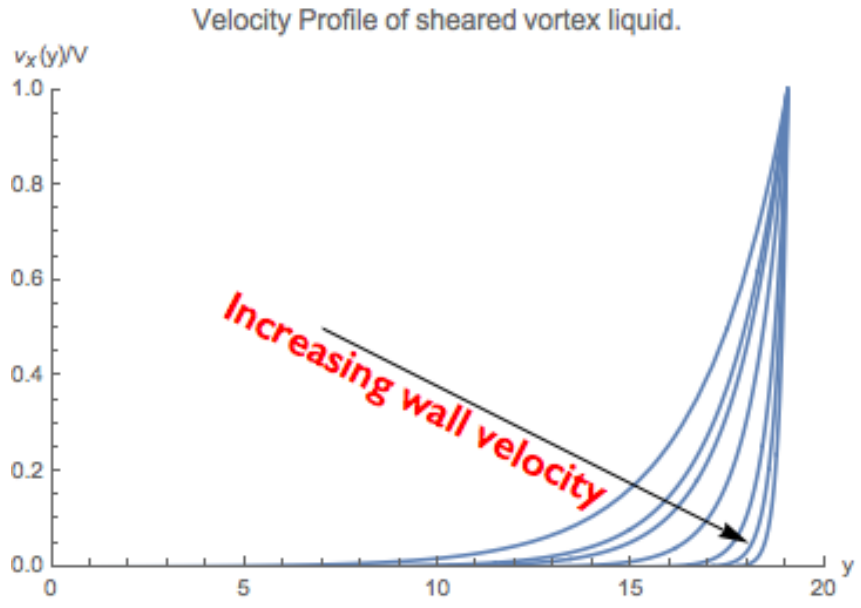

Figure 6.9: Fitted velocity profiles for sheared wall simulations, $V \in (0.001, 0.002, 0.0025, 0.004, 0.006, 0.01, 0.02, 0.04, 0.1)$. Fitted line from continuum solution, Eq. (6.6).

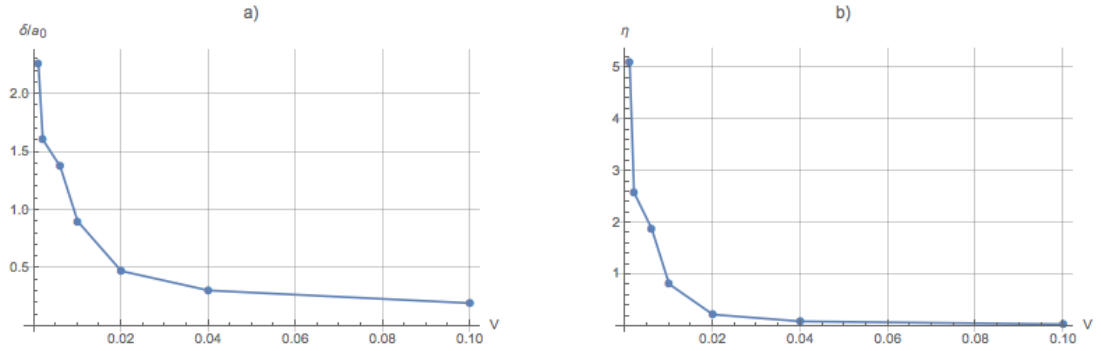

Figure 6.10: **a** Boundary layer calculated from fits to continuum solution. Thickness decreases as sheared wall velocity increases. Limit of resolution is the y_{bin} size of $2b_0$ **b** Viscosity falls with increasing sheared wall velocity. **b** Viscosity.

Further analysis of the vortex trajectories just above T_m^{bulk}, Figs. 6.11 and 6.12, show trajectories for wall velocities of $V = 0.01$ and $V = 0.1$. At $V = 0.01$ the vortices in the edge layer retain partial rotational symmetry and are pulled along with the sheared wall. At the higher shear rate, $V = 0.1$, the edge layer detaches from the wall.

6.5.2 Channel Width Dependence on Boundary Layer Thickness

Next we examine the effect of the channel width. To carefully control the density, the width is increased in quantised values of b_0 while the density of channel and CE are maintained at B_0.

The tabulated velocity profiles in Fig. 6.13 show the boundary layer reaches fully across the channel for channels where $w < 4\delta$. For channels where $w > 4\delta$ portions of the vortex liquid near the lower wall remain stationary. These regions of stationary liquid increase in size with increasing channel width. The cross over occurs at $w_c \approx 12$. Extracting the fitted values for δ demonstrates the boundary layer thickness alters with width. We can see in Fig. 6.14, that above w_c the boundary layer thickness plateaus at a value of $\delta_c \approx 2.8$ (Note: $\delta_c \sim 4\delta_c$). Clearly the channel width only modifies the boundary layer thickness for narrow channels. For wide channels above w_c, all shear is

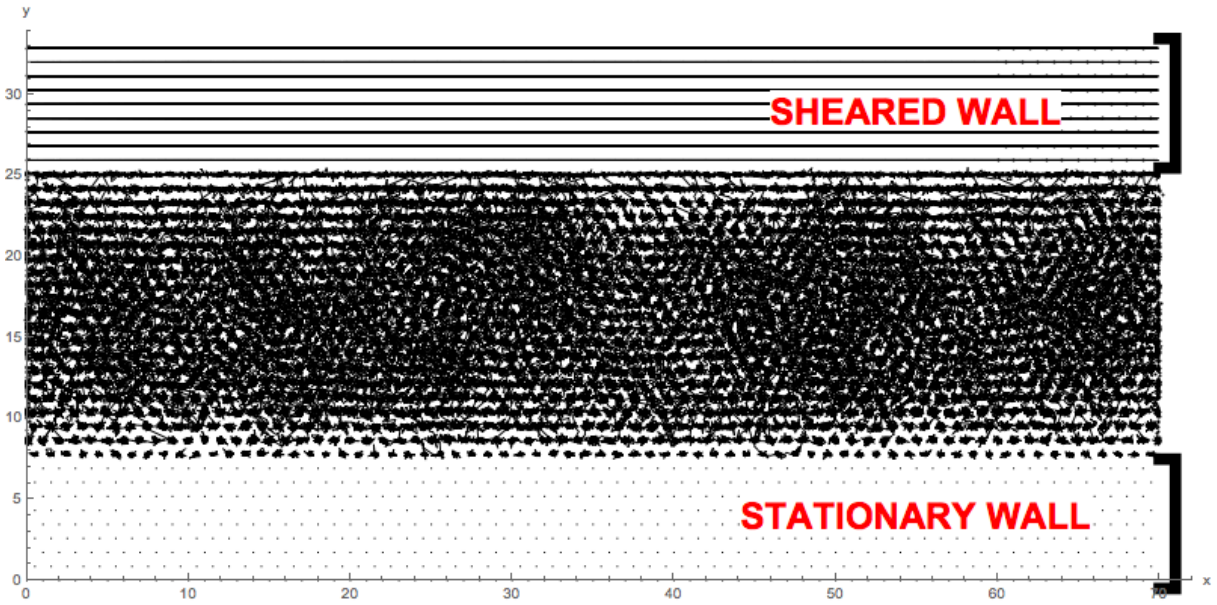

Figure 6.11: Trajectories in sheared wall system. $V = 0.01$, $T = 0.015$, ordering near the channel edges is apparent from this image. Trajectories following the motion of the boundary near the channel edges.

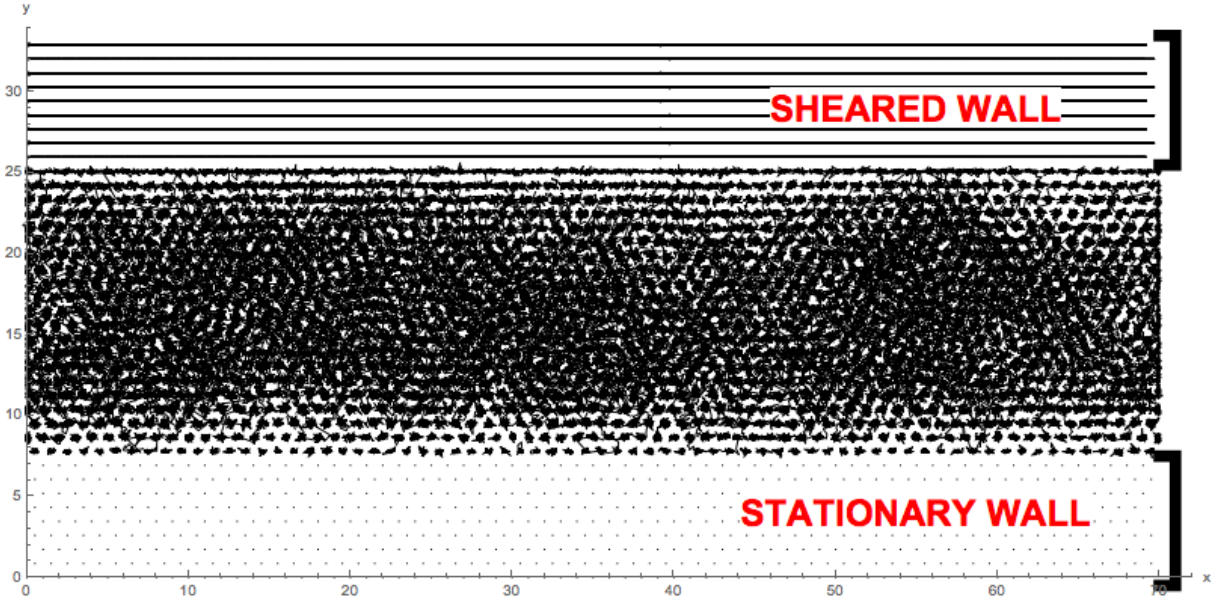

Figure 6.12: Trajectories in sheared wall system. $V = 0.1$, $T = 0.015$, ordering near the channel edges is apparent from this image. Vortex trajectories are stationary near the lower channel edge. The fast moving upper wall separates from the channel vortices resulting in layer of stationary triangular lattice near this boundary.

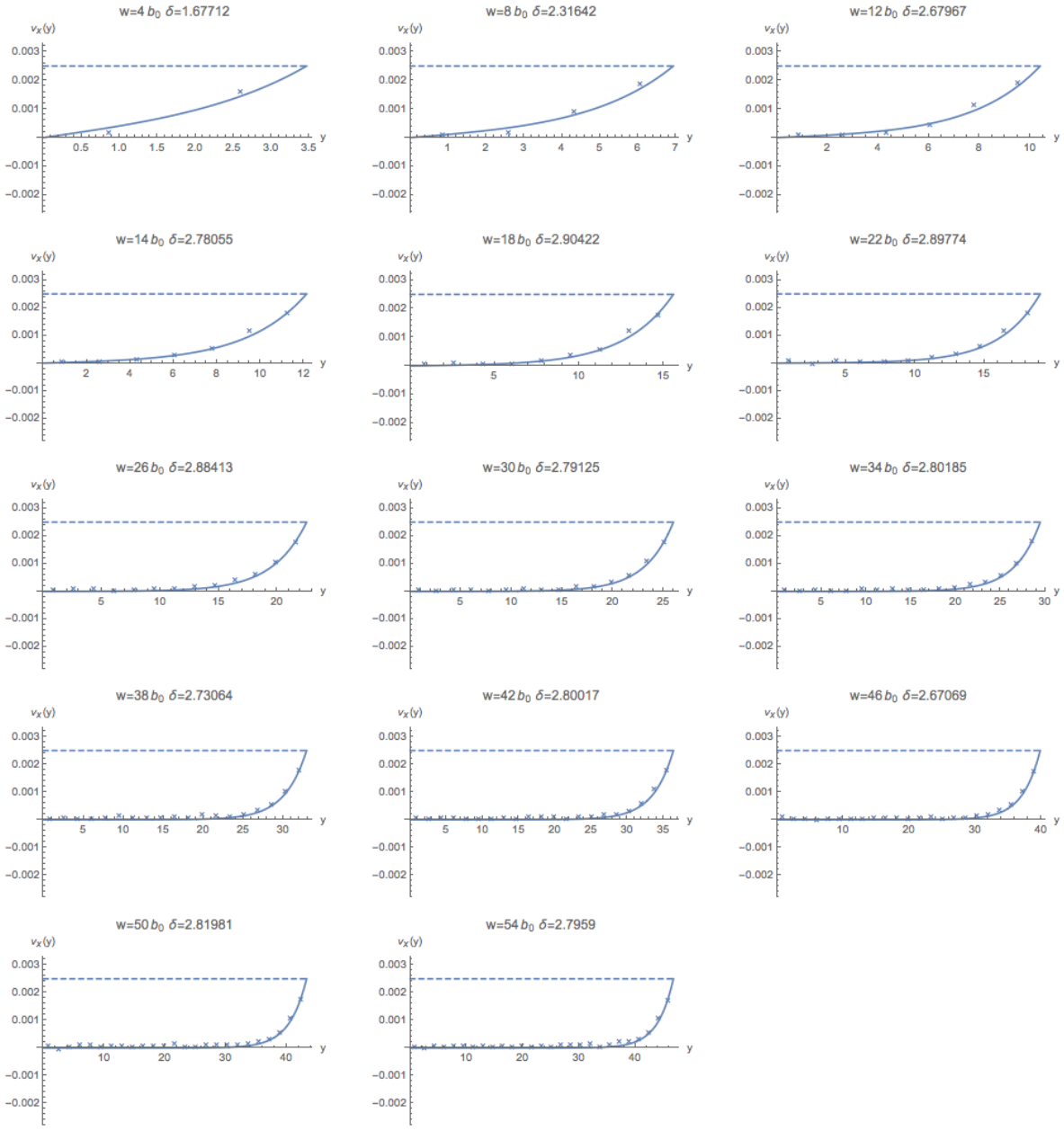

Figure 6.13: Velocity profiles of sheared vortex liquid for a range of channel widths.

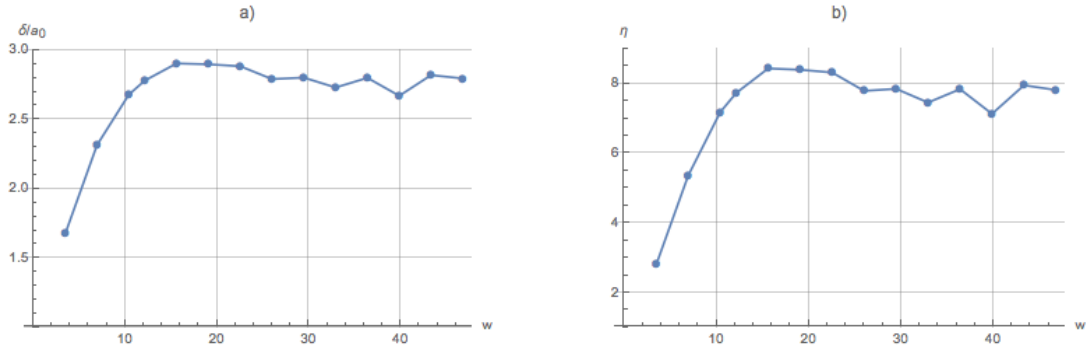

Figure 6.14: **a** As width is increased, the boundary layer thickness plateaus. For channel widths $w \lesssim 12$ the boundary reaches across the whole channel width. **b** Viscosity.

dropped within $4\delta_c$ of the moving boundary and hence the velocity profiles beyond this range reduce to zero.

6.5.3 B-Field Dependence on Boundary Layer Thickness

We would anticipate that the behaviour will be dependent on the background magnetic field, in the bulk this leads to a phase transition. To perform these simulations the CE field is fixed at B_0 but the field of the channel vortices, $B \in (0.30, 0.35, 0.40 \ldots 0.95, 1.0)$. The other simulation parameters chosen are a low wall velocity of $V = 0.004$, channel width of $w = 21b_0$ and $T = 0.02$.

Lowering the field in the channel whilst maintaining the field of the channel edge as B_0 results in two competing effects. Lowering the field reduces the number of vortices in the channel, increasing the average spacing of the vortices. However because the relative density of the channel vortices is less than the CE vortices there is a resultant compression on the channel vortices due to the density differences. This effect acts to decrease the average distance between particles and pushes the channel vortices away from the channel edge by a distance $> a_0$. From Eq. (2.25) we find a low field would soften the vortex lattice and reduce the melting temperature, ensuring we remain in the liquid regime.

These effects are important to consider when deciphering the sheared wall results at varying field strengths. Fig. 6.15 shows the tabulated velocity profiles across the channel

for different values of field, again using the continuum result to fit the profiles. The set of figures show that only fields where $B/B_0 \simeq 1$ fit with the continuum solution. All other results give zero flow field induced by the sheared wall. Any boundary layers have characteristic length below the resolution for these results of $2b_0$. The interpretation of this is the force falls off exponentially with $\lambda = 1.1a_0$. Hence little momentum can be transferred to the channel vortices at low fields where the channel vortices are compressed away from the wall by the higher density CE.

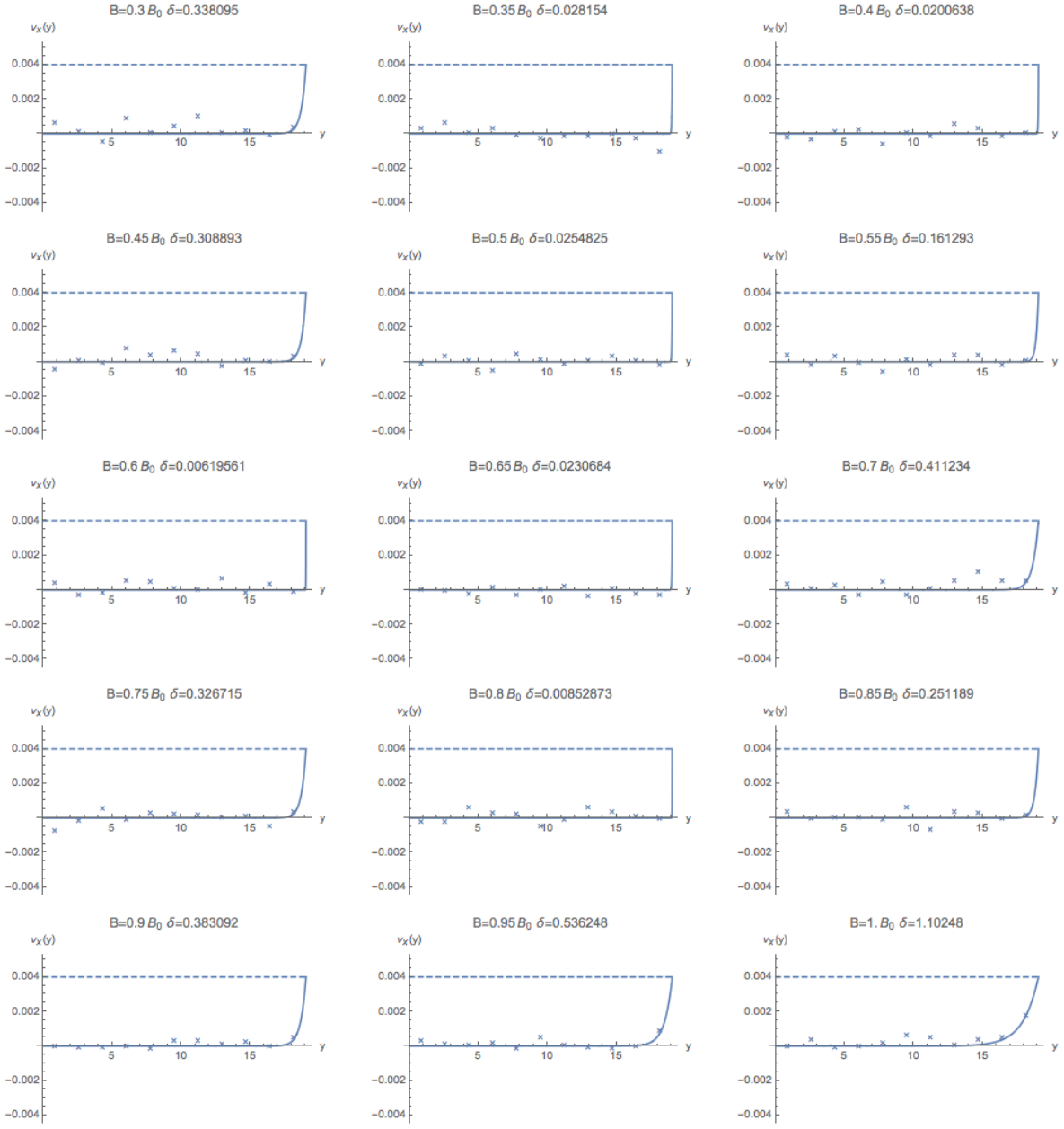

Figure 6.15: Velocity profiles of sheared vortex liquid for a range of B-fields.

6.6 Simulations of Oscillating Couette Flow of the Vortex Liquid

One possible probe of the non-Newtonian nature of the vortex liquid is to perform an oscillating wall simulation. We will first examine the continuum solution with an oscil-

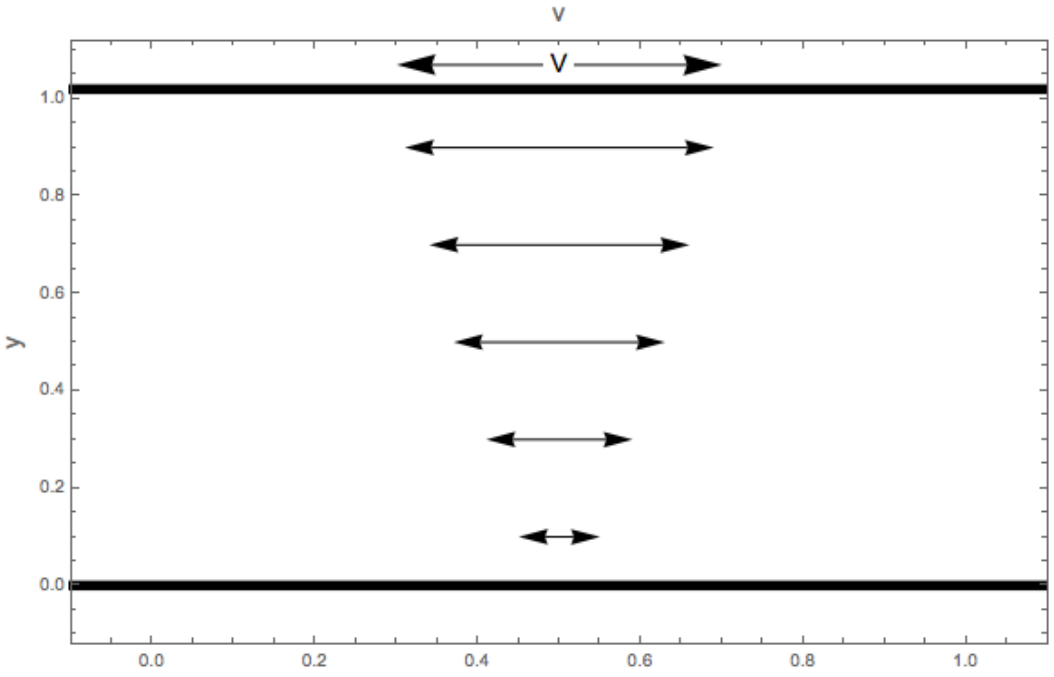

Figure 6.16: Oscillating wall schematic.

lating boundary and then follow this with a study of the harmonics of the CE velocity to determine the presence of non-linear terms in the constitutive equation.

6.6.1 Continuum Solution to Damped Oscillating Flow in the Vortex Liquid

The system of interest is give in Fig. 6.16. The system of equations for this system are (assuming a Newtonian fluid)

$$v = v_x(y) \qquad (6.7) \qquad \frac{\partial v_x}{\partial t} = \eta \frac{\partial^2 v_x}{\partial y^2} - \gamma v_x \qquad (6.8)$$

The boundary conditions on this flow are

$$v_x(y=0)=0 \qquad (6.9) \qquad\qquad v_x(y=W)=V\mathrm{e}^{i\omega t} \qquad (6.10)$$

With these boundary conditions the solution has the form $v_x(y,t)=V_x(y)\mathrm{e}^{i\Omega t}$

Substitution into Eq. (6.8) allows separate the solution into a time dependent part and a spatial part. The spatial part becomes

$$i\omega V_x(y)\mathrm{e}^{i\omega t}=\eta V_x^{''}(y)\mathrm{e}^{i\omega t}-\gamma V_x(y)\mathrm{e}^{i\omega t} \qquad (6.11)$$

$$i\omega V_x(y)=\eta V_x^{''}(y)-\gamma V_x(y) \qquad (6.12)$$

$$(i\omega+\gamma)V_x(y)=\eta V_x^{''}(y) \qquad (6.13)$$

For the boundary conditions on $V_x(y)$ we eliminate the t dependence from the original boundary conditions.

$$v_x(y=0)=0=V_x(y=0)\mathrm{e}^{i\omega t} \qquad (6.14)$$

$$v_x(y=W)=V\mathrm{e}i\Omega t=V_x(y=0)\mathrm{e}^{i\omega t} \qquad (6.15)$$

Assuming the no-slip boundary condition, $\Omega=\omega$, the new system of equations for $V_x(y)$ are

$$(i\omega+\gamma)V_x(y)=\eta V_x^{''}(y)V_x(y=0)=0 \qquad (6.16)$$

$$V_x(y=W)=V \qquad (6.17)$$

The general solution is

$$V_x(y) \;=\alpha\mathrm{e}^{\sqrt{\frac{i\omega+\gamma}{\eta}}y}+\beta\mathrm{e}^{-\sqrt{\frac{i\omega+\gamma}{\eta}}y} \qquad (6.18)$$

$$=\alpha\mathrm{e}^{\lambda y}+\beta\mathrm{e}^{-\lambda y} \qquad (6.19)$$

$$\qquad (6.20)$$

where $\lambda = \sqrt{\frac{i\omega+\gamma}{\eta}}$. To proceed we remove a factor of $\sqrt{\gamma/\eta}$ and let $(1+i\omega/\gamma)^{1/2} = X + iY$. Doing so allows us to resolve λ into real and imaginary parts,

$$\lambda = \sqrt{\frac{\gamma}{\eta}}\left[\frac{1}{\sqrt{2}}\left(\frac{\omega}{\gamma}+1\right)^{1/2} + i\frac{\omega}{\gamma}\frac{1}{\sqrt{2}}\left(\frac{\omega}{\gamma}+1\right)^{-1/2}\right] = R + iI \tag{6.21}$$

where R and I are the real and imaginary parts of λ.

Substitution and expanding of $\lambda = R + iI$ into $V_x(y)$ gives

$$V_x(y) = \alpha\left[\mathrm{e}^{Ry}\mathrm{e}^{iIy} - \mathrm{e}^{-Ry}\mathrm{e}^{-iIy}\right] \tag{6.22}$$

where we have used the boundary conditions to find $\alpha = -\beta$. We now write the exponentials as trigonometric and hyperbolic functions.

$$\mathrm{e}^{Ry} = \cosh(Ry) + \sinh(Ry) = C + S \tag{6.23}$$

$$\mathrm{e}^{-Ry} = \cosh(Ry) - \sinh(Ry) = C - S \tag{6.24}$$

$$\mathrm{e}^{iIy} = \cos(Iy) + i\sin(Iy) = c + is \tag{6.25}$$

$$\mathrm{e}^{-iIy} = \cos(Iy) - i\sin(Iy) = c - is \tag{6.26}$$

$$\tag{6.27}$$

The expression for $V_x(y)$ now simplifies to

$$V_x(y) = \alpha\left[Sc + iCs\right] \tag{6.28}$$

Using the boundary condition $V_x(y = W) = V$ gives the value of the constant.

$$\alpha = \frac{V}{S_W c_W + iC_W s_W} \tag{6.29}$$

where the subscript W indicates the expressions have the same form as C, S, c and s but with $y \to W$. We have now arrived at the solution for our particular boundary conditions as

$$V_x(y,t) = \frac{V\mathrm{e}^{i\omega t}\left[Sc + iCs\right]}{S_W c_W + iC_W s_W} \tag{6.30}$$

We are only interested in the real part of this solution which is found as

$$V(y,t) = V\cos(\omega t)\left[\sinh(Ry)\cos(Iy)\sinh(RW)\cos(IW) + \cosh(Ry)\sin(Iy)\cosh(RW)\sin(IW)\right] \tag{6.31}$$

where $R = \sqrt{\frac{\gamma}{\eta}}\frac{1}{\sqrt{2}}\left(\frac{\omega}{\gamma}+1\right)^{1/2}$ and $I = \sqrt{\frac{\gamma}{\eta}}\frac{\omega}{\gamma}\frac{1}{\sqrt{2}}\left(\frac{\omega}{\gamma}+1\right)^{-1/2}$.

6.6.2 Oscillating Couette Flow Simulations for the Vortex Liquid

It may be possible for the fluid to have a non-Newtonian constitutive relation. We can explore this with simulations if we can understand how the harmonics of the CE oscillation appears in the velocity profiles.

Consider the equation of motion for unidirectional incompressible flow:

$$\frac{\partial v}{\partial t} = \nu\frac{\partial^2 v}{\partial y^2} \tag{6.32}$$

where $\nu = \eta/\rho$ is the "kinematic viscosity". We assume for simplicity that the non-Newtonian nature of the viscosity is of the form:

$$\nu = \nu_0 + \nu_n\left(\frac{\partial v}{\partial y}\right)^m = \nu_0\left[1 + \epsilon\left(\frac{\partial v}{\partial y}\right)^m\right]. \tag{6.33}$$

The following analysis may allow us to deduce or disprove such a relation by comparing the results with those of the simulation. Firstly absorb the ν_0 into the definition of time,

i.e. $t \to \nu t = t'$, but we will drop the prime immediately.

The idea is to determine whether the nonlinearity can be via harmonics of a time-dependent imposed force on the system. For a viscous liquid undergoing plane flow, this could be via one of the plates oscillating with velocity $V \cos \omega t$. Now we know in the Newtonian case[116], that the solution for $v(y,t) = v_x(y,t)$ (we drop the x subscript to simplify notation) is

$$v(y,t) = \Re\{\mathrm{e}^{\mathrm{i}\omega t} v(y)\} \tag{6.34}$$

where $\Re$ denotes the real part and $v(y)$ satisfies:

$$\mathrm{i}\omega v_x = \frac{\mathrm{d}^2 v}{\mathrm{d}y^2} \tag{6.35}$$

with solution, obeying no-slip boundary condition of velocity at the oscillating plate and decaying to zero at large *positive* y is:

$$v(y) = V \exp\left\{-(1+\mathrm{i})(\omega/2\nu)^{1/2} y\right\} \tag{6.36}$$

implying that

$$v(y,t) = V \exp\left\{-(\omega/2\nu)^{1/2} y\right\} \cos[\omega t - (\omega/2\nu)^{1/2} y] \tag{6.37}$$

Now specialise to the case $m = 1$.

We will look for solution of the form $v(y,t) \simeq v^{(0)}(y,t) + \epsilon v^{(1)}(y,t)$, which could easily be generalised to hight powers of ϵ. Then we substitute and find, discarding terms of order ϵ^2 or higher,

$$\frac{\partial v^{(0)}}{\partial t} + \epsilon \frac{\partial v^{(1)}}{\partial t} = \left[1 + \epsilon \left(\frac{\partial v^{(0)}}{\partial y}\right)\right] \left(\frac{\partial^2 v^{(0)}}{\partial y^2} + \epsilon \frac{\partial^2 v^{(1)}}{\partial y^2}\right) \tag{6.38}$$

collecting terms in ϵ^0 we regain the original equation and to order ϵ we find:

$$\epsilon \frac{\partial v^{(1)}}{\partial t} = \epsilon \frac{\partial^2 v^{(1)}}{\partial y^2} + \epsilon \frac{\partial v^{(0)}}{\partial y} \frac{\partial^2 v^{(0)}}{\partial y^2} \tag{6.39}$$

So we get same equation for $v^{(1)}$ as for $v^{(0)}$, but with inhomogeneous term in $v^{(0)}$. so we need to find a CF and PI to the equation for $v^{(1)}$.

But note that we need a solution which vanishes on both the oscillating plate and at infinity. The CF solution to the homogeneous equation can only be a constant then. And we need a particular integral, noting the form of the homogeneous solution it is good to Fourier decompose the inhomogeneous term in terms of time and then to look for a PI for each harmonic. Use the following representations (using scaled time so ν_0 absorbed into t):

$$\begin{aligned}
\frac{\partial v^{(0)}}{\partial y} &= -\left(\frac{\omega}{2}\right)^{1/2} \exp[-(\omega/2)^{1/2}y] \Re\left[\mathrm{e}^{\mathrm{i}\omega t}\mathrm{e}^{-\mathrm{i}(\omega/2)^{1/2}y}(i+\mathrm{i})\right] \\
&= \left(\frac{\omega}{2}\right)^{1/2} \exp[-(\omega/2)^{1/2}y] \left[\cos\{\omega t - (\omega/2)^{1/2}y\} - \sin\{\omega t - (\omega/2)^{1/2}y\}\right] \\
\frac{\partial^2 v^{(0)}}{\partial y^2} &= \left(\frac{\omega}{2}\right) \exp[-(\omega/2)^{1/2}y] \Re\left[\mathrm{e}^{\mathrm{i}\omega t}\mathrm{e}^{-\mathrm{i}(\omega/2)^{1/2}y}(i+\mathrm{i})^2\right] \\
&= -2\left(\frac{\omega}{2}\right) \exp[-(\omega/2)^{1/2}y] \left[\sin\{\omega t - (\omega/2)^{1/2}y\}\right]
\end{aligned}$$

So the product of these terms is (using a couple of trigonometric identities)

$$\begin{aligned}
\frac{\partial v^{(0)}}{\partial y}\frac{\partial^2 v^{(0)}}{\partial y^2} &= \left(\frac{\omega}{2}\right)^{3/2} \exp[-2(\omega/2)^{1/2}y] \left[\sin 2\{\omega t - (\omega/2)^{1/2}y\} - (1 - \cos 2\{\omega t - (\omega/2)^{1/2}y\})\right] \\
&= \left(\frac{\omega}{2}\right)^{3/2} \exp[-(2\omega)^{1/2}y] \left[-1 + \sqrt{2}\cos\left(2\{\omega t - (\omega/2)^{1/2}y\} - \frac{\pi}{4}\right)\right]
\end{aligned}$$

(i.e. using

$$\cos A + \sin A = \sqrt{2}\left(\frac{1}{\sqrt{2}}\cos A + \frac{1}{\sqrt{2}}\sin A\right) \tag{6.40}$$

Now represent the complete equation for $v^{(1)}$ as

$$\frac{\partial v^{(1)}}{\partial t} - \frac{\partial^2 v^{(1)}}{\partial y^2} = \frac{1}{8}(2\omega)^{3/2} \exp[-(2\omega)^{1/2}y] \left[-1 + \sqrt{2}\cos\left(2\{\omega t - (\omega/2)^{1/2}y\} - \frac{\pi}{4}\right)\right] \tag{6.41}$$

A particular integral for the term -1 in the square brackets is

$$v_a^{(1)} = -\frac{\sqrt{2\omega}}{8} \exp[-(2\omega)^{1/2}y] \tag{6.42}$$

For the second term in square brackets, denote the PI by $v_b^{(1)}$, and use complex notation again:

$$\frac{\partial v_b^{(1)}}{\partial t} - \frac{\partial^2 v_b^{(1)}}{\partial y^2} = \frac{\sqrt{2}}{8}(2\omega)^{3/2}\exp[-(2\omega)^{1/2}y]\Re\left[\exp\left\{\mathrm{i}\left(2\omega t - (2\omega)^{1/2}y\right\} - \frac{\pi}{4}\right)\right\] \quad (6.43)$$

Notice the dependence on y and t both have the correct factors of 2ω to satisfy homogeneous equation. To look for a PI, we multiply the right hand side by a function of y. then the terms where the partial derivatives operate on the the terms in the right hand side cancel, leaving the remaining terms.

So let

$$v_b^{(1)} = \Re\left[f(y)\frac{\sqrt{2}}{8}(2\omega)^{1/2}\exp\left\{\mathrm{i}2\omega t - (\mathrm{i}+1)(2\omega)^{1/2}y\right\} - \frac{\pi}{4}\right\}\right]. \quad (6.44)$$

Then upon substitution, the exponentials all cancel and we find:

$$\frac{1}{2\omega}f" + \frac{2}{\sqrt{2\omega}}f' = 1 \quad (6.45)$$

I.e. a linear second order ODE with constant coefficients.

The important point is that the solution is time-dependent with a frequency of 2ω. If we had had $m \neq 1$ in the constitutive relation, then we would have found harmonics of order $m+1$ in the solution - as well as lower ones in general. So the harmonic content of the solution tells us about the highest order term in the constitutive relation.

6.6.3 Key Coding Algorithms for Couette Flow

Here we perform oscillating wall simulations and examine the harmonics of the wall frequency. To do this we choose the bins near the CE and calculate the velocity values $< v_x(y,t) >$.

To perform these simulations we introduce a further geometric object, `GeometryOscWall`, which is a modification to the `GeomterySheared Wall` object. The modifications are to

the update and analysis sections and are listed in the code block below.

```
// class GeometryOscWall implementations

void GeometryOscWall::PerStepUpdates()
{
  // Add functions here to be run every timestep
  OscillateTopCE();
}

 void GeometryOscWall::PerStepAnalysis()
{
  OutputParticlePositions();
  CalculateVxofyProfile();
  CalculateVxofytProfile();
  OutputVxofyEvolveProfile();}

void GeometryOscWall::EndofSimAnalysis()
{
  OutputFinalParticlePositions();
  OutputAverages();
  OutputVxofyProfile();

}
```

We have three new functions. The first `OscillateTopCE()` oscillates the top CE at an amplitude `Amp` and a frequency `omega` specified in the job file.

```
void GeometryOscWall::OscillateTopCE()
{
  double t = sim->get_time();

  static double V0 = omega*Amp;

  for (std::list<CParticle>::iterator p =
    OtherParticlesList->begin();
    p!=OtherParticlesList->end(); ++p)
  {
    if (p->get_type() == "S")
    {
      p->set_vel(V0*cos(omega*t), p->get_vely());
      p->set_x(p->get_x()+p->get_velx()*dt);
    }
  }
}
```

The second function, `VxofytProfile()`, calculates the profile $< v(y,t) >$ (where time is divided up into N_s slices of the wall oscillation period.). This is shown pictorially in

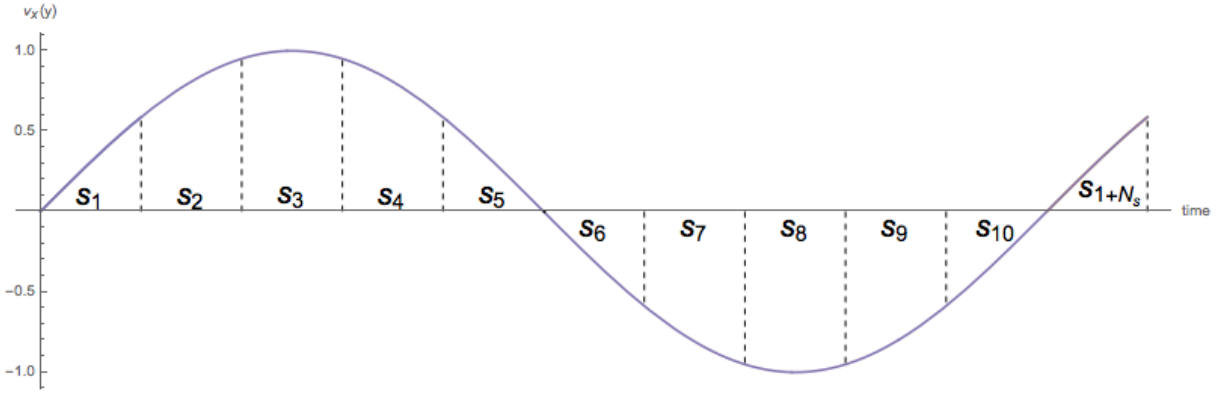

Figure 6.17: To get a profile for $v(y,t)$ we divide each period up into slices and average over that single slice. In the example shown here we have $N_s = 10$ slices.

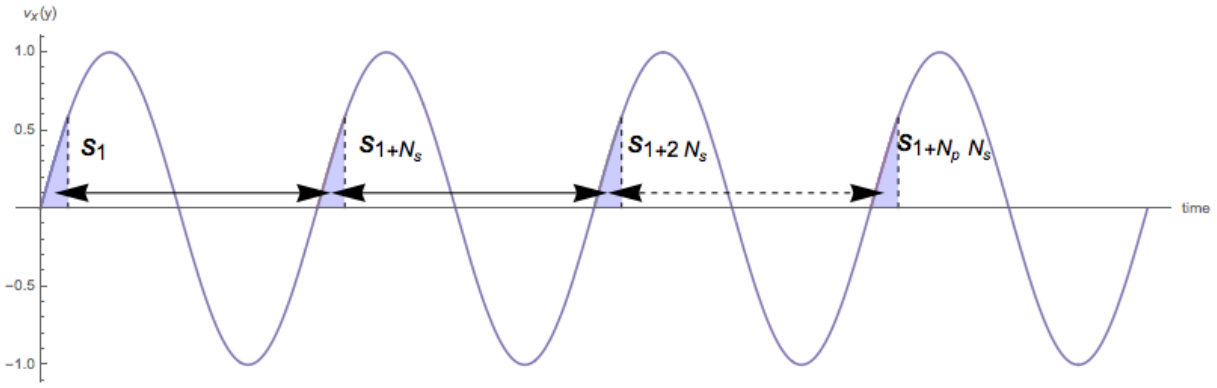

Figure 6.18: To get a profile for $v(y)$ we divide each period up into slices and average over the same slices in each period. With each period we have N_s slices. There are N_p periods in the simulation.

Fig. 6.17.

Finally, to get an average profile for $< v(y) >$ we use the `VxofyProfile()` function. This allows us to average the same time slice of the wall period over the whole simulation. This is shown pictorially in Fig. 6.18, where N_p is the number of periods in the simulation, N_s is the number of slices per period and S_i is the slice index with a period. Its implementation is given in the code block below.

```
1 void GeometryOscWall::CalculateVxofytProfile()
2 {
3   int t = sim->get_t();
4
5   static int numslices = 20;
6   static double period_timesteps = 2*pi/omega/dt;
7   static double slice_timesteps = period_timesteps/numslices;
```

```
8
9     static int lastsliceindex = 0;
10    int sliceindex = (t \% int(period_timesteps))/slice_timesteps;
11    if (sliceindex != lastsliceindex)
12    {
13      OutputVxofytProfile();
14      Vxofyt->ClearValues();
15      lastsliceindex = sliceindex;
16    }
17
18    for (std::list<CParticle>::iterator p =
19      triangulatedParticlesList->begin();
20      p != triangulatedParticlesList->end(); ++p)
21    {
22      double y = p->get_y();
23      double f = p->get_velx();
24      Vxofyt->AddValue(y,f);
25    }
26
27  }
```

A snap shot of the simulation indicating the y_{bin} is given in Fig. 6.19.

6.7 Oscillating Wall Simulation Results

Fig. 6.20, shows power spectrum analysis, of the frequency modes of the velocity profile $v(y,t)$ at a number of points near the oscillating boundary, bin numbers 20, 21, 22, 23 and 24 where 24 is the wall bin and 23 is the first bin in the fluid near the moving wall. Bin widths are $2b_0$. The plots in Fig. 6.20 show clearly the wall frequency, however none of the harmonics can be seen in the figures.

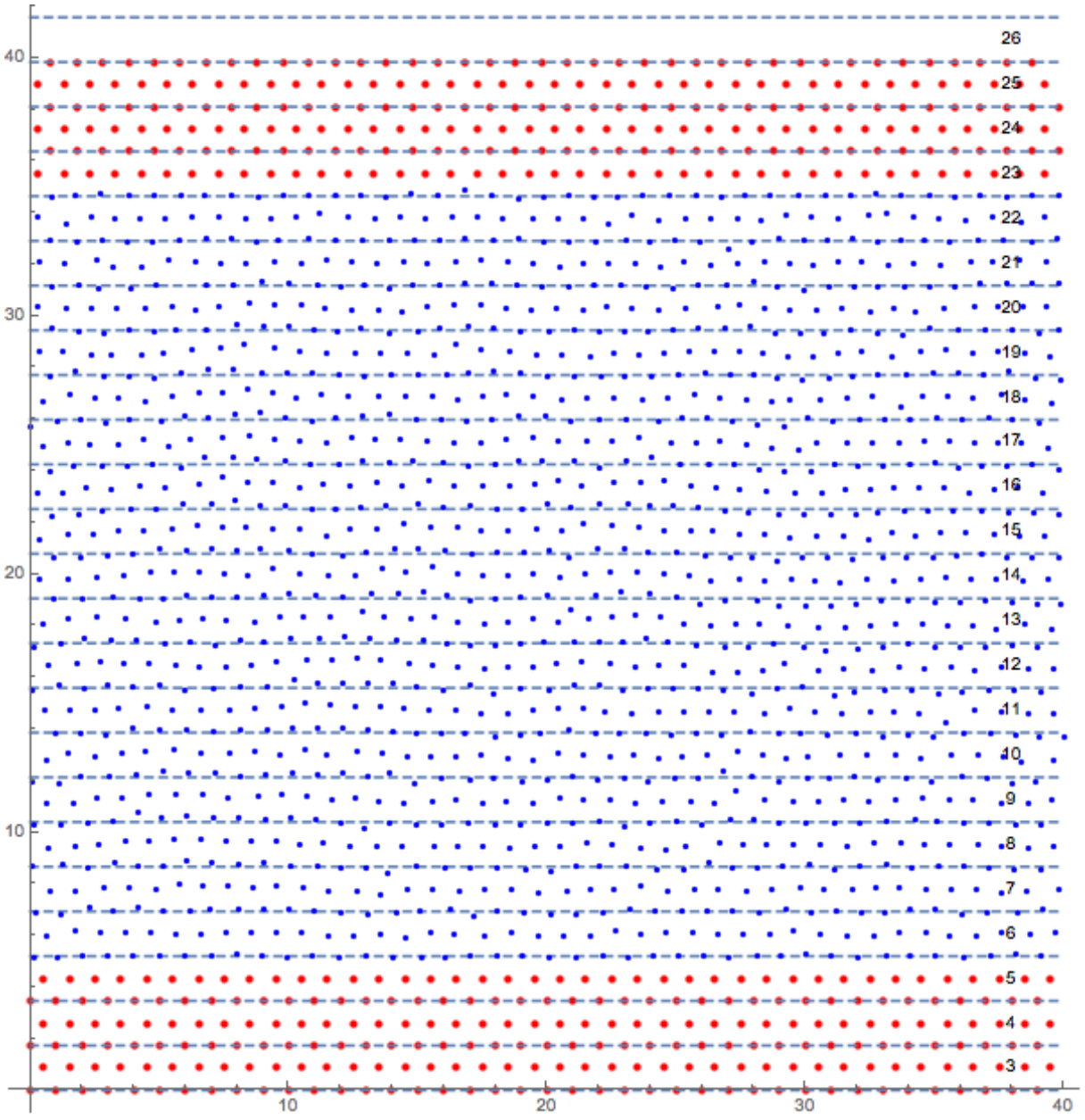

Figure 6.19: Oscillating wall simulations. Shows walls (Red) and channel particles (Blue). Bottom wall is fixed. Top wall is oscillating horizontally with frequency ω. Bins numbers for averaging are marked in the plot.

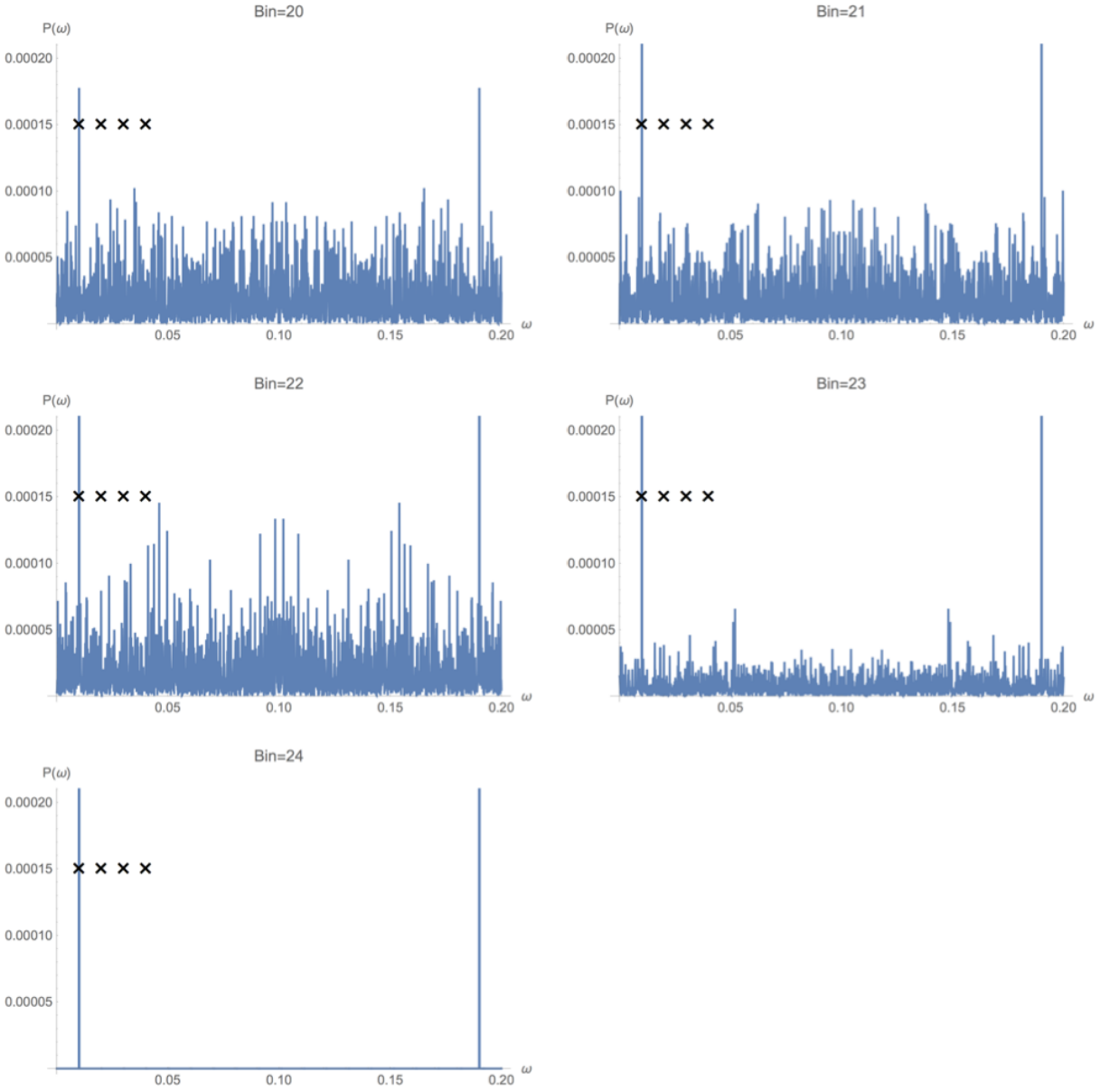

Figure 6.20: Oscillating walls $\omega = 0.01$, "x" marks fundamental and first 3 harmonics. Symmetry in the profiles is an artefact of the power spectrum method.

Chapter 7

DENSITY DRIVEN VORTEX LATTICE

This chapter focuses on a novel channel geometry that provides a new mechanism, via vortex reservoirs for propelling vortices along a narrow channel superconductor. We begin with a summary of the key results and their explanation as we have presented them in a *letter* currently under review for publication. The paper has been reformatted, to fit with the thesis style and we have signposted throughout, via footnotes to later sections in the chapter where the technical details are justified in depth. We finish the chapter with a potential application of the underlying dislocation mechanism in a real material system.

7.1 Paper: Extruding the Vortex Lattice: Two Reacting Populations of Dislocations

Extruding the vortex lattice: two reacting populations of dislocations

J.S. Watkins[1] and N.K. Wilkin[1]

[1]School of Physics and Astronomy, University of Birmingham,Birmingham, B15 2TT, UK

n.k.wilkin@bham.ac.uk

ABSTRACT

A uniquely controllable soft solid is realised in vortex matter[117, 30, 118] in a type II superconductor. The two-dimensional unit cell area can be varied[119] by a factor of 10^4 in the solid phase, without a change of crystal symmetry offering unparalleled, and easy, exploration of extreme regimes compared to ordinary materials. The capacity to confine two-dimensional vortex matter to mesoscopic regions[6, 118] provides an arena for the largely unexplored metallurgy of plastic deformation *at large density gradients*. Our simulations reveal a novel plastic flow in this driven non-equilibrium system, utilising *two* distinct, but strongly interacting, populations of dislocations. One population facilitates the relaxation of density; a second aids the relaxation of shear stresses concentrated at the boundaries. The disparity of the bulk and shear moduli in vortex matter ensures the dislocation motion follows the overall continuum flow reflecting density variation.

Soft matter forms a versatile laboratory to study plastic deformation, including: the observation of dislocation nucleation[120], motion[121, 122, 22, 6, 32], reactions[24] and role in grain boundary processes. Soft *vortex* matter has the specific advantage that the density of vortices can be changed easily by altering the magnetic field applied, and a density *gradient* is created by applying a field gradient. The novel regime of large density gradients is naturally studied by extrusion along a channel between reservoirs of different densities. The resulting time dependent non-equilibrium state is the subject of this article.

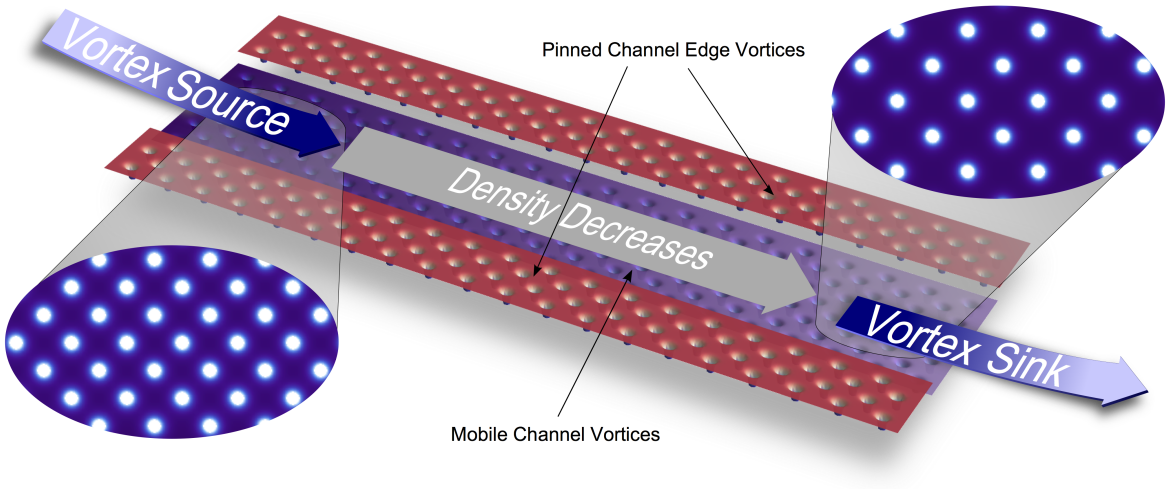

Figure 7.1: **The model of a thin channel superconductor with an imposed magnetic field gradient** $B(x)\hat{\mathbf{z}}$, where z is normal to the plane. Mobile vortices from a high-density source move along the channel under the action of a vortex density gradient. The channel edges are defined by pinned vortices. Figure submitted to Nature.

The channel is formed by a clean (unpinned) region of width w between walls provided by two pinned regions of vortex lattice. Altering the external magnetic field alters the density of vortices within the channel, while the pinned regions are unaltered for moderate changes of field. Except when we explicitly compare with the liquid phase, our simulations are at a sufficiently low temperature that–for our finite sample–there are no thermally excited Halperin-Nelson-Young dislocations.

That vortex dynamics is collective in such a channel was demonstrated[6] by the application of the electrical current to a small region of the channel which generated motion of vortices up to $5\mu\text{m} = 30w$ away. This implies a value of 5μm for the Larkin-Ovchinnikov length[77], over which the vortex lattice is not pinned. Motivated by these results, we will consider the clean limit for the channel in this article, with an ordered pinned lattice defining the channel edges.

To investigate flow (both in solid and liquid phases) at significant and controllable density gradients, our simulations add a reservoir, with a chosen vortex density, to each end of the channel (Fig. 7.1). Experimentally, the reservoirs could be fed via vortex pumps[31]; in the simulation vortices are added or removed sufficiently remotely from the

channel exit and entrance so as not to affect the flow.

The geometry of the channel is shown in Fig. 7.1, where $B_{\rm L}$ and $B_{\rm R}$, with $B_{\rm L} > B_{\rm R}$, are the magnetic fields in the reservoirs, favouring vortex motion from left to right in the channel. We work in the regime where the average density in the channel is comparable to the pinned lattice, so experimental changes of field would be small. We examine a "wide" channel of width, $w \sim 10a_0$, where a_0 is the lattice parameter of the pinned lattice, which is our unit of length (and the associated unit of field, B_0). So, although the channel lattice is only slightly mismatched with the pinned lattice, the cumulative effect *across* the width of the channel can be several lattice parameters. The "wide" channel will allow a continuum description.

Fig. 7.2 shows the yield stress for plastic flow at $B_{\rm L} - B_{\rm R} = \Delta B_{\rm y} = 0.08$ for $T = 0$. Above the yield stress $\overline{v} \propto (\Delta B)$, i.e. linear to a good approximation. In the liquid phase, for $T > T_{\rm m} = 0.012$, linearity is present for all ΔB. That $\Delta B_{\rm y}$ and $T_{\rm m}$ are numerically small reflects the disparity of bulk and shear moduli in the vortex lattice.

A reference for density changes along the channel is provided by the local vortex spacing in the *liquid* phase, $a^{\ell}(x)$, which is smooth:

$$a^{\ell}(x) \simeq \sqrt{\frac{2}{\sqrt{3}} \frac{\Phi_0}{(B_{\rm R} - B_{\rm L})(x/L) + B_{\rm L}}}, \tag{7.1}$$

where L is the channel length and Φ_0 is the flux quantum. If the "solid", plastic, phase were glassy or hexatic, the density might vary continuously as well. However, as can be seen from Fig. 7.4, this is not true. While the inter-vortex spacing *parallel* to the channel, $a^{\rm p}(x)$, tracks the liquid variation, $a^{\ell}(x)$, the *perpendicular component* of the spacing, $b^{\rm p}(x)$ ($b = \sqrt{3}/2a$ for an equilateral triangular lattice), is step-like along the channel.

The interpretation, confirmed by examination of Fig. 7.6, is that the vortex matter is mostly crystalline with the inter-row spacing commensurable with the channel width. The commensurability dictates discrete changes along the channel, where rows disappear, associated with an edge dislocation in the "bulk" of the channel. Because vortex matter has no cohesive energy, the inter-row separation expands (and the unit cell expands) as

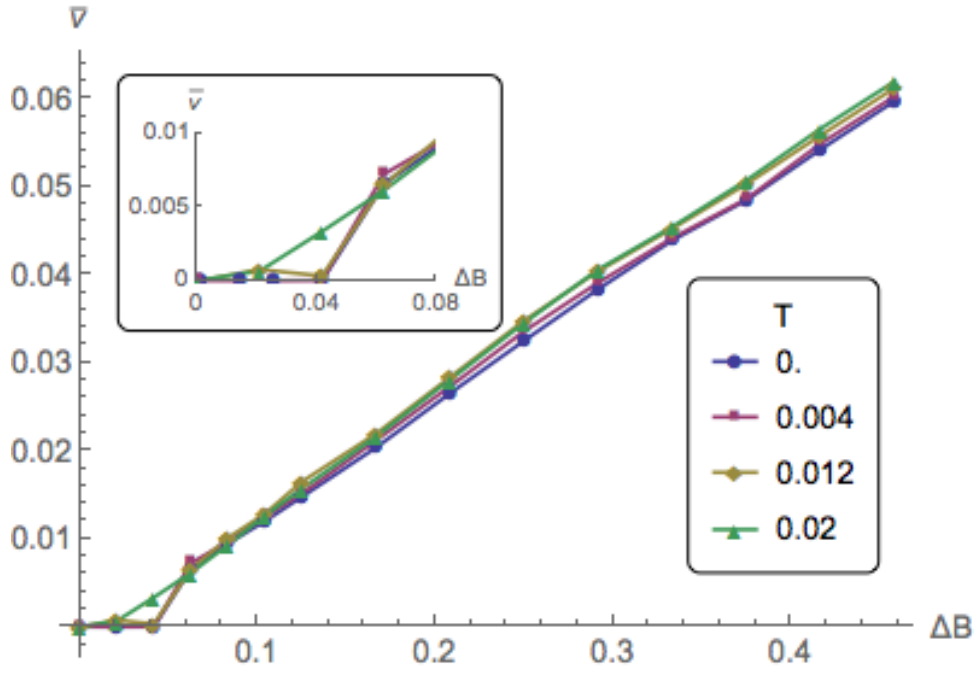

Figure 7.2: **Overall flow and yield along channel.** Shows the variation of the vortices' average velocity, $\overline{v}(\Delta B)$, with field difference. There is a critical field difference for the solid to yield at sufficiently low temperatures, which disappears above the melting temperature (similar to the velocity/Lorentz relation from the Leiden group[22, 6]). Figure submitted to Nature.

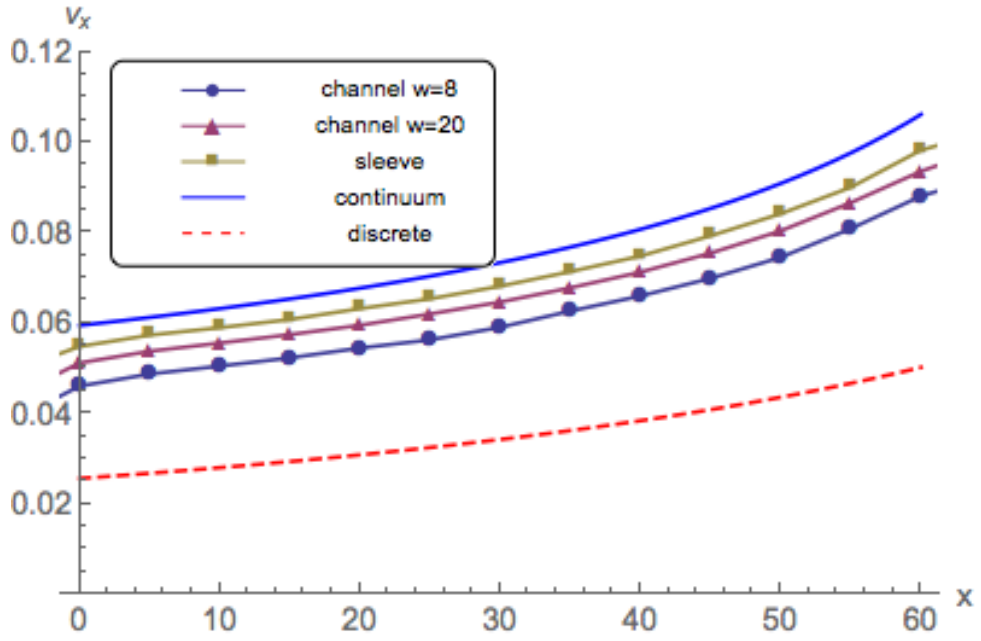

Figure 7.3: Shows the velocity profile, $v_x(x)$, in the channel and sleeve (cylindrical) geometries, with $\Delta B = 0.46$. The continuum expression for $v(x)$ is shown, as is an expression for a cutoff discrete lattice sum. As the channel width grows $v(x)$ approaches the cylindrical result (which is closer to the continuum model), showing the diminishing effect of edge shear. Figure submitted to Nature.

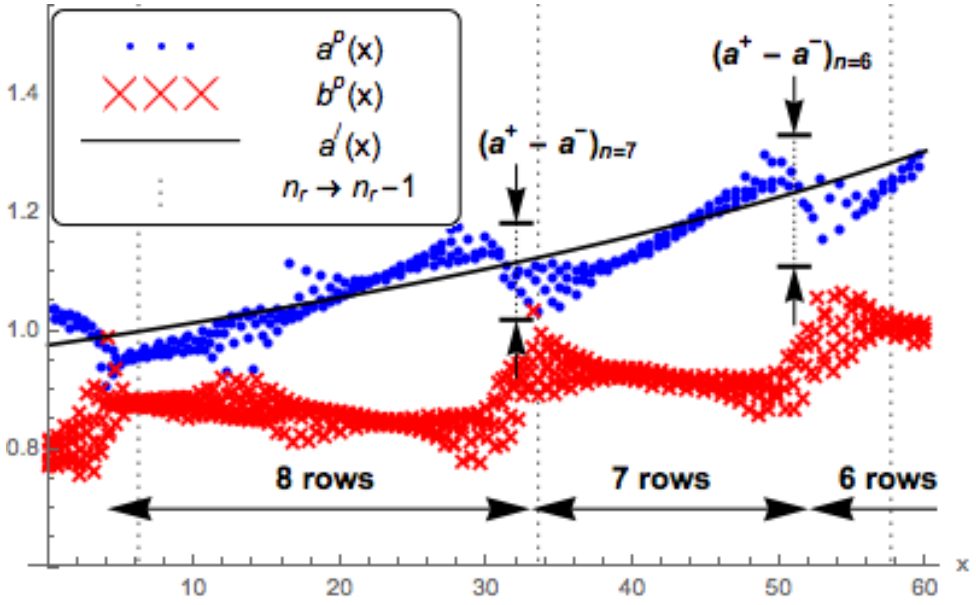

Figure 7.4: **The discontinuous evolution of the lattice along the channel. a** shows the variation in the vortex spacing (found using Delaunay triangulation) parallel to the channel boundary, $a(x)$, with vertical arrows indicating jumps mentioned in the text. The component of the separation *perpendicular* to the channel edges, $b(x)$, is also plotted. The system contains three zones of $n_r = 8$, 7 and 6 rows of vortices. Figure submitted to Nature.

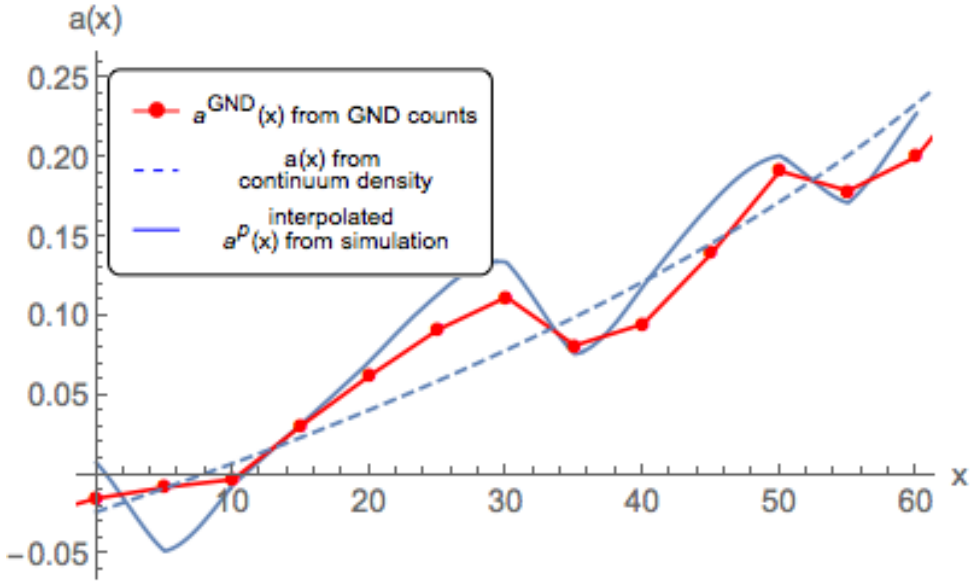

Figure 7.5: Shows the density of GNDs(geometrically necessary dislocations). The solid line is calculated using an interpolated $a^{\mathrm{P}}(x)$ from the simulation and Eq. (7.2). The dashed line is a continuum prediction. The red line is from the simulations. Figure submitted to Nature.

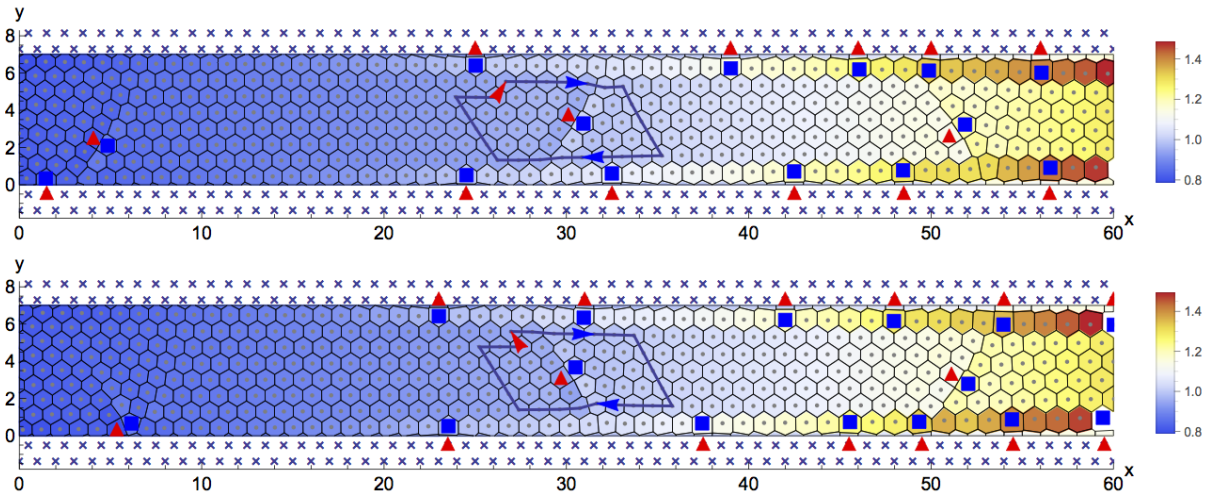

Figure 7.6: **The double dislocation network in the channel.** A snapshot of the vortex positions in a channel, of width $w = 8b_0$, is shown. There are three "bulk" edge dislocations. The Burgers circuit construction[13] for the second dislocation is indicated. Pinned vortices in the channel edges are marked with ($\times$). $\triangle$ and $\square$ mark vortices with 5 and 7 neighbours respectively. All other vortices have 6 neighbours. (Top) An bulk dislocation approaching the lower channel edge. (Bottom) The same dislocation after the interaction with a GND with $\mathbf{b} = -\hat{\mathbf{y}}$. Figure submitted to Nature.

x passes an edge dislocation, the lattice filling the channel laterally with fewer rows. The required number of bulk dislocations is increased by increasing the magnetic field gradient or the width of the channel (which requires more rows to be removed for a given density change). Our simulations demonstrate this for density gradients necessitating up to 4 edge dislocations, with channel widths of up to $30b_0$.

The unit cell changes shape from a compressed isosceles triangle to an equilateral triangle upon passing an edge dislocation. I.e. the transition from $n+1$ rows to n rows occurs when $b = (\sqrt{3}/2)a^{\mathrm{p}}(x) = w/n$. To avoid gross mechanical disequilibrium, we expect the unit cell *area* to be continuous as a function of x. Equating the unit cell sizes in the sections with different rows at the boundary implies a discontinuity in $a^{\mathrm{p}}(x)$, $a^+ - a^- = (2/\sqrt{3})(w/n^2)$, where a^+ is the lattice parameter on the side with $n+1$ rows and a^- that with n rows. This difference is indicated in Fig. 7.4, agreeing with the simulations.

The "geometrically necessary strain" caused by the lattice parameters of the pinned

region and the channel lattice becoming increasingly mismatched as x increases is concentrated in "misfit", or geometrically necessary dislocations (GNDs) at the interface Fig. 7.6). The "charge" density of GNDs, $\rho_{\rm g}$, reflecting the lack of registry due to the variation in $a^{\rm p}(x)$, is:

$$\rho_{\rm g} = \frac{1}{a_0}\left(1 - \frac{a_0}{a^{\rm p}(x)}\right) \tag{7.2}$$

Fig. 7.12 shows the agreement between this expression and the density of GNDs found in the simulation.

The *dynamic* behaviour Fig. 7.7 of the plastic flow reflects the *interacting* populations of GND and "bulk" dislocations. The GNDs glide parallel to the channel edges, lubricating the vortex lattice motion along the channel. The bulk dislocations glide on symmetry-related glide-planes across the channel. The video *appears* to show that bulk dislocations are reflected at the channel edge onto to the other glide-plane not parallel to the channel edge, and repeat this zig-zagging motion between the channel edges. We have followed this periodic motion for more than 100 periods.

However, it *cannot* be a reflection, as the *conserved*[13] Burgers vector changes when gliding on different planes. The resolution is that a "reaction" occurs, visible in Fig. 7.7, a bulk dislocation upon reaching a channel edge combines with a GND producing an bulk dislocation on the third glide-plane (i.e. the three possible Burgers vectors add to zero).

The steady state of plastic flow is constituted by the regions of constant row number, delimited, in the laboratory-frame, by the average x-coordinates of the zig-zagging bulk dislocations. The gliding GND dislocations ensure this.

Building a global picture of the flow down the channel from these local descriptions of dislocation motion is aided by Fig. 7.2. Note the near identity of flow rates in liquid and plastic phases–despite the considerable difference in structure. The underlying cause is that vortex matter is soft but incompressible[10]: the ratio of the bulk, κ, to shear, μ, moduli is $\kappa/\mu = 16\pi(\lambda/\xi)^2 \gg 1$, for strongly type II superconductor, where ξ is the coherence length and λ is the penetration depth of the superconductor. Thus the macroscopic flow rate, reflecting density gradients, is insensitive to crystalline order and

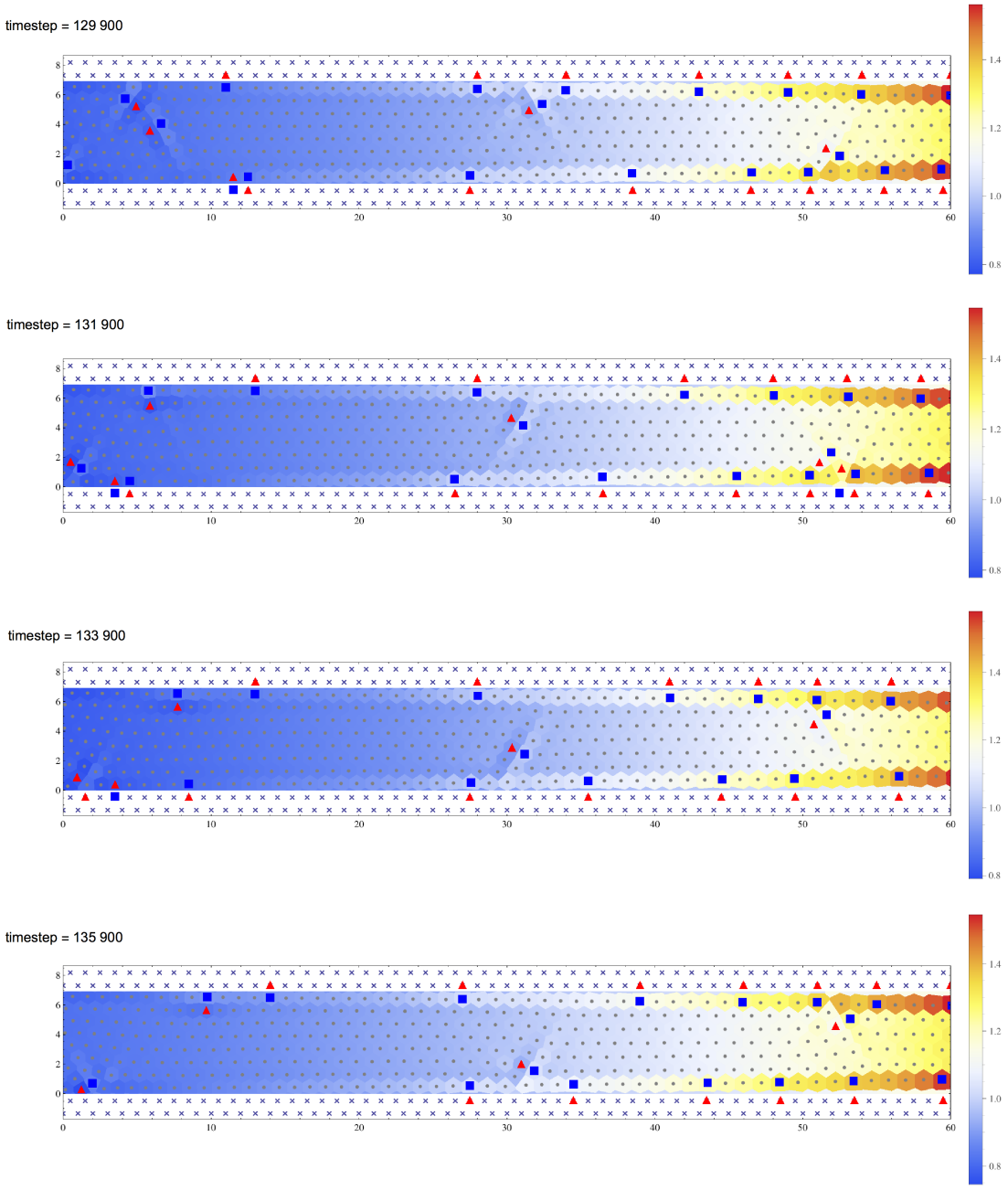

Figure 7.7: Shows the motion of the two populations of dislocations in the channel geometry. The GNDs are confined to the boundary between the mobile vortices and the pinned channel edge vortices. The second population move in the bulk along glide planes tilted at $\pi/3$ to the channel edge and relax the density changes along the channel. The GNDs and bulk dislocations interact at the channel edge through an process that conserves Burgers vector and allows the bulk dislocations to change glide plane.

the steady-state profile for $v(x)$ and $\rho(x)$ along the channel may be derived using the continuity equation for the vortices and the force equation on each vortex [1],

$$v(x) = -\frac{\Phi_0^2}{\gamma\pi\mu_0}\frac{\mathrm{d}\rho}{\mathrm{d}x} \tag{7.3}$$

They yield:

$$\rho^c(x) = \rho^l(0)\sqrt{1-\frac{x}{L_0}}; \quad v(x) = \frac{Q}{\rho(x)}, \tag{7.4}$$

where $x = 0$ has been chosen to be the start of the channel, $Q = \rho(x)v(x)$ is conserved in steady state and $L_0 = \Phi_0^2\rho_0^2/(\pi\gamma Q\mu_0) \gg L$ in our simulations (i.e. the number of rows does not drop to zero). The resulting velocity field is shown in Fig. 7.3.

The microscopic dislocation motion is slaved to this density–gradient dominated continuum description (i.e. determined kinematically) as the Peierls-Nabarro stress for glide is determined[13] by the small shear modulus. The GNDs ensure the average motion of the channel lattice occurs with the velocity $v(x)$: each GND translates the lattice by a_0 as it passes, so their velocity, $v_{\mathrm{g}}(x) = v(x)/(a_0\rho_{\mathrm{g}}(x))$.

The zig-zagging dislocations ensure that the density profile is stationary in the laboratory frame. They move backwards, see Fig. 7.9, at an average velocity $v_{\mathrm{zig}} = -2v(x)$, where the factor of two comes from the angle of the glide plane. Channel-edge friction can be removed by considering a "sleeve", with a periodic boundary condition in the y-direction, Fig. 7.8. On the sleeve there are still preferred row separations due to commensurability with the circumference of the cylinder. Fig. 7.3 shows indeed that the sleeve-system is closer than the channel to the continuum model. This is then reminiscent to the description[123, 124] of bacterial cell wall growth and provides a physical mechanism for the observations in colloidal dynamics as seen in Deutschländer *et al.*[125].

In summary, the first study of plastic deformation under significant density gradients has demonstrated the existence of a new steady-state with a strongly interacting set of dislocations on all of the glide planes of the vortex crystal. Whilst the vortex crystal has no cohesive energy, one would expect similar behaviour for any two-dimensional

[1] see §7.3

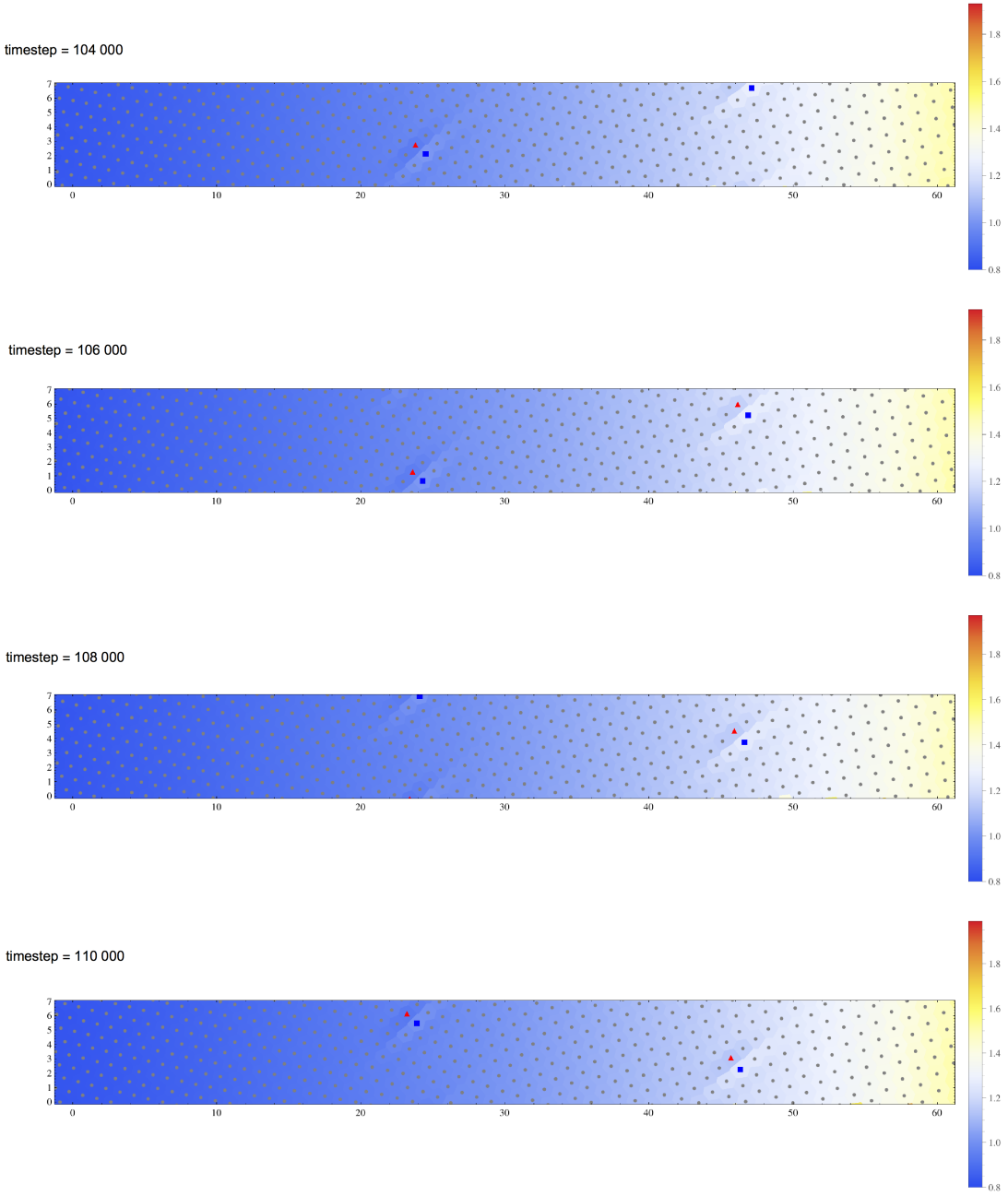

Figure 7.8: Dislocation motion in the sleeve geometry. The removal of the channel edges results in a steady circumferential velocity for the dislocations. The tilt of the lattice also alters the angle of the Burgers vector compared to the channel system.

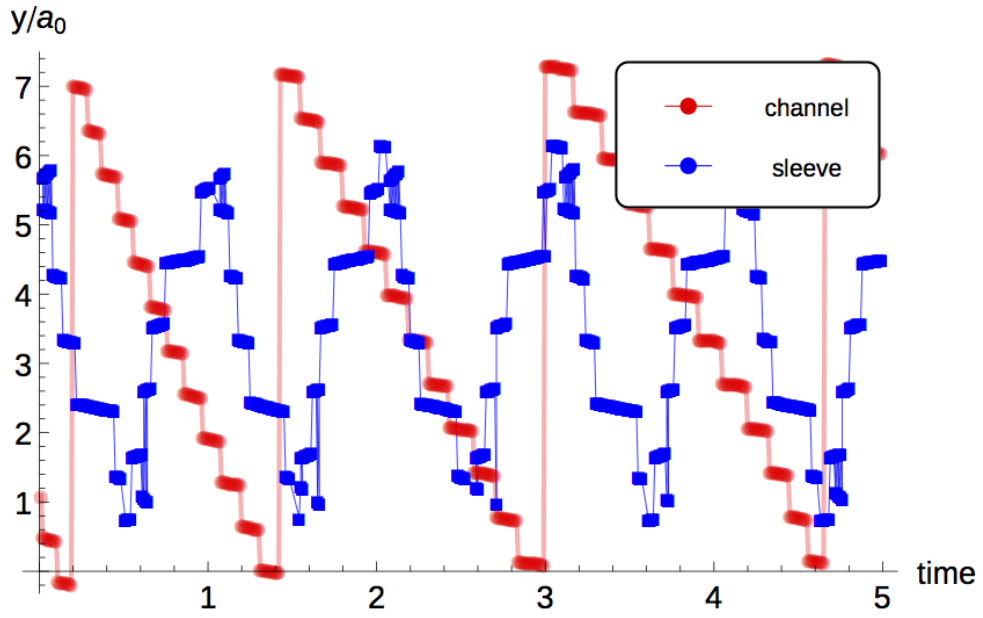

Figure 7.9: **Motion of the "bulk" dislocations, kinematic and dynamic.** Dislocation paths are shown for both the channel and the sleeve, in a reference frame moving with the channel/sleeve lattice. In the case of the channel, non-kinematic influences are implied an additional velocity modulation: moving faster as they leave a channel edge and slowing are they approach an edge. This is due to image forces being repulsive due to the rigid pinned lattice, although this is partly cancelled by the lubrication of the GND's allowing slip along the surface[23]. There is no correlation between the different zig-zagging dislocations–presumably because their velocities are different (as $v(x)$ varies) and interactions are suppressed by exponential screening due to the image arrays. Figure submitted to Nature.

matter compressed sufficiently from its equilibrium density. The generalization to three dimensions–either for flux lines or particles–is an open question, as is the potential of the latter for high/low compressibility (cf pinned/channel) heterogeneous mixtures in geophysical flows.

7.2 Simulating the Density Driven Flow

The results presented in §7.1, require carefully controlled simulations, optimised to enable the full parameter space to be explored. We now review the decisions made and the reasons why. In particular we need to ensure that

- The field in the reservoirs is well controlled
- The system displays physical results
- That the code is optimised subject to these constraints, as the phase space of parameters over which the simulations needed to be run was large.

The extensive simulation literature that exists[2] is based upon the the magnetic field, and therefore density of the vortices, being homogeneous on length scales above a few lattice spacings. The results we have presented rely upon the field gradient induced motion, clearly controlling smoothly the vortex density in the reservoirs, in order not to significantly perturb the channel is essential. We discuss below how this process has been optimised.

Vortices are added at random locations within the source region and removed in a similar fashion in the sink - where both source and sink are identical but with different vortex density imposed. This is relevant to the yield stress results where low field differences are imposed, §7.4.

The channels and vortex baths are lined by pinned vortices, providing a confining potential for all other *mobile* vortices, Fig. 7.1, to flow between. The field for the channel edges (CE) are maintained at $B_0 = 1$ giving a density of $1/(a_0 b_0) = 2/(\sqrt{3}a_0^2)$. For this system we define the source and sink reservoir fields as B_L and B_R, respectively. The subscripts simply indicate the orientation of the system with the source on the left and sink on the right. For reservoirs where $B_L = B_R$, in the solid phase no vortex motion will be perceptible after any initial inhomogeneities have been resolved. The liquid phase allows individual vortices to diffuse but overall density is homogeneous throughout the

[2] See §1.1.

channel, and we select $B_L > B_R$, Fig. 7.1.

For the simulation values for the source and sink fields could be set at any value, however, physically it is required that the fields are similar that they be similar to the CE field B_0 - otherwise the pinned channel edge will no longer be energetically stable.

It is clear that the local field and local density must be related - but the values along the channel are determined by the flow, rather than externally imposed. We proceed by imposing the fields in the source and sink regions. This generates two queries:

- What B-field profile does this give along the channel?
- What is the corresponding density regime?

7.3 Expected Profiles for Field, Density and Lattice Spacing in the Liquid Regime

To address these two questions we call upon a continuum based calculation and simulations of the liquid phase. (Within the solid phase structural inhomogeneities could potentially affect the profile.) We commence with the defined values of the field in the source and sink and the relationship between field and density. We also make a linear extrapolation of the field along the channel between the source and sink. In equilibrium, the number of vortices in an area A in proportional to the applied field strength B, $n_v = BA/\Phi_0$. Rearranging leads to an equation for the density

$$\rho = \frac{n_v}{A} = \frac{B}{\Phi_0} \tag{7.5}$$

We can also use the symmetry of the triangular lattice to relate the field to the lattice parameters. If we set $n_v = 1$ and $A = a_0 b_0$ (which is correct for the triangular lattice) we rearrange to an equation that relates the lattice parameters to the applied field,

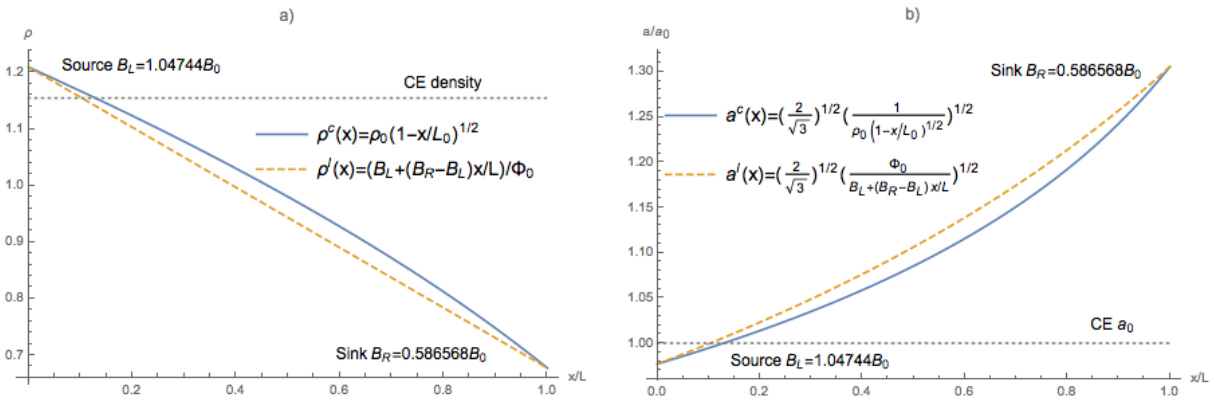

Figure 7.10: Comparison between linear field assumption and continuum analysis for **a** density and **b** lattice parameter.

$$a = \left(\frac{2}{\sqrt{3}}\right)^{1/2} \left(\frac{\Phi_0}{B}\right)^{1/2} \tag{7.6}$$

Assuming$B$ varies linearly with x, $B(x) = B_L + (B_R - B_L)x/L$ where L is the length of the channel. Substitution of $B(x)$ into both the above equations for density and the lattice parameter give a functional form for the variation along the channel.

$$\rho^l(x) = \frac{n_v}{A} = \frac{B_L + (B_R - B_L)x/L}{\Phi_0} \tag{7.7}$$

$$a^l(x) = \left(\frac{2}{\sqrt{3}}\right)^{1/2} \left(\frac{\Phi_0}{B_L + (B_R - B_L)x/L}\right)^{1/2} \tag{7.8}$$

The graphs of these two quantities can be seen in Fig. 7.10.

Deviations from this for both the liquid and solid state are discussed in §7.5 due to energetic constraints which arise from the microscopic structure.

7.4 Langevin Dynamics

It is standard practice to model liquids and vortex lattices via Langevin dynamics. Novel to our work is applying the drive via a density gradient. The primary issue is in fact the simulation of the vortex reservoirs. The reservoirs are required to maintain a fixed average field across the whole reservoir. *How can this be practically achieved?* In a pseudo code approach we write, Algorithm 1.

Algorithm 1 UpdateReservoir - Attempt 1

```
1: procedure UpdateReservoir(B)          ▷ Maintains average field of reservoir
2:     currentB ← CalculateField( )
3:     if currentB < B then
4:         AddVortex( )
5:     else if currentB > B then
6:         RemoveVortex( )
7:     end if
8:     end if
9: end procedure
```

If we attempt this simple approach, further queries arise.

1. Is it safe to assume that the average B- field is the correct quantity to calculate?
2. Where should vortices be added or removed?
3. How often should this routine be run? and is this method computationally efficient?

We address these questions below.

7.4.1 How Should We Calculate the B-Field?

We could perform a Delaunay Triangulation on the particles in the reservoir leading to determination of an average lattice spacing, a. This is potentially slow and problematic when the reservoir B-field is much lower than the channel edge field, B_0. This leads to a slight compression of the vortices in the centre of the reservoir, artificially raising the

local B field. Alternatively one could count the total number of vortices in the reservoir and directly determine the B-field of the reservoir, using the formula

$$B = \Phi_0 \frac{n_v}{L_{\text{res}} w}. \tag{7.9}$$

where n_v is the vortex count in the reservoir, L_{res} is the reservoir length and w the reservoir width. This requires less computation but has the disadvantage that average field is now quantised in Φ_0/A_{res} (where $L_{\text{res}}w$). It also depends where the vortices are added and removed from the reservoir as to whether the average field across the whole source is the correct quantity to calculate.

7.4.2 Where Within the Reservoirs Should Vortices be Added or Removed?

The naive approach is to randomly add or remove a vortex from anywhere in the reservoir. Empirically this was found to have problems. The addition or removal of a vortex is destructive to the local structure in the solid phase. We require the reservoirs to present a stable set of particles, optimally in a triangular lattice formation, at the start of the channel.

If instead, we add and remove particles well away from the start and end of the channel in very large reservoirs,Fig. 7.11, we do create a stable lattice structure at the start and end of the channels.

Unfortunately this creates a field gradient across the reservoir, such that the average field for a large reservoir and the value of the field at the entrance to the channel are significantly different. *What value of field should we be using to respond to changes in the reservoir?*

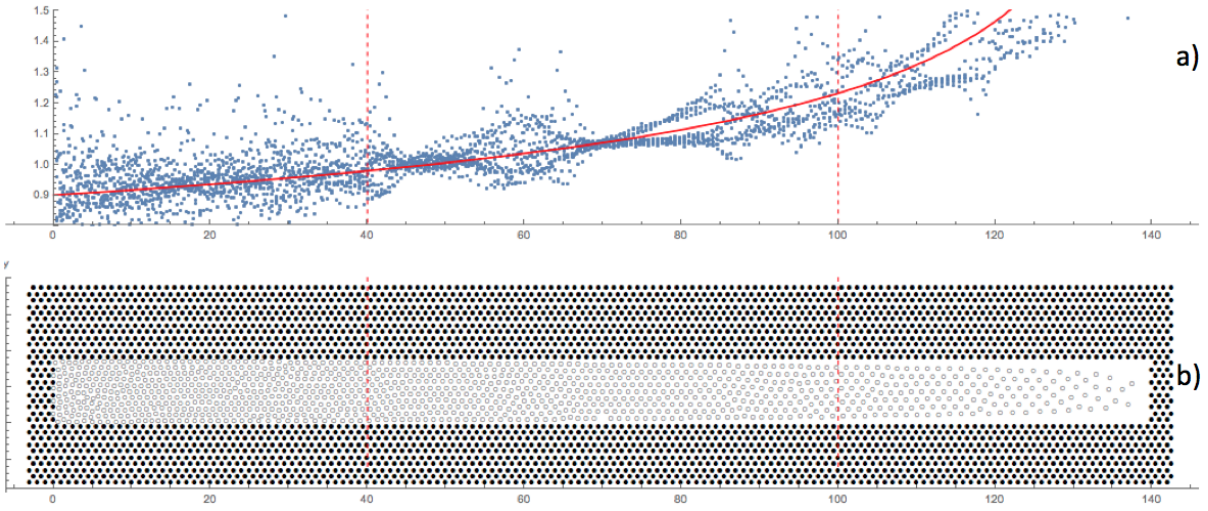

Figure 7.11: **a** Shows a fit to the lattice parameters in the channel, found using Delaunay Triangulation. We see a gradient across the reservoirs due to particles added and remove at the extreme end of the channel. **b** We can see a stable lattice is created by the addition of vortices away from the channel edges. Marked by vertical red lines.

7.4.3 Implementation of the Vortex Reservoir

Taking into account the reservoir issues discussed above, it was found that the most robust approach was to create a small source $\sim 10 - 20a_0$ where vortices are added and removed in the first/last $5a_0$ region. This creates a small gradient across the reservoir but does give the lattice time to stabilise.

We calculate the field at at the boundary between the reservoir and the channel, at $x = 0$ and $x = L$, since this is the field of interest, using a binned approach with bin widths of $5a_0$. Since particles are added/removed away from these regions, changes induced by adding/removing vortices are not felt instantaneously at the channel ends. The relaxation time, can be estimated and we use this as a relaxation time, T_r for the reservoirs and only allow particles to be added/removed at most every $2T_r$ seconds. **This procedure results in a stable lattice of the required B fields at the ends of the channel.**

7.4.4 Is the Routine Computationally Efficient?

Although individual runs of the system take usually less than an couple of hours to run, the phase space to be explored is large, and hence optimisation is essential.

The biggest calculation cost for this comes from the use of triangulation to calculate the B-field. This can be vastly optimised by counting vortices instead, which becomes increasingly accurate with reservoir area.

Incorporating these issues the second algorithm Algorithm 2 captures these modifications, and is run for both reservoirs.

Algorithm 2 UpdateReservoir - Attempt 2

```
1: procedure UpdateReservoir(B)                ▷ Maintains average field of reservoir
2:     if timer >= Trelaxation then                ▷ timer increases each time step
3:         timer ← 0
4:         currentB ← CalculateField( )
5:         if currentB < B then
6:             AddVortex( )
7:         else if currentB > B then
8:             RemoveVortex( )
9:         end if
10:    end if
11: end procedure
12:
13: procedure CalculateField( )    ▷ Calculates field at reservoir/channel interface
14:    N ← CountVorticesInBin( )
15:    Area ← BinArea( )
16:    return EffectiveField(N, Area)    ▷ Calculates field from vortex count and
    area
17: end procedure
18:
19: procedure AddVortex( )                          ▷ Adds a vortex to reservoir
20:    v ← CreateVortex(xLow, yHigh)
21: end procedure
22:
23: procedure RemoveVortex( )                       ▷ Removes a random vortex
24:    vlist ← v from all vortices where v.x ∈ [xLow, xHigh]
25:    vptr ← random v from vlist
26:    Remove(vptr)
27: end procedure
```

With this algorithm deployed, each reservoir can equivalently act as a source or sink.

A further issue can occur if the vortices added to the reservoirs are placed close to other vortices, within a range of $\ll a_0$. This can result in very large forces that can expel a vortex from the system. Within the code this is dealt with by deleting any escaped vortices from the the vortex list and replacing it by a vortex at the same x position but a different random y position. Vortices, escaping the channel ends are not replaced by this algorithm and are instead dealt with by the normal `UpdateReservoir()` procedure. In the liquid systems, thermal noise can also result in vortices becoming very close to each other and then being expelled from the system. If this occurs in the channel region we employ the same proceedure as the reservoirs and replace the escaped vortex at the same x position in order to maintain the field value in a given area.

To facilitate these techniques the average velocities of the vortices needs to be evaluated.

7.5 Application of the Continuum Approximation Results

Modelling the system using the continuum approximations allows for the spatial variation of $\rho(x)$ and $v(x)$ to be determined. The starting point is to ignore edge effects, working more than a penetration depth into the channel, so inter-vortex interactions have decayed to zero. Then the equation of motion becomes a force balance between the viscous drag term and the sum over repulsive vortex-vortex interactions, roughly over a penetration depth area. Replacing the discrete sum over vortices with an integral over density gives an equation of the form

$$\gamma \mathbf{v}(\mathbf{r}) = \int \mathrm{d}\mathbf{r}' f^{vv}(\mathbf{r}-\mathbf{r}')\rho(\mathbf{r}')\widehat{(\mathbf{r}-\mathbf{r}')} \tag{7.10}$$

The viscous term on the left hand side is due to the "normal fluid" of excited quasi-

particles scattering from the vortex, or trapped in its core. We now use the small value for the change in vortex density over a distance of the penetration depth to approximate Eq. (7.10). Performing a change of basis $\mathbf{r}' \to \mathbf{r} + \boldsymbol{\zeta}$ and Taylor expanding $\rho(\mathbf{r} + \boldsymbol{\zeta})$ to first order in $\boldsymbol{\zeta}$ gives the transformed equation

$$\gamma \mathbf{v}(\mathbf{r}) \simeq \int \mathrm{d}\boldsymbol{\zeta} f^{vv}(\boldsymbol{\zeta}) \left[\rho(\mathbf{r}) + \boldsymbol{\zeta} \cdot \nabla \rho(\mathbf{r})\right] \widehat{\boldsymbol{\zeta}} \tag{7.11}$$

Since $\boldsymbol{\zeta} = (\zeta \cos\phi, \zeta \sin\phi)$, $\widehat{\boldsymbol{\zeta}} = (\cos\phi, \sin\phi)$ and $\nabla\rho = (\partial\rho/\partial x, \partial\rho/\partial y)$, only the term in $\partial\rho/\partial x$ survives, which results in

$$v(x) = -\frac{\Phi_0^2}{\gamma\mu_0} \frac{\mathrm{d}\rho}{\mathrm{d}x} \tag{7.12}$$

To determine the density profile the steady state continuity equation is introduced, in 1D this is $Q = \rho^c(x)v(x)$. Substituting Eq. (7.12) and performing the integration gives the density profile

$$\rho^c(x) = \sqrt{\rho(0)^2 - \frac{\gamma Q \mu_0}{\Phi_0^2}\, x} \tag{7.13}$$

where the boundary condition on the entrance to the channel $\rho = \rho^l(0)$ was used and we let $-2Q \to Q$.

To determine Q for given values of B_L, B_R and L we find

$$Q = \frac{\Phi_0^2}{\gamma\mu_0 L} \left[\rho^l(0)^2 - \rho^l(L)^2\right] \tag{7.14}$$

where we can use the local density in the source and sink regions, given by Eq. (7.7).

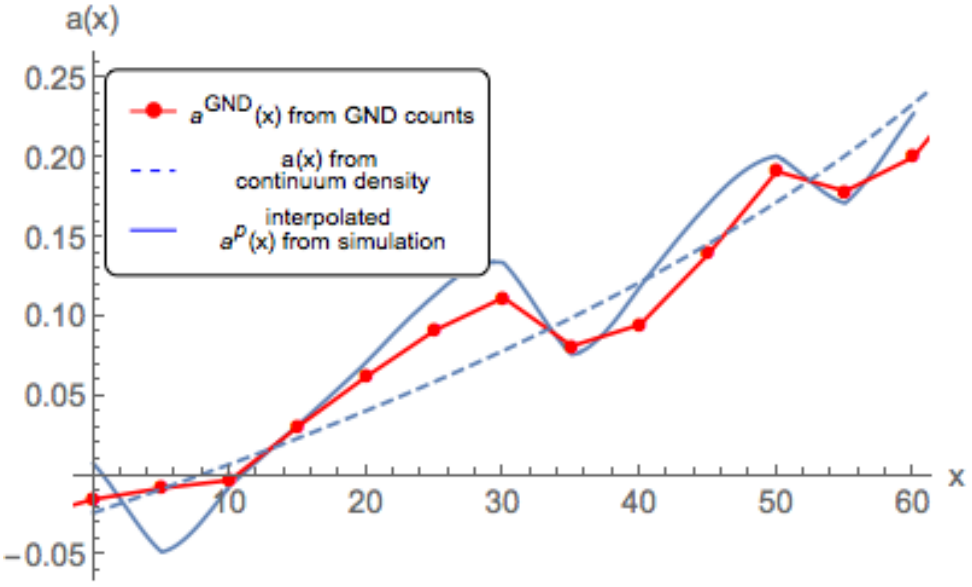

Figure 7.12: Shows the density of GNDs. The solid line is calculated using an interpolated $a^{\text{P}}(x)$ from the simulation and Eq. (7.2). The dashed line is a continuum prediction. The red line is from the simulations. Figure submitted to Nature.

7.6 Peach-Koehler Forces - Dislocation Interactions

The zig-zagging motion of the bulk dislocations, Fig. 7.9, shows the dislocations slowing down when approaching the CE. They are two possible reason for this, both arising due to forces between dislocations. We will first consider the forces between bulk dislocations and the GNDs that inhabit the CE interface. To continue we need to calculate the Peach-Koehler forces between these populations of dislocations. This requires access to the elastic constants for the material in question which is not easy for this system. Even so a qualitative understanding can be gained by examining these stress fields and the interactions of the bulk dislocations and GNDs with these fields. We wish to ask what force the bulk dislocation might feel due to the presence of the GNDs. To simplify this calculation we will just consider a single GND interacting with a bulk dislocation, Fig. 7.13. The GNDs do get removed via the reaction mechanism already described but as they are fast moving a bulk dislocation will always feel the influence of a GND. For this orientation of $\mathbf{b}_1$ we can use the stress field from Eq. (7.17), Eq. (7.18) and Eq. (7.19) but set $b \to -b$ and the force from Eq. (3.10) and Eq. (3.11). The force felt by the

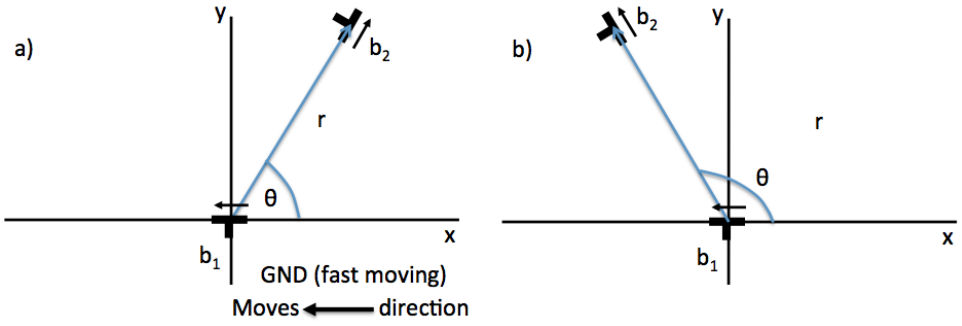

Figure 7.13: **Schematic of GNDs and bulk dislocations system.** Upon approach to the CE the bulk dislocations will feel the influence of the GNDs. Since GNDs are fast moving we will consider that the dislocation always feels the influence of the GND. Figure submitted to Nature.

dislocation $\mathbf{b}_2 = (b/2, \sqrt{3}b/2)$ is then

$$F_x = \sigma_{yx} b_x + \sigma_{yy} b_y \tag{7.15}$$

$$F_y = -\sigma_{xx} b_x - \sigma_{xy} b_y \tag{7.16}$$

With stress terms

$$\sigma^{\bar{b}}_{xx} = \frac{\mu b}{2\pi(1-\nu)} \frac{y(3x^2+y^2)}{(x^2+y^2)^2} \tag{7.17}$$

$$\sigma^{\bar{b}}_{yy} = -\frac{\mu b}{2\pi(1-\nu)} \frac{y(x^2-y^2)}{(x^2+y^2)^2} \tag{7.18}$$

$$\sigma^{\bar{b}}_{xy} = -\frac{\mu b}{2\pi(1-\nu)} \frac{x(x^2-y^2)}{(x^2+y^2)^2} \tag{7.19}$$

Substitution for the stress terms and Burgers vectors gives

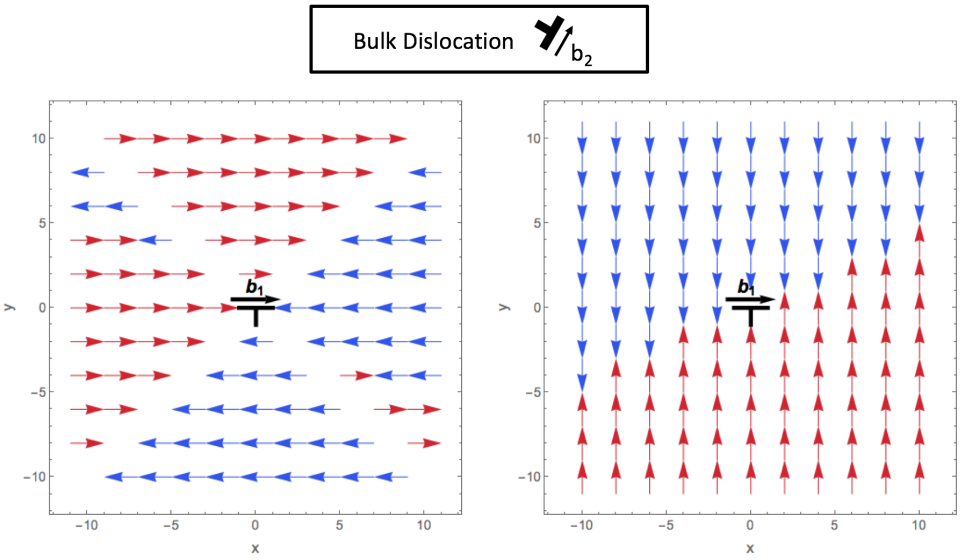

Figure 7.14: ***Direction* of Peach-Koehler force between GNDs and bulk dislocations (*approaching CE*)**. Force components felt by a dislocation $\mathbf{b}_2$ due to a dislocation $\mathbf{b}_1$ at the origin. (left) Force-field in $\hat{\mathbf{x}}$ direction. (right) Force-field in $\hat{\mathbf{y}}$ direction. Bulk dislocation feels an attractive force in the vicinity of the channel edge. Channel is defined as $x > 0$.

$$F_x = -\frac{\mu b^2}{4\pi(1-\nu)}\frac{x(x^2-y^2)}{(x^2+y^2)^2} - \frac{\sqrt{3}\mu b^2}{4\pi(1-\nu)}\frac{y(x^2-y^2)}{(x^2+y^2)^2} \tag{7.20}$$

$$F_y = -\frac{\mu b^2}{4\pi(1-\nu)}\frac{y(3x^2+y^2)}{(x^2+y^2)^2} + \frac{\sqrt{3}\mu b^2}{4\pi(1-\nu)}\frac{x(x^2-y^2)}{(x^2+y^2)^2} \tag{7.21}$$

Figure Fig. 7.14 and Fig. 7.15 show the direction of the force felt by the bulk dislocation. In the y-direction it is always attractive on approach and repulsive when leaving. This effect alone may be enough to generate the profile seen in Fig. 7.9, however we must also consider the image forces felt by the dislocation near the boundary.

Images forces are analogous to those encountered in electromagnetism. A dislocation will feel an image force due to the *reflection* of the dislocations own stress field in the CE. General calculations of image forces are intricate - but we can proceed via a simplified argument as we only require the direction of the force.

The approach is to determine the sign of the image dislocation. A dislocation and

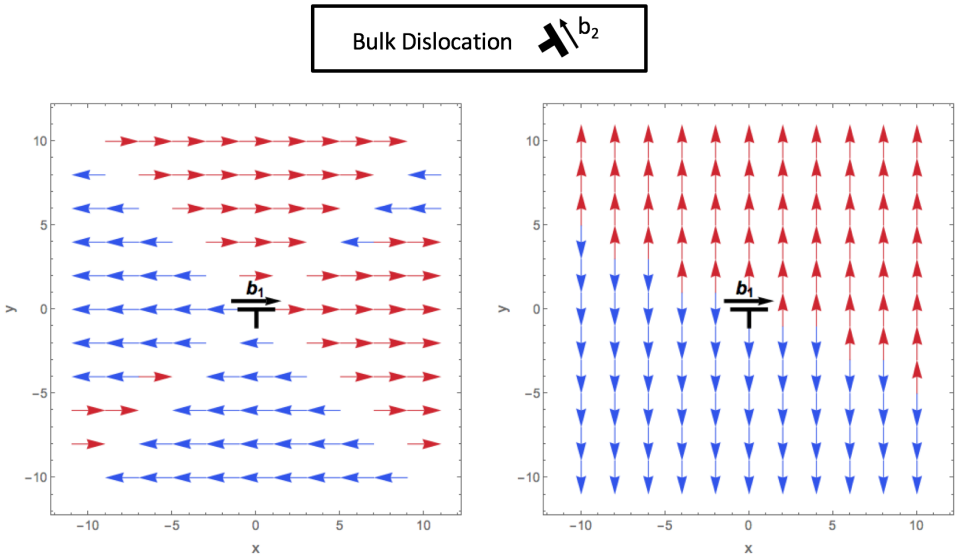

Figure 7.15: ***Direction* of Peach-Koehler force between GNDs and bulk dislocations (*leaving CE*)**. Force components felt by a dislocation $\mathbf{b}_2$ due to a dislocation $\mathbf{b}_1$ at the origin. (left) Force-field in $\hat{\mathbf{x}}$ direction. (right) Force-field in $\hat{\mathbf{y}}$ direction. Bulk dislocation feels a repulsive force in the vicinity of the channel edge. Channel is defined as $x > 0$.

its image with like sign will repel each other and with opposite sign, will attract. A relationship for the Burgers vector of an image dislocations for a screw dislocation can be derived in terms of the shear modulus on either side of the boundary. For a dislocation with a Burgers vector b, the image dislocation has

$$b^{'} = b\frac{c_{66}^{'} - c_{66}}{c_{66}^{'} + c_{66}}, \tag{7.22}$$

where c_{66} is the elastic modulus of the medium containing b and $c_{66}^{'}$ is the elastic modulus of the medium containing the image dislocation, $b^{'}$. For our case where the vortices are pinned in the channel walls this gives $c_{66}^{'} \to \infty$, resulting in $b^{'} = b$. The pinned boundary acts to resist the approach of the dislocation, through stiffening of the vortex matter in the region near the CE. This relationship is not straight forward to derive for edge dislocations, but the general result holds. If $c_{66}^{'} > c_{66}$ we will have a repulsive boundary due to the image forces.

7.7 Approaching the Continuum: The Role of the Channel Edge

We asserted above that the non-constant velocity of the bulk dislocations was as a result of image forces originating from the channel edge. There is a definitive simulation test of this, and that is to wrap the 2D channel onto the surface of a cylinder, effectively periodic boundary conditions in the y-direction. We should note that this is an unlikely physical scenario for a superconducting system - but that systems of this type are currently being investigated for understanding biological cell growth via a dislocation mechanism[1].

We maintain the same vortex-vortex force. We would except the GNDs to disappear, which they do, since there are no stresses created at CE for the GNDs to relax and there is no mis-match between lattice parameters in this region. *What has changed?* As we see from Fig. 7.9 the striking difference between the bulk dislocation profile in the channel and on the cylinder. The dislocations now proceed on a linear trajectory at constant speed. Returning to the channel system, the effect of the CE can clearly be seen in Fig. 7.16, which shows that as we increase channel width the non-linearity of the dislocation trajectories are isolated near the CE, indicating that the effect is due to a localised boundary mechanism.

We now turn back to the Fig. 7.3. In this figure we see the velocity, $v(x)$ along the channel/cylinder as calculated from binned averages in the simulations, a continuum calculation and a numerical calculation based on resolving just the nearest neighbour forces. It is clear that the results for the channel deviate from the continuum result, but that as channel width is increased and then the CE is removed, the profile approaches the continuum solution. For reference, the numerical calculation using just nearest-neighbours is approximately half the continuum $v(x)$ which strongly suggests the asymmetry in local vortex lattice is larger above a_0 and that this asymmetry is contributing to the overall velocity of the vortices.

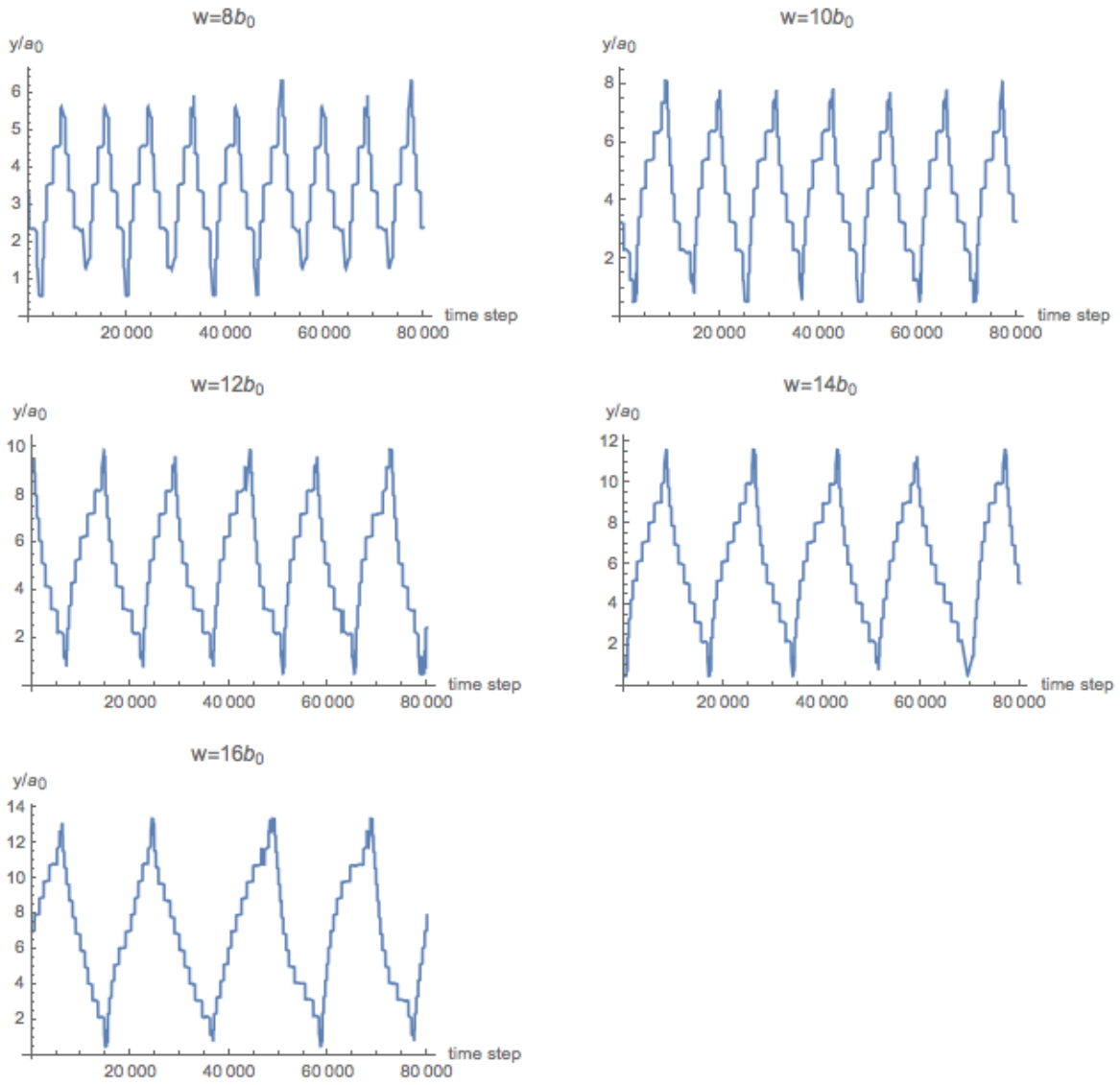

Figure 7.16: As channel width increases we can see a linear profile in the dislocation movement across the channel, with a small non-linear region near the boundary. The steps in the profile are due to the dislocations being confined to the rows of the moving vortex matter.

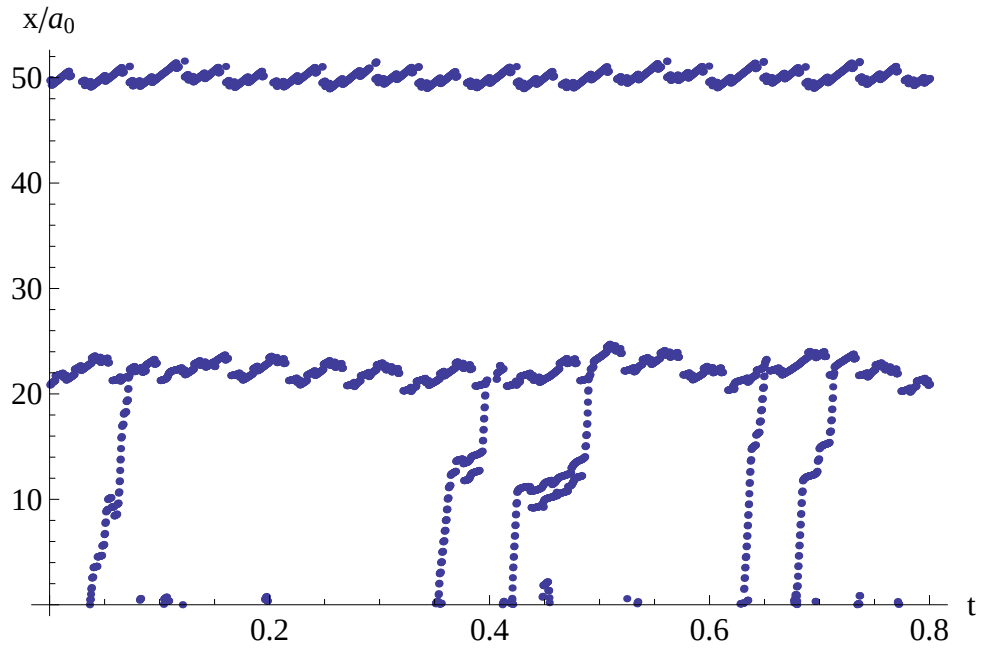

Figure 7.17: Shown are all dislocations that are active in the channel apart from the GNDs. The trajectory in the x-direction is shown. The five dislocations (bottom third of the figure) are due to defects generated by the source. The line at $22a_0$ corresponds to the first bulk dislocation, and it is clearly acting as a grain boundary. Note how "clean" the system is further along the channel.

7.8 Dislocations as a Noise Removal Mechanism

It is inevitable that disorder from the reservoir will enter the channel. What is remarkable is that the noise does not persist past the first dislocation, Fig. 7.17. Resulting in 'clean' crystal structure for the remainder of the channel. The periodicity of the first dislocation is perturbed by the noise from the reservoir, and results in the noise being absorbed. We are able to exploit this phenomenon to produce cleaner data for the remainder of the channel. This "cleaning" of the lattice is of potential interest for real mechanical materials, and is the subject of discussions with experts in the School of Metallurgy and Materials. [126].

Chapter 8

CIRCULAR GRAIN BOUNDARIES IN THE VORTEX LATTICE

The formation and stability of "bubbles" are the focus of recent research in a broad range of physical systems. These are the result of inclusion of a mis-orientated region of lattice within a bigger two dimensional system. This scenario can be arrived at artificially, via, for instance topological tweezers, in a colloidal system, as in the recent paper of Irvine *et al.* [24]. Importantly for our work, they show that they can enable the bubble to move via a commensurate potential placed on one side of the grain boundary. Analysis techniques have focussed on energetic considerations. In particular they show that dislocation motion involved in the rotation of grain boundaries is not reversible. Bubble-like structures can also exist as a result of non-flat geometries, a major area of research in studying the stability and growth of biological cells. The "bubbles" are sometimes described as "grain boundary scars". That is the boundary separating the two mis-orientated phases is separated by a string of dislocations as per a grain boundary - but is curved in order to contain the central region, Fig. 8.1.

The initial selection of results presented here are an indicator of the rich phenomena that exist in the wider system. The potential parameter space to explore is vast, with extensive potential for further study. Discussions with Basoalto [126] indicate that this may be fruitful in understanding dislocation mechanisms within genuine material, in particular titanium.

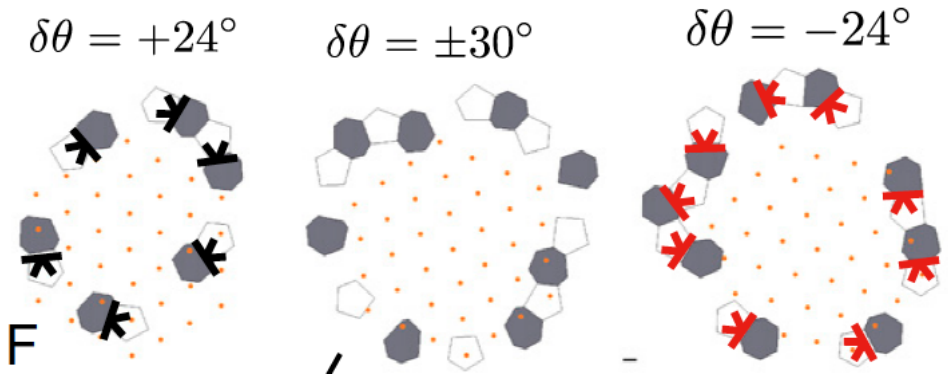

Figure 8.1: Circular grain boundaries consisting of dislocations. Figure from Ref[24].

We have chosen to focus on a system of width $20b_0$ with a fixed field difference of $0.46B_0$. The system has then been observed over 1 000 000 time steps, after the initial transient phase. In this range it is found that the average lattice parameter profile along the length of the channel is well defined over the timescales of the simulation.

8.1 Reservoir Geometry

The particular vortex source described and used in Chapter 7 was intended for investigation into commensurability effects in the channel. The requirement was to minimise the number of defects arising from the source by choosing a geometry aligned with the channel. For the study of grain boundary scars we propose a new geometry that produces vortices in the reservoir with rows tilted at $\pi/6$ to the normal orientation of the rows in the channel and CE vortices. This reservoir geometry is described as the *wedge* geometry, Fig. 8.2.

The walls of the wedge bath are cut at an angle of $\pm\pi/6$ and the lattice vectors for the CE particles surrounding the bath are also tilted. This system can be etched in a aNb_3Ge/Nb bilayer.

A possible physical realisation of the tilted geometry can be found in the work of Plourde *et al.*[25] where thin amorphous MoGe superconductors have been etched with mesoscopic octagonal surface trenches and imaged with SSM, Fig. 8.3. In this system, no

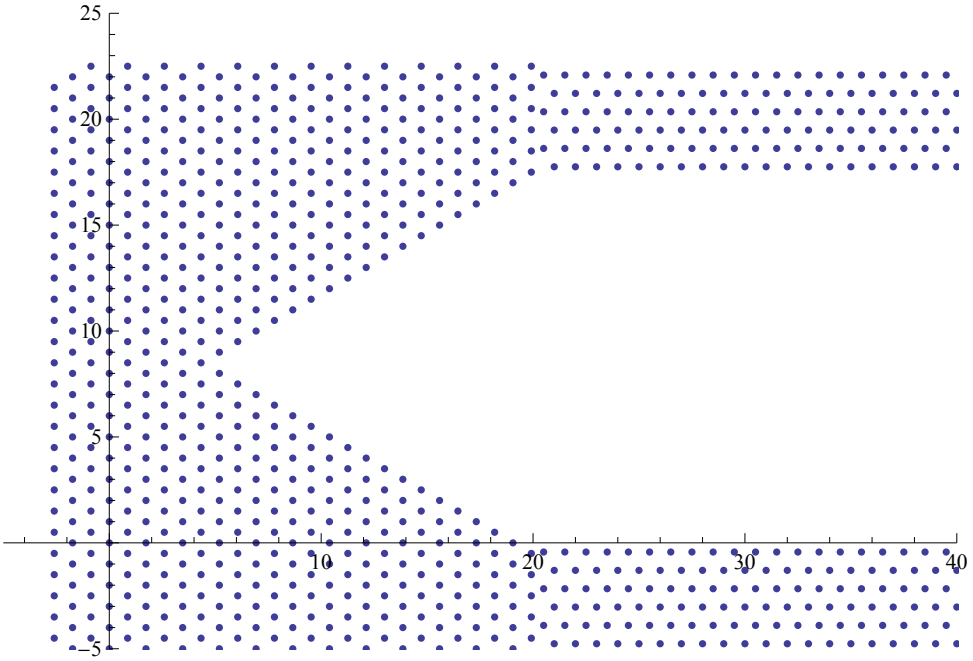

Figure 8.2: Bath with wedge geometry defined by channel edges at $\pm\pi/6$.

drive is applied to the vortices but we can see that vortices aligning themselves with the edge of the channel creating an arrangement of vortices that mimic the CE construction of the wedge bath.

8.2 Production of Circular Grain Boundary 'Bubbles'

Unlike with the bulk dislocation mechanism, described in Chapter 7, the flow in the wider channel does not demonstrate peridocity. Instead, the constructed reservoir leads to a mis-orientated lattice entering the channel intermittently. Observations show that the grain boundary bubbles exist, travel, dissolve, and then reappear. Inspection of the average lattice parameter along the length of the channel, indicates that the bubble does not differ in density compared to systems where it is not present, Fig. 8.4.

In Irvine's work[24] the bubble is created by slowly twisting the trapped section of lattice and monitoring the dislocation creation - with a maxima expected, and observed at

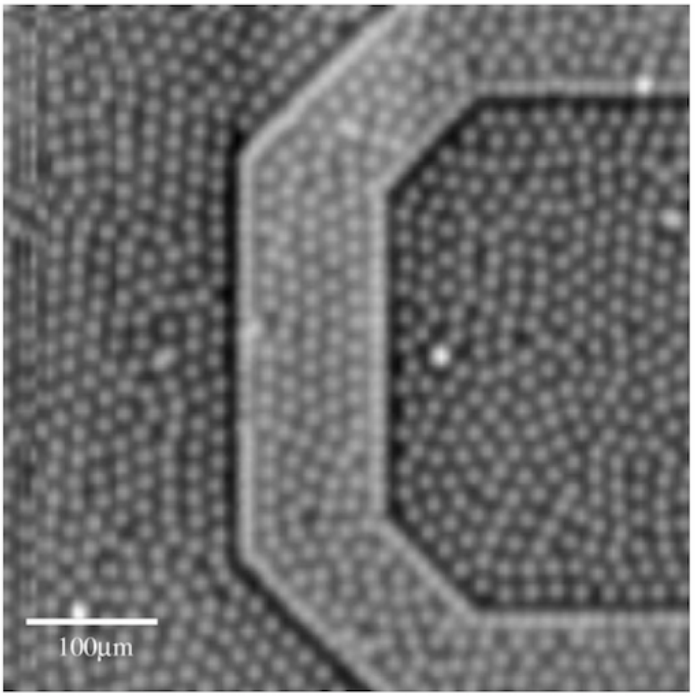

Figure 8.3: 60 nm deep trench in 200nm thick aMoGe. The vortices align with the edges of the trench. Figure from Ref[25].

$\pi/6$. However, continuing to $\pi/3$, where the lattice is now perfectly orientated, there are residual dislocations, which are slow to relax on the timescales that the system is observed on. In the density driven channel system we do not tune the angle of the region inside the bubble - hence we need to measure this once a bubble is isolated[1] with a simulation.

Sample results are shown in Figs. 8.5, 8.6 and 8.8 - we observe that, for bubbles to travel along the channel the bubble lattice, is orientated at $\approx \pi/9$. Shorter lived bubbles also exist, and they are characterised by $\pi/36$, corresponding to a low-angle grain boundary. We will concentrate on the longer-lived high angle grain boundary bubbles(HAB).

Visual inspection of the high-angle grain boundary bubbles (HAB) shows that in comparison to the work of Irvine, the bubbles are elongated along the channel, with the overall "size" changing as the HAB moves down the channel and eventually dissipates. What should we measure to determine the "size"? We currently track,

[1]The routine to determine the bubble relies upon techniques from image processing, and is discussed in Appendix K.

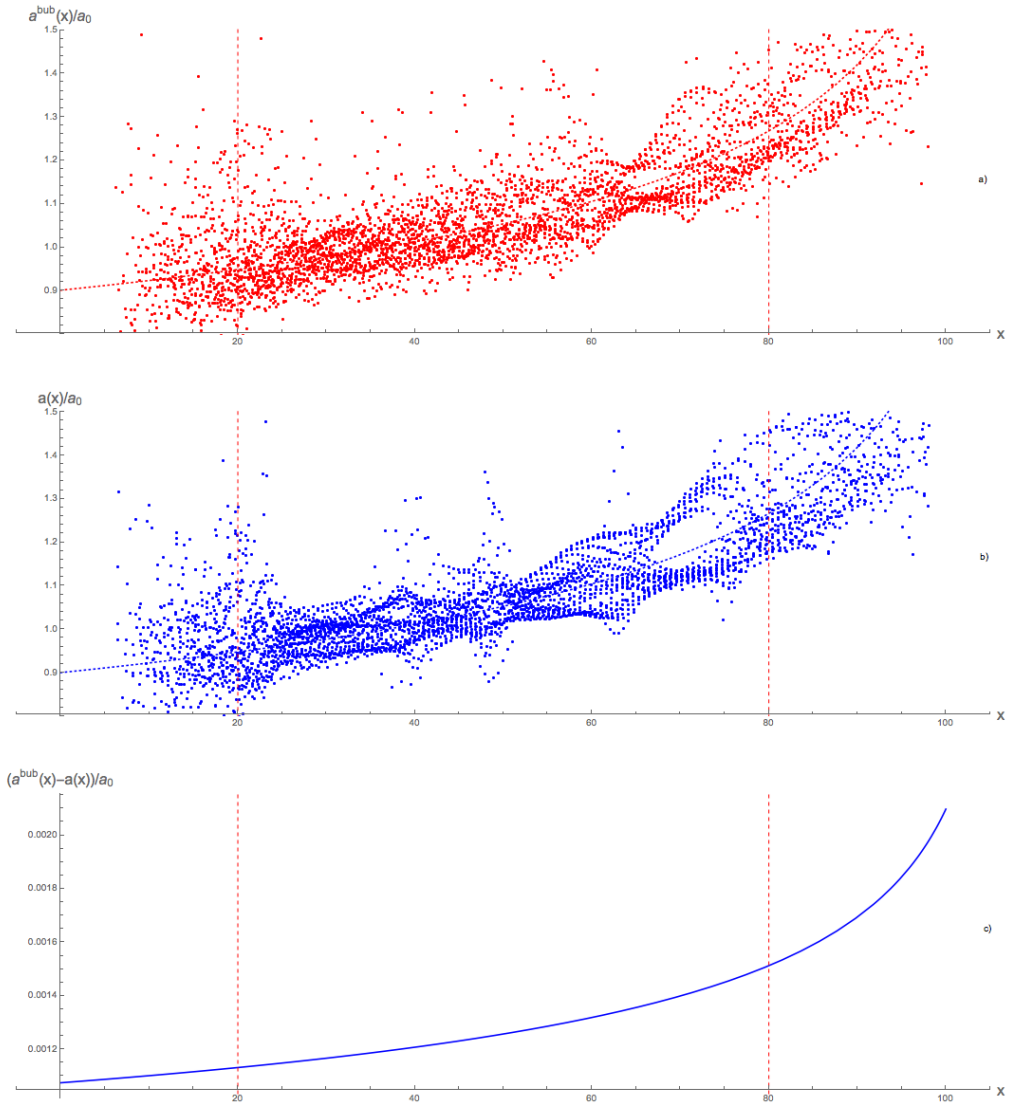

Figure 8.4: Plot of length nearest neighbour lines between vortices **a** with a HAB (seeFig. 8.6), **b** free from bubbles. **c** Shows the difference between the two $(a^{\mathrm{bub}}(x) - a(x))/a_0$.

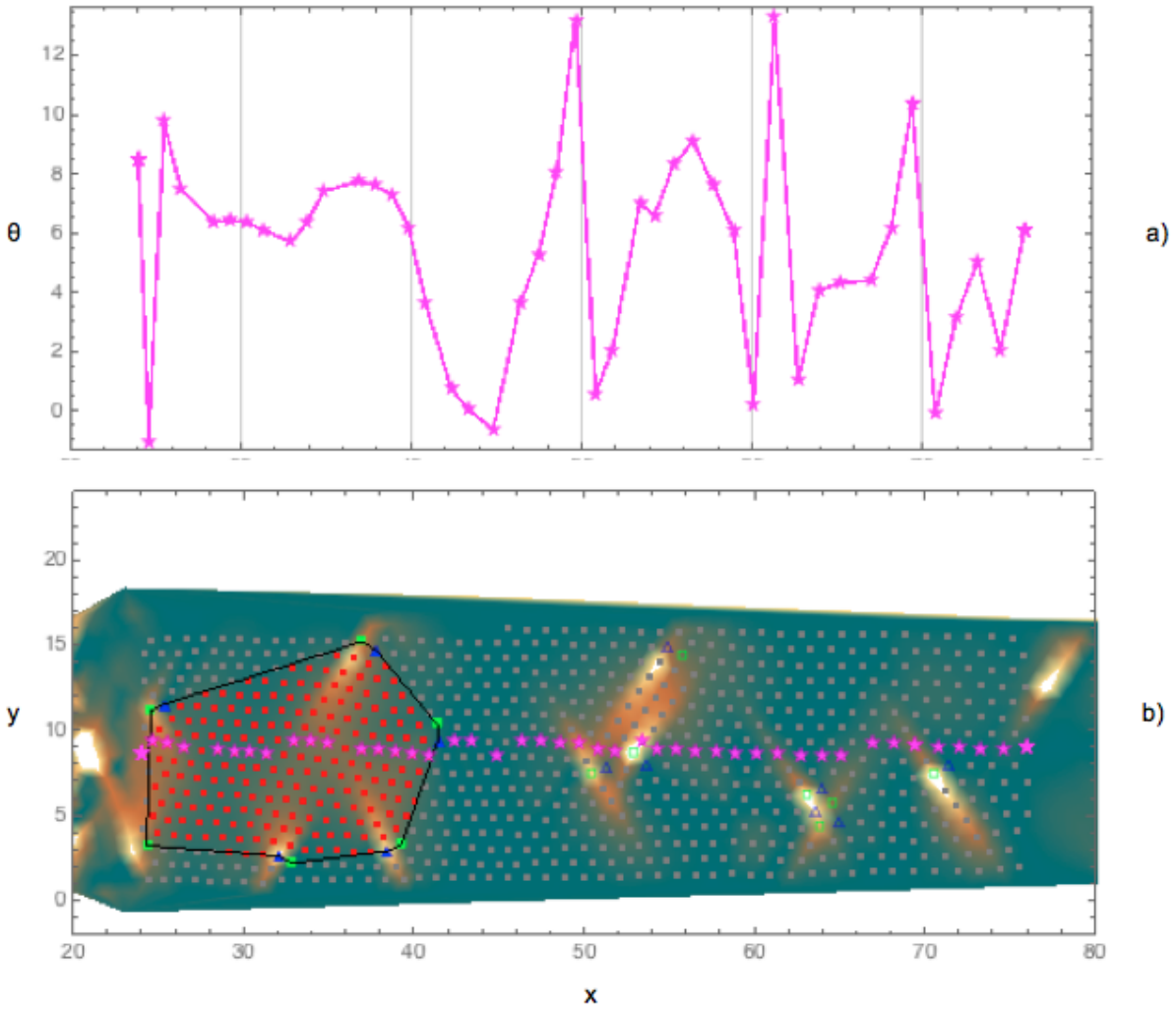

Figure 8.5: **a** Shows the average angle of rotation in the lattice parameter to the horizontal. The low angle bubble is rotated at an angle of $\sim 6^{\text{deg}}$. **b** Shows the dislocations belonging the bubble as a connected path. The population of dislocations in the grain boundary is low due to the small rotation angle. Here dislocations are distinct and separated by $D \gg b$(where b is the magnitude of the Burgers vector). Colour is used to indicate angle of rotation of the lattice parameters away from the CE orientation.

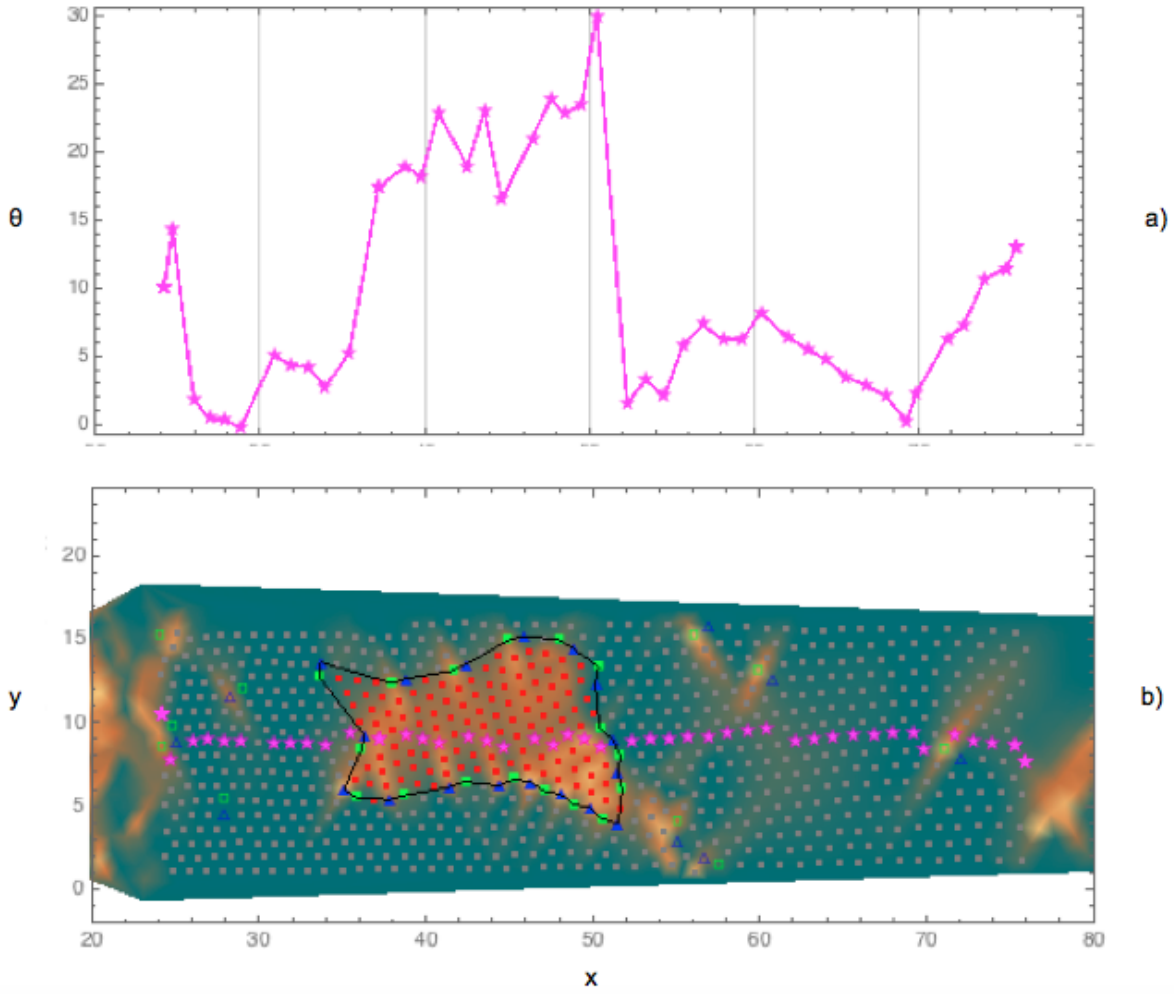

Figure 8.6: **a** Shows the average angle of rotation in the lattice parameter to the horizontal. The high angle bubble is rotated at an angle of $\sim 22^{\text{deg}}$. **b** Shows the dislocations belonging the the bubble as a connected path. The population of dislocations in the grain boundary is high due to the high rotation angle. In this regime dislocation separation $D < b$(where b is the magnitude of the Burgers vector). Colour is used to indicate angle of rotation of the lattice parameters away from the CE orientation.

1. The number of vortices in the HAB, n_v^{aHAB}
2. The number of vortices on the boundary n_v^{pHAB}
3. The number of dislocations on the boundary

If we consider the number of dislocations on the boundary, this indicates that there is a roughness to the boundary - which has been identified as an interesting phenomena, but has not yet been fully analysed.

The results in Chapter 7 were remarkable for their periodicity, and controlled stable population of bulk dislocations. What has happened to these dislocations in this new system? The reservoirs are set such that for our previous mechanism, we would expect three bulk dislocations for the required row drops. With the bubbles present, "rows" will require a more robust count, which can be performed at selected points along the channel. We choose to look for the shortest trajectory that enables one to cross the channel, starting from a given x-position. Sample results can be seen in Figs. 8.7 and 8.8, for the same channel at time steps with and without the bubble present.

8.3 Dislocation and 'Bubble' Interaction

Empirical evidence indicates that the HAB alters the x-positions at which the bulk dislocations would choose to be localised, and in fact it is possible that the bulk dislocations choose to travel along the grain boundary. The persistence and details of this effect, is currently being quantified. Fig. 8.9 shows a sequence of images as a bubble passes a bulk dislocation glide plane. As the bubble passes the bulk dislocation located at x_d the dislocation becomes part of the bubble grain boundary. This configuration lowers stress by confining dislocations to grain boundaries. The addition of the bulk dislocation increases the total Burgers vector of the bubble by the Burgers vector of the bulk dislocation, $\mathbf{b}$. Since this is a high angle grain boundary the location of the bulk dislocation is no longer distinct and cannot easily be found. Interestingly the dislocations emerge from the trailing edge of the bubble $\sim 10a_0$ before its initial glide plane (i.e. smaller x).

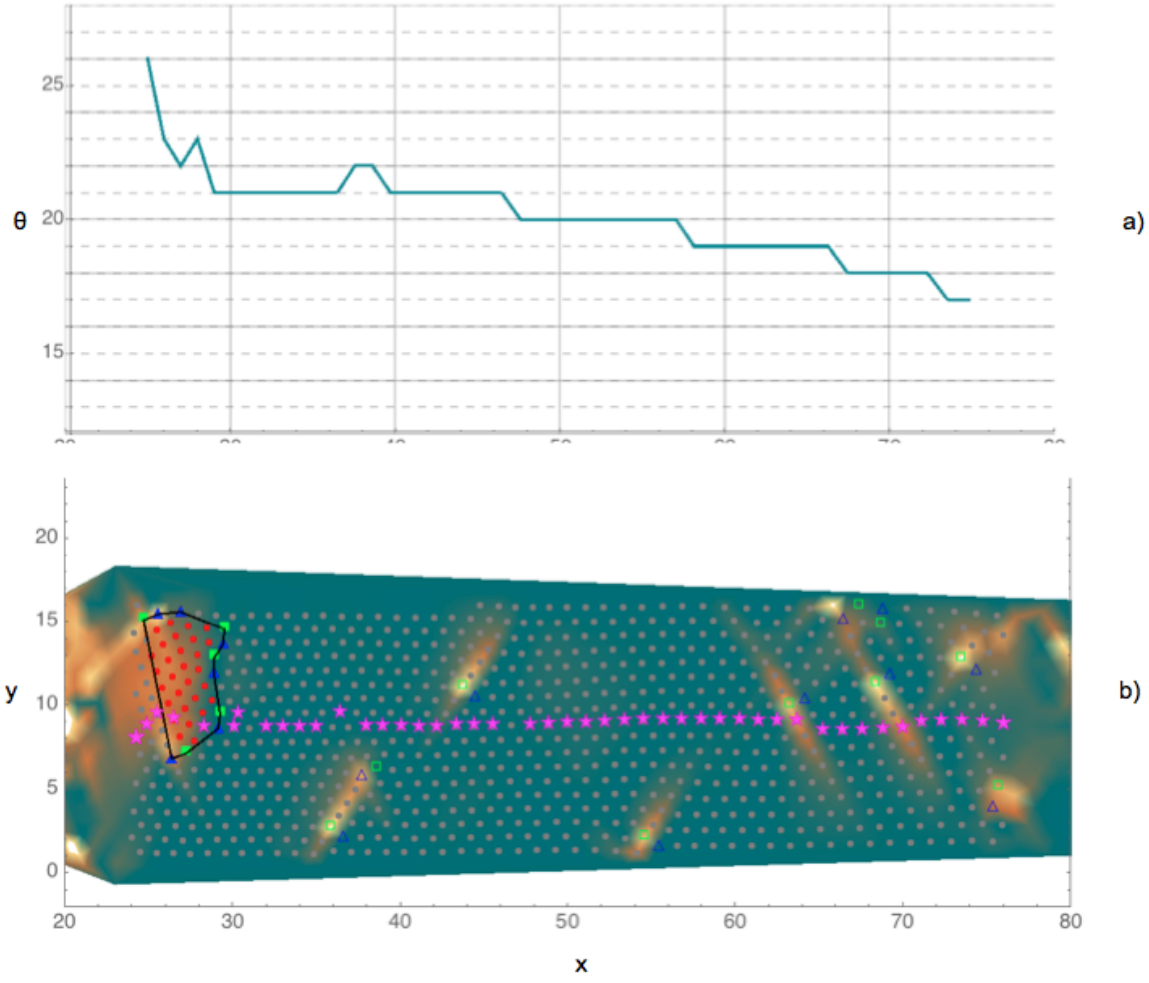

Figure 8.7: **a** Shows the row count in the channel. The channel transitions from 21 down to 18 rows mediated by oscillating dislocations. **b** Shows the locations of the dislocations in the channel. Colour is used to indicate angle of rotation of the lattice parameters away from the CE orientation.

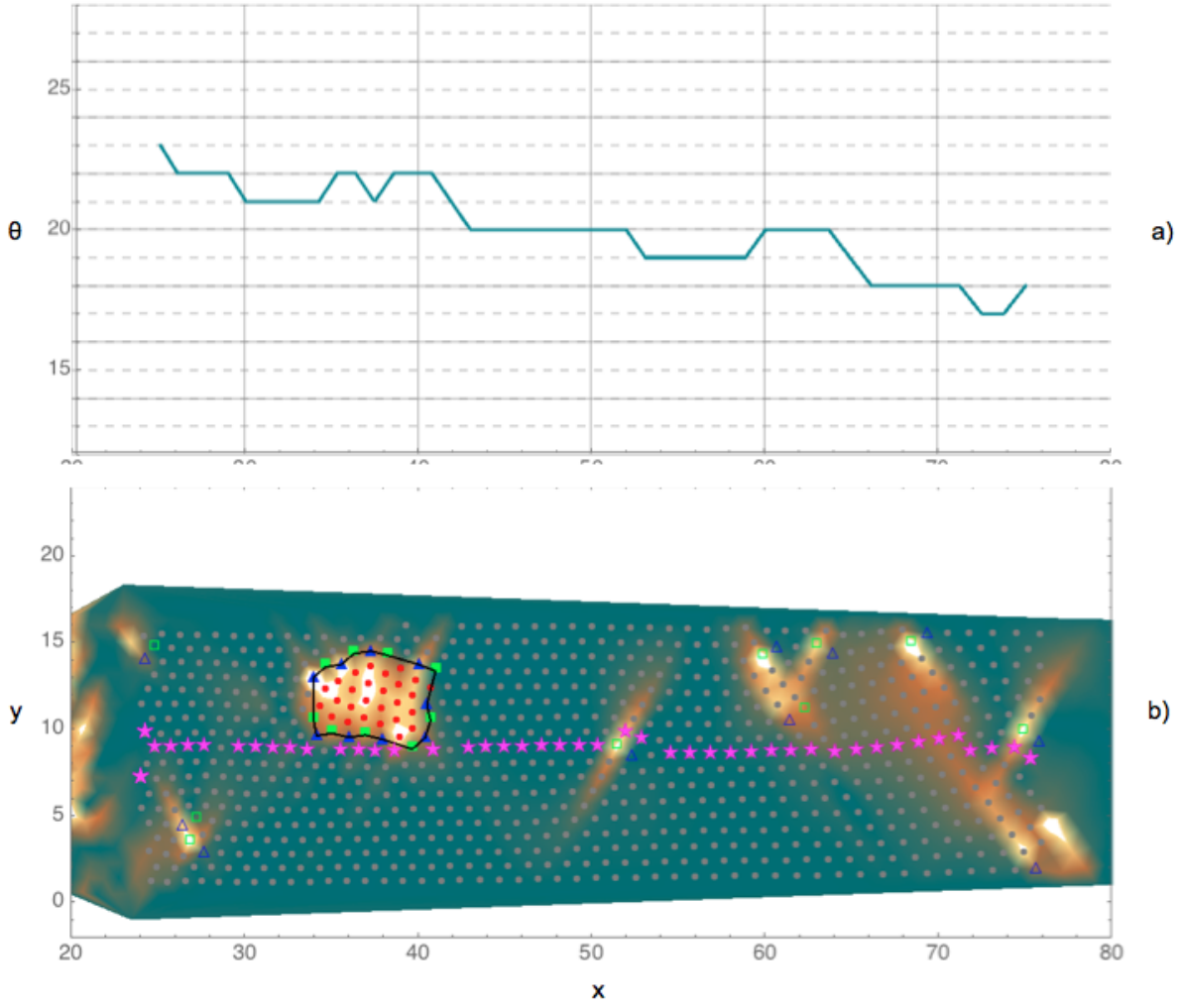

Figure 8.8: **a** Shows the row count in the channel. The channel transitions from 21 down to 18 rows mediated by oscillating dislocations. The row drop across the bubble is 0. **b** Shows the locations of the oscillating dislocations in the channel and a HAB. Colour is used to indicate angle of rotation of the lattice parameters away from the CE orientation.

Indicating the density is in a transient regime after the bubble passes. Local relaxation takes approximately 3 000 time steps, at which time the oscillating dislocation returns to its original position in the channel. The dislocation then remains in its steady state position until another bubble passes, then the process repeats.

8.4 Twin Grain Boundaries

The use of artificial bubbles created by a rotation similar to Irvine's work, can also be used to demonstrate the relationship between twin grain boundaries in the cylindrical geometry and circular grain boundaries in the channel geometry. Fig. 8.10 shows snap shots taken from a channel simulation containing an artificial bubble. The geometry is then modified to wrap the channel periodically in the $y-$direction. Random thermal fluctuations of the grain boundary causes the bubble to notice it is wrapped on the cylindrical geometry and as such is able to find a new configurational state where the bubble joins up to itself in the $y-$direction. The structure is now a twin grain boundary. The result of this procedure is a steady state twin grain boundary that flows down the channel (without collapsing) at the same speed as the underlying vortices.

If instead we start from a twin grain boundary in a cylindrical geometry and then unwrap and place in the channel bounded by pinned vortices, Fig. 8.11, immediately a layer of dislocations appear along the CE creating a "square" bubble. This configuration is unstable and a boundary layer quickly opens up between the bubble and the CE as the bubble transitions into a more circular shape.

These preliminary results indicate that novel phenomena exist in this geometry - and are a potential future research area.

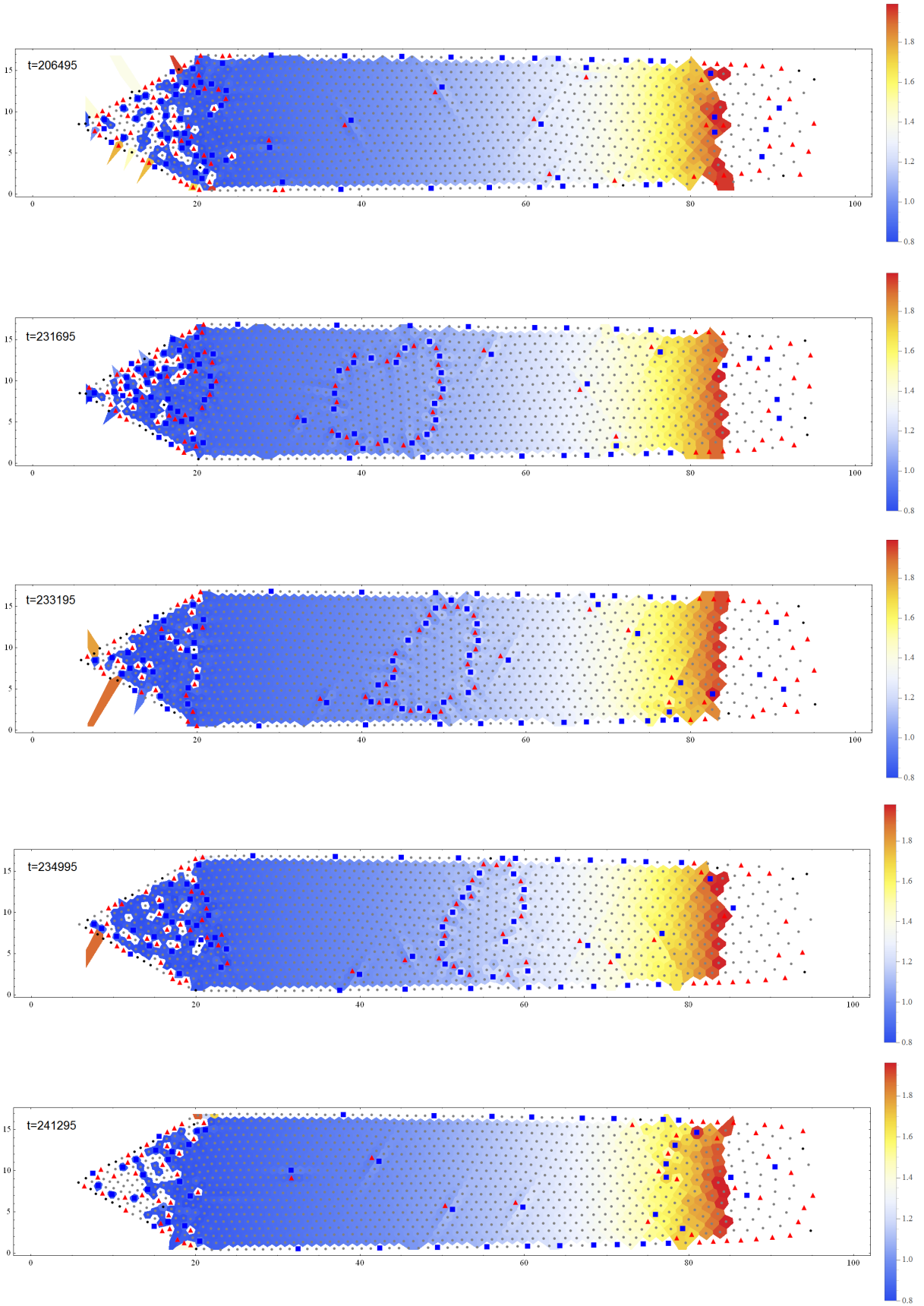

Figure 8.9: Sequence of frames from a simulation with a wedge bath geometry. Initially the channel contains only ODs, a bubble then passes through changing the position of the ODs. The ODs return to their usual location after the bubble has passed.

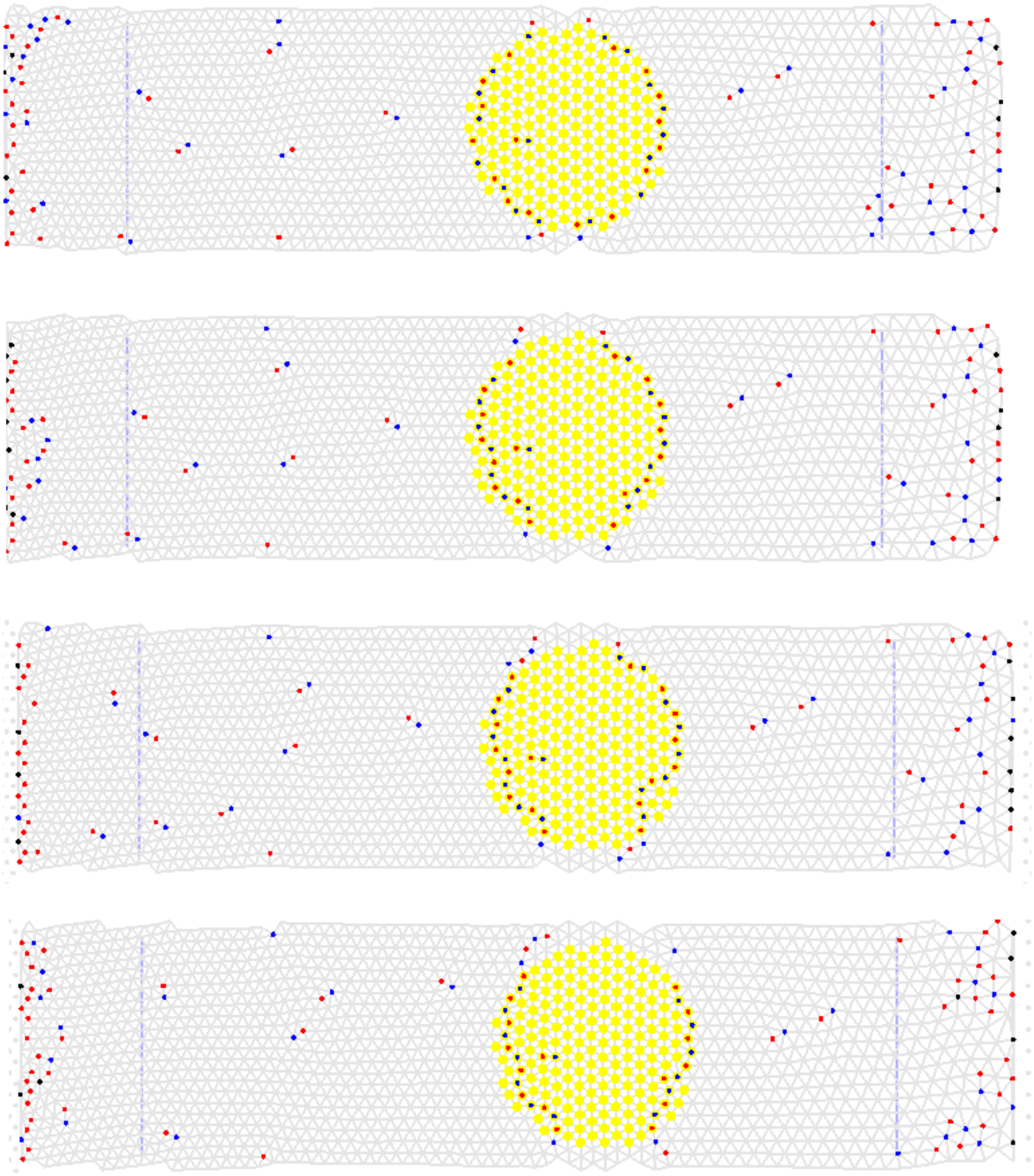

Figure 8.10: A channel containing a bubble is wrapped periodically in the $y-$direction. The bubble is seen to transition into a stable twin grain boundary that flows down the cylinder and remains steady for the entire length of the channel.

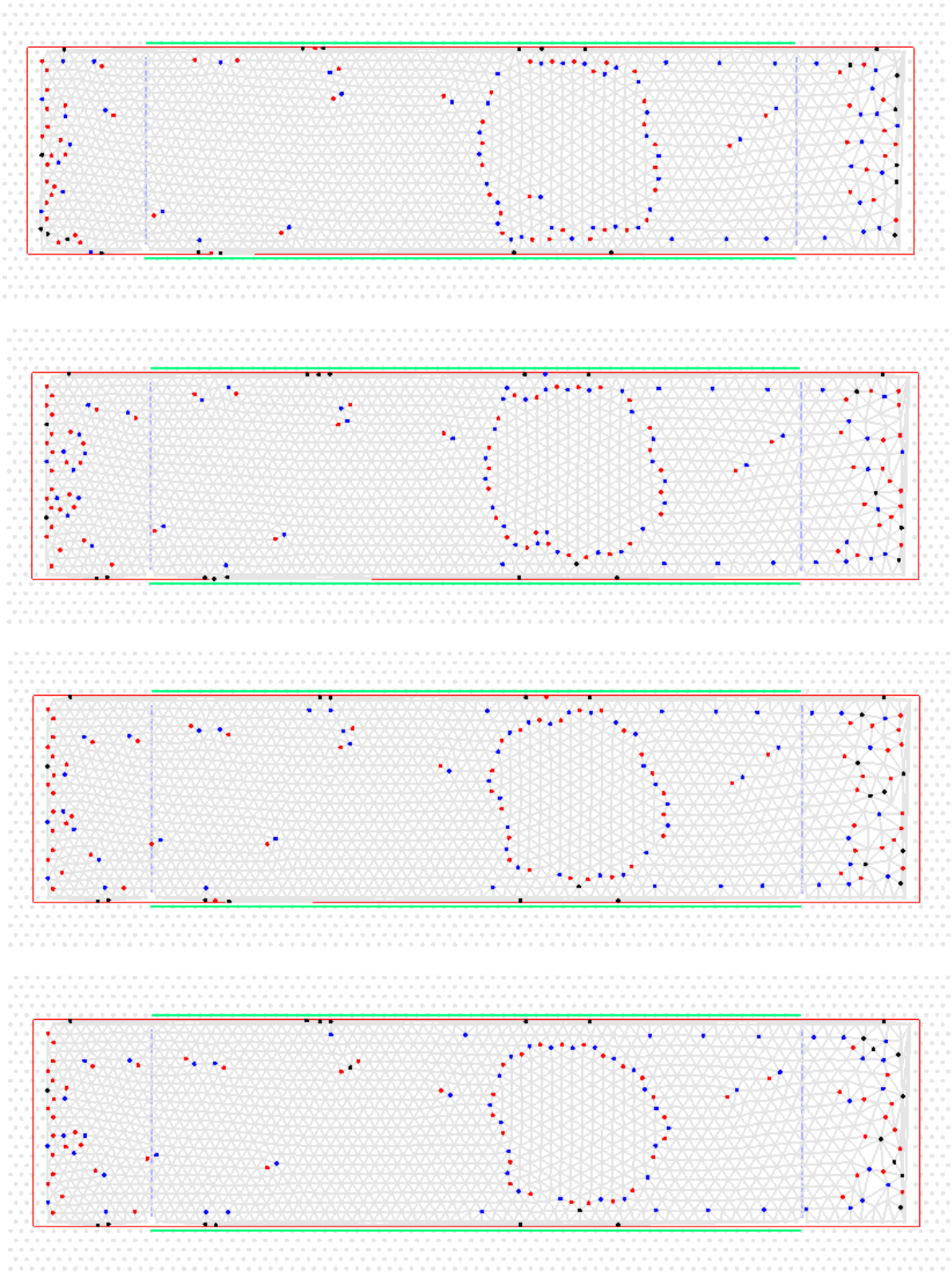

Figure 8.11: A stable twin grain boundary from a cylindrical simulation is placed into a channel geometry with pinned vortices defining the CE. The twin grain boundary transitions into a square bubble then into the standard circular grain with slowly collapses as it flows down the channel.

Chapter 9

CONCLUSIONS

In conclusion, we have reported a novel set of results by undertaking not previously considered investigations into the structure and rheology of vortex matter in thin channel superconductors. Our key results are that

- We show a breakdown of wall-slip in sheared wall experiments in the vortex liquid phase.
- We find ordering of the liquid phase above T_m^{bulk} in regions near the channel edges in static and sheared channel simulations.
- We present a novel field gradient applied to a thin channel geometry that allows the incommensurate vortex matter to remain commensurate along the entire length of the channel, minimising the presence of random defects, via two distinct populations of dislocations.
- We find a defect sink mechanism that cleans the channel of extraneous defects leaving a mostly 6-fold coordinated plastic in the remainder of the channel. This mechanism has potential applications in the aerospace industry.
- Finally we demonstrate a novel vortex reservoir that enable the continuous production of circular grain boundary bubbles.

In the liquid phase we have shown that the continuum solution to Couette flow does not fully capture the rheology of the vortex lattice even in channel widths $w \gg a_0$.

The origin of this is likely to be either the drag forces that prevent the wall imparting momentum to the vortices at high shear rates or viscoelastic effects. From trajectory and structure factor measurements we have found that the boundary layer structure displays 6-fold symmetry above the melting temperature for the bulk T_m^{bulk}. This aspect requires further investigation, but may contribute to the wall slip seen at high shear rates. From oscillating wall simulations we have probed a non linear viscosity $\eta = \eta_0 + \eta_1 dv/dy$ and found no evidence of higher order terms, above η_0.

We have presented a novel vortex matter simulation where we imposed a magnetic field gradient through the use of a vortex source and sink. This system finds a non-equilibrium steady state where two distinct populations of dislocations are present in the system. First a population of *oscillating* dislocations are present in the channel, spaced out at distances that relax stresses along the channel. The longitudinal positions of these oscillating dislocations in the channel remains stable throughout the simulations. These dislocations travel via glide motion along the planes of the triangular vortex matter, tilted at $\pi/3$ to the horizontal. The second population of *geometrically necessary dislocations* are confined to the boundary between the moving vortex matter and the pinned channel edges. Their role is the relaxation of shear stress at boundary. The displacement profiles of the oscillating dislocations have been shown to be linear across the width of the channel except in upon approach to the channel edges. Here image forces provide the source of the non-linear trajectories. That this is a boundary effect was demonstrated through the use of simulations in a cylindrical geometry which removes the channel edges completely and wraps the channel onto the surface of the cylindrical system. In this geometry we show the oscillating dislocations proceed on a purely linear trajectory in the absence of the channel edges, proving that the non-linearity near the boundaries is indeed a boundary effect.

We have demonstrated the mechanism by which the vortex lattice remains commensurate with the channel width throughout the entire length of the channel, in spite of the lack of a commensurate relationship between the B-field and the channel width. It achieves this through the use of two populations of dislocations that relax density and

shear stresses along the channel. This surprising result is achieved through stretching of the lattice parameters parallel to the channel edge allowing a continuous decrease in density whilst retaining a fixed row width in sections of the channel. These effects minimise the density of dislocations in the channel and allow the system to remain almost perfectly 6-fold coordinate throughout the channel. Deviating from this only at the core of the small population of oscillating dislocation. This is perhaps striking given the change in density along the channel is around a factor of two.

We also demonstrated a *defect sink* mechanism. Where, through dislocation reactions this first oscillating dislocation 'collects' defects that arise from the source reservoir allowing the remainder of the channel to be free from extraneous defects. Conversations with Dr. Basoalto[126] suggest further investigation as to whether this mechanism could be deployed in real materials (e.g. titanium) to remove defects.

Finally, using the same field gradient system but changing the structure of the vortex reservoirs to a wedge geometry, we were able to produce circular grains of vortex matter tilted at $\sim \pi/6$ to the remainder of the vortices in the channel. The lattice parameters across these tilted grains also shows an asymmetry in the lattice parameters. Here the perpendicular lattice parameters remain fixed across the bubble, whilst stretch is taken up by the lattice parameters tilted at $\sim \pi/6$ to the channel edge.

In summary, we have shown that the superconducting vortex lattice is a versatile laboratory for investigation into dislocation dynamics, both for isolated dislocations and for the more complex dislocation arrangements as grain boundaries. The vortex liquid deserves further investigation but through the use of simulations we have demonstrated wall slip at the boundary for high shear rates, making this an interesting area for further study. Analogies with colloidal and biological systems are strong and further work would hope to replicate these results for both these scenarios.

Appendix A

SYMBOLS

Symbol	Description
a_0	Lattice parameter for triangular lattice, corresponding to B_0
$a^c(x)$	Lattice parameter from force balance calculation in channel geometry
$a^l(x)$	Vortex liquid average vortex separation in channel geometry
$a^p(x)$	Plastic phase lattice parameter in channel geometry
A_p	Amplitude of random pinning sites
$\mathbf{b}$	Burgers vector
b_0	Row spacing for a the triangular lattice with field B_0
$\tilde{b}$	B/B_{c2} Dimensionless penetrating field
B	Magnitude of magnetic induction or flux denisty
$\mathbf{B}$	Magnetic induction or flux density
B_0	Flux density of channel edge vortices $B_0 = 0.25T$
$\hat{\mathbf{B}}$	Unit vector in direction of B-field

Symbol	Description
c	Velocity of light
c_{11}	Compression (Bulk) modulus
c_{44}	Tilt modulus
c_{66}	Shear modulus
c_L	Lindemann parameter
c_{jklm}	Elastic modulus tensor from elastic theory
d_s	Thickness of superconductor
D_s	Spacing between dislocations in a symmetric low-angle grain boundary
e	Charge of the electron
E_f	Point defect formation energy
E_g	Energy required to break a Cooper pair
f_0	Scale of vortex-vortex force interactions $f_0 = 1$
f_{vv}	Magnitude of force between vortices
$\mathbf{F}_{vv}$	Force between vortices
$\mathbf{F}_L$	Lorentz force vector
$\mathbf{F}_p$	Random pinning sites force vector

h	Plank constant
$\mathbf{H}$	Magnetic field
H_c	Critical applied magnetic field for type I superconductor
H_{c1}	Lower applied critical field for type II superconductor
H_{c2}	Upper applied critical field for type II superconductor
j_c	Critical current for the onset of flux creep
j_t	Crystallisation current in flux pinning
$\mathbf{J}_s$	Supercurrent due to superconducting electrons
k_B	Boltzmann constant $k_B = 1$
K_n	Modified Bessel function of second kind
L_c	Longitudinal coherence length of the flux line
m_e	Mass of the electron
$\mathbf{M}$	Magnetisation
n_l	Number of planes ending in dislocations
n_p	Number of point defects
n_r	Number of rows of vortices in channel geometry

n_s	Number density of superconducting electrons
n_v	Number density of vortices
N_d	Number density of defects from Delaunay triangulation
$\mathcal{N}$	Normal distribution $\mathcal{N}(0,1)$
p	Probability of a particle receiving a thermal kick
r_{cut}^{p}	Polynomial potential cut-off range
r_{cut}	Bessel function potential cut-off range
R_p	Range of random pinning sites
s	Layer separation in HTSC
T_c	Critical transition temperature for a type I superconductor
T_m^{2D}	2D melting temperature of vortex lattice
T_{BKT}	BKT temperature of vortex lattice
T_m^{FDT}	Vortex lattice melting temperature from fluctuation dissipation theory
T_m^{bulk}	Melting temperature in channel from simulations
$\mathbf{u}$	Displacement in elastic theory
u, v, w	Components of displacement in elastic theory
$< u^2(T_m) >_{th}$	Thermal average of mean square displacements of vortex lattice from equilibrium positions
U_{vv}	Interaction energy of vortices
v_x, v_y, v_z	Velocity in x, y, z directions
v_{zig}	Velocity of oscillating dislocations in channel geometry

Symbol	Description
γ	Drag
γ	Shear strain
$\dot{\gamma}$	Shear rate
$\dot{\gamma}_c$	Critical shear rate for non-Newtonian viscoelasticity
δ	Boundary layer thickness
Δ	Time step size in simulations
Δu_d	Burgers vector distribution
ϵ_{ij}	Strain tensor from elastic theory
η	Dynamic Viscosity
κ	Ginzburg-Landau parameter
λ	London penetration depth
μ_0	Permeability of free space
ν	Collision rate in the Andersen thermostat
ν	Poisson ratio
ξ	Ginzburg-Landau Coherence length

Symbol	Description
$\hat{\boldsymbol{\xi}}$	Direction of dislocation line
ρ_n	Normal state resistivity
ρ	Density of vortices
$\rho(x)$	Denisty from force balance calculation in channel geometry
ρ_g	Density of GNDs in channel geometry
σ_{ij}	Stress tensor from elastic theory
τ	Average time between thermal kicks
τ	Shear stress
τ_{fkl}	Frenkel's shear stress
τ_{mac}	Mackenzie's shear stress
τ_{pn}	Peierls-Nabarro stress
Φ_0	Flux quantum
ψ	Order parameter for superconducting electron wavefunction
Ψ_T	Translational order parameter
Ψ_H	Hexatic order parameter

Appendix B

LONDON EQUATIONS

A perfect conductor (ie n conductors moving without collision)

$$\mathbf{J} = -ne^*\mathbf{v} \tag{B.1}$$

In the presence of an electric field, Newton's second law gives

$$m^*\dot{\mathbf{v}} = -e^*\mathbf{E} \rightarrow \dot{\mathbf{J}} = \frac{ne^2}{m^*}\mathbf{E} \tag{B.2}$$

Using the Maxwell equation

$$\nabla \times \mathbf{E} = -\dot{\mathbf{B}} \tag{B.3}$$

and the above equation for $\mathbf{J}$ we get

$$\nabla \times \dot{\mathbf{J}}_s = -\frac{n_s e^{*2}}{m^*}\dot{\mathbf{B}} \tag{B.4}$$

And using Maxwell's

$$\nabla \times \mathbf{B} = \mu_0 \mathbf{J} \tag{B.5}$$

we now have three equations

$$\dot{\mathbf{J}}_s = \frac{n_s e^{*2}}{m^*}\mathbf{E} \qquad \nabla \times \dot{\mathbf{J}}_s = -\frac{n_s e^{*2}}{m^*}\dot{\mathbf{B}} \qquad \nabla \times \mathbf{B} = \mu_0 \mathbf{J}_s \tag{B.6}$$

We can then substitute the time derivative of equation (3) into (2) to give

$$\nabla \times \nabla \times \dot{\mathbf{B}} = -\frac{n_s \mu_0 e^{*2}}{m^*}\dot{\mathbf{B}} \tag{B.7}$$

Using a vector identity we have

$$\nabla(\nabla \cdot \dot{\mathbf{B}}) - \nabla^2 \dot{\mathbf{B}} = -\frac{n_s \mu_0 e^{*2}}{m^*}\dot{\mathbf{B}} \tag{B.8}$$

Which gives

$$\nabla^2 \dot{\mathbf{B}} = \frac{1}{\lambda^2}\dot{\mathbf{B}} \tag{B.9}$$

where

$$\frac{1}{\lambda^2} = \frac{n_s \mu_0 e^{*2}}{m^*} \tag{B.10}$$

This does not predicted field expulsion. It predicts field lock in. To get an equation that predicts the correct behaviour we remove the time dependence from Eq. (B.6) to give

$$\nabla \times \mathbf{J}_s = -\frac{n_s e^{*2}}{m^*}\mathbf{B} \tag{B.11}$$

following the same steps through again we find

$$\nabla^2 \mathbf{B} = \frac{1}{\lambda^2}\mathbf{B} \tag{B.12}$$

where

$$\frac{1}{\lambda^2} = \frac{n_s \mu_0 e^{*2}}{m^*} \tag{B.13}$$

This result originally found by the London brothers gives a phenomenological description of the Meissner effect. The London Equations are therefore

$$\dot{\mathbf{J}}_s = \frac{n_s e^{*2}}{m^*}\mathbf{E} \qquad\qquad \nabla \times \mathbf{J}_s = -\frac{n_s e^{*2}}{m^*}\mathbf{B} \tag{B.14}$$

Appendix C

FLUX QUANTISATION FOR G-L THEORY

London introduced the concept of the fluxoid Φ' associated with each hole or normal region passing through a superconductor.[7]

His definition was

$$\Phi' = \Phi + \left(\frac{4\pi}{c}\right) \oint \lambda^2 \mathbf{J}_s . d\mathbf{s} = \Phi + \left(\frac{m^* c}{e^*}\right) \oint \mathbf{v}_s . d\mathbf{s} \tag{C.1}$$

where $\Phi = \int \mathbf{h} . d\mathbf{S} = \oint \mathbf{A} . d\mathbf{s}$ is the ordinary magnetic flux through the integration circuit. From Eq. (C.1) we can see that any circuit not containing a hole will result in $\Phi' = 0$.

We can quantise this equation by applying the the Bohr-Sommerfeld quantisation condition[7]

$$\oint \mathbf{p} . d\mathbf{q} = nh \tag{C.2}$$

$$\Phi' = \frac{c}{e^*} \oint \left(m^* \mathbf{v}_s + \frac{e^* \mathbf{A}}{c} \right) \cdot d\mathbf{s} = \frac{c}{e^*} \oint \mathbf{p} . \mathrm{d}\mathbf{s} = nh \frac{c}{e^*} = n\Phi_0 \tag{C.3}$$

London was not aware of the Cooper pairs so they believed $e^* = e$ and $m^* = m_e$. However the actual values are $e^* = 2e$ and $m^* = 2m_e$.

$$\Phi_0 = \frac{h}{2e} = 2.067 \times 10^{-15} Wb \tag{C.4}$$

Note: $Wb = \frac{KgM^2}{Cs}$

Appendix D

B-FIELD SURROUNDING A VORTEX FROM THE LONDON EQUATIONS

The superconducting flux line vortex is modelled in two parts. Outside the core of size ξ, the field is represented by the Landau Equation

$$\mu_0 \lambda^2 \nabla \times \mathbf{J}_s + \mathbf{B} = 0 \tag{D.1}$$

Including the core, which carries a flux quantum of $\Phi_0 = \frac{h}{2e}$ as a delta function, gives

$$\mu_0 \lambda^2 \nabla \times \mathbf{J}_s + \mathbf{B} = \Phi_0 \delta^2(\mathbf{r}) \hat{\mathbf{k}} \tag{D.2}$$

Following the London brothers approach for relating the magnetic field to current

$$\nabla \times \mathbf{B} = \mu_0 \mathbf{J}_s \Rightarrow \mathbf{J}_s = \frac{\nabla \times \mathbf{B}}{\mu_0} \tag{D.3}$$

$$\Rightarrow \lambda^2 \nabla \times \nabla \times \mathbf{B} + \mathbf{B} = \Phi_0 \delta^2(\mathbf{r}) \hat{\mathbf{k}} \tag{D.4}$$

Now using the identity

$$\nabla \times \nabla \times \mathbf{B} = \nabla(\nabla \cdot \mathbf{B}) - \nabla^2 \mathbf{B} = -\nabla^2 \mathbf{B} \tag{D.5}$$

and since $\nabla \cdot \mathbf{B} = 0$ (i.e. Maxwell's Equation for no monopoles.)
beginequation0.5cm] Eq. (D.4) now becomes

$$\nabla^2 \mathbf{B} - \frac{1}{\lambda^2}\mathbf{B} = -\frac{\Phi_0}{\lambda^2}\delta^2(\mathbf{r})\hat{\mathbf{k}} \tag{D.6}$$

A vortex tube is assumed to be cylindrically symmetric so, $\mathbf{B} = B(\mathbf{r})\hat{\mathbf{k}}$ and writing ∇^2 in cylindrical polars gives

$$\frac{\hat{\mathbf{k}}}{r}\left(\frac{d}{dr}r\frac{d}{dr}B(r)\right) - \frac{B(r)}{\lambda^2}\hat{\mathbf{k}} = -\frac{\Phi_0}{\lambda^2}\delta^2(r)\hat{\mathbf{k}} \tag{D.7}$$

Away from the core, $r > 0$, the $\hat{\mathbf{k}}$ component is

$$\frac{1}{r}\frac{d}{dr}r\frac{dB(r)}{dr} - \frac{B(r)}{\lambda^2} = 0 \tag{D.8}$$

$$\Rightarrow \frac{d^2B(r)}{dr^2} + \frac{1}{r}\frac{dB(r)}{dr} - \left(\frac{1}{\lambda^2}\right)B(r) = 0 \tag{D.9}$$

The solution to an equation of this form is a modified Bessel's function

$$B = a_1 J_0\left(-i\frac{r}{\lambda}\right) + a_2 Y_0\left(-i\frac{r}{\lambda}\right) = C_1 I_0\left(\frac{r}{\lambda}\right) + C_2 K_0\left(\frac{r}{\lambda}\right) \tag{D.10}$$

where I_0 and K_0 are modified Bessels functions of the first and second kinds respectively.

Since $I_0(\infty) \to \infty$, $C_1 = 0$ for convergence. Therefore

$$B(r) = C_2 K_0\left(\frac{r}{\lambda}\right) = C_2 \int_0^\infty \exp\left(-\frac{r}{\lambda}\cosh t\right) dt \tag{D.11}$$

From the asymptotics

$$K_0(x) \approx \begin{cases} -\ln x & x \to 0 \\ \sqrt{\frac{\pi}{2x}} e^{-x} & x \to \infty \end{cases} \tag{D.12}$$

with $C_2 = \frac{\Phi_0}{2\pi\lambda^2}$.

Therefore the magnetic field away from the core due to a single vortex is found to be

$$B(r) = \frac{\Phi_0}{2\pi\lambda^2} K_0\left(\frac{r}{\lambda}\right) = \frac{\Phi_0}{2\pi\lambda^2} \int_0^\infty \exp\left(-\frac{r}{\lambda}\cosh t\right) dt\hat{\mathbf{k}} \tag{D.13}$$

Appendix E

ORDER PARAMETERS

The order parameters to determine melting temperatures are implemented using Mathematica.

```
Angle[c1_, c2_] := (x = c2[[1]] - c1[[1]];
  y = c2[[2]] - c1[[2]];
  ArcTan[x, y])

nnDistance[i_, j_, set_] := Norm[set[[i]] - set[[j]]]

RemoveLongDistanceNN[nnlist_, set_] := (newnnlist = {};
   Do[i = nnlist[[n, 1]];
    j = nnlist[[n, 2]];
    thislist =
     DeleteCases[If[nnDistance[i, #, set] < 4.0, #, Null] & /@ j,
      Null];
    newnnlist = Append[newnnlist, {i, thislist}], {n, 1,
     Length[nnlist]}];
   newnnlist);

HexaticOP[set_] := (
  thisset = DeleteDuplicates[set];
  nnlist = DelaunayMesh[thisset]["VertexVertexConnectivity"];
  nnlist = Table[{n, nnlist[[n]]}, {n, 1, Length[nnlist]}];
  (*Print[nnlist];
  nnlist=DelaunayTriangulation[thisset];
  Print[nnlist];*)
  nnlist = RemoveLongDistanceNN[nnlist, thisset];

  jSum = Sum[kSum = Sum[jindex = nnlist[[j]][[1]];
      kindex = nnlist[[j]][[2]][[k]];
      pj = thisset[[jindex]];
      pk = thisset[[kindex]];
      Exp[I*6*Angle[pj, pk]], {k, 1, Length[nnlist[[j]][[2]]]}];
    kSum = kSum/Length[nnlist[[j]][[2]]], {j, 1, Length[nnlist]}];
```

```
  jSum = jSum/Length[nnlist];
  ans = Abs[jSum]^2;
  If[NumberQ[ans], ans, -1]
  );
```

```
NdCount[frame_, xl_, xh_, yl_, yh_] :=
  (
   subset =
    DeleteCases[
     If[#[[1]] > xl && #[[1]] < xh && #[[2]] > yl && #[[2]] < yh, #,
        False] & /@ frame, False];
   NTotal = Length[subset];

   NdList =
    DeleteCases[If[Round[#[[3]]] != 6, #, False] & /@ subset, False];
   Nd = Length[NdList];
   {NTotal, Nd, Nd/NTotal}

   );
```

Appendix F

SIZE OF TIME STEP

The time step of the simulation is chosen to ensure the majority of displacements in the simulation are $\ll a_0$. The size of displacements depends on the size of deterministic forces but mostly on the temperature of the simulation. In the solid phase we perform simulations at $T = 0.0025$. For the liquid state, the maximum temperature we will use is $T = 0.05$. We must explore how the displacements at these values depend of the size of the time step. In general the displacement are

$$< |dx| >= \sqrt{A}\sqrt{\Delta t} \tag{F.1}$$

From this we can see that reducing ΔT to $\Delta T/100$ gives a change in $< |dx| >$ of $1/10$. For $T = 0.0025$ and 0.05 we use values of $\Delta t = 0.01$ and $\Delta t = 0.0001$.

The thermostat provides each particle a thermal kick with a probability $p = \Delta/\tau$. To understand how size of these kicks are distribution we look at the aspects of the cumulative distribution function and the moments. Table F gives a breakdown of results from these measures. Two temperatures were chosen and two values of Δ. We require the displacements in any given timestep be $\ll a_0$. We choose a maximum preferred displacement of $a_0/50$. With this value we can calculate the probability that a particle will receive a kick larger than $a_0/50$, $P(dx > a_0/50)$. For all cases this is $< 1\%$.

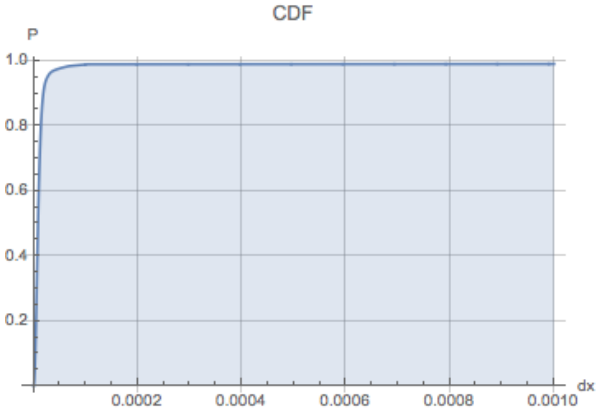

(a) Full distribution

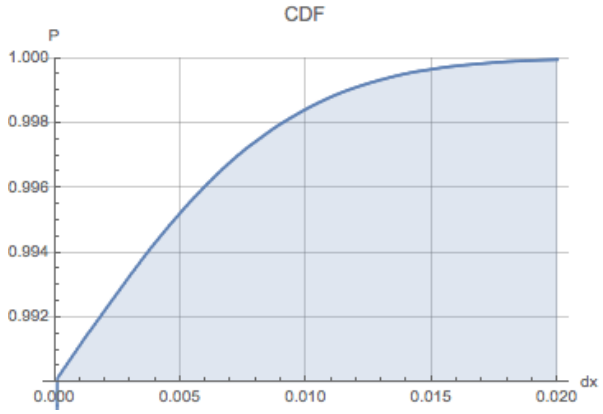

(b) Enlarged distribution.

Figure F.1: Cumulative probability distribution for dx. $T = 0.0025$, $\Delta = 0.0001$.

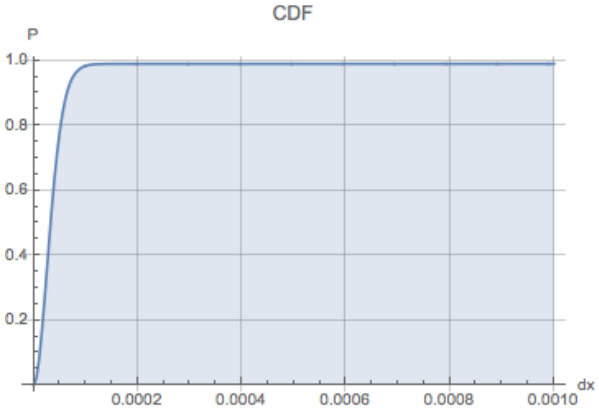

(a) Full distribution

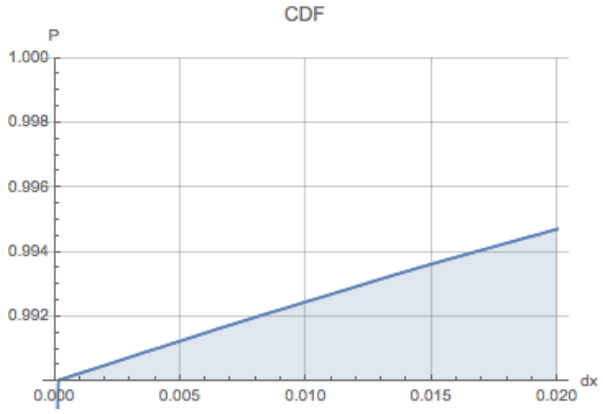

(b) Enlarged distribution.

Figure F.2: Cumulative probability distribution for dx. $T = 0.05$, $\Delta = 0.0001$.

time steps=10 000 N=1000	P(dx> $a_0/50$)	$M_2 = 2Tk_B/\eta$	Max(dx)
$T = 0.0025$ $\Delta = 0.0001$	0.0000437299	0.00497406	0.329977
$T = 0.05$ $\Delta = 0.0001$	0.00528661	0.100641	0.13382
$T = 0.0025$ $\Delta = 0.01$	0.00777666	0.00507433	0.34063
$T = 0.05$ $\Delta = 0.01$	0.0128923	0.102503	2.0814

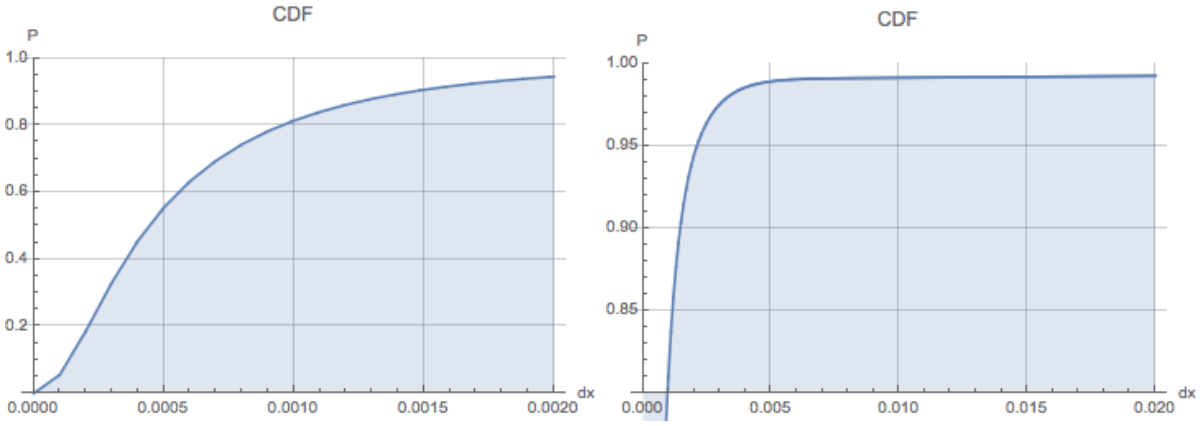

(a) Full distribution (b) Enlarged distribution.

Figure F.3: Cumulative probability distribution for dx. $T = 0.0025$, $\Delta = 0.01$.

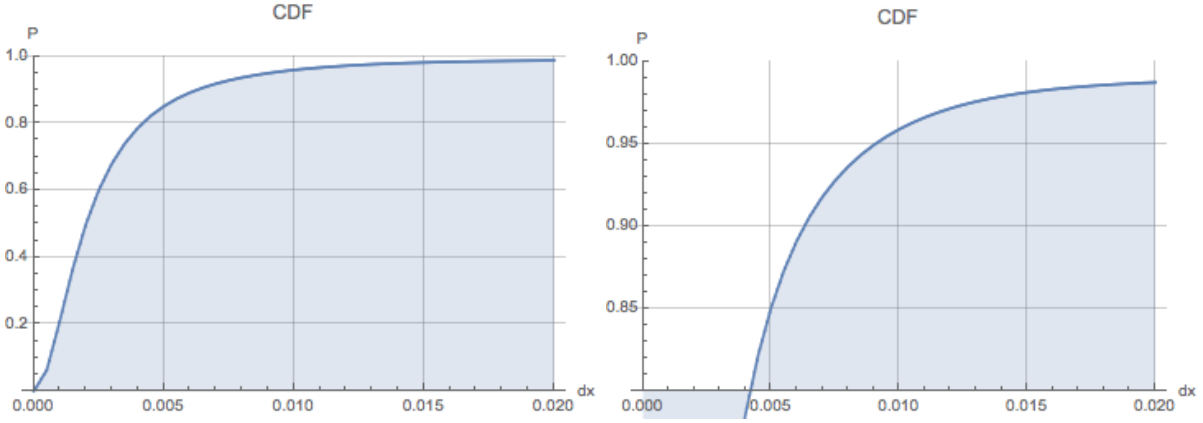

(a) Full distribution (b) Enlarged distribution.

Figure F.4: Cumulative probability distribution for dx. $T = 0.05$, $\Delta = 0.01$.

Appendix G

MOMENTS OF THE FOKKER-PLANCK EQUATION

The aim is to determine the form of the stochastic noise term in Eq. (5.12) if we require the particle energies to obey Boltzmann statistics in equilibrium. To do this we can find the Fokker-Planck equation[127] for Eq. (5.12). The Fokker-Planck (or Kolmogorov forward) equation describes the time evolution of a probability distribution, in this case, for the position of a particle at a time, t. We start with the probability of finding a particle at x and time t if it were at x_0 at time t_0

$$P(x,t|x_0,t_0) = P(x,t-t_0|x_0). \tag{G.1}$$

via the Kramers-Moyal expansion we can say that P obeys

$$\frac{\partial P}{\partial t} = \sum_{n=1}^{\infty} \frac{(-1)^n}{n!} \frac{\partial^n}{\partial^n x} \left[M_n P(x,t|x_0)\right] \tag{G.2}$$

where the moments are defined as

$$M_n = \frac{1}{\tau} \int \xi^n P(x+\xi,\tau|x) \mathrm{d}\xi. \tag{G.3}$$

We need to connect Eq. (G.2) to Eq. (5.12). The method is to replace the moments

M_n by the moments calculated from Eq. (5.12). We begin by assuming the stochastic term is a Gaussian white noise function with

$$\langle \chi_i(t) \rangle = 0 \qquad \langle \chi_i(t_1)\chi_j(t_2) \rangle = A\delta(t_1 - t_2)\delta(i-k) \tag{G.4}$$

The required moments from Eq. (5.12) are $\langle \delta x \rangle$ and $\langle (\delta x)^2 \rangle$.

The first moment is

$$\begin{aligned}
\langle \delta x \rangle &= \langle x(\mathrm{d}t) - x_0 \rangle \qquad (G.5)\\
&= \left\langle \int_0^{\mathrm{d}t} v(t')\mathrm{d}t' \right\rangle \\
&= \int_0^{\mathrm{d}t} \langle v(t') \rangle \, \mathrm{d}t' \\
&= \int_0^{\mathrm{d}t} \left\langle \frac{F}{\gamma} + \frac{\chi(t')}{\gamma} \right\rangle \mathrm{d}t' \\
&= \int_0^{\mathrm{d}t} \frac{1}{\gamma} \langle F \rangle + \underbrace{\frac{1}{\gamma} \langle \chi(t') \rangle}_{=0 \text{ by definition}} \mathrm{d}t' \\
\langle \delta x \rangle &= \frac{\langle F \rangle}{\gamma} \mathrm{d}t \qquad (G.6)
\end{aligned}$$

For the second moment

$$
\begin{aligned}
\left\langle (\delta x)^2 \right\rangle &= \left\langle (x(\mathrm{d}t) - x_0)^2 \right\rangle \\
&= \left\langle \left(\int_0^{\mathrm{d}t} v(t')\mathrm{d}t' \right)^2 \right\rangle \\
&= \int_0^{\mathrm{d}t} \int_0^{\mathrm{d}t} \mathrm{d}t_1 \mathrm{d}t_2 \left\langle \left(\frac{F}{\gamma} + \frac{\chi(t_1)}{\gamma} \right) \left(\frac{F}{\gamma} + \frac{\chi(t_2)}{\gamma} \right) \right\rangle \\
&= \int_0^{\mathrm{d}t} \int_0^{\mathrm{d}t} \mathrm{d}t_1 \mathrm{d}t_2 \left(\left\langle \frac{F^2}{\gamma^2} \right\rangle + \underbrace{\left\langle \frac{F\chi(t_1)}{\gamma^2} \right\rangle}_{=0} + \underbrace{\left\langle \frac{F\chi(t_2)}{\gamma^2} \right\rangle}_{=0} + \underbrace{\left\langle \frac{\chi(t_1)\chi(t_2)}{\gamma^2} \right\rangle}_{A\delta(t_1 - t_2)} \right) \\
&= \int_0^{\mathrm{d}t} \int_0^{\mathrm{d}t} \mathrm{d}t_1 \mathrm{d}t_2 \left(\left\langle \frac{F^2}{\gamma^2} \right\rangle + A\delta\left(t_1 - t_2\right) \right) \\
&= \left\langle \frac{F^2}{\gamma^2} \right\rangle \mathrm{d}t^2 + \int_0^{\mathrm{d}t} \mathrm{d}t_1 A \\
&= \frac{\langle F^2 \rangle}{\gamma^2} \mathrm{d}t^2 + A\mathrm{d}t
\end{aligned}
\tag{G.7}
$$

For small $\mathrm{d}t$ we find

$$
\left\langle (\delta x)^2 \right\rangle \approx A\mathrm{d}t \tag{G.8}
$$

Both the first and second moments can be used as a check in the simulation to ensure the correct distribution is being sampled.

We are now positioned to replace the moments of the Fokker-Planck equation with the moments calculated from the equation of motion. We have

$$
M_1 = \frac{1}{\mathrm{d}t} \left\langle \delta x \right\rangle = \frac{\langle F \rangle}{\gamma} \qquad M_2 = \frac{1}{\mathrm{d}t} \left\langle (\delta x)^2 \right\rangle = A \tag{G.9}
$$

We now substitute these into Eq. (G.2) and find

$$
\frac{\partial P}{\partial t} = -\frac{\partial}{\partial x} \left[\frac{1}{\gamma} F P\left(x, t | x_0\right) \right] + \frac{1}{2} \frac{\partial^2}{\partial x^2} \Big[A P\left(x, t | x_0\right) \Big] \tag{G.10}
$$

Assume in thermal equilibrium we have the Boltzman distribution

$$P\left(x,\infty|x_0\right) \propto \mathrm{e}^{-\beta U(x)} \tag{G.11}$$

where we have used $\beta = 1/k_B T$ so that at $t = \infty$, $\dfrac{\partial p}{\partial t} = 0$. Eq. (G.10) becomes

$$\begin{aligned}
0 &= -\frac{\partial}{\partial x}\left[\frac{1}{\gamma}F\mathrm{e}^{-\beta U(x)}\right] + \frac{1}{2}\frac{\partial^2}{\partial x^2}\left[A\mathrm{e}^{-\beta U(x)}\right] \\
&= -\frac{1}{\gamma}\frac{\partial F}{\partial x}\cancel{\mathrm{e}^{-\beta U(x)}} + \frac{1}{\gamma}\beta F\underbrace{\frac{\partial U}{\partial x}}_{=-F}\cancel{\mathrm{e}^{-\beta U(x)}} - \frac{1}{2}\beta A\underbrace{\frac{\partial^2 U}{\partial x^2}}_{=-\frac{\partial F}{\partial x}}\cancel{\mathrm{e}^{-\beta U(x)}} + \frac{1}{2}\beta^2 A\underbrace{\frac{\partial U}{\partial x}}_{=-F}\cancel{\mathrm{e}^{-\beta U(x)}} \\
&= -\frac{1}{\gamma}\frac{\partial F}{\partial x} - \frac{1}{\gamma}\beta F^2 + \frac{1}{2}\beta A\frac{\partial F}{\partial x} - \frac{1}{2}\beta^2 AF \\
0 &= \left[-\frac{1}{\gamma} + \frac{1}{2}\beta A\right]\frac{\partial F}{\partial x} + \left[-\frac{1}{\gamma}\beta + \frac{1}{2}\beta^2 A\right]F^2
\end{aligned}$$

This is satisfied if

$$A = \frac{2}{\beta\gamma} \qquad \text{or} \qquad A = \frac{2k_B T}{\gamma} \tag{G.12}$$

Appendix H

MELTING TEMPERATURE - FLUCTUATION DISSIPATION THEORY

Calculation of the melting temperature T_m of the flux line lattice follows the approach laid out by Brandt[10].

Assuming small fluctuations, we can write the positions of the flux lines in terms of their in-plane displacements from the ideal lattice positions $\mathbf{R}^i = (X^i, Y^i, z)$ within linear elastic theory as

$$\mathbf{u}^i(z) = \mathbf{r}^i(z) - \mathbf{R}^i = (u_x^i, u_y^i, 0) \tag{H.1}$$

where i labels each particle and z is the coordinate in the $\hat{\mathbf{z}}$ direction.

Starting from the elastic free energy and considering an expansion to second order, the elastic free energy in k-space is[10]

$$F_{\mathrm{E}} = \frac{1}{2}\int_{BZ} \frac{\mathrm{d}^3\mathbf{k}}{8\pi^3} u_\alpha(\mathbf{k})\Phi_{\alpha\beta}(\mathbf{k})u_\beta^*(\mathbf{k}) \tag{H.2}$$

where $\Phi_{\alpha\beta}(\mathbf{k})$ is the elastic matrix and $\alpha, \beta = x$ or y. Let each elastic mode of the flux line lattice have energy $\frac{1}{2}k_BT$. This gives

$$\frac{1}{2}\langle u_\alpha(\mathbf{k})\Phi_{\alpha\beta}(\mathbf{k})u_\beta(\mathbf{k})\rangle = \frac{1}{2}k_BT \tag{H.3}$$

Inverting $\Phi_{\alpha\beta}(\mathbf{k})$ allows us to find

$$\langle u_\alpha(\mathbf{k})u_\beta(\mathbf{k})\rangle = k_BT\,\Phi^{-1}_{\alpha\beta}(\mathbf{k}) \tag{H.4}$$

From Parseval's Theorem the real space average $\langle u^2\rangle$ is obtained by a sum over all the reciprocal space modes. Letting $V \to \infty$ we have

$$\langle u^2\rangle = \langle u_x^2(\mathbf{k}) + u_y^2(\mathbf{k})\rangle = k_BT\int_{BZ}\frac{\mathrm{d}^2k_\perp}{4\pi^2}\int_{-\infty}^{\infty}\frac{\mathrm{d}k_z}{2\pi}\left[\Phi^{-1}_{xx}(\mathbf{k}) + \Phi^{-1}_{yy}(\mathbf{k})\right] \tag{H.5}$$

Returning to the elastic matrix we need an expression for the elastic matrix in terms of the compression, tilt and shear moduli - in compact notation referred to as c_{11}, c_{44} and c_{66} respectively. The general expression for isotropic films in the continuum limit is

$$\Phi_{\alpha\beta}(\mathbf{k}) = (c_{11}-c_{66})k_\alpha k_\beta + \delta_{\alpha\beta}\left[(k_x^2+k_y^2)c_{66} + k_z^2c_{44} + \alpha_{\mathrm{L}}(\mathbf{k})\right] \tag{H.6}$$

where the Labusch parameter α_L is included to describe the interaction of the flux lines with the material defects. Using the general expression, Eq. (H.6), we can generate the matrix entries for Φ_{xx} and Φ_{yy}

$$\Phi_{xx}(\mathbf{k}) = c_{11}k_x^2 + c_{66}k_y^2 + c_{44}k_z^2 + \alpha_{\mathrm{L}}(\mathbf{k}) \tag{H.7}$$

$$\Phi_{yy}(\mathbf{k}) = c_{11}k_y^2 + c_{66}k_x^2 + c_{44}k_z^2 + \alpha_{\mathrm{L}}(\mathbf{k}) \tag{H.8}$$

$$\Phi_{xy}(\mathbf{k}) = (c_{11}-c_{66})k_xk_y \tag{H.9}$$

We need the inverse of $\Phi_{\alpha\beta} = \begin{pmatrix} \Phi_{xx}(\mathbf{k}) & \Phi_{xy}(\mathbf{k}) \\ \Phi_{xy}(\mathbf{k}) & \Phi_{yy}(\mathbf{k}) \end{pmatrix}$

$$\Phi^{-1}_{\alpha\beta}(\mathbf{k}) = \frac{1}{\Phi_{xx}(\mathbf{k})\Phi_{yy}(\mathbf{k}) - \Phi^2_{xy}(\mathbf{k})} \begin{pmatrix} \Phi_{yy}(\mathbf{k}) & -\Phi_{xy}(\mathbf{k}) \\ -\Phi_{xy}(\mathbf{k}) & \Phi_{xx}(\mathbf{k}) \end{pmatrix} \tag{H.10}$$

This gives

$$\Phi^{-1}_{xx}(\mathbf{k}) = \frac{\Phi_{yy}(\mathbf{k})}{\Phi_{xx}(\mathbf{k})\Phi_{yy}(\mathbf{k}) - \Phi^2_{xy}(\mathbf{k})} \qquad \Phi^{-1}_{yy}(\mathbf{k}) = \frac{\Phi_{xx}(\mathbf{k})}{\Phi_{xx}(\mathbf{k})\Phi_{yy}(\mathbf{k}) - \Phi^2_{xy}(\mathbf{k})} \tag{H.11}$$

Substituting the pair of equations Eq. (H.11) into the expression for $\langle u^2 \rangle$

$$\langle u^2 \rangle = k_B T \int_{BZ} \frac{\mathrm{d}^2 k_\perp}{4\pi^2} \int_{-\infty}^{\infty} \frac{\mathrm{d}k_z}{2\pi} \frac{\Phi_{xx}(\mathbf{k}) + \Phi_{yy}(\mathbf{k})}{\Phi_{xx}(\mathbf{k})\Phi_{yy}(\mathbf{k}) - \Phi^2_{xy}(\mathbf{k})} \tag{H.12}$$

now using the expressions for equations Eqs. (H.7 - H.9) we find

$$\langle u^2 \rangle = k_B T \int_{BZ} \frac{\mathrm{d}^2 k_\perp}{4\pi^2} \int_{-\infty}^{\infty} \frac{\mathrm{d}k_z}{2\pi} \frac{c_{11}k_\perp^2 + c_{66}k_\perp^2 + 2c_{44}k_z^2 + \alpha_{\mathrm{L}}(\mathbf{k})}{\left(c_{11}k_x^2 + c_{66}k_y^2 + c_{44}k_z^2 + \alpha_{\mathrm{L}}(\mathbf{k})\right)\left(c_{11}k_y^2 + c_{66}k_x^2 + c_{44}k_z^2 + \alpha_{\mathrm{L}}(\mathbf{k})\right) - \left(c_{11} - c_{66}\right)^2 k_x^2 k_y^2} \tag{H.13}$$

This can be rearranged into a simpler form (see Appendix I), the result is shown below

$$\langle u^2 \rangle = k_B T \int_{BZ} \frac{\mathrm{d}^2 k_\perp}{4\pi^2} \int_{-\infty}^{\infty} \frac{\mathrm{d}k_z}{2\pi} \left[\frac{1}{c_{66}k_\perp^2 + c_{44}k_z^2 + \alpha_{\mathrm{L}}(\mathbf{k})} + \frac{1}{c_{11}k_\perp^2 + c_{44}k_z^2 + \alpha_{\mathrm{L}}(\mathbf{k})} \right] \tag{H.14}$$

The integrand is symmetric in k_z so we pick up a factor of 2 and change the k_z limits from 0 to ∞.

$$\langle u^2 \rangle = k_B T \int_{BZ} \frac{\mathrm{d}^2 k_\perp}{4\pi^2} \int_0^\infty \frac{\mathrm{d}k_z}{\pi} \left[\frac{1}{c_{66} k_\perp^2 + c_{44} k_z^2 + \alpha_\mathrm{L}(\mathbf{k})} + \frac{1}{c_{11} k_\perp^2 + c_{44} k_z^2 + \alpha_\mathrm{L}(\mathbf{k})} \right] \quad \text{(H.15)}$$

In the continuum limit the hexagonal brillouin zone is replaced by a circle of radius $k_{BZ} = (4\pi B/\Phi_0)^{1/2}$ so we let

$$\int_{BZ} \mathrm{d}^2 k_\perp \to \int_0^{k_{BZ}} \mathrm{d}k_\perp k_\perp \int_0^{2\pi} \mathrm{d}k_\theta \quad \text{(H.16)}$$

In the integrand there is no dependence on k_θ as only $k_\perp^2$ appears for the in plane variables. This means we can evaluate the k_θ integral as $\int_0^{2\pi} \mathrm{d}k_\theta = 2\pi$ which leaves us with

$$\langle u^2 \rangle = \frac{k_B T}{2\pi^2} \int_0^{k_{BZ}} \mathrm{d}k_\perp k_\perp \int_0^\infty \mathrm{d}k_z \left[\frac{1}{c_{66} k_\perp^2 + c_{44} k_z^2 + \alpha_\mathrm{L}(\mathbf{k})} + \frac{1}{c_{11} k_\perp^2 + c_{44} k_z^2 + \alpha_\mathrm{L}(\mathbf{k})} \right] \quad \text{(H.17)}$$

Since $c_{11} \gg c_{66}$ the second term is small in comparison with the first, leaving

$$\langle u^2 \rangle \approx \frac{k_B T}{2\pi^2} \int_0^{k_{BZ}} \mathrm{d}k_\perp k_\perp \int_0^\infty \mathrm{d}k_z \left[\frac{1}{c_{66} k_\perp^2 + c_{44} k_z^2 + \alpha_\mathrm{L}(\mathbf{k})} \right] \quad \text{(H.18)}$$

Letting k_z have a maximum value of 2π and performing the k_z integral gives us

$$\langle u^2 \rangle \approx \frac{k_B T}{\pi} \int_0^{k_{BZ}} \mathrm{d}k_\perp k_\perp \left[\frac{1}{c_{66} k_\perp^2 + c_{44} k_z^2 + \alpha_\mathrm{L}(\mathbf{k})} \right] \quad \text{(H.19)}$$

For all of the simulations considered in this work $c_{44} = 0$ and $\alpha_\mathrm{L}(\mathbf{k}) = 0$. This reduces to

$$\langle u^2 \rangle \approx \frac{k_B T}{c_6 6\pi} \int_0^{k_{BZ}} \frac{\mathrm{d}k_\perp}{k_\perp} \quad \text{(H.20)}$$

In order to integrate this we must introduce upper and lower cutoffs on the BZ. We use $\pi/L < k_\perp < \pi/a_0$ which gives

$$\langle u^2 \rangle \approx \frac{k_B T}{c_{66}\pi}\left[\frac{\mathrm{d}k_\perp}{k_\perp}\right]_{\pi/L}^{\pi/a_0} = \frac{k_B T}{\pi c_{66}} \ln\left(\frac{L}{a_0}\right) \tag{H.21}$$

Using the phenomenological Lindemann criteria, that melting occurs when vibrations are on the order of $u \sim c_l a_0$, allows us to replace $\langle u^2 \rangle$ with $(c_L a_0)^2$. The Lindemann parameter usually lies within a range $c_L \sim 0.1 - 0.2$, we set $c_L = 0.2$ in line with previous work by other groups[128]. Rearranging for T gives an estimate of the melting temperature.

$$T_m \approx \frac{c_{66}\pi(c_L a_0)^2}{k_B \ln(L/a_0)} \tag{H.22}$$

The same equation is used by Spencer *et al.*[19] for their simulations of the vortex lattice. The value of c_{66} can be determined from Brandt's[10] expression

$$c_{66} \approx \frac{B\phi_0}{16\pi\lambda^2\mu_0}\left(1 - \frac{1}{2\kappa^2}\right)(1-b^2)(1-0.58b+0.29b^2) \tag{H.23}$$

where $\tilde{b} = B/B_{c2}$. In the London limit $b \ll 1$ and $\kappa \gg 1$ so we can use the k independent shear modulus

$$c_{66} \approx \frac{B\phi_0}{16\pi\lambda^2\mu_0} \tag{H.24}$$

This leaves c_{66} proportional to B and $1/\lambda^2$. We see the effect of reducing λ is to stiffen the lattice and increase the melting temperature.

Appendix I

SIMPLIFYING THE ELASTIC MODULI EXPRESSION

The expression from Eq. (H.13) can be simplified. We start with the integrand

$$\frac{c_{11}k_{\perp}^2 + c_{66}k_{\perp}^2 + 2c_{44}k_z^2 + 2\alpha_{\mathrm{L}}(\mathbf{k})}{\left(c_{11}k_x^2 + c_{66}k_y^2 + c_{44}k_z^2 + \alpha_{\mathrm{L}}(\mathbf{k})\right)\left(c_{11}k_y^2 + c_{66}k_x^2 + c_{44}k_z^2 + \alpha_{\mathrm{L}}(\mathbf{k})\right) - \left(c_{11} - c_{66}\right)k_x^2k_y^2}$$

.

Consider first the expansion of the denominator

$$\begin{aligned}
&c_{11}^2k_x^2k_y^2 + c_{11}c_{66}k_x^4 + c_{11}c_{44}k_x^2k_z^2 + c_{66}c_{11}k_y^4 + c_{66}^2k_y^2k_x^2 + c_{66}c_{44}k_y^2k_z^2 + c_{44}c_{11}k_z^2k_y^2 \\
&+ c_{44}c_{66}k_z^2k_x^2 + c_{44}^2k_z^4 - c_{11}^2k_x^2k_y^2 - c_{66}^2k_x^2k_y^2 + 2c_{11}c_{66}k_x^2k_y^2 \\
&+ \alpha_{\mathrm{L}}(\mathbf{k})\left(c_{11}k_y^2 + c_{66}k_x^2 + c_{11}k_x^2 + c_{66}k_y^2 + 2c_{44}k_z^2\right) + \alpha_{\mathrm{L}}^2(\mathbf{k}) \\
= &\, c_{11}c_{66}\left[k_x^4 + k_y^4 + k_x^2k_y^2\right] + c_{11}c_{44}\left[k_x^2k_z^2 + k_y^2k_z^2\right] + c_{44}c_{66}\left[k_x^2k_z^2 + k_y^2k_z^2\right] + c_{44}^2k_z^4 \\
&+ \alpha_{\mathrm{L}}(\mathbf{k})\left(c_{11}k_y^2 + c_{66}k_x^2 + c_{11}k_x^2 + c_{66}k_y^2 + 2c_{44}k_z^2\right) + \alpha_{\mathrm{L}}^2(\mathbf{k})
\end{aligned}$$

Let $k_{\perp}^2 = k_x^2 + k_y^2$

Reintroducing the numerator

$$\frac{c_{11}k_\perp^2 + c_{66}k_\perp^2 + 2c_{44}k_z^2 + 2\alpha_{\mathrm{L}}(\mathbf{k})}{c_{11}c_{66}k_\perp^4 + c_{44}c_{66}k_\perp^2 k_z^2 + c_{11}c_{44}k_z^2 k_\perp^2 + c_{44}^2 k_z^4 + \alpha_{\mathrm{L}}(\mathbf{k})\left(c_{11}k_\perp^2 + c_{66}k_\perp^2 + 2c_{44}k_z^2\right) + \alpha_{\mathrm{L}}^2(\mathbf{k})}$$

$$= \frac{c_{11}k_\perp^2 + c_{66}k_\perp^2 + 2c_{44}k_z^2 + 2\alpha_{\mathrm{L}}(\mathbf{k})}{\left(c_{66}k_\perp^2 + c_{44}k_z^2 + +\alpha_{\mathrm{L}}(\mathbf{k})\right)\left(c_{11}k_\perp^2 + c_{44}k_z^2 + \alpha_{\mathrm{L}}(\mathbf{k})\right)}$$

$$= \frac{1}{\left(c_{66}k_\perp^2 + c_{44}k_z^2 + +\alpha_{\mathrm{L}}(\mathbf{k})\right)} + \frac{1}{\left(c_{11}k_\perp^2 + c_{44}k_z^2 + \alpha_{\mathrm{L}}(\mathbf{k})\right)}$$

as required.

Appendix J

LOCAL BURGERS VECTOR CALCULATION

A Mathematica implementation of the Burgers vector calculution is given in the code block below. It requires a support function that finds the closest particle to a given point.

```
1
2  calculateBurgersCircuit[lattice_, r0_, moves_] := (
3     burgerslist = {lattice[[findclosestatom[lattice, r0]]]};
4
5     Do[
6      burgerslist =
7       Append[burgerslist,
8        lattice[[
9         findclosestatom[lattice,
10         burgerslist[[ Length[burgerslist]]] + moves[[i]] ]]]]
11
12
13     , {i, 1, Length[moves]}];
14    burgersVector =
15     burgerslist[[Length[burgerslist]]] - burgerslist[[1]];
16    \[Theta]effective =
17     ArcTan[burgersVector[[2]]/burgersVector[[1]]]/\[Pi]*180;
18    {burgerslist, \[Theta]effective, {burgerslist[[
19       Length[burgerslist]]], burgerslist[[1]]} });
20
21       findclosestatom[lattice, pos] := (j = 0;
22    Do[
23     ds2 = (pos[[1]] - lattice[[i, 1]])*(pos[[1]] -
24          lattice[[i, 1]]) + (pos[[2]] - lattice[[i, 2]])*(pos[[2]] -
25          lattice[[i, 2]]);
26     If[i == 1,
27      (smallest = ds2; j = i),
28      If [smallest > ds2, (smallest = ds2; j = i)]
29      ];
```

```
30      , {i, 1, Length[lattice]}]; j);
```

To use this function we must specify the reference circuit in terms of moves on the perfect lattice. These are specified as jumps in terms of lattice vectors. It also requires a starting point for the circuit. The following sets up these conditions and runs the code. The result is a set of coordinates marking the points on the Burgers circuit as well as the angle of the Burgers vector to the horizontal and the Burgers vector itself.

```
1  (* lattice vectors *)
2  e1 = {1, 0};
3  e2 = {-Cos[Pi/3], Sin[Pi/3]};
4
5  (* Moves for burgers circuit *)
6  v = {e1, e1, e1, e1, e1,
7     e1, -e2, -e2, -e2, -e2, -e1, -e1, -e1, -e1, -e1, -e1, -e1, -e1, e2,
8      e2, e2, e2, e2, e1, e1};
9  (* Nelson's convention for the burgers circuit *)
10 (*v=Reverse[-v]; *)
11 \
12
13 (* starting point form burgers circuit *)
14 bvstart = {27, 5.5};
15
16 r0 = full[[findclosestatom[full, r0 = bvstart]]];
17
18 {burgersCircuit, \[Theta]effective, burgersVector} =
19   calculateBurgersCircuit[full, r0, v];
```

Appendix K

BUBBLE ANALYSIS ROUTINES

Finding the bubble and analysis

```
1
2  cluste[data6_, data5_, data7_] :=
3   Block[{}, ftmp = data5;
4    ftmp[[All, 1]] += -Mean[data5 /. {a_, b_} -> a];
5    ftmp[[All, 2]] += -Mean[data5 /. {a_, b_} -> b];
6    data1 = ftmp /. {a_, b_} -> Sqrt[a^2 + b^2];
7    clust = FindClusters[data1 -> Range[Length[data1]]];
8    c50 = Extract[data5,
9      Map[k, Extract[clust, Ordering[Map[Length, clust], -1]]] /.
10      k[a_] -> {a}];
11   gt[ld_] :=
12    Union[Flatten[
13      Table[Complement[Nearest[data5, ld[[i]], 3], {ld[[i]]}], {i, 1,
14        Length[ld]}], 1]];
15   c5 = FixedPoint[gt, c50, 10];
16   tc5a = Table[Norm[c5[[i]] - Median[c5]], {i, 1, Length[c5]}];
17   ac5 = Mean[tc5a];
18   c5f = Extract[c5, Position[tc5a, x_ /; x < 1.5 ac5]];
19   c7 = Flatten[
20     Union[Table[Nearest[data7, c5f[[i]], 2], {i, 1, Length[c5f]}]], 1];
21   bub1 = Union[Join[c5f, c7]]; fst = FindShortestTour[bub1];
22   bubper = bub1[[Last[fst]]];
23   g1 = Graphics[Line[bubper]]; mf = RegionMember[Polygon[bubper], six];
24
25   (*bubble numbers*)
26   countinbubble = Count[mf, True];
27   countperbubble = Length[Union[bubper]];
28   AppendTo[countAP, {tstep, countinbubble, countperbubble}];
29   int = Graphics[{AbsolutePointSize[
30       3], {mf /. {True -> Red, False -> Gray},
31        Point /@ six}\[Transpose]}];
32   g2 = Show[int,
33     ListPlot[{Complement[data5, c5f], Complement[data7, c7], c7, c5f},
```

```
      PlotMarkers -> {{\[EmptySquare], 10}, {\[EmptyUpTriangle],
        10}, {\[FilledSquare], 10}, {\[FilledUpTriangle], 10}},
     PlotStyle -> {Green, Blue, Green, Blue},
     PlotLabel -> {countinbubble, countperbubble}], g1,
    PlotRange -> pra]]
```

Row count

```
df = 1;

row2[val_, testa_] :=
 Block[{}, vala = Nearest[testa, {val, 0}][[1, 1]];
  test3 = Cases[
     testa, {x_, y_} /; x > vala - 2 && x < vala + 2] /. {x_,
      y_} -> {x - vala, y}; test4 = Sort[test3, #1[[2]] < #2[[2]] &]]

va2[{a_, b_}] :=
 Min[VectorAngle[{a - start[[1]], b - start[[2]]}, {1, 0}],
  VectorAngle[{a - start[[1]], b - start[[2]]}, {-1, 0}]]

ty[i_] :=
 Block[{}, start = test4[[i]];
  end = Extract[test4,
    Position[test4[[All, 2]], Max[test4[[All, 2]]]]];
  len = Length[Drop[test4, i]];
  If[len > 0, poss = Nearest[Drop[test4, i], start, Min[3, len]];
   last = IntersectingQ[poss, end]; vang = Map[va2, poss];
   se = Select[vang, # > 0.2 &, 1];
   If[Length[se] > 0,
    Position[test4, Extract[poss, Position[vang, se[[1]]][[1]]][[1,
     1]], i], i]]

pathg[val_] :=
 Block[{},
  path = Extract[test4,
     Map[k, Union[FixedPointList[ty, 1]]] /. k[a_] -> {a}] /. {a_,
      b_} -> {a + vala, b}; AppendTo[pathL, {vala, Length[path]}];
  pg[val] =
   Show[ListPlot[path, Joined -> True, PlotRange -> {All, {0, 19}}],
    Graphics[
     Text[Style[Length[path], "Helvetica", 12, Red], {vala + 0.5,
       17.5}]]]]
```

Orientation of the lattice

With ONLY one argument, finds the six-fold vortex closest to the selected point, area of polygon, perimeter, angle wrt x-axis, and for lattice parameter (min,max,mean, std) OTHERWISE does the same but for the centre of the bubble"

If the second argument is true, it calculates for the centre of the bubble. Angles are in degrees.

```
LocLattice[posi__, isbub_: False] :=
 Block[{}, If[TrueQ[isbub],
   inbub = Cases[({mf /. {True -> 1, False -> 0}, six}\[Transpose]),
        {1, {b_, c_}}] /. {1, {b_, c_}} -> {b, c}; nib =
        Nearest[inbub, Mean[inbub]],
   nib = Nearest[six, posi]];
  part1 = Complement[Nearest[vort, nib, 7][[1]], nib]; {perim, pathp} =
   FindShortestTour[part1]; pathp = Drop[pathp, -1];
  parea = Area[Polygon[part1[[pathp]]]];
  ango = Min[
    Cases[Table[
       ArcTan[(part1[[i]] - nib[[1]]) /. List -> Sequence], {i, 1, 6}]
       180/Pi, x_ /; x > 0]];
  lens = Map[Norm, Table[part1[[i]] - nib[[1]], {i, 1, 6}]]; {minlen,
  maxlen, meanlen, stdlen} = {Min[lens], Max[lens], Mean[lens],
    StandardDeviation[lens]};
  dpos =
  {nib[[1]], parea, perim, ango,
  {minlen, maxlen, meanlen, stdlen},
    Line[{part1[[Position[lens, Min[lens]]
    /. {{a_}} -> a]] , nib[[1]]}]}]

m60[a_] := If[a < 65, Min[a, 60 - a], a]


prx = {20, 80}; pry = {-2, 24}; pra = {prx, pry}; aratio =
 Differences[pry]/Differences[prx];

LocLatticeTrack[yval_] :=
 Block[{}, llt = Table[LocLattice[{i, yval}], {i, 10, 80, 1.2}];
  posM = llt [[All, 1]];
  listDensityBubble =
   Show[lp, g2,
    ListPlot[posM, PlotStyle -> {Magenta},
     PlotMarkers -> \[FivePointedStar]], PlotRange -> pra,
    AspectRatio -> aratio[[1]], ImagePadding -> {{30, 30}, {30, 0}}];
  lpang = Show[
    ListPlot[Transpose[{llt[[All, 1, 1]], Map[m60, llt[[All, 4]]]}],
     PlotMarkers -> {\[FivePointedStar]}, PlotStyle -> Magenta,
     Joined -> True, Frame -> True, PlotRange -> {prx, All}],
    AspectRatio -> aratio[[1]], ImagePadding -> {{30, 30}, {4, 0}},
    GridLines -> {gridx, None}];
  ava[tstep] = Transpose[{llt[[All, 1, 1]], llt[[All, 5, 3]]}];
  latp = ListPlot[{Transpose[{llt[[All, 1, 1]], llt[[All, 5, 1]]}],
     Transpose[{llt[[All, 1, 1]], llt[[All, 5, 2]]}],
     Transpose[{llt[[All, 1, 1]], llt[[All, 5, 3]]}]},
    Joined -> {False, False, True}, AspectRatio -> aratio[[1]],
    ImagePadding -> {{30, 30}, {4, 30}}, GridLines -> {gridx, None}];
  plotOrient[ToExpression[tstep]] =
```

```
   GraphicsGrid[{{latp}, {lpang}, {pathLP}, {gmin}, {listDensityBubble}},
    Frame -> True, ImageSize -> 600,
    PlotLabel ->
     Style[Framed[
       StringJoin["tstep=", ToString[tstep], "\n", ToString[countinbubble],
        " vortices in the Bubble \n" , ToString[countperbubble],
        " vortices on the Bubble perimeter "]], 16, blue, Bold,
      FontFamily -> "Helvetica", Background -> GrayLevel[0.8]]],
    FrameStyle -> Directive[blue]]]

grids[min_, max_] :=
  Join[Range[Ceiling[min], Floor[max], 2],
    Table[{j + 1, Dashed}, {j, Round[min], Round[max - 1], 1}]]

gridx = Table[i, {i, 20, 70, 10}];



createP[jj_] :=
 Block[{}, tstep = tstepL[[jj]]; Print[tstep];
 fileinFull[tstepLFull[[jj]]];
  cluste[six, five, seven]; orient1[vort]; orient3[dela];
  test = Cases[vort, {x_, y_} /; x > 20 && x < 80]; pathL = {};
  Table[{row2[i, test];, pathg[i]}, {i, 25, 75, 1}];
  Show[lp, g2, PlotRange -> All,
   PlotLabel ->
    StringJoin[ToString[countinbubble], " vortices in the Bubble \n" ,
     ToString[countperbubble], " vortices on the Bubble perimeter "]];
  pathL = {}; Table[{row2[i, test];, pathg[i]}, {i, 25, 75, 1}];
  pathLP = ListPlot[pathL, Joined -> True, GridLines -> { gridx, grids},
    AspectRatio -> aratio[[1]], ImagePadding -> {{30, 30}, {4, 0}},
    PlotRange -> {prx, {12, 28}}];
  minlatL = Table[LocLattice[vort[[i]]] // Last, {i, 1, Length[vort]}];
  gmin = Show[g2,
    Graphics[Map[gchoose, minlatL] /. gchoose[a__] -> {Magenta, a}],
    AspectRatio -> aratio[[1]], ImagePadding -> {{30, 30}, {4, 0}},
    PlotRange -> pra, GridLines -> {gridx, None}, Frame -> True];
  LocLattice[{0, 0}, True]; AppendTo[countBubbleC, dpos];
  Show[LocLatticeTrack[9]]]
```

Bibliography

[1] Amir, A. & Nelson, D. R. Dislocation-mediated growth of bacterial cell walls. *Proceedings of the National Academy of Sciences* **109**, 9833–9838 (2012).

[2] Chen, C.-C. *et al.* Three-dimensional imaging of dislocations in a nanoparticle at atomic resolution. *Nature* **496**, 74–77 (2013).

[3] CAE. University of wisconsin-madison,computer-aided engineering (2015). URL `http://homepages.cae.wisc.edu/~stone/bubbleraftmovies.htm`.

[4] Kuijk, A., Byelov, D. V., Petukhov, A. V., van Blaaderen, A. & Imhof, A. Phase behavior of colloidal silica rods. *Faraday Discuss.* **159**, 181–199 (2012).

[5] Harada, K. *et al.* Direct observation of vortex dynamics in superconducting films with regular arrays of defects. *Science* **274**, 1167–1170 (1996).

[6] Kes, P. H., Kokubo, N. & Besseling, R. Vortex matter driven through mesoscopic channels. *Physica C: Superconductivity* **408**, 478 – 481 (2004).

[7] Tinkham. *Introduction to Superconductivity (2nd Edition)* (McGraw Hill, USA, 1996).

[8] Tilley, D. T. . J. *Superfluidity and Superconductivity (3rd Edition)* (IOP Publishing, 1990).

[9] Adwaele. Image from wikipeadia (2012). URL `https://en.wikipedia.org/wiki/Macroscopic_quantum_phenomena#/media/File:Flux_lines_in_a_superconductor01.jpg`.

[10] Brandt, E. H. The flux-line lattice in superconductors. *Rep. Prog. Phys.* **58**, 1465 (1995).

[11] Koshelev, A. E. & Vinokur, V. M. Dynamic melting of the vortex lattice. *Phys. Rev. Lett.* **73**, 3580–3583 (1994).

[12] Marchetti, M. & Nelson, D. R. Dynamics of flux-line liquids in high-tc superconductors. *Physica C: Superconductivity* **174**, 40 – 62 (1991).

[13] Hull, D. & Bacon, D. J. *Introduction to Dislocations (4th Edition)* (Butterworth-Heinemann, 2001).

[14] Hirth, J. P. & Lothe, J. *Theory of Dislocations* (John Wiley and Sons, New York, 1982).

[15] Tarr, M. Metal basics (2015). URL `http://www.mtarr.co.uk/courses/topics/0131_mb/index.html`.

[16] Weertman, J. & Weertman, J. *Elementary Dislocation Theory* (The Macmillan Company, New York, 1965).

[17] Bir, L. P. & Lambin, P. Grain boundaries in graphene grown by chemical vapor deposition. *New Journal of Physics* **15**, 035024 (2013).

[18] Irvine, W. T. M., Vitelli, V. & Chaikin, P. M. Pleats in crystals on curved surfaces. *Nature* **468**, 947–951 (2010).

[19] Spencer, S. & Jensen, H. J. Absence of translational ordering in driven vortex lattices. *Phys. Rev. B* **55**, 8473–8481 (1997).

[20] Oswald, P. *Rheophysics - The Deformation and Flow of Matter* (Cambridge University Press, UK, 2009).

[21] Marchetti, M. C. & Nelson, D. R. Hydrodynamics of flux liquids. *Phys. Rev. B* **42**, 9938–9943 (1990).

[22] Kokubo, N., Besseling, R., Vinokur, V. & Kes, P. Mode locking of vortex matter driven through mesoscopic channels. *Phys. Rev. Lett.* **88**, 247004 (2002).

[23] Head, A. K. Edge dislocations in inhomogeneous media. *Proceedings of the Physical Society. Section B* **66**, 793 (1953).

[24] Irvine, W. T. M., Hollingsworth, A. D., Grier, D. G. & Chaikin, P. M. Dislocation reactions, grain boundaries, and irreversibility in two-dimensional lattices using topological tweezers. *Proceedings of the National Academy of Sciences* **110**, 15544–15548 (2013).

[25] Plourde, B. L. T. *et al.* Vortex distributions near surface steps observed by scanning squid microscopy. *Phys. Rev. B* **66**, 054529 (2002).

[26] Blatter, G., Feigelman, M. V., Geshkenbein, V. B., Larkin, A. I. & Vinokur, V. M. Vortices in high-temperature superconductors. *Reviews of Modern Physics* **66**, 1125–1388 (1994).

[27] Brass, A. & Jensen, H. J. Algorithm for computer simulations of flux-lattice melting in type-ii superconductors. *Phys. Rev. B* **39**, 9587–9590 (1989).

[28] Besseling, R., Kes, P. H., Dröse, T. & Vinokur, V. M. Depinning and dynamics of vortices confined in mesoscopic flow channels. *New Journal of Physics* **7**, 71 (2005).

[29] Kokubo, N., Besseling, R., Vinokur, V. & Kes, P. Mode locking of vortex matter driven through mesoscopic channels. *Phys. Rev. Lett.* **88**, 247004 (2002).

[30] Guillamon, I. *et al.* Enhancement of long range correlations in a 2d vortex lattice by an incommensurate 1d disorder potential. *Nat Phys* **10**, 851 – 856 (2014).

[31] Cole, D. *et al.* Ratchet without spatial asymmetry for controlling the motion of magnetic flux quanta using time-asymmetric drives. *Nat Mater* **5**, 305 (2006).

[32] Miguel, M.-C., Mughal, A. & Zapperi, S. Laminar flow of a sheared vortex crystal: Scars in flat geometry. *Phys. Rev. Lett.* **106**, 245501 (2011).

[33] Dong, J. M. Simulation of the vortex motion in high-tc superconductors. *Journal of Physics-Condensed Matter* **5**, 3359–3364 (1993).

[34] Reichhardt, C., Olson, C. J., Scalettar, R. T. & Zimányi, G. T. Commensurate and incommensurate vortex lattice melting in periodic pinning arrays. *Phys. Rev. B* **64**, 144509 (2001).

[35] Pruymboom, A., Kes, P. H., van der Drift, E. & Radelaar, S. Flux-line shear through narrow constraints in superconducting films. *Phys. Rev. Lett.* **60**, 1430–1433 (1988).

[36] Onnes, H. K. Further experiments with liquid helium. *Leiden Comm.* (1911).

[37] Meissner, W. & Ochsenfeld, R. Short initial announcements. *Naturwissenschaften* **21**, 787–788 (1933).

[38] Bednorz, J. & Mller, K. Possible hightc superconductivity in the ba-la-cu-o system. *Zeitschrift fr Physik B Condensed Matter* **64**, 189–193 (1986).

[39] Gao, L. *et al.* Superconductivity up to 164 k in $\mathrm{hgba_2ca_{m-1}cu_mo_{2m+2+\delta}}$ (m =1, 2, and 3) under quasihydrostatic pressures. *Phys. Rev. B* **50**, 4260–4263 (1994).

[40] Kim, Y. C., Thompson, J. R., Ossandon, J. G., Christen, D. K. & Paranthaman, M. Equilibrium superconducting properties of grain-aligned $\mathrm{hgba_2ca_2cu_3o_{8+\delta}}$. *Phys. Rev. B* **51**, 11767–11772 (1995).

[41] London, F. & London, H. The electromagnetic equations of the supraconductor. *Proceedings of the Royal Society of London Series A-Mathematical and Physical Sciences* **149**, 0071–0088 (1935).

[42] Daunt, J. G. & Mendelssohn, K. An Experiment on the Mechanism of Superconductivity. *Proceedings of the Royal Society of London Series A-Mathematical and Physical Sciences* **185**, 225–239 (1946).

[43] Corak, W. S., Goodman, B. B., Satterthwaite, C. B. & Wexler, A. Exponential Temperature Dependence of the Electronic Specific Heat of Superconducting Vanadium. *Physical Review* **96**, 1442–1444 (1954).

[44] Glover, R. E. & Tinkham, M. Transmission of Superconducting Films at Millimeter-Microwave and Far Infrared Frequencies. *Physical Review* **104**, 844–845 (1956).

[45] Glover, R. E. & Tinkham, M. Conductivity of Superconducting Films for Photon Energies between 0.3 and 40K-Tc. *Physical Review* **108**, 243–256 (1957).

[46] Ginzburg, V. L. & Landau, L. D. *Zh. Eksperim. i Teor. Fiz.* **20**, 1064 (1950).

[47] Gor'kov, L. P. *Zh. Eksperim. i Teor. Fiz.* **36**, 1918 (1959).

[48] Foundation, T. N. P. Nobel prize biography page (2003). URL `http://www.nobelprize.org/nobel_prizes/physics/laureates/2003/abrikosov-bio.html`.

[49] Abrikosov, A. A. On the magnetic properties of superconductors of the second group. *Soviet Physics JETP-USSR* **5**, 1174–1183 (1957).

[50] Cribier, D., Jacrot, B., Rao, L. M. & Farnoux, B. *Phys. Lett.* **9**, 106 (1964).

[51] Essman, U. & Trauble, H. The direct observation of individual flux lines in type ii superconductors. *Phys. Lett.* **24A**, 526 (1967).

[52] Hess, H. F., Robinson, R. B., Dynes, R. C., Valles, J. M. & Waszczak, J. V. Scanning-tunneling-microscope observation of the abrikosov flux lattice and the density of states near and inside a fluxoid. *Phys. Rev. Lett.* **62**, 214–216 (1989).

[53] Hess, H. F., Robinson, R. B. & Waszczak, J. V. Vortex-core structure observed with a scanning tunneling microscope. *Phys. Rev. Lett.* **64**, 2711–2714 (1990).

[54] Bending, S. J., Vonklitzing, K. & Ploog, K. 2-Dimensional Electron-Gas as a Flux Detector for a Type-II Superconducting Film. *Physical Review B* **42**, 9859–9864 (1990).

[55] Stoddart, S. T., Bending, S. J., Geim, A. K. & Henini, M. Quantum-Resolved Investigations of Flux Dynamics - Collective and Single Vortex Effects. *Physical Review Letters* **71**, 3854–3857 (1993).

[56] Schuster, T. *et al.* Flux penetration into yba2cu3ox thin films covering substrate step edges. *Applied Physics Letters* **62**, 768–770 (1993).

[57] Brüll, l. P., Kirchgässner, D. & Leiderer, P. *Physica* **182C**, 339 (1991).

[58] Brawner, D. A. & Ong, N. P. *J. Appl. Phys.* **73**, 3890 (1993).

[59] Brawner, D. A., Ong, N. P. & Wang, Z. Z. *Phys. Rev. B* **47**, 1156 (1993).

[60] Xing, W., Heinrich, B., Hu, Z., Fife, A. A. & Cragg, A. R. *J. Appl. Phys.* **76**, 4244 (1994).

[61] Tamegai, T. *et al. Phys. Rev. B* **45**, 8201 (1992).

[62] Zeldov, E. *et al.* Geometrical barriers in high-temperature superconductors. *Phys. Rev. Lett.* **73**, 1428–1431 (1994).

[63] Gammel, P. L. *et al.* Observation of hexagonally correlated flux quanta in $yba_2cu_3o_7$. *Phys. Rev. Lett.* **59**, 2592–2595 (1987).

[64] Kes, P. H. & Tsuei, C. C. Two-Dimensional Collective Flux Pinning, Defects, and Structural Relaxation in Amorphous Superconducting Films. *Physical Review B* **28**, 5126–5139 (1983).

[65] Reichhardt, C. & Zimanyi, G. Melting of moving vortex lattices in systems with periodic pinning. *Physical Review B* **61**, 14354–14357 (2000).

[66] Barrozo, P., Moreira, A. A., Aguiar, J. A. & Andrade, J. S. Model of overdamped motion of interacting magnetic vortices through narrow superconducting channels. *Phys. Rev. B* **80**, 104513 (2009).

[67] Jensen, H. J. Simulations of relaxation, pinning and melting in flux lattices. In *Phase Transitions and Relaxation in Systems with Competing Energy Scales*, vol. 415, 129–185. NATO (Kluwer Academic Publ, Netherlands, 1993).

[68] Brandt, E. Elastic energy of the vortex state in type ii superconductors. i. high inductions. *Journal of Low Temperature Physics* **26**, 709–733 (1977).

[69] Brandt, E. H. Elastic and plastic properties of the flux-line lattice in type-ii superconductors. *Phys. Rev. B* **34**, 6514–6517 (1986).

[70] Bardeen, J. & Stephen, M. J. Theory of the motion of vortices in superconductors. *Phys. Rev.* **140**, A1197–A1207 (1965).

[71] Anderson, P. W. *Phys. Rev. Lett.* **9**, 309 (1962).

[72] Anderson, P. W. & Kim, Y. B. *Rev. Mod. Phys.* **36**, 39 (1964).

[73] Giamarchi, T. & Le Doussal, P. Moving glass phase of driven lattices. *Phys. Rev. Lett.* **76**, 3408–3411 (1996).

[74] Labusch, R. Elastic Constants f Fluxoid Lattice near Upper Critical Field. *Physica Status Solidi* **32**, 439–& (1969).

[75] Brandt, E. H. Treatment of Defects in Vortex Lattices of Type-2 Supraconductors in London Approximation. *Physica Status Solidi* **35**, 1027–& (1969).

[76] Wördenweber, R. & Kes, P. H. Dimensional crossover in collective flux pinning. *Phys. Rev. B* **34**, 494–497 (1986).

[77] Larkin, A. & Ovchinnikov, Y. Pinning in type ii superconductors. *Journal of Low Temperature Physics* **34**, 409–428 (1979).

[78] Berghuis, P., Vanderslot, A. & Kes, P. H. Dislocation-Mediated Vortex-Lattice Melting in Thin-Films Of Alpha-Nb3Ge. *Physical Review Letters* **65**, 2583–2586 (1990).

[79] Lindemann, F. The calculation of molecular natural frequencies. *Physikalische Zeitschrift* **11**, 609–612 (1910).

[80] Nelson, D. R. & Halperin, B. I. Dislocation-mediated melting in two dimensions. *Phys. Rev. B* **19**, 2457–2484 (1979).

[81] Huberman, B. A. & Doniach, S. Melting of 2-Dimensional Vortex Lattices. *Physical Review Letters* **43**, 950–952 (1979).

[82] Fisher, D. S. Flux-lattice melting in thin-film superconductors. *Phys. Rev. B* **22**, 1190–1199 (1980).

[83] Berezinskii, V. L. *Zh. Eksp. Teor. Fiz.* **59**, 907 (1970).

[84] Kosterlitz, J. M. & Thouless, D. I. *J. Phys. C: Solid State Phys.* **6**, 1181 (1973).

[85] Šášik, R. & Stroud, D. Flux-lattice melting in layered superconductors. *Phys. Rev. B* **48**, 9938–9941 (1993).

[86] Franz, M. & Teitel, S. Vortex lattice melting in 2d superconductors and josephson arrays. *Phys. Rev. Lett.* **73**, 480–483 (1994).

[87] Schmidt, M. F., Israeloff, N. E. & Goldman, A. M. Vortex-lattice melting in nb. *Phys. Rev. Lett.* **70**, 2162–2165 (1993).

[88] Theunissen, M. H., Van der Drift, E. & Kes, P. H. Size effects in flow of flux-line solids and liquids. *Phys. Rev. Lett.* **77**, 159–162 (1996).

[89] Blakemore, J. S. *Solid State Physics - Second Edition* (Cambridge University Press, UK, 1974).

[90] Frenkel, J. *Z. Phys.* **37**, 572 (1926).

[91] Brenner, S. S. *Properties of Whiskers - Growth and Perfection of Crystals* (John Wiley and Sons, New York, 1958).

[92] Orowan, E. *Z. Phys.* **89**, 605, 634 (1934).

[93] Polanyi, J. *Z. Phys.* **89**, 660 (1934).

[94] Taylor, G. I. *Proc. Roy. Soc.* **A145**, 362 (1926).

[95] Peierls, R. The size of a dislocation. *Proc. Phys. Soc.* **52**, 34 (1940).

[96] Nabarro, F. R. N. Dislocations in a simple cubic lattice. *Proc. Phys. Soc.* **59**, 256 (1947).

[97] Burgers, J. M. *Proc. Kon. Ned. Akad. Wetenschap.* **42**, 293, 378 (1939).

[98] Frank, F. C. *Phil. Mag.* **42**, 809 (1951).

[99] Nabarro, F. R. N. *Dislocations in Solids - Vol 1* (Elsevier North-Holland, New York, 1979).

[100] Peach, M. & Koehler, J. S. The force exerted on dislocations and the stress fields produced by them. *Phys. Rev.* **80**, 436 (1950).

[101] Upmanyu, M., Srolovitz, D., Lobkovsky, A., Warren, J. & Carter, W. Simultaneous grain boundary migration and grain rotation. *Acta Materialia* **54**, 1707–1719 (2006).

[102] Vogel, F. L., Pfann, W. G., Corey, H. E. & Thomas, E. E. Observations of dislocations in lineage boundaries in germanium. *Phys. Rev.* **90**, 489–490 (1953).

[103] Hirsch, P. B., Horne, R. W. & Whelan, M. J. Direct observations of the arrangement and motion of dislocations in aluminum. *Phil. Mag.* **1**, 677 (1956).

[104] Hedges, J. M. & Mitchell, J. W. The Observation of Polyhedral Sub-Structures in Crystals of Silver Bromide. *Phil. Mag.* **44**, 223–224 (1953).

[105] de Berg, M., Cheong, O., van Kreveld, M. & Overmars, M. *Computational Geometry - Algorithms and Applications (3rd Edition)* (2010).

[106] Paterson, A. *A First Course on Fluid Dynamics* (Cambridge University Press, UK, 1983).

[107] Cross, M. M. *J. Colliod Sci.* **20**, 417 (1965).

[108] Langevin, P. Sur la thèorie du mouvement brownien. *PC. R. Acad. Sci. (Paris)* **146**, 530–533 (1908).

[109] Lemons, D. S. & Gythiel, A. Paul Langevin's 1908 paper "On the Theory of Brownian Motion" ["Sur la théorie du mouvement brownien," C. R. Acad. Sci. (Paris) 146, 530-533 (1908)]. *American Journal of Physics* **65**, 1079–1081 (1997).

[110] Einstein, A. The motion of elements suspended in static liquids as claimed in the molecular kinetic theory of heat. *Annalen Der Physik* **17**, 549–560 (1905).

[111] Andersen, H. C. Molecular-Dynamics Simulations at Constant Pressure and-or Temperature. *Journal of Chemical Physics* **72**, 2384–2393 (1980).

[112] Plimpton, S. Fast Parallel Algorithms for Short-Range Molecular-Dynamics. *Journal of Computational Physics* **117**, 1–19 (1995).

[113] A., A. J., Lorenz, C. A. & Travesset, A. General purpose molecular dynamics simulations fully implemented on graphics processing units. *Journal of Computational Physics* **227**, 5342 – 5359 (2008).

[114] Rapaport, D. C. *The Art of Molecular Dynamics Simulation* (Cambridge University Press, Cambridge, UK, 1995).

[115] Thompson, P. A. & Robbins, M. O. Shear flow near solids: Epitaxial order and flow boundary conditions. *Phys. Rev. A* **41**, 6830–6837 (1990).

[116] Batchelor, G. K. *An Introduction of Fluid Dynamics* (Cambridge University Press, UK, 2000).

[117] Eskildsen, M. R., Forgan, E. M. & Kawano-Furukawa, H. Vortex structures, penetration depth and pairing in iron-based superconductors studied by small-angle neutron scattering. *Reports on Progress in Physics* **74**, 124504 (2011).

[118] Lukyanchuk, I. *et al.* Rayleigh instability of confined vortex droplets in critical superconductors. *Nat Phys* **11**, 21–25 (2015).

[119] Fasano, Y. & Menghini, M. Magnetic-decoration imaging of structural transitions induced in vortex matter. *Superconductor Science and Technology* **21**, 023001 (2008).

[120] Schall, P., Cohen, I., Weitz, D. & Spaepen, F. Visualizing dislocation nucleation by indenting colloidal crystals. *Nature* **440**, 319–323 (2006).

[121] Schall, P., Cohen, I., Weitz, D. & Spaepen, F. Visualization of dislocation dynamics in colloidal crystals. *Science* **305**, 1944–1948 (2004).

[122] Hirth, J. P. & Kubin, L. Dislocations in solids (volume 16) the 30th anniversary volume (2009).

[123] Amir, A. & Nelson, D. R. Dislocation-mediated growth of bacterial cell walls. *Proc. Natl. Acad. Sci. USA* **109**, 9833–9838 (2012).

[124] Amir, A., Babaeipour, F., McIntosh, D. B., Nelson, D. R. & Jun, S. Bending forces plastically deform growing bacterial cell walls. *Proceedings of the National Academy of Sciences* **111**, 5778–5783 (2014).

[125] Deutschländer, S. *et al.* Effects of boundaries on structure formation in low-dimensional colloid model systems near the liquid-solid-transition in equilibrium and in external fields and under shear. *The European Physical Journal Special Topics* **222**, 2973–2993 (2013).

[126] Basoalto, H. University of Birmingham - personal communication.

[127] Mahnke, R., Kaupužs, J. & Lubashevsky, I. *Physics of Stochastic Processes* (Wiley, Germany, 2009).

[128] Kierfeld, J. & Vinokur, V. Lindemann criterion and vortex lattice phase transitions in type-ii superconductors. *Phys. Rev. B* **69**, 024501 (2004).